MOFs in Motion
Piezoelectricity and Rotational Dynamics of linkers in Metal-Organic Frameworks

Mula, S.

Important note
To cite this publication, please use the final published version (if applicable).
Please check the document version above.

MOFs in Motion

Piezoelectricity and Rotational Dynamics of linkers in Metal–Organic Frameworks

Srinidhi Mula

MOFs in Motion

Piezoelectricity and Rotational Dynamics of linkers in Metal–Organic Frameworks

Dissertation

for the purpose of obtaining the degree of doctor
at Delft University of Technology,
by the authority of the Rector Magnificus prof.dr.ir.T.H.J.J. van der Hagen,
chair of the Board for Doctorates,
to be defended publicly on
Wednesday 20 March 2024 at 12:30 o'clock

by

Srinidhi MULA

Master of Science in Materials Science and Engineering,
University of Florida, Gainesville
born in Kazipet, India.

This dissertation has been approved by the promotors.

Composition of the doctoral committee:

Rector Magnificus	chairman
Prof. dr. F.C. Grozema,	Delft University of Technology, promotor
Dr. ir. M.A. van der Veen,	Delft University of Technology, promotor

Independent members:

Prof.dr. F. Kapteijn	Delft University of Technology
Prof.dr. E.A. Pidko	Delft University of Technology
Prof.dr. F.X. Coudert	Chimie ParisTech-PSL, France
Dr. A.B. Bansode	Delft University of Technology
Dr.ir. L. Vanduyfhuys	Ghent University , Belgium

Contents

Summary

Metal–organic frameworks (MOFs) are a class of hybrid materials with metal-based inorganic nodes connected by organic linkers via strong coordination bonds. These building blocks can be arranged in 3-D crystalline lattices to synthesize structures with varying pore sizes and a variety of structures (tuneability). These hybrid materials possess exceptional porosity and large surface areas, making them suitable for applications in gas separation and storage, catalysis, and biomedical fields. MOFs also exhibit remarkable flexibility, which is determined by the topology of the framework and the degrees of freedom between bond angles in the organic linkers or coordination bonds between the organic linkers and inorganic nodes. One among the major categories of flexibility in MOFs is the rotational dynamics of organic linkers. The structural dynamics can have a pronounced influence on gas adsorption, diffusion and optical properties. **Chapter 4** and **Chapter 5** study the rotational dynamics of terephthalate linkers in functionalized MIL-53 MOFs by varying the steric interactions between the linkers using computational methods like ab initio molecular dynamics and classical molecular dynamics.

Using the remarkable porosity, structural flexibility, and tuneability features of MOFs as central handles, in this thesis, we aim to study the (a) Piezoelectric properties in MOFs for their application as energy harvesters and (b) Rotational dynamics of linkers in MOFs. It is well-known that MOFs possess a high degree of flexibility and permanent porosity. High porosity of MOFs leads to low dielectric constants. This, together with higher flexibility of MOFs, makes them promising candidates for piezoelectric energy harvesting. Although all non-centrosymmetric MOFs are piezoelectric, their piezoresponse has hardly been studied thoroughly. **Chapter 2** and **Chapter 3** of this thesis will investigate the structure-property relationships of piezoelectric properties in MOFs through computational methods, and provide design guidelines that can contribute to the development of high-performing piezo-electrics.

Chapter 1 provides an overview of the existing piezoelectrics and their mechanical, piezoelectric, dielectric, and acoustic properties that are important for piezoelectric energy harvesting. The chapter highlights the potential of MOFs as piezoelectric energy harvesters based on the current literature on the piezoelectric, mechanical, and dielectric properties of MOFs. Further, the chapter discusses the types of rotational dynamics of linkers that occur in MOFs and their implications on the applications of MOFs. Finally, a brief discussion is presented on the computational techniques used in this thesis to study both topics.

In the **first part** of this thesis, we delve into the computational investigation of the piezoelectric properties of MOFs to explore their potential as energy harvesters. The piezoelectric constant d, crucial for energy harvesting applications, depends on the piezoelectric constant e and the flexibility or mechanical properties of the MOF framework, as shown in the equation $d = es$, where s represents the compliance constant. The piezoelectric constant e can be divided into two contributions: the clamped-ion and the internal strain piezoelectric constant. The internal strain contribution depends on the born effective charges (BEC)

and the relative change in positions of atoms due to the strain applied. In high-performing inorganic piezoelectrics of ABO_3 type, anomalously high BEC of the metals are responsible for a high piezoelectric constant e.

Chapter 2 of this thesis aims to systematically investigate the structure-property relationships of piezoelectric properties (e and d) in a specific subfamily of MOFs- Zeolitic Imidazolate Frameworks (ZIFs). Using Density Functional Theory (DFT), we have computed the piezoelectric and mechanical properties for six non-polar ZIFs with Zn/Cd metal nodes and varying substituents (R= CH_3 for ZIF-8/CdIF-1, CHO for ZIF-90, Cl for ZIF-Cl, NO_2 for ZIF-65/CdIF-8) on the imidazolate linker. The piezoelectric constant e values we obtained for ZIFs are relatively low (~0.01 C/m^2) compared to the conventional inorganic piezoelectric materials. CdIF-1 showed the highest magnitude of piezoelectric constant d with a theoretical value ranging from 38 pC/N to 46 pC/N. This high d value in CdIF-1 is primarily due to the MOF framework's low shear modulus or high flexibility. Although this value is lower than inorganic piezoelectrics like PZT, it is comparable to the d value of common organic piezoelectric PVDF. We have also estimated the figure of merit (FOM) of CdIF-1, using its d value and the dielectric constant of ZIF-8. The FOM of CdIF-1 is notably higher than that of inorganic PZT and organic PVDF, despite its d value being lower than that of PZT. This is due to the high porosity of MOFs, which results in their low dielectric constant.

Although the e values obtained in this study for ZIFs were low, it is possible to tune the structure of MOFs to achieve higher e values, potentially increasing the value of d. However, e values of MOFs have hardly been explored. To address this, **Chapter 3** involved the calculation of the piezoelectric constant e for a large database of MOFs that were previously synthesized. Starting from the computationally ready QMOF database, the initial MOF dataset for piezoelectric calculations was finalized by applying a few criteria related to the point group and total number of atoms in the structure. This work generated a database of piezoelectric constants e for 1263 MOF structures. The results from these calculations include the total piezoelectric tensor e, its two contributions, i.e., the clamped-ion and internal strain tensors, and the BECs of all the atoms in the unit cell.

In this study, the MOFs exhibit a wide range of piezoelectric constant e values (ranging between 0.004 C/m^2 and 1.55 C/m^2), with the highest value being almost two orders of magnitude higher than the e for ZIFs computed in chapter 2. Compared to organic polymers and metal-free perovskites, MOFs in this study exhibit up to an order of magnitude higher e values but compared to traditional inorganic ceramics, their piezoelectric constants e are an order of magnitude lower. The driving factor for achieving a higher e for MOFs in this study is the internal strain contribution, which varies depending on the MOF's structure. This contribution takes into account the BEC of all atoms within the MOF, including both the inorganic cations within the secondary building unit (SBU) and the atoms within the organic linkers of the MOF, as well as the relative changes in their atomic positions. Unlike inorganic ceramics like $BaTiO_3$, where a high BEC of inorganic cations results in a high e value, in MOFs, a high BEC value for inorganic cations does not necessarily correlate to a high e value. Therefore, the phenomenon for achieving a high e cannot be generalized across all MOFs.

Based on our findings of MOFs with e values exceeding 1.0 C/m^2, we have compiled a series of guidelines for the design of MOF structures that can lead to high e values. These guidelines include MOFs:

1. belonging to a polar point group.

2. having high BEC for the inorganic cation in combination with an anisotropic coordination environment around them due to long-short-long-short.... pattern of bonds organized in a polar manner.

3. coexisting different inorganic cations with varying BECs, linked together by organic linkers that are further polarly aligned along a specific direction.

4. the presence of polar molecules such as water, directly bonded to the inorganic cations and further aligned along a specific direction in the unit cell.

Additionally, MOFs with long-short-long-short-....bond patterns identified in this study can potentially be ferroelectric showing a spontaneous and reversible polarization upon the application of an electric field. That is, upon application of an external electric field the long-short-long... bonds could be altered to short-long-short-.... that could result in a change in sign of the polarity of the material, thus behaving as a ferroelectric material. This is especially advantageous for the processability of MOFs into energy harvesting devices.

In the **second part** of the thesis, we delved into the rotational dynamics of organic linkers in metal-organic frameworks, particularly the MIL-53 family with the terephthalate organic linkers. The rotational dynamics of linkers in MOFs is one of the four major categories of flexibility in MOFs. The organic linkers act as rotors and embedding them in MOF lattices provides a unique platform for tunable spacing of molecular rotors. A comprehensive understanding of rotational linker dynamics in MOFs has the potential to lead to novel applications, such as the design of artificial molecular machines or controlled rotation of polar linkers in the presence of an electric field for ferroelectric switching.

To utilize linker rotation to its fullest potential, it is important to engineer correlated dynamics between the linkers to achieve their cooperative functional motion. The linkers in MOFs are separated by adjustable free space, allowing for a wide range of linker dynamics to occur. In **Chapter 4**, the dynamics of the MIL-53(Al) family of linkers were examined, which have a topology with conveniently spaced rotors. By modifying the free space between the linkers through the functionalization of the phenylene groups, the rotor's steric environment can be adjusted. Through a combination of computational techniques such as DFT and ab initio molecular dynamics, along with experimental techniques such as solid-state ^2H NMR and broadband dielectric spectroscopies, the rotor dynamics of linkers in nitro and amino functionalized MIL-53 were analyzed. It was found that there are two extremes of linker dynamics - unfunctionalized phenylene units that can rotate independently and amino-functionalized phenylene units that cannot rotate due to increased steric hindrance in narrow pore configuration and intralinker hydrogen bonding. However, for nitro-functionalized phenylene linkers, complex dynamic behavior emerges that evolves with temperature in NO_2-MIL-53. With ab initio MD (finite temperature calculations) for a single unit cell, we see 60° and 120° jumps between the potential energy minima, consistent with ^2H SSNMR and DFT results. Ab initio MD (AIMD) results for a 211 unit cell with two rotating nitro phenylene linkers in the unit cell along the pore direction show correlated large and small angle motions when the nitro groups of the neighboring linkers along the pore direction are in proximity. This study marks the first identification of correlated rotational dynamics between neighboring linkers in MOFs, specifically in NO_2-MIL-53(Al).

The understanding of the correlated rotational linker dynamics in NO_2-MIL-53 in chapter 4 is based on the ab initio molecular dynamics simulations for a 211 unit cell. However, due to the periodic boundary conditions of the simulations, there are only two rotating linkers per MOF chain along the pore direction in a 211 unit cell. Because of this, the long-range effects of the linker dynamics could not be fully investigated. In addition, longer simulation times could not be reached due to the high computational cost of ab initio MD simulations, preventing the reliable determination of free energy profiles for the coupled linker dynamics in NO_2-MIL-53(Al).

To address these limitations, a force field was developed and validated in **Chapter 5** for studying the rotational linker dynamics of NO_2-MIL-53(Al) using classical molecular dynamics simulations for larger supercells. The force field was derived based on the data from the previous DFT, and AIMD simulations in chapter 4 and was used to simulate four and six rotating nitro phenylene linkers per MOF chain along the pore direction in larger unit cells of 422 and 622 respectively. The simulations revealed a distinct *PNPNPNPN....* arrangement of linkers where *P*= librations around 0°/±180° [planar] and *N*= librations between ±50° and ±120° [NonPlanar]. Here direct neighbors have planar and non planar angles, and alternate neighbors were either planar-planar or non planar-non planar. The planar linkers also underwent 180° rotational flips, resulting in the librations becoming wider or narrower for direct neighbors depending on whether the nitro group is pointing away from them or towards them respectively. The planar alternate neighbors are thus changing between the parallelly aligned state [(0°, 0°) or (±180°, ±180°)] and the anti-parallelly aligned state [(0°, ±180°)]. The correlated rotations of planar alternate neighbors occurred over nanoseconds, and the estimated free energy barrier for the 180° flips was around 24.375 kJ/mol at 300 K. The presence of correlated dynamics in these dipolar linkers over long length-scales occurring at nanoseconds timescales is desirable for applications in ferroelectric switching in the presence of an electric field and work in this chapter provides insight into the design for such applications.

Samenvatting

Metaal–organische roosters (Engels: metal-organic frameworks, MOFs) zijn een klasse van hybride materialen met op metaal gebaseerde anorganische knooppunten die via sterke coördinatiebindingen verbonden zijn met organische linkers. Deze verbindingen leiden tot 3D kristallijne roosters om structuren met verschillende poriegroottes en een verscheidenheid aan structuren (aanpasbaarheid). Deze hybride materialen hebben een uitzonderlijke porositeit en grote inwendige oppervlaktes, waardoor ze geschikt zijn voor toepassingen in gasscheiding en –opslag en katalyse, en biomedische toepassingen. MOFs vertonen ook een opmerkelijke structurele flexibiliteit, die wordt bepaald door de topologie van het rooster en de vrijheidsgraden tussen bindingshoeken in de organische linkers of coördinatiebindingen tussen de organische linkers en anorganische knooppunten. Eén van de belangrijkste categorieën van flexibiliteit in MOFs is de rotatiedynamica van organische linkers. De dynamica van de structuur kan een uitgesproken invloed hebben op gasadsorptie, -diffusie en optische eigenschappen. **Hoofdstuk 4** and **Hoofdstuk 5** onderzoeken de rotatiedynamica van tereftalaat-linkers in MIL–53 MOFs, waar verschillende functionele groepen de sterische interacties tussen de linkers variëren, met computationele methoden zoals ab initio moleculaire dynamica en klassieke moleculaire dynamica.

Met de opmerkelijke porositeit, structurele flexibiliteit en aanpasbaarheid van MOFs als centrale handvatten, richten we ons in dit proefschrift naast het bestuderen van de vermelde rotatiedynamica van de linkers, op het bestuderen van de piëzo-elektrische eigenschappen in MOFs voor hun toepassing om vibrationele energie te oogsten. De hoge porositeit van MOFs leidt namelijk tot lage diëlektrische constanten. Dit maakt ze, samen met de hoge structurele flexibiliteit van MOFs, veelbelovende kandidaten voor het oogsten van piëzo-elektrische energie. Hoewel alle niet-centrosymmetrische MOFs piëzo-elektrisch zijn, is hun piëzorespons nog nauwelijks bestudeerd. **Hoofdstuk 2** and **Hoofdstuk 3** van dit proefschrift zullen de structuur–eigenschap relaties van piëzo-elektrische eigenschappen in MOFs door middel van computationele methoden onderzoeken, en ontwerprichtlijnen geven die kunnen bijdragen aan de ontwikkeling van goed presterende piëzo-elektrische materialen voor het oogsten van mechanische energie.

Hoofdstuk 1 geeft een overzicht van de bestaande piëzo-elektrische materialen en hun mechanische, piëzo-elektrische, diëlektrische en akoestische eigenschappen die belangrijk zijn voor piëzo-elektrische energie-oogst. Het hoofdstuk belicht de potentie van MOFs als piëzo-elektrische energie-oogsters gebaseerd op de huidige literatuur over de piëzo-elektrische, mechanische en diëlektrische eigenschappen van MOFs. Verder bespreekt het hoofdstuk de soorten linker-rotatiedynamica die voorkomen in MOFs en hun implicaties voor de toepassingen van MOFs. Tot slot wordt een korte discussie gepresenteerd over de computationele technieken die in dit proefschrift gebruikt zijn om beide onderwerpen te bestuderen.

In het **eerste deel** van dit proefschrift verdiepen we ons in het computationele onderzoek van de piëzo-elektrische eigenschappen van MOFs om hun potentie om energie te oogsten

te onderzoeken. De piëzo-elektrische constante d, cruciaal voor dezetoepassingen, hangt af van de piëzo-elektrische constante e en de flexibiliteit of mechanische eigenschappen van het MOF-rooster, zoals weergegeven in de vergelijking $d = es$, waarbij s de elasticiteitsmodules voorstelt. De piëzo-elektrische constante e kan worden opgedeeld in twee bijdragen: de vastgeklemd-ion en de interne rek piëzo-elektrische constante. De interne rekbijdrage hangt af van de Born effectieve ladingen (Engels: born effective charges, BEC) en de relatieve verandering in positionering van atomen als gevolg van de aangebrachte rek. In goed presterende anorganische piëzo-elektrische materialen van het ABO_3–type zijn abnormaal hoge BEC van de metalen verantwoordelijk voor een hoge piëzo-elektrische constante e.

Hoofdstuk 2 van dit proefschrift is gericht op het systematisch onderzoeken van de structuur-eigenschap relaties van piëzo-elektrische eigenschappen (e en d) in een specifieke subfamilie van MOFs–zeolitische imidazolaat roosters (Engels: zeolitic imidazolate frameworks, ZIFs). Met behulp van dichtheidsfunctionaaltheorie (DFT) hebben we de piëzo-elektrische en mechanische eigenschappen berekend voor zes apolaire ZIFs met Zn/Cd metaalknooppunten en variërende substituenten (R= CH_3 voor ZIF-8/CdIF-1, CHO voor ZIF-90, Cl voor ZIF-Cl, NO_2 voor ZIF-65/CdIF-8) op de imidazolaat-linker. De waarden van de piëzo-elektrische constante e die we verkregen voor ZIFs zijn relatief laag (~0.01 C/m^2) in vergelijking met de conventionele anorganische piëzo-elektrische materialen. CdIF-1 toonde de hoogste grootte van de piëzo-elektrische constante d met een theoretische waarde tussen 38 pC/N to 46 pC/N. Deze hoge d-waarde in CdIF-1 is voornamelijk toe te schrijven aan de lage schuifmodulus of hoge structurele flexibiliteit van het MOF-rooster. Hoewel deze waarde lager is dan anorganische piëzo-elektrische materialen zoals PZT, is hij vergelijkbaar met de d-waarde van het gangbare organisch piëzo-elektrisch materiaal PVDF. We hebben ook het getal van verdienste (Engels: figure of merit, FOM) van CdIF-1 geschat aan de hand van de d-waarde en de diëlektrische constante van ZIF-8. Het FOM van CdIF-1 is beduidend hoger dan die van anorganisch PZT en organisch PVDF, ondanks dat de d-waarde lager is dan die van PZT. Dit komt door de hoge porositeit van MOFs, die resulteert in hun lage diëlektrische constante.

Hoewel de e-waarden die in dit onderzoek voor ZIFs werden verkregen laag waren, is het mogelijk om de structuur van MOFs af te stemmen om hogere e-waarden te verkrijgen, waardoor de waarde van d mogelijk toeneemt. De e-waarden van MOFs zijn echter nauwelijks onderzocht. Daarom werd in **hoofdstuk3** de piëzo-elektrische constante e berekend voor een grote database van eerder gesynthetiseerde MOFs. Uitgaande van de rekenklare QMOF-database werd de initiële MOF-dataset voor piëzo-elektrische berekeningen afgemaakt door het toepassen van een aantal criteria gerelateerd aan de puntgroep en het totale aantal atomen in de structuur. Dit werk genereerde een database van piëzo-elektrische constanten e voor 1263 MOF-structuren. De resultaten van deze berekeningen omvatten de totale piëzo-elektrische tensor e, zijn twee bijdragen, d.w.z. de vastgeklemd-ion- en interne-rektensoren, en de BECs van alle atomen in de eenheidscel.

In deze studie vertonen de MOFs een breed bereik van piëzo-elektrische constante e waarden (variërend tussen 0.004 C/m^2 en 1.55 C/m^2), waarbij de hoogste waarden bijna twee-orden van grootte hoger zijn dan de e's voor ZIFs berekend in hoofdstuk 2. Vergeleken met organische polymeren en metaalvrije perovskieten vertonen MOFs in deze studie tot een orde van grootte hogere e waarden, maar vergeleken met traditionele anorganische keramieken zijn hun piëzo-elektrische constanten e een orde van grootte lager. De aandrijvende factor voor het bereiken van een hogere e voor MOFs in deze studie is de interne-

rekbijdrage, die varieert afhankelijk van de structuur van de MOF. Deze bijdrage houdt rekening met de BEC van alle atomen binnen de MOF, inclusief zowel de anorganische kationen binnen de secundaire bouweenheid (Engels: secondary building unit, SBU) als de atomen in de organische linkers van de MOF, evenals de relatieve veranderingen van hun atoomposities. In tegenstelling tot anorganische keramieken zoals $BaTiO_3$, waar een hoge BEC van anorganische kationen resulteert in een hoge e waarde, hoeft in MOFs een hoge BEC-waarde voor anorganische kationen niet noodzakelijkerwijs te correleren met een hoge e waarde. Daarom kan het fenomeen voor het bereiken van een hoge e niet gegeneraliseerd worden voor alle MOFs.

Gebaseerd op onze bevindingen van MOFs met e waarden hoger dan $1.0\,C/m^2$, hebben we een reeks richtlijnen opgesteld voor het ontwerp van MOF-structuren die kunnen leiden tot hoge e-waarden. Deze richtlijnen omvatten MOFs:

1. die behoren tot een polaire puntgroep.

2. met een hoge BEC voor het anorganische kation in combinatie met een anisotrope coördinatieomgeving eromheen als gevolg van een lang-kort-lang-kort.... patroon van bindingen georganiseerd op een polaire manier.

3. met verschillende naast elkaar bestaande anorganische kationen met verschillende BEC's, aan elkaar gekoppeld door organische linkers die verder polair uitgelijnd zijn langs een specifieke richting.

4. de aanwezigheid van polaire moleculen zoals water, rechtstreeks gebonden aan de anorganische kationen en verder uitgelijnd langs een specifieke richting in de eenheidscel.

Bovendien kunnen MOFs met lang-kort-lang-kort-bindingenpatronen die in deze studie zijn geïdentificeerd mogelijk ferro-elektrisch zijn met een spontane en omkeerbare polarisatie bij aanleggen van een elektrisch veld. Dat wil zeggen, bij het aanleggen van een extern elektrisch veld kunnen de lang-kort-lang... bindingen worden veranderd in kort-lang-kort-lang.... wat kan resulteren in een verandering in het teken van de polariteit van het materiaal, waardoor het zich gedraagt als een ferro-elektrisch materiaal. Dit is vooral voordelig voor de productie van energie-oogstapparaten gebaseerd op deze materialen.

In het **tweede deel** van het proefschrift hebben we ons verdiept in de rotatiedynamica van organische verbindingen in metaal-organische roosters, in het bijzonder de MIL-53 familie met de tereftalaat organische linkers. De rotatiedynamica van linkers in MOFs is één van de vier hoofdcategorieën van flexibiliteit in MOFs. De organische linkers fungeren als rotors en het inbedden in MOF-roosters biedt een uniek platform voor het afstemmen van de afstand tussen moleculaire rotors. Een uitgebreid begrip van de linkerrotatiedynamica in MOFs kan leiden tot nieuwe toepassingen, zoals het ontwerp van kunstmatige moleculaire machines of gecontroleerde rotatie van polaire linkers in aanwezigheid van een elektrisch veld om ferro-elektrisch te schakelen.

Om het volledige potentieel van linkerrotatie te benutten, is het belangrijk om gecorreleerde dynamica tussen de linkers te ontwerpen om coöperatieve functionele beweging te bereiken. De linkers in MOFs worden gescheiden door aanpasbare vrije ruimte, waardoor een breed scala aan linkerdynamica kan optreden. In **hoofdstuk 4** werd de dynamica van de MIL-53(Al) familie van linkers onderzocht, die een topologie hebben met

gunstig geplaatste rotoren. Door de vrije ruimte tussen de linkers aan te passen door de functionalisatie van de fenyleengroepen, kan de sterische omgeving van de rotor worden aangepast. Door een combinatie van computationele technieken zoals DFT en ab initio moleculaire dynamica, samen met experimentele technieken zoals vastestof-^2H-NMR en breedband diëlektrische spectroscopie, werden de rotordynamica van linkers in nitro- en amino-gefunctionaliseerd MIL-53 geanalyseerd. Het bleek dat er twee uitersten van linkerdynamica zijn-niet-gefunctionaliseerde fenyleeneenheden die onafhankelijk kunnen roteren en amino-gefunctionaliseerde fenyleeneenheden die niet kunnen roteren vanwege verhoogde sterische hinder in nauwe porieconfiguratie en intralinkerwaterstofbruggen. Echter, voor nitro-gefunctionaliseerde fenyleenlinkers ontstaat een complex dynamisch gedrag dat evolueert met de temperatuur in NO_2-MIL-53. Met ab initio MD (eindige temperatuurberekeningen) voor een enkele eenheidscel zien we sprongen van 60° en 120° tussen de potentiële-energieminima, consistent met ^2H-SSNMR- en DFT-resultaten. Ab initio MD (AIMD) resultaten voor een 211 eenheidscel met twee roterende nitrofenyleenbindingen in de eenheidscel in de porierichting laten gecorreleerde grote en kleine rotatiebewegingen zien wanneer de nitrogroepen van de naburige linkers in de porierichting in de buurt zijn. Deze studie markeert de eerste identificatie van gecorreleerde rotatiedynamica tussen naburige linkers in MOFs, specifiek in NO_2-MIL-53(Al).

Het begrip van de gecorreleerde rotationele linkerdynamica in NO_2-MIL-53 in hoofdstuk 4 is gebaseerd op de ab initio moleculaire dynamica simulaties voor een 211 eenheidscel. Vanwege de periodieke randvoorwaarden van de simulaties zijn er echter maar twee roterende linkers per MOF-keten in de porierichting in een 211 eenheidscel. Hierdoor konden de lange-afstandseffecten van de linkerdynamica niet volledig worden onderzocht. Bovendien konden langere simulatietijden niet bereikt worden vanwege de hoge computationele kosten van ab initio MD simulaties, wat de betrouwbare bepaling van vrije-energieprofielen voor de gekoppelde linkerdynamica in NO_2-MIL-53(Al) verhindert.

Om deze beperkingen aan te pakken, werd een krachtveld ontwikkeld en gevalideerd in **hoofdstuk 5** voor het bestuderen van de rotationele linkerdynamica van NO_2-MIL-53(Al) met behulp van klassieke moleculaire dynamica simulaties voor grotere supercellen. Het krachtveld werd afgeleid op basis van de gegevens van de eerdere DFT- en AIMD-simulaties in hoofdstuk 4 en werd gebruikt om vier en zes naburige roterende nitrofenyleenbindingen in de porierichting te simuleren door grotere eenheidscellen van respectievelijk 422 en 622 te simuleren. De simulaties onthullen een duidelijke *PNPNPNPN....* rangschikking van linkers waarbij *P* = libraties rond 0°/±180° [vlak] en *N* = libraties tussen ±50° and ±120° [niet vlak]. Hier hebben directe buren vlakke en niet-vlakke conformaties, en afwisselende buren waren ofwel vlak-vlak of niet-vlak-niet-vlak. De vlakke linkers ondergingen ook 180°-rotatieomwentelingen, waardoor de libraties van de directe buren breder of smaller worden, afhankelijk van of de nitrogroep respectievelijk van hen weg of naar hen toe wijst. De vlakke op een na naaste buren veranderen dus tussen een parallel uitgelijnde toestand [(0°, 0°) or (±180°, ±180°)] en de anti-parallel uitgelijnde toestand [(0°, ±180°)]. De gecorreleerde rotaties van vlakke op een na naaste buren vonden plaats in nanoseconden en de geschatte vrije energiebarrière voor de 180°-omwentelingen was ongeveer 24.375 kJ/mol bij 300 K. De aanwezigheid van gecorreleerde dynamica in deze dipolaire linkers over lange lengteschalen die zich voordoen op nanoseconden tijdschalen is wenselijk voor toepassingen in ferro-elektrisch schakelen in aanwezigheid van een elektrisch veld en het werk in dit hoofdstuk geeft inzicht in het ontwerp voor dergelijke toepassingen.

Chapter 1

Introduction

1.1 Metal–Organic Frameworks: Introduction

Metal–Organic Frameworks (MOFs) are porous hybrid crystalline materials consisting of inorganic nodes or clusters and organic ligands as building blocks connected by strong coordination bonds. The arrangement of these building blocks allows for synthesizing well-defined periodic structures with varying pore sizes. Owing to their adaptability with the choice of building blocks (tuneability), the number of MOFs that are synthesized and studied has seen an explosive growth in the past two decades.[1] Among the unique properties of these hybrid materials, exceptionally high porosity and large surface areas have led to their application in gas separation and storage, catalysis and biomedical applications like drug delivery.[2]

Along with the high porosity and tuneable structures of MOFs as key properties, they are soft and have remarkable flexibility. The flexibility of MOF frameworks is usually seen under the influence of external stimuli like the presence of guest molecules, adsorption-desorption induced stress, mechanical stress and temperature. One representative example of these flexibility modes is sorption-induced linker reorientation in Zeolitic Imidazolate Framework, ZIF-8 [3] where the movement of the imidazolate linker (also called gate opening) causes expansion in pore size and adsorbs larger molecules than expected. Another example is, the swelling mode of flexibility observed in the MIL-88 family where the cell parameters and volume of the unitcell gradually change upon the uptake of solvent molecules.[4] Third example, is the breathing phenomenon in the MIL-53 family wherein reversible transitions in the structure of the MOF are seen. During this, substantial change occurs in the atomic positions and angles of the unit cell between the narrow pore and large pore phases.[5, 6] This breathing effect can be due to guest-induced stress or temperature in MIL-53.[7] Flexibility mode of breathing involves change in the dihedral angle between the plane of inorganic node and the plane of connecting bonds between the organic linker and inorganic node. Hence, this mode of flexibility is a cooperative effect from both the inorganic node and organic linkers of the MOF. Flexibility in general for MOFs is majorly due to the framework's topology and the degrees of freedom between bond angles in the connecting organic linkers or between the coordination bonds connecting the inorganic nodes and the organic linkers.

1.2 Motivation for work in this thesis

Using the exceptional porosity, structural flexibility, and tuneability features of MOFs as central handles, we study two important yet relatively unexplored topics in this thesis: **Piezoelectricity in metal–organic frameworks** and **Rotational dynamics of linkers in metal–organic frameworks**.

MOFs have huge potential as piezoelectric energy harvesters owing to their flexible frameworks. For a polar metal–organic framework, the application of a small strain could potentially lead to large changes in polarization implying a large electromechanical response. Additionally, due to the permanent porosity in MOFs, a very low dielectric constant can be achieved.[8–10] A high electromechanical response achieved by tuning the building blocks of MOFs, combined with their low dielectric constant presents a very interesting and potentially a new class of materials for energy harvesting. The relevant theory of piezoelectricity,

energy harvesting, and literature on currently used piezoelectrics are presented in section 1.3.

The study of rotational dynamics of linkers in MOFs has been gaining interest in the past few years due to its influence on properties like guest adsorption and diffusion, optical and mechanical properties.[11] Importantly, MOFs offer a unique platform to organize the molecular rotors, and motors in solid-state crystalline networks to achieve collectively working artificial molecular machines.[12] This thesis enables us to understand the design and existence of cooperative and long-range correlated dynamics in molecular rotors which remains a challenge for applications in stimuli-responsive solids.[13]

1.3 Piezoelectricity in Metal-Organic Frameworks

1.3.1 Discovery and history of piezoelectricity

Piezoelectric effect was first discovered in 1880 by Pierre and Jacques Curie while conducting experiments on a variety of crystals like Rochelle salt and quartz, that displayed surface charges when a mechanical stress was applied.[14] The word "piezo" in Greek means "to press". Hence, piezoelectricity was coined to this effect, meaning electricity is generated from pressure. Later in 1881, converse piezoelectricity was discovered by Lippman from the fundamental laws of thermodynamics [15] where applying an electric field to a crystal should result in the materials' deformation. This was later experimentally confirmed by the Curie brothers.

The first practical application of piezoelectric materials appeared during World War I, when Paul Langevin and his co-workers in France developed an ultrasonic submarine transducer based on thin quartz crystals to measure the depth of the ocean. Following this, piezoelectric materials were then used in widely known practical applications like microphones, quartz watches, and inkjet printers.[16]

1.3.2 Theory of Piezoelectricity

The phenomenon of piezoelectricity describes The coupling between the mechanical and electrical properties of materials. Direct piezoelectric effect is where an electric dipole moment is generated via the application of mechanical stress on a material and the converse piezoelectric effect is where mechanical strain is induced in the material when an electric field is applied. Piezoelectric materials are a class of materials with a non-centrosymmetric structure (lacking an inversion center in the crystal structure). The electromechanical coupling in piezoelectric materials is described mathematically in the IEEE standard for piezoelectricity by a set of four constitutive equations relevant to the work in this thesis.[17] All the equations in the IEEE standard are based on linear piezoelectricity in which the elastic, piezoelectric, and dielectric coefficients are treated as constants independent of the magnitude and frequency of applied mechanical stresses and electric fields.

$$T_{ij} = c_{ijkl}^{E} S_{kl} - e_{kij} E_k \tag{1.1}$$

$$D_i = e_{ikl} S_{kl} + \varepsilon_{ik}^{S} E_k \tag{1.2}$$

3

$$S_{ij} = s_{ijkl}^{E} T_{kl} + d_{kij} E_k \qquad (1.3)$$

$$D_i = d_{ikl} T_{kl} + \varepsilon_{ik}^{S} E_k \qquad (1.4)$$

where T_{ij}/T_{kl} : second rank stress tensor [N/m^2], c_{ijkl}^{E} : fourth rank elastic stiffness tensor [N/m^2], S_{kl}/S_{ij} : second rank strain tensor (dimensionless), E_k : first rank electric field component [V/m], D_i : first rank electric displacement (polarization) [C/m^2], ε_{ik}^{S} : second rank dielectric constant [F/m], s_{ijkl}^{E} : fourth rank elastic compliance tensor [m^2/N]. **e_{ikl}/e_{kij} and d_{ikl}/d_{kij} are third rank piezoelectric tensors with units** C/m^2 **and** pC/N.

The coupling between the electrical and mechanical properties of materials is represented pictorially by the Heckmann diagram shown in Figure 1.1 adapted from the book by JF Nye.[18] In order to write the elastic and piezoelectric tensor in the form of a matrix, a
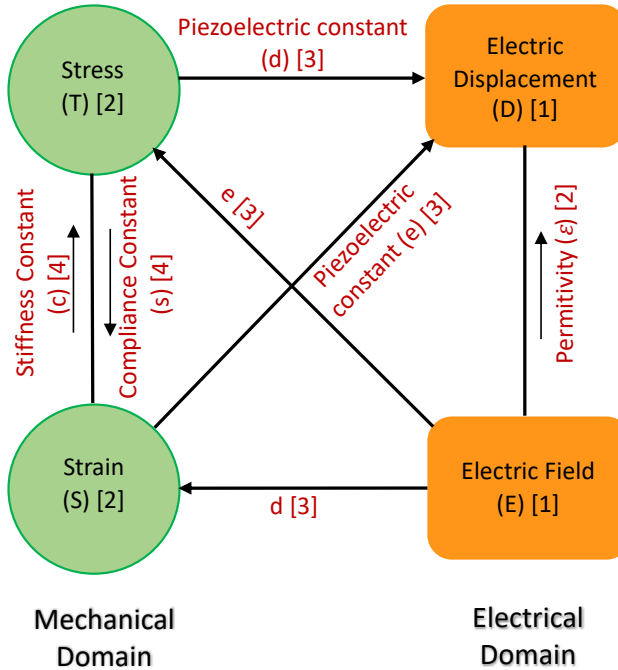
Figure 1.1: Part of Heckmann diagram showing the relation between mechanical and electrical properties, various variables, and their symbols. The tensor rank of the properties and variables is shown in square brackets.

compressed matrix notation is used instead of tensor notation. This is called the Voigt notation. This means ij or kl are replaced by p or q where $i, j, k, l = 1, 2, 3$ (cartesian axis x,y,z) and p, q take the values 1, 2, 3, 4, 5, 6 according to the notation shown in Table 1.1. The elastic and piezoelectric tensors can then be written as $c_{ijkl}^{E} \equiv c_{pq}^{E}$, $s_{ijkl}^{E} \equiv s_{pq}^{E}$, $e_{ikl} \equiv e_{ip}$ and $d_{ikl} \equiv d_{ip}$.

Table 1.1: Tensor to Matrix Notation

ij or kl	p or q
11	1
22	2
33	3
23 or 32	4
31 or 13	5
12 or 21	6

The elastic stiffness c (and analogously the compliance tensor s) can be written in the matrix form shown below.

$$
c = \begin{bmatrix}
c_{11} & c_{12} & c_{13} & c_{14} & c_{15} & c_{16} \\
c_{21} & c_{22} & c_{23} & c_{24} & c_{25} & c_{26} \\
c_{31} & c_{32} & c_{33} & c_{34} & c_{35} & c_{36} \\
c_{41} & c_{42} & c_{43} & c_{44} & c_{45} & c_{46} \\
c_{51} & c_{52} & c_{53} & c_{54} & c_{55} & c_{56} \\
c_{61} & c_{62} & c_{63} & c_{64} & c_{65} & c_{66}
\end{bmatrix}
$$

Various elastic properties of a material like the Young's modulus, the shear modulus, and poisson ratio can be computed from a tensorial analysis of the elastic stiffness tensor. Similarly the piezoelectric tensor d (analogously the piezoelectric tensor e) in matrix form is

$$
d = \begin{bmatrix}
d_{11} & d_{12} & d_{13} & d_{14} & d_{15} & d_{16} \\
d_{21} & d_{22} & d_{23} & d_{24} & d_{25} & d_{26} \\
d_{31} & d_{32} & d_{33} & d_{34} & d_{35} & d_{36}
\end{bmatrix}
$$

The elastic stiffness tensor and the compliance tensor are related by $c_{pr}^{E} s_{qr}^{E} = \delta_{pq}$ where δ_{pq} is a 6 by 6 unit matrix.[17] The compliance tensor (s) is the inverse of the stiffness tensor (c). Piezoelectric tensors e, d are related by

$$
e_{ip} = d_{iq} c_{qp}^{E} \tag{1.5}
$$

$$
d_{iq} = e_{ip} s_{pq}^{E} \tag{1.6}
$$

Computationally, the piezoelectric constant e_{ip} can be calculated as the change in polarization in the structure on application of an external strain with constant electric field written as

$$
e_{ip} = \left(\frac{\partial P_i}{\partial S_p} \right)_{E} \tag{1.7}
$$

1.3.3 Applications of piezoelectric materials in energy harvesting

Piezoelectric materials have a wide range of conventional applications in various fields including electronics, engineering, and healthcare. One of the applications is their use in various types of sensors, such as accelerometers, pressure sensors, and strain sensors to

measure and detect mechanical stimuli. They are also used in ultrasonic transducers that convert electrical energy to mechanical form and vice versa for generating and detecting the echo. In the healthcare and medical industry, they are mainly used in ultrasonic imaging.[19]

Another major application of piezoelectric materials that has been of significant interest to researchers is piezoelectric energy harvesting. It is a process in which vibrational energy available in the environment can be converted into and stored as electrical energy. At present, a large amount of electrical energy is stored in batteries. However, single-use batteries have an adverse effect on the environment, have a limited life span, and need frequent replacement. In such cases, piezoelectric energy harvesting could provide a renewable solution by harnessing the wasted vibrational energy in the environment.[20] Practical areas where piezoelectric energy harvesting can find relevant applications include for example in healthcare as in-ear hearing aids and pacemakers; in consumer electronics as wearables and self-powered navigation devices.[21] The performance of an energy harvester in practical applications is described by its figure of merit $FOM_{iq} = \frac{d_{iq}^2}{\varepsilon_0 \varepsilon_{iq}}$ where d_{iq} is the piezoelectric tensor, ε_{iq} is the dielectric constant of the material and ε_0 is the dielectric constant of free space. The FOM is used to describe and assess the properties of materials as energy harvesters.[22, 23] A high FOM for a material indicates an efficient energy harvester. This can be achieved by optimizing for the intrinsic properties in materials like **piezoresponse** d and **dielectric constant** ε of the material. Additional key factors that are considered important for energy harvesting applications are the **mechanical flexibility**, the **acoustic impedance** of the material, the **thermal stability**, and the **biocompatibility** of the material for their use in medical and wearable device applications.

1.3.4 Existing Piezoelectric materials

Inorganic ceramics

Piezoelectricity has been found in conventional materials like inorganic ceramic oxides of ABO_3 type (PZT-PbZrTiO$_3$, BaTiO$_3$, LiNbO$_3$, etc.), which have very high piezoelectric constants. However bulk inorganic ceramics are brittle. Therefore, large strains cannot be absorbed without causing damage to the piezoelectric layer. They require high processing temperatures and have high densities, making them unfavorable for wearable and flexible device applications. Several techniques have been used by researchers to fabricate them into thin films and nanowires, to form relatively flexible systems compared to bulk materials. Still, they have high dielectric constants thus reducing the figure of merit of energy harvesting. Moreover, PZT-based piezoelectrics with superior piezoelectric properties than other ABO_3 type ceramics contain bio incompatible lead limiting their use in wearable and medical applications.[24, 25]

Organic materials

Organic polymers are naturally flexible, durable, and easy to process compared to inorganic piezoelectric materials. The most common piezoelectric polymers include poly(vinylidene fluoride) (PVDF), its copolymers poly(vinylidene fluoride-co-trifluoroethylene) (PVDF-TrFE), poly(vinylidene fluoride-co-hexafluoropropylene) (P(VDF-HFP) and poly(L-lactic acid) (PLLA). Although inorganic ceramics have higher piezoresponse than polymers (see

Table 1.2), polymers have much lower dielectric constants; thereby enhancing the figure of merit of the harvester. Additionally, polymers better match the acoustic impedance of water and living tissues making them better equipped to harvest energy in these media.[24, 25]

In addition to widely researched ceramics and polymers, naturally occurring biological materials like bones, sugar cane, cellulose, peptide, etc. also show a piezoelectric response. They are non-toxic and biocompatible, making them viable materials for energy harvesting applications.[25]

Composites

To combine the favorable properties of both ceramics and polymers, composites have been synthesized by embedding nanosized ceramics in a polymer matrix. In composites, the inherent brittleness of ceramics is reduced through the polymer matrix's flexibility and the low piezoresponse of the polymers can be compensated by the piezoelectric properties of the ceramic particles. This is indeed shown to be true in the case of PZT/PVDF composites, that exhibit comparable flexibility to native PVDF with a greater piezoelectric coefficient than native PVDF.[25, 26]

Table 1.2: Piezoelectric constant d_{iq}, Dielectric constant ε_r and acoustic impedance z of inorganic ceramics, organic polymers, biological materials, composites, hybrid inorganic-organic perovskites and metal-free perovskites.

Material	Piezoelectric constant d_{ip} (pC/N)	Dielectric constant (ε_r)	Acoustic impedance z(MRayl)
Inorganic Ceramics[27, 28]			
PZT (PbZrTiO$_3$)	410	1300	36.15
BaTiO$_3$	260	1700	30
LiNbO$_3$	69	25	34
Organic Polymers[28, 29]			
PVDF	1.5 to 38.3	12	20
P(VDF-TrFE)	7 to 50	12	4.51
Biological Materials[25]			
Cellulose	26-60		
Composites[30]			
PZT$_{0.3}$-PVDF$_{0.7}$	84	73	
Hybrid Inorganic-Organic Perovskites[31–33]			
TMCM – MnCl$_3$	185		
TMCM – CdCl$_3$	220 to 240	35	10.61
Metal-free Perovskites[34, 35]			
MDABCO – NH$_4$Br$_3$	248 (calculated d_{x5})		
MDABCO – NH$_4$I$_3$	178 (calculated d_{x5})	< 40	

Organic-Inorganic Hybrid materials

In the recent years, hybrid materials like organic-inorganic perovskites have emerged as potential piezoelectric materials for energy harvesting. Organic-inorganic hybrid perovskites have a common general formula of ABX$_3$ (A = organic anion, B = metal ions, and X = halogens, CN$^-$, NO$_2^-$, HCCO$^-$ etc.) and other structures of the form ABX$_4$, ABX$_5$, and ABX$_6$ have also been synthesized.[36]. They have easy solution-based processing methods and show

high piezoelectric responses comparable to and larger than some of the inorganic ceramics shown in Table 1.2.[24]. Both inorganic and organic contributions in a single-phase crystalline structure provide opportunities for tuning the structure for specific properties. This promotes the potential application of hybrid perovskites in wearable piezoelectric devices. However the dielectric constant of some hybrid perovskites like $MAPbX_3$ ($CH_3NH_3PbX_3$) is not as low as the organic polymers, hence the figure of merit will be reduced.[37] Both lead-based and lead-free hybrid perovskites have been developed and the measured piezoresponse for some of them is shown in the Table 1.2.

Another step towards developing non-toxic metal-free piezoelectrics was achieved by the synthesis of metal-free organic perovskite with general formula $A(NH_4)X_3$.[34, 36] The organic composition allows for greater chemical diversity and flexibility than metal hybrid perovskites, making them favorable for flexible devices. Importantly, superior piezoelectric response was observed in some of the metal-free perovskites of type $MDABCO - NH_4 - X_3$ (MDABCO is N-methyl-N'-diazabicyclo[2,2,2] octonium).

1.3.5 Metal-Organic Frameworks as potential energy harvesters

The efficiency of an energy harvester, characterized by the figure of merit (FOM), depends on the piezoelectric response d_{iq} and dielectric constant ε_{iq} of the material. The piezoresponse d_{iq} further depends on the piezoelectric constant e_{ip} (change in polarization P_i with applied strain S_p) and elastic properties of the material (specifically elastic stiffness (c_{qp}) or the compliance constant (s_{pq})) as indicated in equation 1.6. The following sections summarize the mechanical, piezoelectric, dielectric, and acoustic properties of MOFs investigated so far.

1.3.5.1 Mechanical Properties

The mechanical properties of MOFs are of importance not just for piezoelectric applications, but also to determine the long-term reliability and to regulate the manufacturing and processing of these materials for practical applications. For example, for using MOFs as catalysts in reactors, it is vital to understand the thermomechanical stability of the material under temperature and pressure to avoid stress-induced structural collapse of the material during application.[38] Hence, the mechanical properties of a large number of MOFs have been reported in the literature.[39]

The piezoelectric properties (d) are dependent on the elastic properties of a material; d scales directly with compliance tensor ($s = 1/c$) as shown in equation 1.6. Another way to estimate the elastic properties of a material is through the Young's (E in Pa) and shear moduli (G in Pa) of the material, since the piezoelectric effect involves uniaxial and shear modes. Low values for Young's (E) and shear modulus (G) indicate the high flexibility of the framework and is beneficial for obtaining a high piezoelectric constant. Theoretically aggregate properties of a bulk crystalline solid, Young's and shear moduli can be calculated using averaging methods such as the Voigt-Reuss-Hill (VRH) scheme using the elastic stiffness and compliance tensors (c_{qp}/s_{pq}).[40] Young's (elastic) modulus E is a measure of the mechanical stiffness of the structures when subjected to uniaxial tensive or compressive strains. The shear modulus G is a measure of the torsional stiffness of the material subjected to shear strains.

Several reviews in the literature summarize the mechanical properties of sub-families in MOFs and the underlying effects on their mechanical properties due to structural factors, guest interactions, and framework density.[41, 42] Here, we briefly present the Young's and shear moduli of a few families of MOFs that were reported either experimentally or from ab initio DFT calculations. Note here that, the elastic moduli calculated from DFT could be higher than experimental values measured from nano-indentation methods. This can be attributed to the derivation scheme; DFT calculations for mechanical properties at 0 K are expected to yield higher elastic moduli than the experimental measurements at room temperature (~300 K) because of the variation in thermal vibrations in materials with temperature. The other thing to consider in DFT calculations is that the elastic property predictions for hybrid systems are sensitive to the choice of exchange-correlation functional and the pseudopotential used. We discuss here the magnitudes of Young's modulus and shear modulus for specific families of MOFs and compare them with other classes of piezoelectric materials to provide the reader with a broader context.

Young's Modulus (E)

Among the MOFs, the average young's modulus of widely known MOF-5 ($ZnO_4(BDC)_3$; BDC=1,4-benzenedicarboxylate) was measured from single-crystal nanoindentation to be around 7.9 GPa after accounting for the elastic anisotropy in a cubic crystal. This is along the direction parallel to rigid BDC linkers.[43]HKUST-1 (consisting of dimeric Cu-paddlewheel bridged by 1,3,5-benzenetricarboxylate ligands) is one of the prototypical carboxylate MOFs with Young's modulus (E) of almost up to 10 GPa.[44] Another family of widely known carboxylates MOFs are the MILs. The E values for MIL-53(Al) and other wine-rack type MILs were reported using DFT calculations. The expected E values for MIL-53(Al) and MIL-47 range between 0.9 GPa and 96.6 GPa for softest to stiffest directions.[45]

Mechanical properties of UiO-66 type MOF-one of the most stable MOFs was experimentally measured. UiO-66(Hf) possesses higher E values of 46 GPa to 104 GPa while UiO-66(Zr) has values 34 GPa to 100 GPa. By varying the substituent in the organic linkers, the mechanical properties are also varying in this family of MOFs.[46] Another DFT study on isoreticular series of Zr-based MIL-140(A-D) MOFs predicts E values of 3 GPa to 11.3 GPa along the softest direction and 99.2 GPa to 142 GPa along the stiffest direction.[47]

ZIFs (Zeolitic Imidazolate Frameworks) are another sub-family of MOFs known for their thermal and chemical stability. The structure of ZIFs consists of tetrahedral metal centers (Zn^{2+}, Co^{2+}, and Cd^{2+}) coordinated to nitrogen atoms of 1,3 positions of the imidazolate organic ligands. In the family of ZIFs, seven ZIFs (ZIF-zni, -4, -7, -8, -9, -20, and -68) with varying densities and topologies have been considered for investigation of their mechanical properties. Young's moduli for different ZIF systems scale non-linearly with framework density and the values range from 3.5 GPa to 9 GPa. Further, Young's moduli (E) of three ZIFs with the same sodalite topology were reported: ZIF-7, -8, -9 wherein the ZIF-7 (Zn^{2+}) and ZIF-9 (Co^{2+}) have bulky 2-benzimidazolate and ZIF-8 (Zn^{2+}) with 2-methylimidazolate as organic linkers. ZIF-7 and -9 have higher E values (6 GPa) compared to ZIF-8 (3 GPa) due to sterically bulkier organic linkers in the structure.[43]

Shear Modulus (G)

Experimental measurements of the shear modulus of hybrid materials like MOFs are limited, because of the requirement of sizeable samples for measurements using ultrasonic techniques.[43] Single crystal elastic properties of ZIF-8 were measured using Brillouin scattering and the shear modulus (G) was calculated from the elastic tensor. G_{min} was found to be around 0.97 GPa and G_{max} is 1.33 GPa for ZIF-8. For CuPA-2, G was estimated to be 10 GPa to 11 GPa. Using DFT calculations, the shear modulus was estimated for the MIL-140 series of MOFs: G_{min} 0.8 GPa to 3.2 GPa and G_{max} 26.8 GPa to 36.9 GPa. For MIL-53(Al) and MIL-47, G_{min} is reported to be 0.29 GPa, 0.35 GPa, and G_{max} 39.5 GPa and 40.8 GPa respectively.

To summarize, due to the hybrid inorganic-organic nature of MOFs structurally, the mechanical properties are inherently anisotropic, meaning they vary with the measuring direction. This is an influencing factor for piezoelectric tensorial properties (specifically d_{ip}) which depends on the magnitude of piezoelectric constant e_{iq} and the elastic properties (c_{qp}^{-1} or s_{pq}) in a specific direction. Generally, MOFs show low shear modulus compared to Young's modulus suggesting that they are more prone to deformation under shear stress than uniaxial stresses. Figure 1.2; materials property chart shows Young's modulus for different materials, including ceramics, polymers, hybrid framework materials, and MOFs. Young's modulus values of hybrid materials (including hybrid inorganic-organic perovskites, metal-free perovskites, and MOFs) lie in between the values of inorganic ceramics and organic polymers. In the hybrid framework domain, the lower bound is occupied by softer, porous MOFs (low E), while the dense hybrid frameworks have high E values. MOFs show lower values of Young's modulus than inorganic ceramics, indicating the high flexibility of MOF frameworks. This is especially favorable for obtaining a high piezoelectric constant d.

1.3.5.2 Piezoelectric Properties

Piezoelectric properties are observed in non-centrosymmetric materials, hence in principle all non-centrosymmetric MOFs are piezoelectric. However, very few MOFs have been tested experimentally or computationally for their piezoelectric properties. For measuring the piezoresponse in materials experimentally using quasi-static measurements like PM200 piezometer, it requires large single crystals of the material which are challenging to synthesize in the case of MOFs. Piezoelectricity can also be measured using piezoelectric force microscopy (PFM), but with PFM it is difficult to measure in a quantitative manner because of several nonpiezoelectric effects that can be induced during the measurement.

The piezoresponse for $Cd(Imazethapyr)_2$ which crystallizes in a non-centrosymmetric space group Fdd2 was measured using quasi-static measurements (measured using a PM200 piezometer) and the d_{33} value is around 60.1 pC/N.[48] In another work, for Mn-based homochiral coordination framework $Mn_2(D-cam)_2(2\text{-Hpao})_4$ (D-cam = D-(+)-camphoric acid; 2-Hpao = 2-pyridinealdoxime); experimentally measured d_{22} value for this material is around 6.9 pC/N.[49] There are other works on piezoelectricity in MOFs where the electromechanical (EM) response was measured using piezoelectric force microscopy (PFM).[50–53] Whereas they are worthy to be mentioned, as mentioned previously several nonpiezoelectric effects can induce additional contributions to PFM response, thus leading to misinterpretation. Several issues due to the calibration of the microscope and challenges
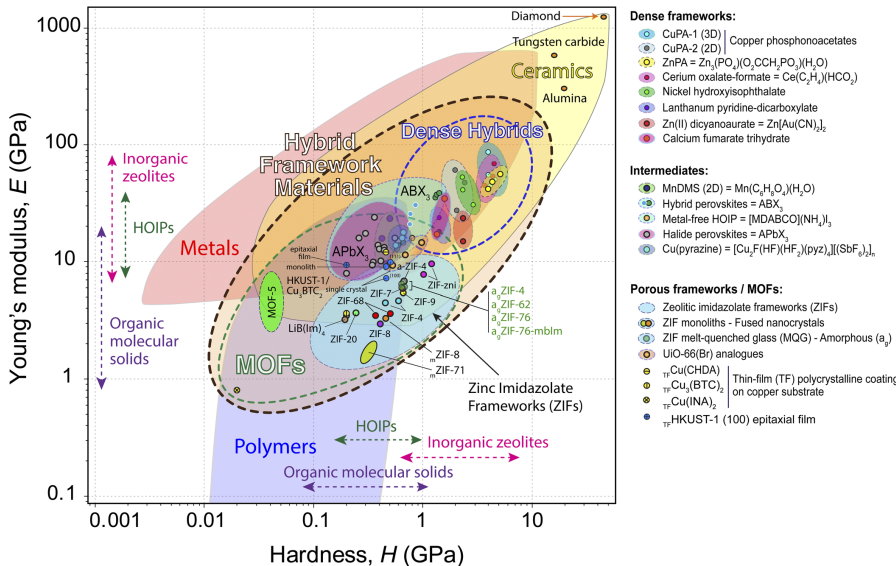
Figure 1.2: Young's modulus (E) plotted against the hardness (H) of MOFs and the wider families of materials, augmented with the latest (E, H) datasets (published up to May 2022) determined mostly by nanoindentation measurements. Reproduced with permission from ref [38]

in excluding the contribution of electrostatic and other forces have been discussed in the literature,[54–56] thus indicating that piezoelectric constants cannot be measured using PFM with high precision in most cases. In a recent theoretical work, the piezoelectric constant for QMOF-1 ($Zn(ISN)_2$; ISN = isonicotinate), QMOF-2 ($InH(BDC)_2$; BDC = 1,4-benzendicarboxylate) and $[DMA][Mg(HCOO)_3]$ (DMA = $(CH_3)_2(NH_2)^+$) was calculated using density functional perturbation theory (DFPT) and the values respectively were 23.64 pC/N (d_{14}), 2.52 pC/N (d_{14}) and −10.5 pC/N (d_{14}).[57] Most of the above-mentioned MOFs differ widely in their building units and structure, making it difficult to identify structure-property relationships. The goal of the chapters 2 and 3 in this thesis is to establish structure-property relationships for piezoelectric properties in MOFs to enable the design of better-performing piezoelectrics.

1.3.5.3 Dielectric and Acoustic Properties

A low dielectric constant is advantageous for obtaining a high figure of merit for piezoelectric energy harvesting. In MOFs, because of their high porosities, a very low dielectric constant is possible. Some of the most important families of MOFs for which the dielectric constant was investigated, experimentally or computationally are shown in Table 1.3. The values range between 1.3 to 6 which are much lower than the dielectric constants of other piezo-electric materials shown in Table 1.2, making them better candidates as piezoelectric energy harvesters. Note that the computationally obtained dielectric constants for MOFs are static dielectric constants and that the experimental determination via dielectric spectroscopy is

often done on air–MOF composites (pellets), both leading to some underestimation of the dielectric constant. Yet, the reported values are very low and for example, a study where the determination of the dielectric constant of ZIF-8 was performed via ellipsometry on a continuous film, a method not prone to underestimation reports a low value of 2.3.[8]

Table 1.3: Dielectric constant ε_r of Metal-Organic Frameworks

MOF	Dielectric constant (ε_r)
ZIF-8 [8]	2.33
$[Sr_2(1,3-bdc)_2]_n$[a][58]	2.40
$[Co(amtd)_2]_n$[b][10]	2.43
$[Mn(amtd)_2]_n$[b][10]	2.57
$[[Zn_2(L-trp)_2(bpe)(H_2O)_2] \cdot 2\,H_2O \cdot 2\,NO_3]_n$[c][59]	2.53
$[Pb(tab)_2(4,4'-bipy)](PF_6)_2$[d][60]	2.53
$[(Co_2(D-cam)_2(3-apt)_2(H_2O)_3)]_n$.5nH_2O [e][49]	2.81
$[(C_3H_7)_2NH_2][Cr_7NiF_8(O_2C_4H_5)_{16}]-MMA$[f][61]	2.90
$[Zn_2(Hbbim)_2(bbim)]_n$[g][62]	3.05
$[[Co(L-trp)(bpe)(H_2O)] \cdot H_2O \cdot NO_3]_n$[c][59]	3.30
$[Zn(TMPT)_2]_n$[h][63]	6.00

[a] 1,3-bdc = benzene-1,3-dicarboxylate
[b] amtd = 2-amino-5-mercapto-1,3,4-thiadiazole)
[c] L-trp = L-tryptophanate, bpe = 1,2-bis(4-pyridyl)ethylene)
[d] tab = 4(trimethylammonio)benzenethiolate, 4,4'-bipy = 4,4'-bipyridine.
[e] Dcam = D(+)-camphorate, 3-apt = 4-amino-3,5-bis(3-pyridyl)-1,2,4-triazolate
[f] MMA = methyl methacrylate
[g] H_2bbim = bisbenzimidazole
[h] TMPT= 5-(4-((1H-1,2,4-triazol-1-yl)methyl)phenyl)-2H-tetrazolate

For an efficient piezoelectric energy harvesting device, the acoustic properties of the harvesting material and the medium in which energy is being harvested should match each other. The acoustic impedance is a measure of the ease with which sound travels through a particular medium. It is calculated as the product of acoustic velocity and density of the material. Recent theoretical work on the acoustic properties of MOFs presented the longitudinal acoustic impedance values for a set of 19 MOFs.[57] Among them, the lowest values for acoustic impedance were reported for ZIF-8 [$Zn(mim)_2$, mim =2-methylimidazolate] and MAF-7 [$Zn(mtz)_2$, mtz = 3-methyl-1, 2, 4-triazolate] with values of 3.55 MRayl and 3.66 MRayl respectively. For some of the widely known MOFs like MOF-5 [$Zn_4O(BDC)_3$, BDC =1,4-benzendicarboxylate], MIL-47 [$V^{IV}(O)(BDC)$], MIL-53(Al)lp[$Al(OH)(BDC)$], and MIL-53(Ga) [$Ga(OH)(BDC)$] the values are shown in Table 1.4. The acoustic properties of MOFs are lower than inorganic ceramics and in the same order of magnitudes as organic polymers and hybrid piezoelectrics as seen from Table 1.2 and 1.4. More importantly, they are closer to values of harvesting media like water (1.45 -1.5 MRayl) and living tissue (1.99 MRayl).

1.4 Rotational Dynamics of Linkers in Metal–Organic Frameworks

Metal–organic frameworks are hybrid materials with organic ligands acting as linkers between inorganic building units through coordination bonds. The third-generation MOFs, also called soft porous crystals (SPCs), display fascinating structural dynamics in response

Table 1.4: Acoustic properties of Metal-Organic Frameworks

MOF [57]	Acoustic Impedance (MRayl)
ZIF-8	3.55
MAF-7	3.67
MOF-5	4.50
MIL-47	10.04
MIL-53(Al)	11.70
MIL-53 (Ga)	13.28

to external stimuli such as light, temperature, guest molecules, and electric fields.[64] These structural dynamics have a pronounced influence on gas adsorption, diffusion, and optical properties. The organic linkers are the flexible components in MOFs and the four major categories of flexibility in MOFs identified in the literature include breathing, swelling phenomena, linker rotation, and subnetwork displacement as shown in Figure 1.3.[5]
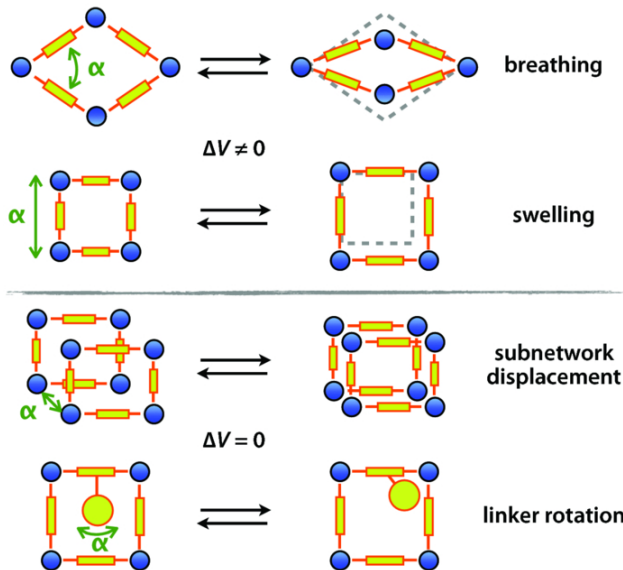
Figure 1.3: Schematics of different modes of flexibility in soft porous crystals. Reproduced with permission from ref [65]

In this thesis, among the different categories of flexibility, we specifically focus on understanding the rotational linker dynamics of MOFs. These organic linkers act as rotors and MOFs offer a unique platform for embedding these molecular rotors that can be spaced at tuneable distances in their crystalline lattices. Apart from the consequences of linker rotation on the adsorption properties, a deeper understanding of the rotational dynamics of linkers can pave the path to novel applications like the design of artificial molecular machines.[13]

1.4.1 Types of rotational dynamics in linkers

Michl and coworkers conceptualized the rotational motions in molecules was reviewed in the work by Michl *et al*[66] and defined them as rotor systems analogous to macroscopic machines. Definitions for various molecular rotor systems used in [66] which are of relevance here are:

a. **Molecular rotor**: a molecular system in which a molecule or part of a molecule rotates against another part of the molecule

b. **Rotator**: the part of the molecule or system that rotates against the rest

c. **Stator**: the stationary part of the system with respect to which the rotator turns

d. **Axle**: the portion of the molecule that carries the rotator and about which the rotator turns
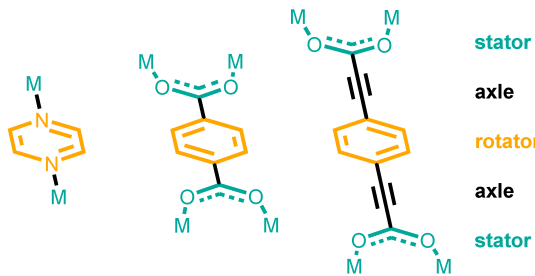
Figure 1.4: Common types of axles in metal–organic framework (MOF) rotor linkers. Reproduced from ref [11]

The above definitions of a rotator, stator, and axle for rotational molecules were adapted for metal–organic frameworks as shown in Figure 1.4. The inorganic building units along with the coordinated functional groups can be considered as the stator units. The axle is the portion of the molecule that carries the rotator and about which the rotator turns. The topic of rotational dynamics of linkers has been previously reviewed in detail in the work of Nelson *et al*.[11] Here, we present a brief overview of the types of rotational linker dynamics along with a few examples of MOFs.

The rotational dynamics of MOF linkers can be categorized into four groups: (shown in Figure 1.5)

A. Complete rotation

B. Partial rotation

C. Rotation of side groups

D. Mechanically interlocked molecule rotation
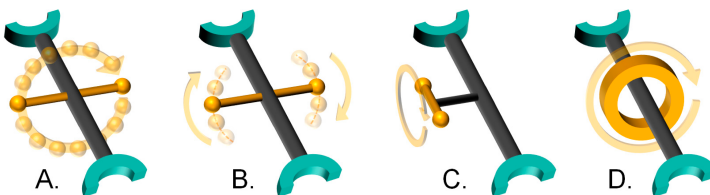
**Figure 1.5:** Illustration of the four types of rotational linker dynamics: (A). Complete rotation, (B). Partial rotation, (C). Side group rotation, (D). Mechanically interlocked molecule rotation. Reproduced from ref [11]

A. Complete rotation   A complete rotation of 360° often occurs in steps which are called jumps or flips. The nature of these flips will depend on the torsional potential of the rotor and the jump angles for the rotors will vary with structural factors. When the system's thermal energy is higher than the rotational energy barrier for conformational change, linkers can rotate freely, referred to as free rotation.
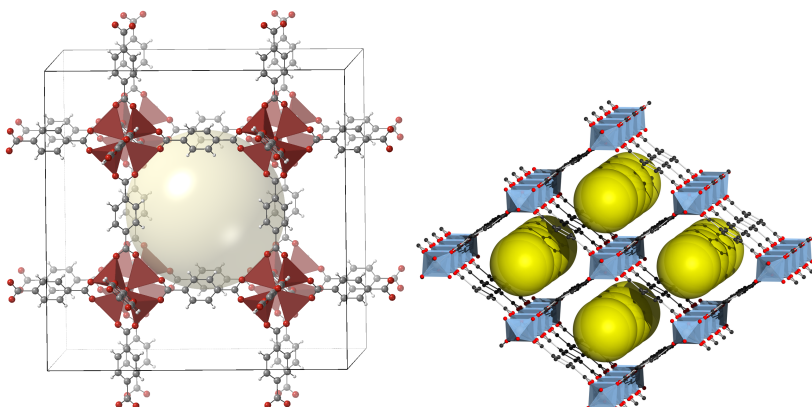

Figure 1.6: Structure of some terephthalate linker MOFs, MOF-5 (left) and MIL-53 (right)

Common examples where complete rotation of linkers is observed in MOFs with terephthalate (1,4-benzenedicarboxylate) linkers. In MOF-5, it was found that phenylene units are static at room temperature but undergo fast 180° (π flips) at 373 K. The activation energy barrier predicted from DFT calculations and the experimentally assigned barrier is around 52 kJ/mol. There is no steric hindrance on the rotating linkers in the MOF-5 due to the available pore space and the linker-to-linker distance in the structure. Hence the high energy barrier is mainly attributed to the electronic effects. The planar conformation of the terephthalate linkers is stabilized through π-electron delocalization between benzene rings and carboxylate planes and the rotation to a 90° conformation involves loss of this π-system delocalization. The same mechanism is also observed for other terephthalate-based MOF systems such as MIL-47(V), MIL-53(Al), MIL-53(Cr), UiO-66, and DMOF series. The rotational barriers for these systems range between 30 kJ/mol to 50 kJ/mol for varying metal centers. This indicates an intrinsic barrier for the rotating linker itself. Further variations in
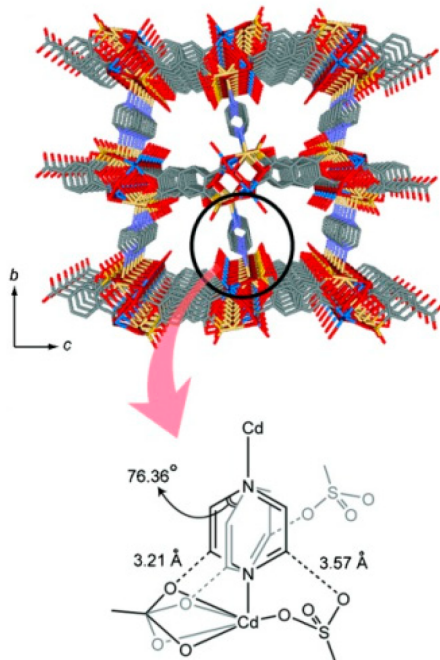
Figure 1.7: Structure of N-linker rotor-based MOFs; CdNa(2-stp)(pyz)$_0$ · 5 (H$_2$O) with an illustration of the two disorder positions of the linker. Reproduced with permission from ref [67]

the energy barrier can be due to the crystal lattice's steric effects and linkers' substituents with electron withdrawing or donating groups.[11]

Apart from terephthalate-based linkers, rotational dynamics of N-linker based MOFs were also observed. In CdNa(2-stp)(pyz)$_{0.5}$(H$_2$O), with layers consisting of Cd^{2+} and 2-sulfoterephthalate (2-stp) ions, the pillars are pyrazine (pyz) linkers.(see Figure 1.7) The complete 360° rotation of pyrazine linkers occurs in four steps around the N-N axis precisely at 0°, 76.4°, 180°, and 256.4°. The activation energy derived was around 7.7 kJ/mol.[67] This is very low compared to the energy barrier for the terephthalate linkers discussed above. This could be because the axle of the pyrazine rotator is a σ bond without any π electron delocalization effect in contrast to the terephthalate linkers. Hence the low electronic limitations for the rotation of pyrazine linkers.

Other examples of linker dynamics where complete rotation of linkers was observed include octacarboxylate and tri-branched, hexacarboxylate linker MOFs like MFM-180, MFM-181, MFM-112, and MFM-115.(see Figures 1.8,1.9) In these linkers, a complete rotation of 360° of a phenylene group occurs in a four-site model. For MFM-180 and MFM-181 the four jumps are unequal, where one involves smaller angle partial rotation at a temperature of 100 K and the other involves wider angle jumps occurring at a high temperature of 330 K. Because of the phenylene group's C2 symmetry, the smaller and wider jumps occur twice within a complete 360° rotation.[11]
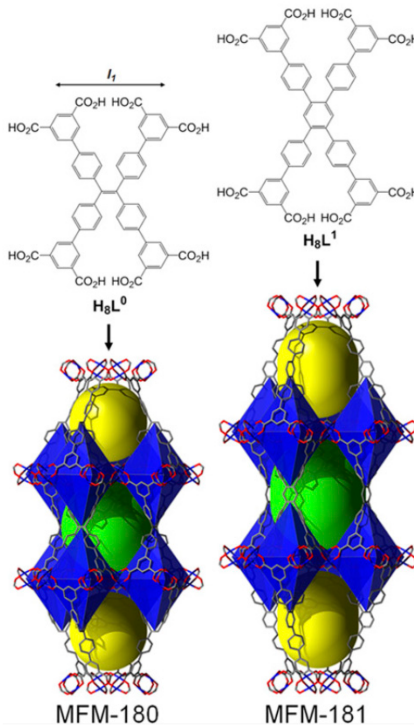
Figure 1.8: Structure of MFM-180 and MFM-181 and their respective linkers. Reproduced from [68]
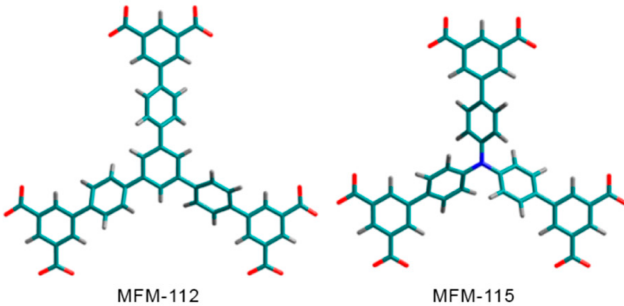
Figure 1.9: Structure of rotor linkers used in MFM-112, MFM-115. Reproduced from [69]

Recent works on linker dynamics aim to obtain very fast and free rotors in solid state that exist even at low temperatures.[70–73] In one case, a central p-phenylene unit (rotor) is connected through a triple bond (axle) to two pyrazole units 1,4-bis(1H-pyrazol-4-ylethynyl)benzene (BPEB) which coordinates to Zn^{2+} ions (Zn-BPEB). Very fast π flips were observed down to 150 K and a low activation energy of 2.0 kJ/mol is observed for

these linkers. In BODCA-MOF with Zn_4O SBU and high-symmetry bicyclo[2.2.2]octane dicarboxylate linkers; the linkers can achieve full rotation in six jumps of equal activation energy. These activation energies were as low as 0.5 kJ/mol to 0.77 kJ/mol. Two other works from Jacopo *et al.*,[72, 73] investigate the presence of fast motion of molecular rotors in the solid state up to very low temperatures of 2 K. In Zn-based MOF with a bicyclopentane rotator connected to dicarboxylate stators, the three-fold symmetry of the rotor conflicts with the four-fold symmetry of the carboxylates which are perpendicular to each other due to the cubic crystal cell of the Zn MOF and results in a flat energy profile (see Figure 1.10B). This frustrates the formation of stable conformations. MD simulations reveal the inertial behavior of the rotor, which combined with a flat energy profile allows for continuous, uni-directional, and fast rotation of the bicyclic units with an energy barrier up to ~ 0.026 kJ/mol.
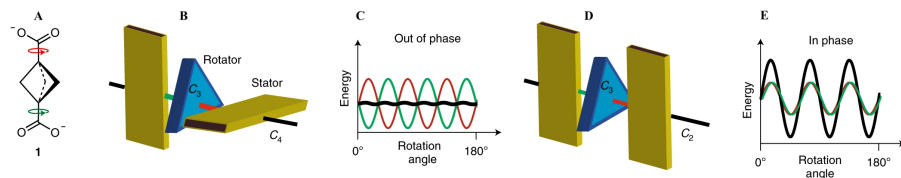
**Figure 1.10:** A) Chemical structure of the bicyclo[1.1.1]pentane-1,3-dicarboxylate linker. B,D) Sketches of the linker conformation highlighting the symmetry of both the rotator and stator. Dicarboxylate planes, as depicted by yellow parallelopipeds, are arranged perpendicular and parallel to each other. The blue triangles represent the bicyclic rotator. C,E) Individual torsional energy profiles about the bonds connecting the rotator to the stators (green and red lines) contributing out of phase to form an almost flat total energy profile (black line) (C) and in phase to increase energy barriers (E). Reproduced with permission from ref [72]

To summarize, we discussed the complete rotation of phenylene groups in terephthalate and N-based linkers. Additionally, recent efforts on achieving ultra-fast rotors in the solid state through molecular design and reaching rates as high as those in gas or liquid phases that can occur even at low temperatures have been highlighted. Large variations in rotor systems and the mechanism of rotation can be observed in MOFs, mainly from the frameworks' steric environment, and the rotors' electronic configuration. The number of steps that are taken by rotors for a complete rotation depends on the location of the maxima and minima of the torsional potential curve.

B. Partial rotation   This involves rotations that do not lead to complete rotations of 360°. Two types of dynamics can happen in partial rotations:

- Rotor performs short rotational motions about a minimum in torsional potential energy, also called librations.

- The rotor crosses the torsional barrier (maximum in potential energy) to achieve a second minima conformation, referred to as hops.

Systems with Type A motions may also exhibit librations around the local minima along with complete rotations. An example of this in MOFs is observed in UiO-66 for complete rotation of linkers, soft mode attributed to librations in MOF-5.[74, 75] In contrast to the MFM hexacarboxylate series discussed in Type A rotations where full rotation of linkers is observed, MFM-132 with 9,10-anthracenylene linkers do not show full rotation even at high temperatures of 573 K due to steric hindrance from adjacent groups. Yet, small amplitude librations of 32° were observed.


<center>(a)</center> <center>(b)</center>
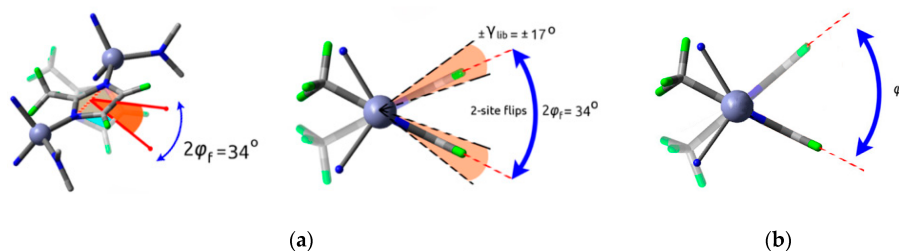
Figure 1.11: Diverse linker dynamics of 2-methylimidazolate linker in ZIF-8. (a) Small-amplitude two site hopping (34°) and fast librations (± 17°) centered on both hop positions; (b) slow, large-amplitude swing. Reproduced from [76]

Hops are thermally activated conformational changes between the local minima similar to Type A rotations, but they do not achieve a complete 360° rotation. MOFs where small amplitude librations and hops are observed is in the family of Zeolitic Imidazolate Frameworks (ZIFs). Multiple modes of rotations have been identified in the 2-methylimidazolate linker such as fast, small-angle librations, small-amplitude two-site hopping, and slow, large amplitude swinging between two sites as shown in Figure 1.11.[76] These small amplitude rotations in ZIFs have been shown to have a pronounced effect on the size of molecules that can fit through the pores. Partial rotations in ZIFs are also a result of the linker coordination geometry to the metal nodes being angular and deviating from 180°.

C. Rotation of side groups   In this type, the rotors are within the MOF linkers where they are a side group to the main linker. Hence, the main linker component can be considered the stator, and the functional group (rotor) is attached to it via a covalent bond (axle). One of the widely known examples of this kind is methylimidazolate in ZIF-8. Methyl C_3 rotations are observed around the C-C bond and the activation barrier is very low around 0.6 kJ/mol to 0.8 kJ/mol.[77, 78]

D. Mechanically interlocked molecule rotation   This rotation involves systems where the rotator is a separate molecule that is mechanically interlocked to the axle. Here, only weak interactions—such as dispersion forces and hydrogen bonds—are the basis of contact between the two. This is mainly observed in a separate class of MOFs called Metal–organic rotaxane frameworks (MORFs).[79, 80]

<center>19</center>

1.4.2 Implications of rotational dynamics on applications of MOFs

Diffusion and Adsorption

The rotational dynamics of linkers have a significant effect on the adsorption and diffusion properties of MOFs. The gate-opening effect is usually observed as a step or hysteresis in the adsorption isotherm due to a structural transition in the MOF. In some MOFs, the pore size predicted from XRD doesn't match with the size of molecules that can be adsorbed. Molecules larger than the pore size can diffuse into the pores. A typical example for this is seen in ZIF-8 crystals (Zn^{2+} and $-CH_3$ substituent) when submitted to a pressure up to 1.47 GPa via a methanol-ethanol hydrostatic mixture.[81] A phase transition to a previously unobserved phase is observed involving the rotation of methylimidazolate linkers. This resulted in an enlarged pore opening allowing more methanol and ethanol molecules to enter the pores. A similar phase transition in ZIF-8 also takes place upon gas adsorption at lower pressures, for instance for N_2 at 77 K it occurs at ~0.02 bar.[82] This enlarged pore opening is also observed for ZIF-90 (Zn^{2+} and $-CHO$ substituent), however, for ZIF-65 (Zn^{2+} and $-NO_2$ substituent), the nitro substituted imidazolate linker rotates in the opposite direction leading to a smaller pore opening.[83] Other examples of MOFs where linker dynamics affect the adsorption properties are described in [11]. Thus, rotational dynamics can increase or decrease the adsorption selectivity based on the interactions between the MOF's structure, its flexibility, and the type of guest molecules. Additionally, a recent theoretical work highlights the relation between pore size and the size of molecular rotor when they are comparable begin to affect the global transport properties of the fluid. Specifically, cooperative rotation and specific arrangement of unidirectional rotors, systems with directed diffusion in a specific direction is possible.[84]

Optical properties

The linker's dynamics can influence the optical properties of MOFs such as fluorescence and non-linear optical light generation. The non-linear optical (NLO) response can be turned on and off by modifying the linker dynamics, hence acting as a switch. This was identified in NH_2-MIL-53; it is a non-centrosymmetric structure in the closed pore configuration where the linkers experience significant steric hindrance for rotation. Since it is non-centrosymmetric, NLO response can be obtained in a closed pore configuration. When the guest molecules are introduced, the structure transforms to an open pore configuration, where the linkers can rotate now. In the open pore configuration, the NLO response is off because of randomization of the linker orientation due to linker rotations.[85] Fluorescence properties in MOFs can be influenced based on the changes in the linker dynamics upon guest adsorption/desorption. This is similar to aggregation-induced emission (AID) where chromophores with this property are more fluorescent as aggregates than in dilute solutions.[86] When aggregated, the rotation is hindered, hence fluorescence is switched on. One typical example for this is MOF with Zn^{2+} or Cd^{2+} and tetrakis(4-carboxyphenyl)ethylene (TCPE) linkers. The energy barrier for the rotation of phenyl rings in these linkers is higher in the MOF when compared to a free molecule in the gas phase. Owing to the geometrical constraint of MOF topology, this leads to hindered rotation of phenyl rings in the MOF compared to the unhindered rotation in the free molecule phase. These decreased phenyl rotations suffice for retaining the fluorescence properties of the MOF. The authors hypoth-

esize for MOFs that the guest-free MOF should hardly fluoresce because of unhindered rotation, while upon guest inclusion the fluorescence should be turned on due to hindered rotation.[87, 88]

Molecular Machines

Other novel applications where linker dynamics of MOFs are important, is their use as molecular rotors in artificial molecular machines. MOF offers ideal platforms for spatially organizing these molecular rotors (dynamic linker units) in a precise and predictable manner. Further, the linker motion in MOFs can be controlled by external stimuli like light and electric field. Recent work by the group of Feringa *et al* demonstrated the light-driven unidirectional motion of molecular rotors in the crystalline state in the MOF framework.[89] To fully realize the potential of MOF-based molecular machines and harness the collective motion of these rotors at the molecular scale; it is crucial to understand and engineer the cooperative behavior of linkers. Work by Evans *et al* already highlights the importance of cooperative rotation and specific arrangement of unidirectional rotors to obtain directional transport properties in molecular machine containing frameworks.[84] Chapters 4 and 5 of this thesis aim to understand the cooperative behavior of substituted terephthalate linkers in the MIL-53 family by tuning the steric interactions in the framework.

1.5 Computational modeling of piezoelectric behavior and rotational linker dynamics in MOFs

1.5.1 Computational modeling: Piezoelectric properties

Computational chemistry methods help to identify the candidates with high piezoelectric response and provide insight into the structural factors leading to enhanced piezoelectric properties. Hence, structure-property relationships of piezoelectric properties can be established for the design of better-performing and efficient piezoelectrics. Unlike experimental methods where exploration of piezoelectric properties for different materials is limited, computational methods enable this for a large number of materials. The piezoelectric properties are obtained using first-principles quantum-mechanical calculations based on Density Functional Theory (DFT). The general concepts of DFT are briefly described in the next section.

1.5.1.1 Density Functional Theory (DFT)

DFT is an approach to calculate the electronic structure based on the electron density, rather than the wave function that is used in traditional electronic structure methods. In 1964, Hohenberg and Kohn proposed the first theorem; *"The ground-state electron density (ρ) is a unique functional of the total electronic energy $E(\rho)$."* Unfortunately, the exact form of the functional that connects the electron density with the energy is unknown, but the second Hohenberg-Kohn theorem provides a way for it. The second theorem states *"The functional delivers the ground state energy if and only if the input density is the true ground state electron density".* It proposes a variational principle that can be used to find the electron density which gives the lowest ground state energy. Collectively, the two HK theorems, reduce the

many-body electron problem into a three-dimensional electron density problem but do not solve it in practice. In 1965, Kohn and Sham extended this theory and made solvable by considering the n-electron interacting system as an imaginary one-electron non-interacting system that can be solved using the same approaches as in wave function-based methods.

The DFT electronic energy can then be written as the sum of one-electron kinetic energy T, the nuclear attraction energy E_{ne}, the coulomb repulsion energy between the electrons J, and the exchange-correlation energy E_{XC}.[90]

$$E_{DFT}[\rho] = T[\rho] + E_{ne}[\rho] + J[\rho] + E_{XC}[\rho] \tag{1.8}$$

E_{XC} is a term that encompasses all the other contributions to the energy which are not accounted for in the previous terms such as electron exchange interaction and correlation interaction. Based on this, the exact energy of the system could in principle be calculated from the exact electron density. However, the exchange-correlation functional is unknown. Different approximation methods have been developed to describe the E_{XC} functional as accurately as possible. The simplest approximations are based on the density of a uniform electron gas (LDA) or include the gradient of the density in the uniform electron gas (GGA). Over the last decades a whole hierarchy of more accurate methods has emerged. More accurate approaches are usually also accompanied by being more demanding computationally. Some of the approximations proposed include LDA (Local Density Approximation), GGA (Generalized Gradient Approximation), meta-GGA, and hybrid functionals. These approximations have been described in detail in the literature.[90] In chapters 2 and 3, we used DFT functionals at the GGA level of theory. These functionals accurately describe piezoelectric properties of materials since they give insight in to how the energy and other properties depend on the geometry of the materials and have been used widely for inorganic ceramics.

1.5.1.2 Computational modeling of piezoelectric constants *e* and *d*

Note: In this section, the notation for the variables is followed as per IEEE standard on Piezoelectricity[17] and Voigt notation for the indices of the tensors is used as shown in section 1.3.2.

Computationally the piezoelectric constant e_{ip} is expressed as the second derivative of energy (E_{DFT}) with respect to electric field E_i and lattice strains S_p and also as the first derivative of the magnitude of the polarization P_i induced by strain S_p shown in equation 1.9.

$$e_{ip} = \frac{1}{V_0}\left(\frac{\partial^2 E_{DFT}}{\partial E_i \partial S_p}\right) = \left(\frac{\partial P_i}{\partial S_p}\right)_E \tag{1.9}$$

The piezoelectric constants *e* are evaluated from the numerical Berry phase approach, within the modern theory of polarization of solids [91–93]. According to this, e_{ip} is obtained from finite differences of polarization (i.e. berry phase) at strained configurations in equation 1.10 where $\bar{S}$ is the amplitude of the applied strain in the calculations.[94]

$$e_{ip} = \left[P_i|_{S_p=\bar{S}} - P_i|_{S_p=-\bar{S}}\right]/2\bar{S} \tag{1.10}$$

The piezoelectric tensor e_{ip} can be further written as two contributions: clamped ion (e_{ip}^0) and internal strain (e_{ip}^{int}) contributions. As indicated in the work by Catti *et al.*[95] for a general case, piezoelectric constant e is shown in the equation 1.11.

$$e_{ip} = e_{ip}^0 + e_{ip}^{int} \tag{1.11}$$

The elastic tensors for a crystal at its equilibrium volume V_0 are expressed as second order energy (E_{DFT}) derivatives with respect to pairs of homogeneous strains (S_q, S_p) shown in equation 1.12.[94]

$$C_{qp} = \frac{1}{V_0}\left(\frac{\partial^2 E_{DFT}}{\partial S_q \partial S_p}\right)_E = \frac{1}{V_0}\left(\frac{\partial g_q}{\partial S_p}\right)_E \tag{1.12}$$

where derivatives are at a constant electric field E and lattice strain energy gradients $g_q = (\partial E_{DFT}/\partial S_q)_E$. The strain energy gradients g_q are computed analytically and the second energy derivatives are evaluated as their numerical finite differences between strained configurations as in equation 1.13 where $\bar{S}$ is the amplitude of the applied strain in the calculations.

$$C_{qp} = \frac{1}{V_0}\left[g_q|_{S_p=\bar{S}} - g_q|_{S_p=-\bar{S}}\right]/2\bar{S} \tag{1.13}$$

The piezoelectric constant d_{iq} can be computed from the piezoelectric constant e_{ip} and the elastic compliance tensor s_{pq}/elastic stiffness tensor c_{qp} using equations 1.6 also shown here.

$$\begin{aligned} e_{ip} &= d_{iq} c_{qp}^E \\ d_{iq} &= e_{ip} s_{pq}^E \end{aligned} \tag{1.14}$$

Practically, the piezoelectric and elastic constants are calculated using two different approaches as discussed below:

1. **Geometry optimizer approach**[94] The clamped ion piezoelectric (e_{ip}^0) and elastic constants are evaluated from strain derivatives in equations 1.15 and 1.12 respectively at fixed atomic positions (x) in strained lattice configurations.

$$e_{ip}^0 = \left(\frac{\partial P_i}{\partial S_p}\right)_x \tag{1.15}$$

Essentially, the clamped ion contribution (e_{ip}^0) is the change in polarization P_i due to the reorganization of electron density with external strain S_p, while the fractional coordinates x are kept constant in the strained unit cell.

The total piezoelectric (e_{ip}) and elastic constants (c_{qp}) are obtained by evaluating strain derivatives using equations 1.9, 1.10, 1.12 and 1.13 at relaxed atomic positions in strained lattice configurations. The difference between the total and clamped ion values is the internal strain contribution shown in equations 1.16.

$$\begin{aligned} C_{qp}^{int} &= \frac{1}{V_0}\left[\left(\frac{\partial g_q}{\partial S_p}\right)_E - \left(\frac{\partial g_q}{\partial S_p}\right)_{E,x}\right] \\ e_{ip}^{int} &= \left[\left(\frac{\partial P_i}{\partial S_p}\right) - \left(\frac{\partial P_i}{\partial S_p}\right)_x\right] \end{aligned} \tag{1.16}$$

Piezoelectric constant d_{iq} is then evaluated from total piezoelectric and elastic tensors using equations 1.14. In chapter 2, the geometry optimizer approach implemented in CRYSTAL17[96] was used to evaluate the piezoelectric tensors e, d and the elastic compliance s/ elastic stiffness tensors c for all the ZIFs in consideration.

2. **Density Functional Perturbation Theory (DFPT)** Density functional perturbation theory (DFPT) was proposed in 1987 by Baroni *et al* [97] which provides the general formulation of total energy change with respect to atomic displacement and other perturbations. DFPT can compute response properties from perturbations of strain, atomic displacement, and electric field using the linear response theory.[98] The definition of piezoelectric tensors within the framework of DFPT is discussed below. The total energy of material under perturbation of atomic displacement x, electric field E, and strain S, $E_{DFT}(x, E, S)$ is defined as shown in equation1.17.[98]

$$E_{DFT}(x, E, S) = \frac{1}{V_0}\left[E_{DFT}^0 - V E.P\right] \tag{1.17}$$

where E_{DFT}^0 is the total energy of material in the ground state, V_0 is the volume of the unit cell, V is the volume of deformed unit cell and P is the polarization. The second-order derivatives of equation 1.17 with respect to different perturbations can be defined as follows.

$$\text{Force constant matrix}: K_{mn} \quad = \quad V_0 \left(\frac{\partial^2 E_{DFT}}{\partial x_m \partial x_n}\right)_{E,S} \tag{1.18}$$

$$\text{Born effective charge tensor}: Z_{mi} = -V_0 \left(\frac{\partial^2 E_{DFT}}{\partial x_m \partial E_i}\right)_{S} \tag{1.19}$$

$$\text{Force response internal strain tensor}: \Lambda_{mp} = -V_0 \left(\frac{\partial^2 E_{DFT}}{\partial x_m \partial S_p}\right)_{E} \tag{1.20}$$

$$\text{Clamped ion piezoelectric tensor}: e_{ip}^0 = \left(\frac{\partial^2 E_{DFT}}{\partial E_i \partial S_p}\right)_{x} \tag{1.21}$$

The subscripts m and n are the degrees of freedom in the cell. They range from 1 to 3i, where i is the number of irreducible atoms because each atom has three degree of freedom along x, y, and z directions. The internal strain contribution of the piezoelectric tensor $\left(e_{ip}^{int}\right)$ in the framework of DFPT is shown in equation 1.22.

$$e_{ip}^{int} = \frac{1}{V_0} Z_{mi}(K^{-1})_{mn}\Lambda_{np} \tag{1.22}$$

The total piezoelectric constant is obtained from equations 1.21 and 1.22 and indicated in equation 1.23.

$$e_{ip} = \left(\frac{\partial^2 E_{DFT}}{\partial E_i \partial S_p}\right)_{x} + \frac{1}{V_0} Z_{mi}(K^{-1})_{mn}\Lambda_{np} \tag{1.23}$$

These formulations of DFPT are specifically implemented in VASP. For chapter 3, we use DFPT formalism in VASP[99, 100] to calculate the piezoelectric tensor e_{ip} for a large number of MOFs in the database.

1.5.2 Computational modeling: Rotational Dynamics of linkers

Rotational dynamics of linkers is modelled at different levels of theory and techniques viz. single-point density functional theory (DFT) calculations, ab-initio and classical molecular dynamics simulations (AIMD, MD). In both single-point DFT and AIMD simulations, the energy of structures is calculated based on DFT. Even though the rotational energies obtained are accurate, the number of linkers that can be considered to rotate independently is limited and only smaller supercells can be simulated. With classical molecular dynamics, pre-defined force-fields are used to estimate the rotational energies of structures and are computationally less expensive than DFT calculations. Hence, a larger number of linkers that can rotate independently in bigger supercells can be simulated in classical molecular dynamics simulations.

In periodic DFT single-point calculations a rotational energy scan is performed in small angular steps. This gives the rotational energy barrier, the minimum and maximum energy conformations on the potential energy surface of the rotating linker. This methodology is the simplest way to computationally characterize the rotation of a given linker. The computational cost is relatively low because it corresponds to a series of single-point energy calculations at rotated configurations of the linker. In single-point energy calculations, it is difficult to ensure that the obtained conformations are at a global minima especially in the case of steric interactions and the information obtained is static, not dynamic. Additionally, the rotation of the MOF linkers also involves entropic contributions which are not taken into consideration in DFT energy calculations at 0 K. These effects can be studied with dynamic molecular dynamics (MD) simulations at finite temperature T where the dynamics of linkers are studied over time.

In MD simulations, Newton's equations of motion are solved on-the-fly to propagate the system in time. $F_i = m_i a_i$ is followed for each atom i in a system with N atoms. Here, m_i is the mass of the atom and a_i is the acceleration given by $d^2 r_i / dt^2$ (second order derivative of atomic positions r with time t) and F_i is the force acting on it due to the interactions with other atoms. The forces acting on atoms can be obtained from classic interatomic potentials (classical MD) or quantum chemical ab initio calculations (AIMD).

Classical MD simulations use pre-defined empirical force fields that use mathematical functionals to describe the intramolecular interactions using bonds, angles, and torsions. Non-bonded interactions i.e., Van der Waals and electrostatic interactions are also included in the form of mathematical functions. These functions are parameterized to reproduce experimental data or ab initio electronic structure calculations. Ab initio molecular dynamics (AIMD) is MD simulation based on quantum chemistry calculations of the interatomic forces. The interaction energies and forces on the atoms are accurately calculated using DFT calculations. Even though AIMD simulations provide accurate energies of conformations, long simulation times and large supercells cannot be reached in these simulation due to the high computational cost of the calculations. Classical MD simulations depend on the fitted terms for the intramolecular and non-bonded interactions in the force field and can be less accurate in terms of the conformational energies based on the force field fitting procedure. However, larger supercells and longer simulation times can be reached with classical MD simulations allowing for obtaining information for numerical and statistical analysis.

In chapter 4, we used DFT to obtain the potential energy surface for rotation of the substituted linker specifically for NO_2-MIL-53. Then we performed AIMD simulations

implemented in CP2K[101] to investigate the linker dynamics in the MIL-53 family with varying steric interactions due to the substituted linkers. In chapter 5, we developed and validated a force field for NO_2-MIL-53 and the FF was used to explore the correlated linker dynamics in NO_2-MIL-53 through classical MD simulations.

1.6 Scope of the thesis

This thesis focuses on two topics: **Piezoelectricity in metal–organic frameworks** and **rotational dynamics of linkers in metal–organic frameworks**. Metal–organic frameworks (MOFs) are highly porous hybrid materials with exceptional flexibility and tuneability. Precisely because of these properties, MOFs have a huge potential as a piezoelectric energy harvester. The second topic, rotational dynamics of linkers in MOFs, has been gaining interest due to its impact on adsorption, separation and optical properties. Moreover, MOFs offer a unique platform to organize the molecular rotors in solid state that can be spaced at tuneable distances. Owing to the flexibility, porosity, and tuneability of MOF frameworks, by varying the rotational linker dynamics it can pave the path to novel applications like the design of artificial molecular machines.

Even though the concepts of piezoelectricity and molecular rotors have been known for a few decades, the relevance of these topics for metal–organic frameworks is relatively new and has not been studied in detail. This thesis aims to investigate the structure-property relationships of piezoelectric properties in MOFs and provide some design rules that contribute to obtaining high-performing piezoelectrics. Additionally, the rotational dynamics of terephthalate linkers in MIL-53 is studied by combining different computational methodologies along with experimental techniques.

Chapter 2 computationally investigates the piezoelectric and elastic properties of Zeolitic Imidazolate Frameworks (ZIFs)- a cubic non-centrosymmetric sub-family of MOFs. ZIFs are known for their thermal and chemical stability and have exceptionally low shear modulus, hence high flexibility. The main aim of this chapter is to establish the structure-property relationship for piezoelectric properties (e and d) in sodalite ZIFs by varying their structural building units (viz. metal node and linker substituent of imidazolate). The figure of merit of the ZIF with the highest piezoelectric constant d was estimated and compared with the approximate figures of merit of best-performing inorganic (PZT) and organic (PVDF) piezoelectrics indicating the huge potential of MOFs as energy harvesting devices.

Piezoelectric constant d for a material is dependent on both piezoelectric constant e and elastic properties. Several studies in the literature highlight and summarize the elastic properties of MOFs. However, the piezoelectric constant e for MOFs has not yet been investigated and is difficult to predict. In chapter 2, we focused on a specific sub-family of MOFs i.e., ZIFs. In **chapter 3**, we adopt a broader approach and present a computational database of piezoelectric constant e for ~ 1260 MOFs. Based on the structural features of MOFs with high e, design rules that can enhance the e value for MOFs are presented.

In **Chapter 4**, the rotational dynamics of the linkers in the MIL-53 family of MOFs is discussed by varying steric interactions in the frameworks via functionalization of the linkers. Through a combined study of computational (DFT, AIMD) and experimental techniques, we see the emergence of cooperative linker rotation in one of the functionalized MIL-53 MOFs. This discovery paves the path for designing materials with correlated dynamics which

is crucial for achieving collective motion in crystalline MOF-based molecular machines. With AIMD simulations in this chapter, supercell size of only 211 and simulation time scales in the order of picoseconds was achieved.

Chapter 5 builds up on the work of chapter 4 and computationally investigates the coupled linker dynamics observed in Nitro functionalized MIL-53 MOFs. We developed and validated a force field that can predict the linker dynamics of terephthalate linkers in the Nitro functionalized MIL-53 MOF. Using the developed force field, MD simulations for unitcells up to 622 were performed and free energy profiles of neighboring linkers and their dynamics are obtained. Unlike AIMD simulations in chapter 4, larger supercells and longer simulation timescales up to nanoseconds was achieved with force field simulations. The presence of long-range correlated linker dynamics observed in this work is especially desirable for applications in ferroelectric switching in the presence of an electric field.

Bibliography

(1)   H. Furukawa, K. E. Cordova, M. O'Keeffe and O. M. Yaghi, "The Chemistry and Applications of Metal-Organic Frameworks," *Science*, 2013, **341**, 1230444–1230444.

(2)   C. Pettinari, F. Marchetti, N. Mosca, G. Tosi and A. Drozdov, "Application of Metal – Organic Frameworks," *Polymer International*, 2017, **66**, 731–744.

(3)   D. Fairen-Jimenez, S. A. Moggach, M. T. Wharmby, P. A. Wright, S. Parsons and T. Düren, "Opening the Gate: Framework Flexibility in ZIF-8 Explored by Experiments and Simulations," *Journal of the American Chemical Society*, 2011, **133**, 8900–8902.

(4)   C. Serre, C. Mellot-Draznieks, S. Surblé, N. Audebrand, Y. Filinchuk and G. Férey, "Role of Solvent-Host Interactions That Lead to Very Large Swelling of Hybrid Frameworks," *Science*, 2007, **315**, 1828–1831.

(5)   A. Schneemann, V. Bon, I. Schwedler, I. Senkovska, S. Kaskel and R. A. Fischer, "Flexible Metal-Organic Frameworks," *Chemical Society Reviews*, 2014, **43**, 6062–6096.

(6)   F.-X. Coudert, A. Boutin, A. H. Fuchs and A. V. Neimark, "Adsorption Deformation and Structural Transitions in Metal–Organic Frameworks: From the Unit Cell to the Crystal," *The Journal of Physical Chemistry Letters*, 2013, **4**, 3198–3205.

(7)   S. Biswas, T. Ahnfeldt and N. Stock, "New Functionalized Flexible Al-MIL-53-X (X = -Cl, -Br, -CH 3 , -NO 2 , -(OH) 2) Solids: Syntheses, Characterization, Sorption, and Breathing Behavior," *Inorganic Chemistry*, 2011, **50**, 9518–9526.

(8)   S. Eslava, L. Zhang, S. Esconjauregui, J. Yang, K. Vanstreels, M. R. Baklanov and E. Saiz, "Metal-Organic Framework ZIF-8 Films As Low-κ Dielectrics in Microelectronics," *Chemistry of Materials*, 2013, **25**, 27–33.

(9)   S. Mendiratta, C. H. Lee, M. Usman and K. L. Lu, "Metal-Organic Frameworks for Electronics: Emerging Second Order Nonlinear Optical and Dielectric Materials," *Science and Technology of Advanced Materials*, 2015, **16**, 054204.

(10)   Y. C. Kao, S. Mendiratta, M. Usman, Y. S. Wen, C. M. Wang, L. Zhao, M. K. Wu and K. L. Lu, "Exceptional Low Dielectric Behavior of Chemically Robust, Guest-Free Co- and Mn-Based Coordination Polymers," *ChemElectroChem*, 2019, **6**, 623–626.

(11)   A. Gonzalez-Nelson, F.-X. Coudert and M. van der Veen, "Rotational Dynamics of Linkers in Metal–Organic Frameworks," *Nanomaterials*, 2019, **9**, 330.

(12)   P. Martinez-Bulit, A. J. Stirk and S. J. Loeb, "Rotors, Motors, and Machines Inside Metal–Organic Frameworks," *Trends in Chemistry*, 2019, **1**, 588–600.

(13)   S. Krause and B. L. Feringa, "Towards Artificial Molecular Factories from Framework-Embedded Molecular Machines," *Nature Reviews Chemistry*, 2020, **4**, 550–562.

(14)   J. Curie and P. Curie, "Development, via Compression, of Electric Polarization in Hemihedral Crystals with Inclined Faces," *Bulletin de la Societe de Minerologique de France*, 1880, **3**, 90–93.

(15)   G. Lippman, "Principal of the Conservation of Electricity," *Annales de Chemie et de Physique*, 1881, **24**, 145.

(16)   P. Paufler, "Fundamentals of Piezoelectricity," *Zeitschrift für Kristallographie*, 1992, **199**, 158–158.

(17)   "IEEE Standard on Piezoelectricity," *ANSI/IEEE Std 176-1987*, 1988, 0_1–.

(18)   J. F. Nye, *Physical Properties of Crystals: Their Representation by Tensors and Matrices*, Oxford university press, New York, 1985.

(19)   K. Uchino, The Development of Piezoelectric Materials and the New Perspective, in *Advanced Piezoelectric Materials*, Elsevier, 2017, pp. 1–92.

(20)   Y. Wu, Y. Ma, H. Zheng and S. Ramakrishna, "Piezoelectric Materials for Flexible and Wearable Electronics: A Review," *Materials & Design*, 2021, **211**, 110164.

(21)   E. L. Pradeesh, S. Udhayakumar, M. G. Vasundhara and G. K. Kalavathi, "A Review on Piezoelectric Energy Harvesting," *Microsystem Technologies*, 2022, **28**, 1797–1830.

(22)   D. B. Deutz, J.-A. Pascoe, B. Schelen, S. van der Zwaag, D. M. de Leeuw and P. Groen, "Analysis and Experimental Validation of the Figure of Merit for Piezoelectric Energy Harvesters," *Materials Horizons*, 2018, **5**, 444–453.

(23)   Y. Zhang, M. Xie, J. Roscow, Y. Bao, K. Zhou, D. Zhang and C. R. Bowen, "Enhanced Pyroelectric and Piezoelectric Properties of PZT with Aligned Porosity for Energy Harvesting Applications," *Journal of Materials Chemistry A*, 2017, **5**, 6569–6580.

(24)   T. Vijayakanth, D. J. Liptrot, E. Gazit, R. Boomishankar and C. R. Bowen, "Recent Advances in Organic and Organic–Inorganic Hybrid Materials for Piezoelectric Mechanical Energy Harvesting," *Advanced Functional Materials*, 2022, **32**, 2109492.

(25)   N. Sezer and M. Koç, "A Comprehensive Review on the State-of-the-Art of Piezoelectric Energy Harvesting," *Nano Energy*, 2021, **80**, 105567.

(26)   M. Habib, I. Lantgios and K. Hornbostel, "A Review of Ceramic, Polymer and Composite Piezoelectric Materials," *Journal of Physics D: Applied Physics*, 2022, **55**, 423002.

(27)   H. Schlaberg and J. Duffy, "Piezoelectric Polymer Composite Arrays for Ultrasonic Medical Imaging Applications," *Sensors and Actuators A: Physical*, 1994, **44**, 111–117.

(28)   V. T. Rathod, "A Review of Acoustic Impedance Matching Techniques for Piezoelectric Sensors and Transducers," *Sensors*, 2020, **20**, 4051.

(29)   K. Omote, H. Ohigashi and K. Koga, "Temperature Dependence of Elastic, Dielectric, and Piezoelectric Properties of "single Crystalline" Films of Vinylidene Fluoride Trifluoroethylene Copolymer," *Journal of Applied Physics*, 1997, **81**, 2760–2769.

(30)   V. Tiwari and G. Srivastava, "Structural, Dielectric and Piezoelectric Properties of 0–3 PZT/PVDF Composites," *Ceramics International*, 2015, **41**, 8008–8013.

(31)   Y.-M. You, W.-Q. Liao, D. Zhao, H.-Y. Ye, Y. Zhang, Q. Zhou, X. Niu, J. Wang, P.-F. Li, D.-W. Fu, Z. Wang, S. Gao, K. Yang, J.-M. Liu, J. Li, Y. Yan and R.-G. Xiong, "An Organic-Inorganic Perovskite Ferroelectric with Large Piezoelectric Response," *Science*, 2017, **357**, 306–309.

(32)   T.-M. Guo, F.-F. Gao, Z.-G. Li, Y. Liu, M.-H. Yu and W. Li, "Mechanical and Acoustic Properties of a Hybrid Organic–Inorganic Perovskite, TMCM-CdCl$_3$, with Large Piezoelectricity," *APL Materials*, 2020, **8**, 101106.

(33)   H.-P. Lv, W.-Q. Liao, Y.-M. You and R.-G. Xiong, "Inch-Size Molecular Ferroelectric Crystal with a Large Electromechanical Coupling Factor on Par with Barium Titanate," *Journal of the American Chemical Society*, 2022, **144**, 22325–22331.

(34)   H. Y. Ye, Y. Y. Tang, P. F. Li, W. Q. Liao, J. X. Gao, X. N. Hua, H. Cai, P. P. Shi, Y. M. You and R. G. Xiong, "Metal-Free Three-Dimensional Perovskite Ferroelectrics," *Science*, 2018, **361**, 151–155.

(35)   H. Wang, H. Liu, Z. Zhang, Z. Liu, Z. Lv, T. Li, W. Ju, H. Li, X. Cai and H. Han, "Large Piezoelectric Response in a Family of Metal-Free Perovskite Ferroelectric Compounds from First-Principles Calculations," *npj Computational Materials*, 2019, **5**, 1–9.

(36)   T. Zhang, K. Xu, J. Li, L. He, D.-W. Fu, Q. Ye and R.-G. Xiong, "Ferroelectric Hybrid Organic–Inorganic Perovskites and Their Structural and Functional Diversity," *National Science Review*, 2023, **10**, nwac240.

(37)   V. Jella, S. Ippili, J.-H. Eom, S. V. N. Pammi, J.-S. Jung, V.-D. Tran, V. H. Nguyen, A. Kirakosyan, S. Yun, D. Kim, M. R. Sihn, J. Choi, Y.-J. Kim, H.-J. Kim and S.-G. Yoon, "A Comprehensive Review of Flexible Piezoelectric Generators Based on Organic-Inorganic Metal Halide Perovskites," *Nano Energy*, 2019, **57**, 74–93.

(38)   J.-C. Tan, Fundamentals of MOF Mechanics & Structure–Mechanical Property Relationships, in *Mechanical Behaviour of Metal – Organic Framework Materials*, ed. J.-C. Tan, The Royal Society of Chemistry, 1st edn., 2023, pp. 1–64.

(39)   K. Li, Y. Qin, Z.-G. Li, T.-M. Guo, L.-C. An, W. Li, N. Li and X.-H. Bu, "Elastic Properties Related Energy Conversions of Coordination Polymers and Metal–Organic Frameworks," *Coordination Chemistry Reviews*, 2022, **470**, 214692.

(40)   R. Gaillac, P. Pullumbi and F.-X. Coudert, "ELATE: An Open-Source Online Application for Analysis and Visualization of Elastic Tensors," *Journal of Physics: Condensed Matter*, 2016, **28**, 275201.

(41)   N. C. Burtch, J. Heinen, T. D. Bennett, D. Dubbeldam and M. D. Allendorf, "Mechanical Properties in Metal-Organic Frameworks: Emerging Opportunities and Challenges for Device Functionality and Technological Applications," *Advanced Materials*, 2018, **30**, 1704124.

(42)   L. R. Redfern and O. K. Farha, "Mechanical Properties of Metal-Organic Frameworks," *Chemical Science*, 2019, **10**, 10666–10679.

(43)   J. C. Tan and A. K. Cheetham, "Mechanical Properties of Hybrid Inorganic–Organic Framework Materials: Establishing Fundamental Structure–Property Relationships," *Chemical Society Reviews*, 2011, **40**, 1059–1080.

(44)   S. Bundschuh, O. Kraft, H. K. Arslan, H. Gliemann, P. G. Weidler and C. Wöll, "Mechanical Properties of Metal-Organic Frameworks: An Indentation Study on Epitaxial Thin Films," *Applied Physics Letters*, 2012, **101**, 101910.

(45)   A. U. Ortiz, A. Boutin, A. H. Fuchs and F. X. Coudert, "Metal-Organic Frameworks with Wine-Rack Motif: What Determines Their Flexibility and Elastic Properties?" *Journal of Chemical Physics*, 2013, **138**, 174703.

(46) Y. Sun, Z. Hu, D. Zhao and K. Zeng, "Mechanical Properties of Microcrystalline Metal–Organic Frameworks (MOFs) Measured by Bimodal Amplitude Modulated-Frequency Modulated Atomic Force Microscopy," *ACS Applied Materials & Interfaces*, 2017, **9**, 32202–32210.

(47) M. R. Ryder, B. Civalleri and J. C. Tan, "Isoreticular Zirconium-Based Metal-Organic Frameworks: Discovering Mechanical Trends and Elastic Anomalies Controlling Chemical Structure Stability," *Physical Chemistry Chemical Physics*, 2016, **18**, 9079–9087.

(48) D.-W. Fu, W. Zhang and R.-G. Xiong, "The First Metal–Organic Framework (MOF) of Imazethapyr and Its SHG, Piezoelectric and Ferroelectric Properties," *Dalton Transactions*, 2008, 3946.

(49) P. Yang, X. He, M.-X. Li, Q. Ye, J.-Z. Ge, Z.-X. Wang, S.-R. Zhu, M. Shao and H.-L. Cai, "The First Homochiral Coordination Polymer with Temperature-Independent Piezoelectric and Dielectric Properties," *Journal of Materials Chemistry*, 2012, **22**, 2398.

(50) Y. Sun, J. Gao, Y. Cheng, Y.-W. Zhang and K. Zeng, "Design of the Hybrid Metal–Organic Frameworks as Potential Supramolecular Piezo-/Ferroelectrics," *The Journal of Physical Chemistry C*, 2019, **123**, 3122–3129.

(51) F. Xue, J. Cao, X. Li, J. Feng, M. Tao and B. Xue, "Continuous-Flow Synthesis of MIL-53(Cr) with a Polar Linker: Probing the Nanoscale Piezoelectric Effect," *Journal of Materials Chemistry C*, 2021, **9**, 7568–7574.

(52) Y. Sun, Z. Hu, D. Zhao and K. Zeng, "Probing Nanoscale Functionalities of Metal-Organic Framework Nanocrystals," *Nanoscale*, 2017, **9**, 12163–12169.

(53) Y. Chen, S. Guerin, H. Yuan, J. O'Donnell, B. Xue, P.-A. Cazade, E. U. Haq, L. J. W. Shimon, S. Rencus-Lazar, S. A. M. Tofail, Y. Cao, D. Thompson, R. Yang and E. Gazit, "Guest Molecule-Mediated Energy Harvesting in a Conformationally Sensitive Peptide–Metal Organic Framework," *Journal of the American Chemical Society*, 2022, **144**, 3468–3476.

(54) D. Seol, B. Kim and Y. Kim, "Non-Piezoelectric Effects in Piezoresponse Force Microscopy," *Current Applied Physics*, 2017, **17**, 661–674.

(55) T. Jungk, Á. Hoffmann and E. Soergel, "Challenges for the Determination of Piezoelectric Constants with Piezoresponse Force Microscopy," *Applied Physics Letters*, 2007, **91**, 253511.

(56) E. Soergel, "Piezoresponse Force Microscopy (PFM)," *Journal of Physics D: Applied Physics*, 2011, **44**, 464003.

(57) Z.-G. Li, K. Li, L.-Y. Dong, T.-M. Guo, M. Azeem, W. Li and X.-H. Bu, "Acoustic Properties of Metal-Organic Frameworks," *Research*, 2021, **2021**, 1–11.

(58) M. Usman, C.-H. Lee, D.-S. Hung, S.-F. Lee, C.-C. Wang, T.-T. Luo, L. Zhao, M.-K. Wu and K.-L. Lu, "Intrinsic Low Dielectric Behaviour of a Highly Thermally Stable Sr-based Metal–Organic Framework for Interlayer Dielectric Materials," *J. Mater. Chem. C*, 2014, **2**, 3762–3768.

(59) S. Mendiratta, M. Usman, T.-T. Luo, B.-C. Chang, S.-F. Lee, Y.-C. Lin and K.-L. Lu, "Anion-Controlled Dielectric Behavior of Homochiral Tryptophan-Based Metal–Organic Frameworks," *Crystal Growth & Design*, 2014, **14**, 1572–1579.

(60) F. Wang, C.-Y. Ni, Q. Liu, F.-L. Li, J. Shi, H.-X. Li and J.-P. Lang, "Pb(Tab)2(4,4′-Bipy)](PF6)2: Two-Step Ambient Temperature Quantitative Solid-State Synthesis, Structure and Dielectric Properties," *Chemical Communications*, 2013, **49**, 9248.

(61) V. Di Noto, A. B. Boeer, S. Lavina, C. A. Muryn, M. Bauer, G. A. Timco, E. Negro, M. Rancan, R. E. P. Winpenny and S. Gross, "Functional Chromium Wheel-Based Hybrid Organic-Inorganic Materials for Dielectric Applications," *Advanced Functional Materials*, 2009, **19**, 3226–3236.

(62) S. Mendiratta, a. Muhammad Usman, C.-C. Chang, Y.-C. Lee, J.-W. Chen, M.-K. Wu, Y.-C. Lin, C.-P. Hsu and K.-L. Lu, "Zn(II)-Based Metal-Organic Framework: An Exceptionally Thermally Stable, Guest-Free Low Dielectric Material †," *J. Mater. Chem. C*, 2017, **5**, 1508.

(63) L.-Z. Chen, J. Zou, Y.-M. Gao, S. Wan and M.-N. Huang, "A 2-D Tetrazole-Based Zn(II) Coordination Polymer: Crystal Structure, Dielectric Constant, and Luminescence," *Journal of Coordination Chemistry*, 2011, **64**, 715–724.

(64) S. Wang, N. Xhaferaj, M. Wahiduzzaman, K. Oyekan, X. Li, K. Wei, B. Zheng, A. Tissot, J. Marrot, W. Shepard, C. Martineau-Corcos, Y. Filinchuk, K. Tan, G. Maurin and C. Serre, "Engineering Structural Dynamics of Zirconium Metal–Organic Frameworks Based on Natural C4 Linkers," *Journal of the American Chemical Society*, 2019, **141**, 17207–17216.

(65) D. Bousquet, F.-X. Coudert, A. G. J. Fossati, A. V. Neimark, A. H. Fuchs and A. Boutin, "Adsorption Induced Transitions in Soft Porous Crystals: An Osmotic Potential Approach to Multistability and Intermediate Structures," *The Journal of Chemical Physics*, 2013, **138**, 174706.

(66) G. S. Kottas, L. I. Clarke, D. Horinek and J. Michl, "Artificial Molecular Rotors," *Chemical Reviews*, 2005, **105**, 1281–1376.

(67) S. Horike, R. Matsuda, D. Tanaka, S. Matsubara, M. Mizuno, K. Endo and S. Kitagawa, "Dynamic Motion of Building Blocks in Porous Coordination Polymers," *Angewandte Chemie International Edition*, 2006, **45**, 7226–7230.

(68) F. Moreau, D. I. Kolokolov, A. G. Stepanov, T. L. Easun, A. Dailly, W. Lewis, A. J. Blake, H. Nowell, M. J. Lennox, E. Besley, S. Yang and M. Schröder, "Tailoring Porosity and Rotational Dynamics in a Series of Octacarboxylate Metal-Organic Frameworks," *Proceedings of the National Academy of Sciences*, 2017, **114**, 3056–3061.

(69) Y. Yan, D. I. Kolokolov, I. Da Silva, A. G. Stepanov, A. J. Blake, A. Dailly, P. Manuel, C. C. Tang, S. Yang and M. Schröder, "Porous Metal–Organic Polyhedral Frameworks with Optimal Molecular Dynamics and Pore Geometry for Methane Storage," *Journal of the American Chemical Society*, 2017, **139**, 13349–13360.

(70) S. Bracco, F. Castiglioni, A. Comotti, S. Galli, M. Negroni, A. Maspero and P. Sozzani, "Ultrafast Molecular Rotors and Their CO2 Tuning in MOFs with Rod-Like Ligands," *Chemistry - A European Journal*, 2017, **23**, 11210–11215.

(71) C. S. Vogelsberg, F. J. Uribe-Romo, A. S. Lipton, S. Yang, K. N. Hou, S. Brown and M. A. Garcia-Garibay, "Ultrafast Rotation in an Amphidynamic Crystalline Metal Organic Framework," *Proceedings of the National Academy of Sciences of the United States of America*, 2017, **114**, 13613–13618.

(72) J. Perego, S. Bracco, M. Negroni, C. X. Bezuidenhout, G. Prando, P. Carretta, A. Comotti and P. Sozzani, "Fast Motion of Molecular Rotors in Metal–Organic Framework Struts at Very Low Temperatures," *Nature Chemistry*, 2020, **12**, 845–851.

(73) J. Perego, C. X. Bezuidenhout, S. Bracco, G. Prando, L. Marchiò, M. Negroni, P. Carretta, P. Sozzani and A. Comotti, "Cascade Dynamics of Multiple Molecular Rotors in a MOF: Benchmark Mobility at a Few Kelvins and Dynamics Control by CO $_2$," *Journal of the American Chemical Society*, 2021, **143**, 13082–13090.

(74)   A. E. Khudozhitkov, D. I. Kolokolov and A. G. Stepanov, "Characterization of Fast Restricted Librations of Terephthalate Linkers in MOF UiO-66(Zr) by ^{2}H NMR Spin–Lattice Relaxation Analysis," *The Journal of Physical Chemistry C*, 2018, **122**, 12956–12962.

(75)   W. Zhou and T. Yildirim, "Lattice Dynamics of Metal-Organic Frameworks: Neutron Inelastic Scattering and First-Principles Calculations," *Physical Review B*, 2006, **74**, 180301.

(76)   D. I. Kolokolov, A. G. Stepanov and H. Jobic, "Mobility of the 2-Methylimidazolate Linkers in ZIF-8 Probed by ^{2}H NMR: Saloon Doors for the Guests," *The Journal of Physical Chemistry C*, 2015, **119**, 27512–27520.

(77)   Q. Li, A. J. Zaczek, T. M. Korter, J. A. Zeitler and M. T. Ruggiero, "Methyl-Rotation Dynamics in Metal-Organic Frameworks Probed with Terahertz Spectroscopy," *Chemical Communications*, 2018, **54**, 5776–5779.

(78)   W. Zhou, H. Wu, T. J. Udovic, J. J. Rush and T. Yildirim, "Quasi-Free Methyl Rotation in Zeolitic Imidazolate Framework-8," *The Journal of Physical Chemistry A*, 2008, **112**, 12602–12606.

(79)   V. N. Vukotic, K. J. Harris, K. Zhu, R. W. Schurko and S. J. Loeb, "Metal–Organic Frameworks with Dynamic Interlocked Components," *Nature Chemistry 2012 4:6*, 2012, **4**, 456–460.

(80)   K. Zhu, V. N. Vukotic, C. A. O'Keefe, R. W. Schurko and S. J. Loeb, "Metal–Organic Frameworks with Mechanically Interlocked Pillars: Controlling Ring Dynamics in the Solid-State via a Reversible Phase Change," *Journal of the American Chemical Society*, 2014, **136**, 7403–7409.

(81)   S. A. Moggach, T. D. Bennett and A. K. Cheetham, "The Effect of Pressure on ZIF-8: Increasing Pore Size with Pressure and the Formation of a High-Pressure Phase at 1.47 GPa," *Angewandte Chemie International Edition*, 2009, **48**, 7087–7089.

(82)   D. Fairen-Jimenez, R. Galvelis, A. Torrisi, A. D. Gellan, M. T. Wharmby, P. A. Wright, C. Mellot-Draznieks and T. Düren, "Flexibility and Swing Effect on the Adsorption of Energy-Related Gases on ZIF-8: Combined Experimental and Simulation Study," *Dalton Transactions*, 2012, **41**, 10752.

(83)   C. L. Hobday, T. D. Bennett, D. Fairen-Jimenez, A. J. Graham, C. A. Morrison, D. R. Allan, T. Düren and S. A. Moggach, "Tuning the Swing Effect by Chemical Functionalization of Zeolitic Imidazolate Frameworks," *Journal of the American Chemical Society*, 2018, **140**, 382–387.

(84)   J. D. Evans, S. Krause and B. L. Feringa, "Cooperative and Synchronized Rotation in Motorized Porous Frameworks: Impact on Local and Global Transport Properties of Confined Fluids," *Faraday Discussions*, 2021, **225**, 286–300.

(85)   P. Serra-Crespo, M. A. van der Veen, E. Gobechiya, K. Houthoofd, Y. Filinchuk, C. E. A. Kirschhock, J. A. Martens, B. F. Sels, D. E. De Vos, F. Kapteijn and J. Gascon, "NH$_2$-MIL-53(Al): A High-Contrast Reversible Solid-State Nonlinear Optical Switch," *Journal of the American Chemical Society*, 2012, **134**, 8314–8317.

(86)   Y. Hong, J. W. Y. Lam and B. Z. Tang, "Aggregation-Induced Emission," *Chemical Society Reviews*, 2011, **40**, 5361.

(87)   N. B. Shustova, T. C. Ong, A. F. Cozzolino, V. K. Michaelis, R. G. Griffin and M. Dincă, "Phenyl Ring Dynamics in a Tetraphenylethylene-Bridged Metal-Organic Framework: Implications for the Mechanism of Aggregation-Induced Emission," *Journal of the American Chemical Society*, 2012, **134**, 15061–15070.

(88)   N. B. Shustova, B. D. McCarthy and M. Dincă, "Turn-On Fluorescence in Tetraphenylethylene-Based Metal–Organic Frameworks: An Alternative to Aggregation-Induced Emission," *Journal of the American Chemical Society*, 2011, **133**, 20126–20129.

(89)   W. Danowski, T. van Leeuwen, S. Abdolahzadeh, D. Roke, W. R. Browne, S. J. Wezenberg and B. L. Feringa, "Unidirectional Rotary Motion in a Metal–Organic Framework," *Nature Nanotechnology*, 2019, **14**, 488–494.

(90)   F. Jensen, *Introduction to Computational Chemistry*, John Wiley & Sons, Chichester, UK ; Hoboken, NJ, Third edition, 2017, 638 pp.

(91)   R. D. King-Smith and D. Vanderbilt, "Theory of Polarization of Crystalline Solids," *Physical Review B*, 1993, **47**, 1651–1654.

(92)   R. Resta, "Macroscopic Polarization in Crystalline Dielectrics: The Geometric Phase Approach," *Reviews of Modern Physics*, 1994, **66**, 899–915.

(93)   D. Vanderbilt, "Berry-Phase Theory of Proper Piezoelectric Response," *Journal of Physics and Chemistry of Solids*, 2000, **61**, 147–151.

(94)   A. Erba, D. Caglioti, C. M. Zicovich-Wilson and R. Dovesi, "Nuclear-Relaxed Elastic and Piezoelectric Constants of Materials: Computational Aspects of Two Quantum-Mechanical Approaches," *Journal of Computational Chemistry*, 2017, **38**, 257–264.

(95)   M. Catti, Y. Noel and R. Dovesi, "Full Piezoelectric Tensors of Wurtzite and Zinc Blende ZnO and ZnS by First-Principles Calculations," *Journal of Physics and Chemistry of Solids*, 2003, **64**, 2183–2190.

(96)   R. Dovesi, A. Erba, R. Orlando, C. M. Zicovich-Wilson, B. Civalleri, L. Maschio, M. Rérat, S. Casassa, J. Baima, S. Salustro and B. Kirtman, "Quantum-mechanical Condensed Matter Simulations with CRYSTAL," *WIREs Computational Molecular Science*, 2018, **8**, e1360.

(97)   S. Baroni, P. Giannozzi and A. Testa, "Green's-Function Approach to Linear Response in Solids," *Physical Review Letters*, 1987, **58**, 1861–1864.

(98)   K. Nakamura, S. Higuchi and T. Ohnuma, Density Functional Perturbation Theory to Predict Piezoelectric Properties, in *Perturbation Methods with Applications in Science and Engineering*, ed. İ. Bakırtaş, InTech, 2018.

(99)   G. Kresse and D. Joubert, "From Ultrasoft Pseudopotentials to the Projector Augmented-Wave Method," *Physical Review B*, 1999, **59**, 1758–1775.

(100) G. Kresse and J. Furthmüller, "Efficient Iterative Schemes for Ab Initio Total-Energy Calculations Using a Plane-Wave Basis Set," *Physical Review B*, 1996, **54**, 11169–11186.

(101) T. D. Kühne, M. Iannuzzi, M. Del Ben, V. V. Rybkin, P. Seewald, F. Stein, T. Laino, R. Z. Khaliullin, O. Schütt, F. Schiffmann, D. Golze, J. Wilhelm, S. Chulkov, M. H. Bani-Hashemian, V. Weber, U. Borštnik, M. Taillefumier, A. S. Jakobovits, A. Lazzaro, H. Pabst, T. Müller, R. Schade, M. Guidon, S. Andermatt, N. Holmberg, G. K. Schenter, A. Hehn, A. Bussy, F. Belleflamme, G. Tabacchi, A. Glöß, M. Lass, I. Bethune, C. J. Mundy, C. Plessl, M. Watkins, J. VandeVondele, M. Krack and J. Hutter, "CP2K: An Electronic Structure and Molecular Dynamics Software Package - Quickstep: Efficient and Accurate Electronic Structure Calculations," *The Journal of Chemical Physics*, 2020, **152**, 194103.

Part I

Piezoelectricity in Metal–Organic Frameworks

Chapter 2

Structure-Property Relationship of Piezoelectric Properties in Zeolitic Imidazolate Frameworks (ZIFs): A Computational Study

Metal-Organic Frameworks (MOFs) are a class of nanoporous crystalline materials with very high structural tunability. They possess a very low dielectric permittivity ε_r due to their porosity, hence are favorable for piezoelectric energy harvesting. Even though they have a huge potential as piezoelectric materials, a detailed analysis, and structure-property relationship of the piezoelectric properties in MOFs is lacking so far. This work focuses on a class of cubic non-centrosymmetric MOFs namely ZIFs (Zeolitic Imidazolate Frameworks) to rationalize how the variation of different building blocks of the structure i.e., metal node and linker substituent affects the piezoelectric constants. The piezoelectric tensor for the ZIFs is computed from ab initio theoretical methods. From the calculations, we analyze the different contributions to the final piezoelectric constant d_{14}, namely the clamped ion (e_{14}^0) and the internal strain (e_{14}^{int}) contributions and the mechanical properties. For the studied ZIFs, even though e_{14} ($e_{14}^0 + e_{14}^{int}$) is similar for all ZIFs, the resultant piezoelectric coefficient d_{14} calculated from piezoelectric constant e_{14} and elastic compliance constant s_{44} varies significantly amongst the different structures. It is the largest for CdIF-1 (Cd^{2+} and -CH_3 linker substituent). This is mainly due to the higher elasticity or flexibility of the framework. Interestingly, the magnitude of d_{14} for CdIF-1 is higher than II-VI inorganic piezoelectrics, and of a similar magnitude as the quintessential piezoelectric polymer polyvinylidene fluoride (PVDF).

2.1 Introduction

Energy harvesting is a process where ambient energy in the environment like mechanical vibrations, light, and heat can be stored and converted into electrical energy. This has been of significant interest to researchers, due to its ability to achieve self-powered low-power electronic devices for the Internet-of-Things and can pave a path to alternate sustainable sources of power. Among the different sources of available energy, kinetic energy in the form of mechanical vibrations is widely available in the environment and various human activities. It can be harvested by piezoelectric materials. The phenomenon of piezoelectricity describes the coupling between mechanical and electrical properties of materials. It is observed in non-centrosymmetric crystalline structures, where either an electric dipole moment is generated on the application of mechanical stress, or a mechanical strain is induced on the application of the electric field.[1]

Piezoelectricity has been found in traditional materials like inorganic ceramic oxides and organics polymers among which a high piezoelectric constant was found in Lead Zirconate Titanate (PZT, 360 pC/N), Barium Titanate (BaTiO$_3$, 191 pC/N) for inorganics while among soft materials polyvinylidene fluoride (PVDF) and its copolymers (-40 pC/N) have a high piezoelectric constant. Ceramics and polymers have their own set of advantages and disadvantages as piezoelectric materials which are summarized and reviewed in previous literature.[2, 3] Ceramics have strong piezoelectric properties but are stiff and brittle whereas polymers have mild processing conditions and excellent flexibility making them suitable for physically flexible electronics but do not have very high piezoelectric coefficients.[3, 4] Moreover, in contrast with inorganics, the acoustic static impedance of polymers are better matched to that of water and living tissue, making them better equipped to harvest energy in these media.[5] With the aim of combining the best of both polymer and ceramic piezoelectric components, composite and hybrid materials were fabricated. For example, in recent years, hybrid organic-inorganic pervoskite materials emerged as potential candidates with high piezoelectric response close to conventional ceramic oxides. One of the initial works on trimethylchloromethyl ammonium trichloromanganese (TMCM-MnCl$_3$) hybrid pervoskite (a BaNiO$_3$- like structure) shows a piezoresponse d_{33} as large as 185 pC/N.[6] These hybrid perovskites have features from both organic and inorganic materials and have advantages of being easy to process, lightweight and structural tunability. Other recent works on hybrid perovskites show the huge potential of these materials in terms of their piezoelectric constants.[7, 8] Additionally, due to the regulations imposed on the use of hazardous substances such as lead and other heavy metals in electrical and electronic equipment, there has been a need for exploring lead-free environmentally friendly piezoelectrics. Even among the traditional ceramics, lead-free ceramics like modified Potassium sodium niobate (KNN), Bismuth sodium titanate (BNT), and other bulk materials were explored as alternatives to PZT.[9, 10] Yet, the disadvantages of ceramics are still relevant for these lead-free materials. Another step towards lead-free piezoelectrics was also achieved by obtaining a large piezoelectric response in metal-free organic perovskites: the d_{15} of metal-free MDABCO $-$ NH$_4$ $-$ X$_3$ (with X = Cl, Br or I) calculated from first principle calculations show large values of 119, 248, 178 pC/N respectively.[11]. Like hybrid perovskites, metal–organic Frameworks (MOFs) have a major advantage of structural tunability, the building blocks of MOFs i.e., the metal node and connecting organic linker can be chosen and varied to obtain lead-free piezoelectric structures.

Metal–organic frameworks (MOFs) are materials that consist of metal ions or inorganic clusters connected by organic linkers through directional coordination bonds into a three-dimensional crystalline nanoporous framework. They are distinguished for their permanent porosity and high surface areas. By proper selection of the metal nodes and organic linkers in MOFs, structural control can be achieved to obtain desired properties for the target application. The pore size of MOFs can be changed from several angstroms to nanometers by varying the length of organic linkers in the MOF. Because of these features, MOFs are ideal candidates for applications including but not limited to: gas separation and storage, catalysis and biomedical imaging.[12, 13] In addition to these applications, the second order nonlinear optical properties via rationally design of non-centrosymmetric MOFs has also been explored previously.[14–16]

So far, only two papers show piezoelectric response experimentally in MOFs by quasi-static measurements (measured with a PM200 piezometer): in one d_{33} value of 60.10 pC/N was measured for MOF based on Cd[Imazethapyr][17]; in the other d_{22} value of Mn/Co-based homochiral coordination frameworks is measured to be 6.9 pC/N.[18] There are other works on piezoelectricity in MOFs where electromechanical (EM) response was measured using Piezoelectric Force Microscopy (PFM).[19–21] Whereas they are worthy to be mentioned, it must be noted that several non-piezoelectric effects can induce additional contributions to PFM response thus leading to misinterpretation. Several issues due to calibration of the microscope and challenges in excluding the contribution of electrostatic and other forces have been discussed in the literature, thus indicating that piezoelectric constants with high precision cannot be measured from PFM in most cases.[22–24] Recently, also the theoretical prediction of the piezoelectric tensor for three MOFs whose d_{ik} values range between 2 pC/N to 23 pC/N have been reported.[25]

Another factor that is considered important in piezoelectric energy harvesting applications is the dielectric constant of the material, as noted from the figure of merit $FOM_{ij} = \frac{d_{ij}^2}{\varepsilon_0 \varepsilon_{33}^T}$ with units m^2/N, where ε_{33}^T is the relative permittivity (or dielectric constant) of the material at constant stress (T). [26] In relation to the dielectric constant of MOFs, because of their inherent permanent porosity, they generally have low dielectric constants (ε_r) ranging between 1.3 to 6.[27–32] Note that the computationally obtained dielectric constants are static dielectric constants, and that the experimental determination via dielectric spectroscopy is often done on air-MOF composites (pellets), both leading to some underestimation of the dielectric constant. Yet, the reported values are very low, and e.g. a study where the determination of the dielectric constant of ZIF-8 was performed via ellipsometry on a continuous film, a method not prone to underestimation, reports the low value of 2.3.[27] These values are very low compared to dielectric constants of BaTiO$_3$, PZT and PVDF & copolymers shown previously. If a high electromechanical (EM) response can be achieved by tuning the topology and building blocks of the material, this combined with such low dielectric constants, MOFs present an interesting class of materials to explore for efficient energy harvesters.

The experimental and computed data for MOFs are thus quite promising in terms of the piezoresponse. However, the MOFs studied differ widely in their building units and structure. Thus, it is hard to derive a structure-property relationship that will guide the design of better performing piezoelectric MOFs. In the present work, we aim at filling this gap. To this purpose, we chose to focus on Zeolitic Imidazolate frameworks (ZIFs), a

subfamily of MOFs consisting of M-Im-M, where M is the metal cation (i.e., Zn, Cd, or Co) and Im is the Imidazolate organic ligand and its derivatives. The reference to zeolites in the naming of ZIFs relates to their topological similarity. Zeolites consist of tetrahedrally bonded Si^{4+} (or Al^{3+}) atoms connected by oxygen atoms, forming Si/Al-O-Si/Al angles of ~145°. Similarly, in ZIFs, the metal (M^{2+}) cations are tetrahedrally coordinated to nitrogen at 1,3-positions of the organics imidazolate linkers leading to M-Im-M angle of 145°. This leads to this class of metal–organic frameworks forming the same net topologies as zeolites. Due to the organic linkers and metal–organic bonds, ZIFs generally have higher flexibility compared to zeolites. ZIFs are also known to have excellent thermal (can withstand up to 550°C) and chemical stability.[33] In this work, we specifically focus on sodalite (sod) ZIFs with Zn or Cd metal nodes and R substituted imidazolate linkers (R= CH_3, Cl, CHO, NO_2) as shown in Figure 2.1. Examined ZIFs belong to non-centrosymmetric space groups (i.e., $I\bar{4}3m$) with a large degree of tunability while keeping the same topology of the prototypical ZIF i.e., ZIF-8 (with Zn and R= CH_3). We calculated the pore size, which is the diameter of the largest sphere that will fit into the ZIF framework. The largest pore size for Zn ZIFs in this work (i.e., ZIF-8, ZIF-90, ZIF-Cl, ZIF-65) ranges between 11.5 Å to 12 Å.[33] For Cd-ZIFs (i.e., CdIF-1, CdIF-8), the pore size varies between 14.2 Å to 15.2 Å,[34] slightly higher than Zn-ZIFs. This is due to the slightly longer Cd-N bond compared to Zn-N. Such a high porosity should contribute to a lower dielectric constant favorable for piezoelectric energy harvesting. And indeed the total porosity for ZIFs in this work varies between 48-60% of volume of the unit cell. Notably, from an application point-of-view, among the studied ZIFs, ZIF-8 was already shown to have a very low dielectric constant of 2.3-2.45 with a low loss factor,[27, 35] and can be grown into thin films showing good processibility. Overall, the selected ZIFs are ideal candidates for studying structure-property relationships.

In this chapter, we present a systematic computational study on how piezoelectric response varies with change in building units of ZIFs. For this, we change the metal node (Zn, Cd) and substituent on the imidazolate linker in ZIFs. Piezoelectric coefficients for the investigated ZIFs were calculated with different DFT methods. To understand the contributing factors of piezoelectric response in ZIFs, we dissect the different contributions of piezoresponse to a mechanical strain into clamped ion, internal strain contributions and Born effective charges. We then discuss the results of mechanical properties (specifically the compliance constant s_{44}) and the piezoelectric coefficient for the different ZIFs. For this class of materials, we show that the mechanical properties have a dominant contribution to the piezoelectric constant d than the contribution from the piezoresponse e. In the last part of the paper, we compare these results of ZIFs with some existing Zn/Cd based inorganic and organic piezoelectrics.

2.2 Theory

Piezoelectricity is mathematically described in the IEEE standard for piezoelectricity[36] by a set of four constitutive equations that describe the response of a piezoelectric material to a mechanical load (stress/strain) and electric fields. The relevant set of equations involving the mechanical, electrical variables and their units are discussed in detail in the appendix section 2.A.1. The piezoelectric tensors with units $[C/m^2]$ and $[pC/N]$ respectively and of importance in piezoelectric energy harvesting applications to store as energy is the value of d

which effectively links the applied stress (T) to the electric displacement (D). We use Voigt notation for the third order piezoelectric tensors (e_{ikl}, d_{kij}) and fourth-order compliance tensor (s^E_{ijkl}) where the indices are given in compressed matrix notation instead of the tensor notation. Hence, they can be rewritten as e_{iq}, d_{ip} and s^E_{qp}. The piezoelectric constant d_{ip} can be computed from the piezoelectric constant e and the elastic compliance constant s using $d_{ip} = e_{iq}s^E_{qp}$. Computationally, the piezoelectric constant e_{iq} is calculated as the first derivative of the magnitude of the polarization P induced by strain $e_{iq} = \left(\frac{\partial P_i}{\partial \varepsilon_q}\right)_E$.

The piezoelectric tensor e can be further separated into two parts: clamped ion (e^0_{14}) and internal strain (e^{int}_{ik}) contributions. This is according to a well-known scheme used for many inorganic piezoelectrics to understand the origin of piezoelectricity in the material.[37–39] As indicated in work by Catti, M. et al[40] for a general case, piezoelectric constant e is shown in equation 2.1.

$$e_{ik} = \frac{\partial P_i}{\partial \varepsilon_k}$$

$$e_{ik} = \left(\frac{\partial P_i}{\partial \varepsilon_k}\right)_x + \sum_s \sum_j \left(\frac{\partial P_i}{\partial x_{sj}}\right)_{\varepsilon=0} \left(\frac{\partial x_{sj}}{\partial \varepsilon_k}\right)_{\varepsilon=0} \qquad (2.1)$$

$$e_{ik} = e^0_{ik} + e^{int}_{ik}$$

Essentially the clamped ion contribution (e^0_{ik}) is the change in polarization P_i due to the reorganization of electron density with external strain ε_k while the fractional coordinates x

| MOF	Metal & Substituent (R)
ZIF-8	Zn & CH_3
CdIF-1	Cd & CH_3
ZIF-90	Zn & CHO
ZIF-Cl	Zn & Cl
ZIF-65	Zn & NO_2
CdIF-8	Cd & NO_2
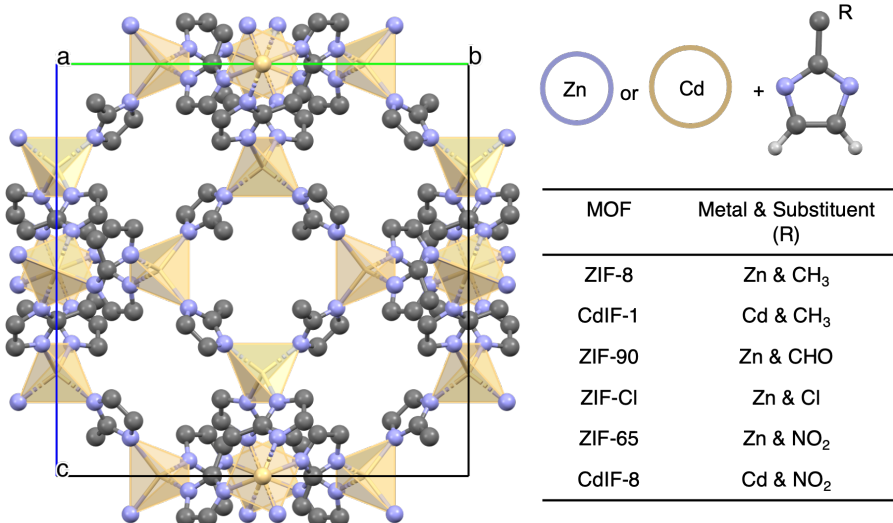
Figure 2.1: Representation of the unit cell of ZIFs (left) and Name of the ZIF along with their metal node and the substituent on imidazolate linker included for different ZIFs in this work.

are kept constant in the strained unit cell i.e., $\left(\frac{\partial P_i}{\partial \varepsilon_k}\right)_x$. The internal strain contribution (e_{ik}^{int}) provides the change in polarization P_i where the atoms are allowed to relax in the strained unit cell in response to the strain. This means that the internal strain contribution and the clamped ion contribution are typically opposite in sign. For the internal strain contribution, e_{ik}^{int} we sum over all the atoms s in the unit cell along three directions j $(1, 2, 3)$. In this contribution the change in polarization P_i with fractional coordinate $x_{sj} = 0$, $\left(\frac{\partial P_i}{\partial x_{sj}}\right)_{\varepsilon=0}$, is multiplied by the change in fractional coordinates x_{sj} with lattice strain, also termed the relaxation coefficient $\left(\frac{\partial x_{sj}}{\partial \varepsilon_k}\right)_{\varepsilon=0}$. Essentially, the internal strain contribution refers to the inner deformation of the crystal structure to keep the energy minimum. Moreover $\left(\frac{\partial P_i}{\partial x_{sj}}\right)_{\varepsilon=0}$, is related to, $Z_{s,ij}^*$ i.e., the Born effective charge (BEC). [40] BEC is a dynamical charge introduced by Max Born and Maria Göppert Mayer. It refers to a change in polarization induced by an atomic displacement under the condition of zero macroscopic electric field.[41]

So, for a cubic system, such as the investigated ZIFs, the internal strain contribution can be written in terms of Born effective charges as indicated in equation 2.2.

$$e_{ik}^{\text{int}} = \frac{ea}{V} \sum_s \sum_j Z_{ij}^* \frac{\partial x_{sj}}{\partial \varepsilon_k} \tag{2.2}$$

where a is the lattice parameter and V is the unit cell volume of the unstrained structure. Thus, the internal strain contribution is obtained by summing the product of Born effective charges, a second-order tensor (BECs $Z_{s,ij}^*$) and respective relaxation coefficient ($\frac{\partial x_{sj}}{\partial \varepsilon_k}$). From equations 2.1 and 2.2, to fully understand the e_{ik} in any piezoelectric material requires the determination of three quantities a) e_{ik}^0 clamped ion contribution b) $Z_{s,ij}^*$ Born effective charges (BEC's) and c) $\frac{\partial x_{sj}}{\partial \varepsilon_k}$, the relaxation coefficient, for all atoms in the unit cell.

Note the relevance of the Born effective charges: the high piezoelectric response of the best performing ceramics is due to very high anomalous dynamical Born effective charges of their transition metals (M) (vide infra). Further research on these dynamical charges in ceramic oxides indicated the mixed covalent and ionic character of the M-O bonds. Dynamical changes in the hybridization of these bonds with atomic displacement results in charge reorganization, which is observed as the Born effective charge of atoms.[41]

The piezoelectric tensors for the investigated ZIFs space group $I\bar{4}3m$ have only one independent piezoelectric constant: e_{14} and d_{14}. Specifically, for these space groups, equations 2.1 and 2.2 can be rewritten as shown in equation 2.3. The relation between piezoelectric constants e and d via compliance constant s is shown in equation 2.4.

$$e_{14} = e_{14}^0 + e_{14}^{\text{int}} \tag{2.3}$$

$$\text{with} \quad e_{14}^{\text{int}} = \frac{ea}{V} \sum_s \sum_{j=1,2,3} Z_{s,1j}^* \frac{\partial x_{sj}}{\partial \varepsilon_4}$$

$$d_{14} = e_{14} s_{44}^E \quad \text{and} \quad s_{44} = \frac{1}{c_{44}} \tag{2.4}$$

where c_{44} is the shear elastic constant and s_{44} is the compliance constant.

2.3 Methods

All the calculations reported in this chapter are performed using the ab initio periodic code Crystal17[42] based on the atoms centered Gaussian basis set. Triple zeta basis sets with polarization functions for all atoms [43–47] and Grimme D3 dispersions corrections were used.[48] For metal atoms Zn and Cd extra polarization functions were included.[49, 50] We adopted five DFT functionals at generalized gradient approximation (GGA) level of theory, namely hybrid functionals B3LYP and PBE0[51, 52] with 20% and 25% of HF exchange, meta GGA functional M06L[53] with 0% HF exchange and meta hybrid functionals M06 and M062X[54] which include 27% and 54% HF exchange. First, we performed a full relaxation (cell parameters and atomic positions) of the ZIF structures with all DFT functionals. Lattice parameters of structures taken from experimentally determined parameters reported in CSD database[55] were used for structural relaxation. The deviation between experimental and simulated lattice parameters for all functionals is always below ±2% as shown in Table 2.A.1. Using the optimized structure as starting geometry, full piezoelectric and elastic tensors were calculated using the numerical approach based on the geometry optimization of atomic positions at strained lattice configurations. Piezoelectric constant e is evaluated using the berry phase approach in the modern theory of polarization[56–58] as a first derivative of berry phase[59] with respect to strain[60]. This is done in Crystal17 by applying finite strains to the lattice as finite differences of polarization at strained configurations. The elastic or compliance constants c or s are expressed as second derivatives of energy with respect to pairs of strains, wherein Crystal17 the first derivative is computed analytically while the second derivative is evaluated as numerical finite differences between strained structures described in work by Erba *et al.* [61]. The other piezoelectric constant d is evaluated from the relation between e and c or s shown in equation 2.4. ZIF structures were subjected to a finite strain of ±1.5% for the numerical differentiation of the analytic cell gradients. We obtained piezoelectric and mechanical properties for all five DFT functionals, however, our most elaborate discussion in the main text of the chapter will involve the results using B3LYP which will be motivated later in the text.

2.4 Results and Discussions

In this study, we consider six different ZIFs with Zn/Cd as the metal node and substituted imidazolate as linker namely ZIF-8, CdIF-1, ZIF-90, ZIF-Cl, ZIF-65, and CdIF-8. The four different substituents of imidazolate considered are CH_3, CHO, Cl, and NO_2. Figure 2.2 shows the equilibrium structure of methyl and nitro substituted ZIFs, where part of the linkers are oriented along the dipolar direction x (denoted as 1 in the Voigt's notation), the direction along which we model the change in the electric response while applying a shear deformation along the depicted y and z directions (i.e., 2 and 3 directions denoted as 4 in the Voigt's notation). This is also the same for other studied ZIFs.

We first present the detailed outcomes of e_{14} for all ZIFs in terms of the clamped ion (e_{14}^0) and internal strain contributions (e_{14}^{int}). Later we will discuss the mechanical properties, i.e., s_{44} and resultant d_{14}. The analysis of piezoelectric constant 'e' by separating into the clamped ion and internal strain contributions is also applicable to perovskite materials, and has been done previously for inorganic piezoelectrics.[37, 39, 40, 62] We used a series of different functionals (B3LYP, PBE0, M06, M06L and M062X) and the lattice parameters
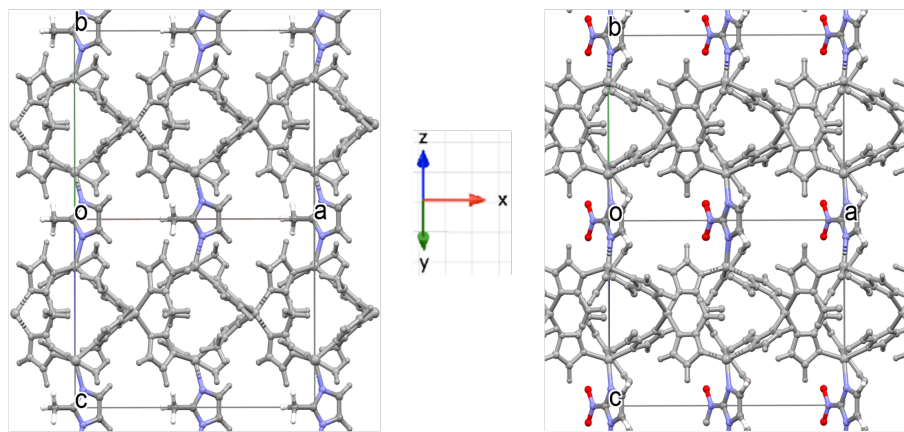
Figure 2.2: Geometry optimized equilibrium structures of ZIF-8 (left) and ZIF-65 (right) shown along the (011) plane showcasing the linkers with their C2 axis aligned dipolarly along x.
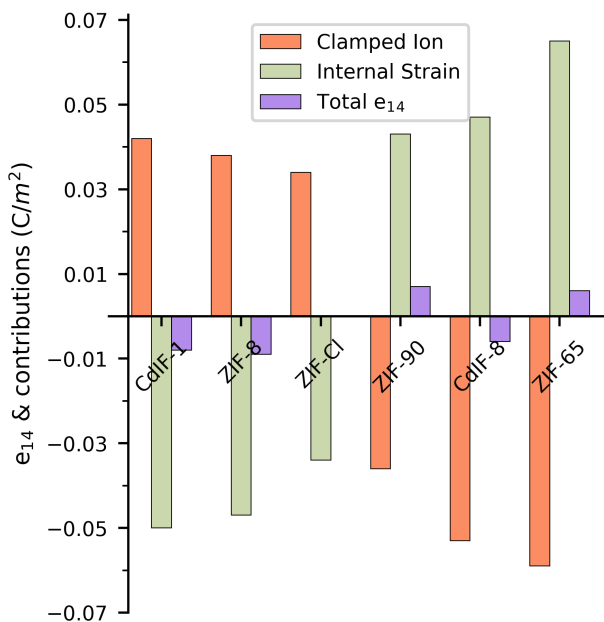

Figure 2.3: Bar graph showing the total piezoelectric constant (e_{14}) and its components, the clamped ion (e_{14}^0) and internal strain contributions (e_{int}^0) for the ZIFs considered ZIFs, modelled with the B3LYP functional.

of geometry optimized structures with all functionals are very close to experimental values with a deviation < 2% as indicated in Table 2.A.1 in the appendix. However, variation of piezoelectric and mechanical properties with the DFT functional is small for some ZIF's, while large for others. Here in the main text of the chapter, we draw only conclusions on variations in properties between different ZIFs, when these variations between ZIFs are larger than the variation between functionals for the same ZIF. In the main text of the chapter, we elaborate and discuss in depth the results obtained with B3LYP, as this functional has shown the best correspondence with experimental values for the elastic properties of ZIF-8.[63]

Figure 2.3 shows the total e_{14}, the clamped ion contribution (e_{14}^0) and internal strain contribution (e_{14}^{int}) for all ZIFs. As seen in Figure 2.3, the sum of both contributions e_{14} has much lower absolute values, due to the expected opposing sign of the two contributions, with the absolute magnitude of both contributions being very similar. Due to the small magnitude of e_{14} compared to the variation in magnitude between different DFT functionals, it is most meaningful to discuss changes in e_{14}^0 and e_{14}^{int} between the different ZIF structures, rather than the differences in the resultant e_{14}.

2.4.1 Clamped Ion Contribution (e_{14}^0)

The sign of e_{14}^0 changes from positive for -CH$_3$ ZIFs to negative e_{14}^0 for -NO$_2$ ZIFs (Figure 2.3), in effect this is a manifestation of the dipole moment of the linker changing sign going from an electron-donating to an electron-withdrawing side group. As the clamped ion contribution is a purely electronic contribution that indicates the effect of redistribution of electron density upon strain, it is informative to compare trends in the clamped ion contribution with the well-established and easily accessible parameter Hammett σ constant. It can be considered a measure of the electronic nature of the linker substituents, with a more positive Hammett constant for electron-withdrawing substituent groups, and a more negative one for electron-donating ones. The Hammett σ constant has been published in the literature for substituted phenyl systems based on meta or para substitution as σ meta or σ para constants respectively.[64, 65] It was also used for other chemically distinct systems like pKa values of imidazole derivatives and electronic, spectroscopic properties of pyrazole derivatives.[66, 67] Figure 2.4 shows a plot of the clamped ion e_{14}^0 of ZIFs with Zn/Cd as the metal node and σ meta, σ para constants. Linear fit in the plot shows a good correlation with the coefficient of determination $R^2 = 0.76$ with σ meta and $R^2 = 0.88$ with σ para Hammett constants, hence the electronic nature as captured in the Hammett constant is a good approximation to describe the effect of the linker substituent to e_{14}^0 in terms of changing the dipole moment of the linker. As can be seen from Figure 2.4, the value of e_{14}^0 is hardly affected by the choice of metal ion (Zn^{2+} vs. Cd^{2+} for -CH$_3$ and -NO$_2$ substituents).

2.4.2 Internal Strain Contribution (e_{14}^{int})

For all studied ZIF's the internal strain contribution is opposite in sign, and nearly equal in magnitude to the clamped ion contribution (e_{14}^0). As ZIFs are relatively soft material, it is indeed expected the nuclei relax (internal strain contribution) in a manner to counter the polarization created via the clamped ion contribution. As a result, the final e_{14} is much smaller for all ZIFs when compared to some inorganics like Zn, Cd oxides and sulphides.[68,
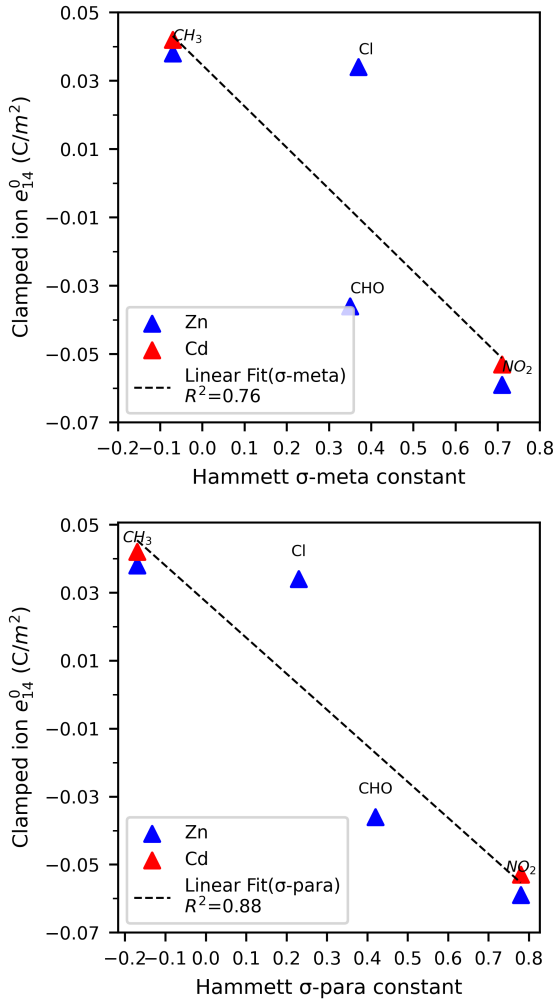
Figure 2.4: Correlation between clamped ion contribution e_{14}^0 and Hammett σ meta and para constants for four different substituents of Imidazolate.

69] As shown in equation 2.3, the internal strain e_{14}^{int} is a product of the Born effective charges (BEC's) $Z_{s,1j}^*$ and the relaxation coefficient $\frac{\partial x_{sj}}{\partial \varepsilon_4}$ which depends on the change in positions of the atoms during strain. Concerning the latter, we look at changes due to external shear in all bond lengths and angles in the structure. The largest variation above a cut-off of 0.05% for the relative change in bond lengths and absolute change of 1 degree for angles in response to an external shear deformation of 3% is considered and shown in Table 2.A.2 in the appendix. For all ZIFs we see that the highest change in bond length occurs in the Metal–N bonds ranging from 0.24% for ZIF-65 to 0.06% for ZIF8. The variation in the bond lengths for all ZIFs being less than 0.24% indicates that bond lengths

play a minor role in the shear deformation. Among the angles, the maximum variation for each ZIF constitutes that of the N-Metal-N bond angle (from 2.90°to 3.48°), followed by the variation of the Metal-N-C bond angle (from 0.69°to 1.44°) (see Table 2.A.2). This indicates that the flexibility is centered around the position of the linkers relative to the Zn^{2+} or Cd^{2+} ions, and that the organic linker is comparatively rigid. Additionally, the structural changes observed are mainly due to bond angle changes around the metal tetrahedra while the changes in bond lengths are minimal. The other factor that influences e_{14}^{int} are the Born effective charges (BECs, Z^*) which are second-rank tensors and can be represented in matrix form in Voigt notation as

$$Z^* = \begin{bmatrix} Z_{11}^* & Z_{12}^* & Z_{13}^* \\ Z_{21}^* & Z_{22}^* & Z_{23}^* \\ Z_{31}^* & Z_{32}^* & Z_{33}^* \end{bmatrix}$$

In inorganics like $BaTiO_3$ anomalously high BEC's are responsible for superior piezoelectric constants where the BEC is much higher than the nominal charge of the atom (e.g. a BEC (Z_{Ti}^*) of +6.7 for Ti with a nominal charge of +4 in $BaTiO_3$).[41] Hence, we analyzed the magnitude of BEC's of all atoms in the ZIF structures. For all ZIFs, the acoustic sum rule (ie $\sum_s Z_{s,ij}^* = 0$ meaning charge neutrality in all directions) is satisfied, indicating good convergence of our calculations within an accuracy of 0.07 charge units. From equation 2.3, BEC $Z_{s,1j}^*$ with $j = 1, 2, 3$ are the relevant elements of BEC tensor that contribute to e_{14}^{int}. Figure 2.5 shows a scatter plot of $Z_{Zn/Cd,11}^*$, $Z_{Zn/Cd,12}^*$ and $Z_{Zn/Cd,13}^*$ of all metal atoms Zn and Cd in the unit cell, for all six ZIFs in this work. We see that $Z_{Zn/Cd,11}^* > Z_{Zn/Cd,12}^*$, $Z_{Zn/Cd,13}^*$ and values of $Z_{Zn/Cd,11}^*$ are around +2.0 to +2.5. Thus, the overall Born effective charge of the metal node in these ZIFs is close to their nominal charge of +2.0, and not anomalous. The influence of the linker substituent on the BEC of the metal node is negligible, with a variation around ±0.2. The variation of the BEC of the organic atoms in discussed in the appendix in Section 2.A.4.2. Overall, metal atoms have the highest BEC among all atoms in the ZIF system. In the case of the organic part of ZIFs, there is a lot of variation in the BEC's depending on the displacement direction, and they mostly range from +1 to −1 indicating the covalent bond nature between them. None of the magnitudes of BEC's are exceptionally high, which is one of the reasons why the internal strain component of e_{14} i.e., e_{14}^{int} is not high enough to overcome the clamped ion component e_{14}^0 significantly, as does happen for the best performing inorganic piezoelectrics (like PZT and $BaTiO_3$).

As e_{14}^{int} is defined by the product of the BEC's and relaxation coefficients (equation 2.3), we now identify the atoms which have the highest magnitude for this product 'A' $= \left(Z_{s,1j}^* * \frac{\partial x_{sj}}{\partial \varepsilon_4} \right)$ for all ZIFs. This product was calculated numerically from DFT calculated Born effective charge tensor and change in positions of atoms obtained from unstrained and strained structures. For each ZIF, a cutoff value of 5% of $|e_{14}^{int}|$ was chosen to consider the product 'A' $= \left| Z_{s,1j}^* * \frac{\partial x_{sj}}{\partial \varepsilon_4} \right|$ for all atoms. This value is ~ 0.002 to 0.003 C/m² depending on the ZIF. All atoms with absolute contributions greater than this value are highlighted in Figure 2.6 (for ZIF-8 and CdIF-1) and Figure 2.A.6 in the appendix (for ZIF-90, ZIF-Cl, ZIF-65 and CdIF-8), where green indicates a positive contribution and red indicates a negative contribution to internal strain contribution e_{14}^{int}. Since the e_{14}^{int} refers to polarization along $x(1)$ when a shear strain is applied along $yz(4)$, this orientation to show the (011) plane was
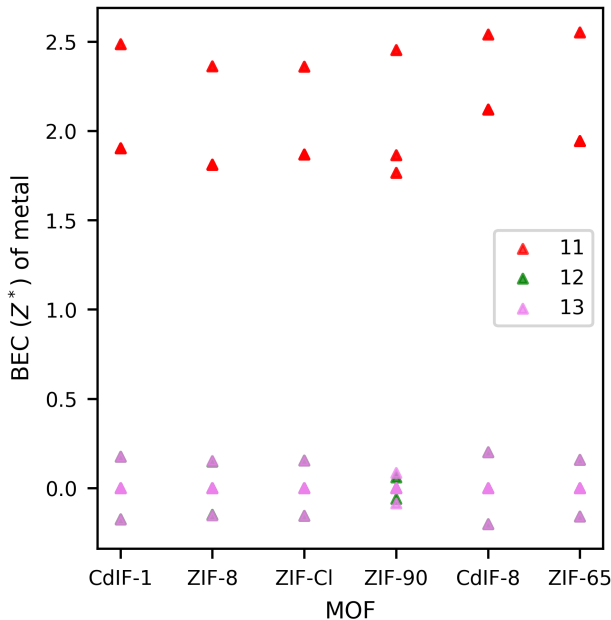
Figure 2.5: Born effective charges (BEC) of all metal nodes for the six ZIFs. BEC in relevant directions 11, 12, 13 is shown with different colored markers.

chosen in Figure 2.6. For the linkers aligned with their C2-axis along the x-direction, these are dipolarly aligned. Note however, that the other linkers are orientated in a manner that diminished the overall polarization caused by the linkers.

For ZIF-8 and CdIF-1, we see a similarity in the atoms that have a higher magnitude for 'A', hence Figure 2.6. We see that overall the organic linker, which as a mostly rigid unit is tilted with respect to the M^{2+} tetrahedra (vide infra) contributes most to the internal strain piezoelectric coefficient e_{14}^{int}. The larger relocation of the organic atoms $\left(\frac{\partial x_{sj}}{\partial \varepsilon_4}\right)$, trumps the contribution of the larger Born effective charges of the inorganic atoms $(Z_{s,1j}^{*})$. Most studied ZIF structures show a similar behavior, except for aldehyde and the nitro-substituted ZIFs (ZIF-90, ZIF-65 and CdIF-8): for these structures also the inorganic atoms show a 'A' value above the cut-off.

2.4.3 Elastic compliance constant (s_{44}) and Piezoelectric constant (d_{14})

The piezoelectric coefficient that determines the performance in piezoelectric device is d_{14}, which we can be derived from e_{14} and the elastic compliance constant s_{44} (see equation 2.4). To be specific, d is one of the factors responsible for high figure of merit in energy harvesting applications. As shown in theoretical and experimental work on shear modulus and mechanical properties of ZIF-8 by Tan et al.,[63] the theoretical estimation of elastic constants
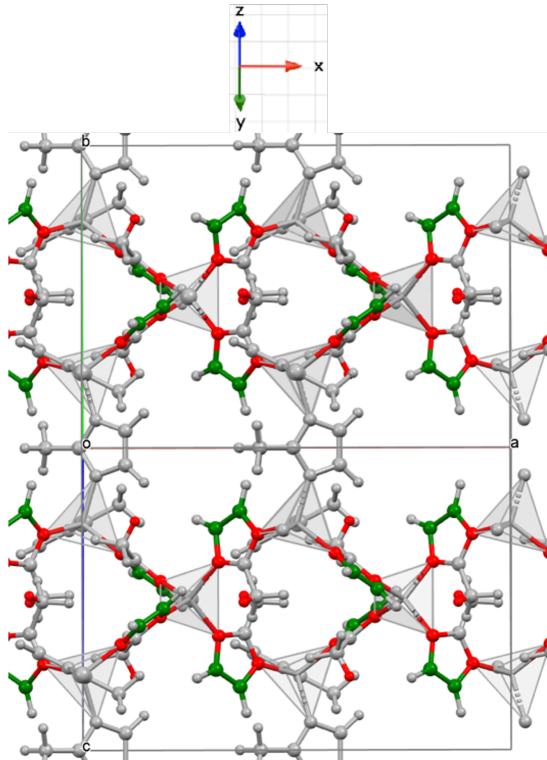
Figure 2.6: ZIF structure highlighting the atoms with contribution 'A' = $\left| Z_{s,1j}^{*} * \dfrac{\partial x_{sj}}{\partial \varepsilon_{4}} \right|$ greater than 5% of $|e_{14}^{\text{int}}|$ for both ZIF8 and CdIF-1. The positive contribution of 'A' is indicated with green color and negative contribution in red colour.

depends on the choice of exchange-correlation functionals and dispersion corrections. We calculated c_{44} and s_{44} with different DFT functionals shown in Figure 2.A.7a in the appendix and the ratio of the standard deviation to the average varies from $0.1 - 18\%$ except for CdIF-1 and CdIF-8 a deviation of 30% is observed. Although c_{44} and s_{44} vary with the choice of DFT functionals for each ZIF, variation between different ZIFs is consistent in most cases. As shown in Figure 2.A.10 in appendix, correspondingly there is a lot of variation of d_{14} with the choice of DFT functional, due to the variability of both e_{14} and s_{44} with choice of functional. However, the variation between different ZIF-structures (the trend) is mostly consistent. Since B3LYP functional with and without dispersion corrections estimates reliable values close to experimentally measured mechanical properties at 295 K in ZIF-8,[63] we will discuss and compare results of s_{44} and d_{14} with B3LYP for all ZIFs in the main text of the chapter. Moreover, we will only point out differences between structures when this difference is larger than the variation of the property with the functional. c_{44} was previously calculated with DFT for ZIF-90, ZIF-Cl and values are 2.502 and 3.578 GPa respectively.[70] Despite having different values for c_{44} in comparison to the previous work,

the values in our work computed with all the five different DFT functionals are in the same range i.e., $0.75 - 1.18$ GPa and $0.81 - 0.91$ GPa for ZIF-90 and ZIF-Cl respectively (see Figure 2.A.7a).
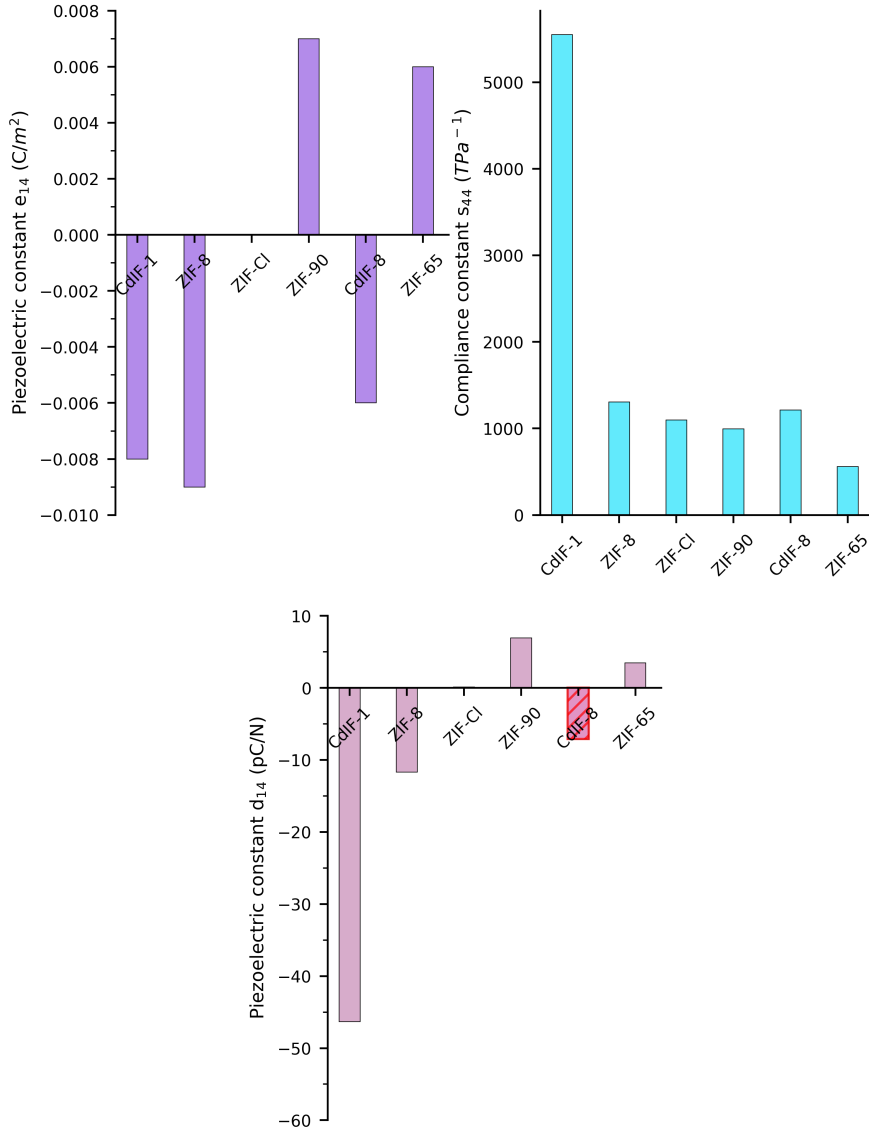

Figure 2.7: Bar graphs showing e_{14}, s_{44}, d_{14} for all six ZIFs with B3LYP functional (d_{14} for CdIF-8 marked in graph, is unreliable due to huge variation with DFT functional).

Mechanical properties of the investigated ZIFs indicate a change in flexibility of the framework with metal node and linker substituent. High s_{44} (or low c_{44}) means more

flexibility of the framework, while low s_{44} (high c_{44}) indicates stiffer mechanical properties. As seen in Figure 2.7, s_{44} is the highest for CdIF-1 with Cd and CH_3 as substituent and lowest for ZIF-65. Overall, we see that for the same substituent, s_{44} increases significantly going from Zn^{2+} to Cd^{2+}, and that overall CH_3 is the substituent leading to most flexibility, and NO_2 to the least. Compliance constant s_{44} of ZIF-90 and ZIF-Cl range in between CH_3 and NO_2 substituent Zn-ZIFs. We hypothesize the cause for NO_2 ZIFs being stiffer than CH_3 ZIFs, despite the weaker Zn-N bond in the former, is due to the increased steric interactions of the larger NO_2 groups. For example, as shown in Figure 2.A.11 in appendix, the oxygens of the NO_2 group in adjacent linkers are closer than the hydrogens of the CH_3 group (3.095 Å vs 3.297 Å where van der Waals radii of O and H are 1.5 Å and 1.2 Å respectively[71]) due to which there is more resistance during shear resulting in higher c_{44}/lower s_{44}. It is clear that Cd^{2+} ZIFs are more flexible with regard to the shear modulus than Zn^{2+} ZIFs. This could be due to the longer Cd-N bond distance of 2.2 Å compared to the Zn-N bond distance of 2.0 Å.

In the end, looking at piezoelectric constant d_{14}, it is the highest in magnitude for CdIF-1 compared to other ZIFs for all DFT functionals used in this work. Since e_{14} is the same order of magnitudes for all ZIFs, flexibility is the key contributing factor responsible for higher d_{14} of CdIF-1. The value of d_{14} for CdIF-1 is in the range −38 to −46 pC/N (except for M06L functional it is −94 pC/N, see Figure 2.A.10 in appendix). After CdIF-1, ZIF-8 seems to have d_{14} values in the range −9 to −14 pC/N. For ZIF-90, ZIF-Cl and ZIF-65, due to huge variation of d_{14} with DFT functional it is difficult to conclude a trend, but the magnitudes of d_{14} are in the same range for these three MOFs i.e., $< \pm 8$ pC/N. d_{14} for CdIF-8 (marked in Figure 2.7) varies between 2 to 50 pC/N due to a large variation in both e_{14} and s_{44} with the functional, making it difficult to conclude about d_{14} in CdIF-8.

2.5 Comparison with existing inorganic and organic piezoelectrics

2.5.1 Piezoelectric Properties

Here we compare the results of piezoelectric and mechanical properties of ZIFs in this work with some existing Zn/Cd inorganic and widely known organic piezoelectrics like PVDF and its copolymers. Table 2.1 lists the compliance constants (s_{44}, s_{pq}), clamped ion (e_{ik}^0), internal strain (e_{ik}^{int}), final piezoelectric constant e_{ik} and d_{ik} of these materials, and the ZIFs in this work.

Comparing the results of e_{ik}^0 and e_{ik}^{int} for inorganic ZnO/ZnS with ZIFs, we see that inorganics have almost an order to 2 orders of magnitude higher than ZIFs. However, one of the factors that influence e_{ik}^{int} is Born effective charges (BEC) and BEC of metal $Z_{Zn/Cd}^*$ in ZIFs is similar to BEC of Zn, Cd in inorganics presented in Table 2.1. This value is around +2.10 to +2.12 for Zn, +2.13 to +2.27 for Cd in inorganics mentioned here, and it is comparable to values of +2.0 to +2.5 for the ZIFs. The low BEC for Zn^{2+} and Cd^{2+} in both ZnX, CdY and ZIFs could be due to the completely occupied d orbitals, unlike Ti^{4+} in $BaTiO_3$ with anomalous BEC which has unoccupied d orbitals. [41] To further understand the differences in e_{ik}^0 and e_{ik}^{int} between ZnO/ZnS and ZIFs, we looked at the extent of clamped ion contribution that is compensated by internal strain using the ratio $-e_{ik}^0/e_{ik}^{int}$. For ZnO

and ZnS this is $28 - 40\%$ and $69 - 83\%$ respectively, whereas for all ZIFs it is $80 - 100\%$. Higher compensation in ZnS than ZnO is attributed to the bigger electronic polarizability of sulphide than the oxide anion.[40] But for ZIFs in this work, the clamped ion contribution is much smaller than that of inorganics ($\sim 0.06 \, \mathrm{C/m^2}$(ZIFs) vs $\sim 0.59 \, \mathrm{C/m^2}$(ZnX)), so there is less to compensate for by the internal strain contribution. Plausible reasons for the higher compensation of clamped ion contribution are a) ZIFs belong to a non-polar cubic space group and highly symmetric and b) higher flexibility of the framework, by which indeed atoms relax easily in a manner to counter the polarization created via clamped ion contribution. Finally, comparing $|e_{14}|$ of all ZIFs which is $0.01 \, \mathrm{C/m^2}$ while Zn/Cd inorganic piezoelectrics with values between $0.03 \, \mathrm{C/m^2}$ to $1.19 \, \mathrm{C/m^2}$, indicates a low piezoelectric constant e.

Table 2.1: Comparison of piezoelectric constants e_{ik}, its components e_{ik}^0 & e_{ik}^{int}, d_{ik} and compliance constant s_{44} and s_{pq} of some inorganic, organic piezoelectric with ZIFs.

Properties	ZnX (X=O,S)[68, 69]	ZnX (X=Se,Te)[68, 69]	CdY (Y=S,Se,Te)[68, 69]	PVDF[72]	PVDF-TrFE[72]	ZIFs
$\lvert e_{ik}^0 \rvert$ (C/m^2)	0.22 to 0.59					≤0.06
$\lvert e_{ik}^{\mathrm{int}} \rvert$ (C/m^2)	0.41 to 1.63					≤0.07
$\lvert e_{ik} \rvert$ (C/m^2)	0.11 to 1.19	0.03, 0.05	0.03 to 0.49	0.01 to 0.27	0.07 to 0.18	≤0.01
s_{44} (1/TPa)	10.42 to 34.48	22.67 to 32.15	50.25 to 75.95	454.45	400	558.72 to 5584.61
s_{pq} (1/TPa)	4.63 to 23.25	8.5 to 24.0	5.72 to 69.20	94.34 to 227.27	90.90 to 714.28	
$\lvert d_{ik} \rvert$ (pC/N)	1.1 to 12.3	0.9 to 1.1	3.92 to 13.98	1.5 to 38.3	7 to 50	0.12 to 46.33

Looking at the mechanical properties, the magnitude of s_{44} for all ZIFs in this study is greater than, $\sim 560 \, 1/\mathrm{TPa}$ and the highest s_{44} among them is for CdIF-1 with a magnitude of $\sim 5500 \, 1/\mathrm{TPa}$. Between Zn/Cd inorganics and ZIFs, we see that the compliance constant s_{pq} is very low for inorganics almost one to two orders of magnitude lower than ZIFs. One thing commonly observed in both Zn/Cd inorganics and Zn/Cd ZIFs is an increase in s_{pq} or improvement of flexibility with change in metal from Zn to Cd.

Since data for e_{ik}^0 and e_{ik}^{int} are not available in literature for organic piezoelectrics PVDF and polyvinylidene fluoride-trifluoroethylene (P(VDF-TrFE)), we compare here the Born effective charges (Z^*), one of the key contributors to e_{ik}^{int} in these materials with ZIFs charges. Previous work on ferroelectric phase β-PVDF shows Z^* for C $-0.2/1.45$, for F and H -0.75 and 0.14 respectively.[73] Recent work on metal free organic perovskite material like MDABCO-NH$_4$-X$_3$ (X=Cl, Br, I) show C, N, H with a magnitude of Z^* around 0.14 to 0.67.[11] These values are similar to Born effective charges of the atoms in the organic linkers for ZIFs. Comparing $|e_{14}|$ of all ZIFs with PVDF and its copolymers, some e_{ik} values are also as low as ZIFs, but few e_{ik} values are up to an order of magnitude larger than ZIFs.

Also, these organic piezoelectrics are polar materials, hence a spontaneous polarization is present by virtue of structure. Mechanical properties of organic materials considered here is lower than most ZIFs in some directions but in a few directions s_{pq} is comparable with s_{44} of ZIFs (except CdIF-1 for which s_{44} is one order of magnitude higher). Literature on clamped ion (e_{ik}^0) and internal strain contributions (e_{ik}^{int}) of e for Zn/Cd Se, Te, and polymer piezoelectrics considered here are not available, and those values are not included in Table 2.1.[‡]

Overall comparison of ZIFs, with Zn/Cd based piezoelectric inorganics and specified organics; even though piezoelectric constant e of ZIFs is lower; they are softer and flexible which is the main contributing factor for obtaining a high piezoelectric coefficient d. This is observed in the case of CdIF-1 where $|e_{14}|$ =~ 0.01 C/m^2 is less than most materials shown in Table 2.1, but it has a $|d_{14}|$ of 38 to 46 pC/N higher than all II-VI type inorganics and is in the same range of value as polymers PVDF. After CdIF-1, ZIF-8 with $|d_{14}|$ = 9 to 14 pC/N is comparable to P(VDF-TrFE) and some Cd inorganics.

Comparing ZIFs with piezoelectrics other than Zn/Cd inorganics and PVDF, ZIF-8 has a d_{14} comparable to d_{33} of LiNbO$_3$ (11 pC/N), Poly-L-lactic acid (PLLA) (11 pC/N) and metal-free organic piezoelectric MDABCO-NH$_4$I$_3$ (14 pC/N).[74]. Piezoelectrics like PZT (410 pC/N), BaTiO$_3$ (191 pC/N), KNN (80-160 pC/N)(Potassium sodium niobate), recent hybrid materials like TMCM-MnCl$_3$ (185 pC/N) (Trimethylchloromethyl ammonium trichloromanganese) have a large piezoelectric response [3, 74] than CdIF-1 in this work. Specifically, for the metal-free MDABCO $-$ NH$_4$ $-$ X$_3$ (X=Cl, Br, or I),[11] highest d_{ik} (250 pC/N) of MDABCO-NH$_4$X$_3$ is larger than all the ZIFs investigated in this work, it is mainly due to large e_{ik} (0.35 C/m^2) than ZIFs, because the highest s_{pq} (650 1/TPa) is lower than s_{44} of ZIFs.

The study of cadmium ZIFs in this work provides a good understanding of how flexibility can influence the piezoelectric properties. However, Cd is also a heavy metal like lead, which is toxic and carcinogenic for the human body. Hence, Cd ZIFs are a proof of concept to show the potential of MOFs as piezoelectric materials, but are not ideal candidates for future applications.

2.5.2 Acoustic properties

Another factor on which the efficiency of piezoelectric devices depends is, the proper matching of acoustic impedance (z) of energy harvesting materials and the media in which energy is being harvested. Hence, we discuss in brief the acoustic impedance of the ZIFs in this work and compare with some piezoelectric ceramics, polymers and also the acoustic impedance of typical harvesting media. The acoustic impedance is a measure of the ease with which sound travels through a particular medium. It can be calculated as the product of acoustic velocity and density of the material. Theoretically calculated maximum longitudinal acoustic impedance values of ZIFs are shown in Table 2.2 and detailed maximum and minimum values of longitudinal and transverse velocities are provided in appendix in Table 2.A.3.

The acoustic impedance values of ZIFs are lower than both piezoelectric ceramics and organics. Among the ZIFs, CdIF-1 specifically has a lower acoustic impedance than other

---

[‡]II-VI type inorganics with Zn and Cd like ZnO, ZnS exist either in hexagonal wurtzite phase or cubic zinc blende phase and have 3 (e_{33}, e_{31}, e_{15}) and 1 (e_{14}) independent piezoelectric constant respectively.

ZIFs. Importantly, the acoustic impedance of ZIFs is much closer to harvesting media like water and living tissue, compared to ceramics and some of the polymers. This is an advantage for harvesting energy from these media.

Table 2.2: Comparison of acoustic impedance (z) of ZIFs in this work with piezoelectric ceramics, organics, and some energy harvesting media.

Material	Acoustic Impedance z(MRayl)
ZIFs	
ZIF-8	3.10
CdIF-1	2.40
ZIF-90	3.24
ZIF-Cl	3.38
ZIF-65	4.10
CdIF-8	3.37
Ceramics[5]	
$BaTiO_3$	30.00
PZT4	36.15
$LiNbO_3$	34.00
Polymers[5]	
PVDF	20
P(VDF-TrFE)	4.51
Harvesting media[5]	
Water	1.45-1.5
Tissue(skin)	1.99

2.6 Conclusions

To obtain a structure property relationship in MOFs, we systematically investigated the piezoelectric and mechanical properties of six non-centrosymmetric, non-polar ZIFs with Zn/Cd as metal nodes and varying the substituent on imidazolate linker (R=CH_3, Cl, CHO, NO_2) using density functional theory (DFT) calculations. Piezoelectric coefficient e is similar in magnitude for all ZIFs because of the huge compensation of clamped ion contribution e_{14}^0 by internal strain e_{14}^{int} possibly from the higher flexibility of the frameworks. The magnitude of e for the current ZIFs ~ 0.01 C/m^2 is low compared to most inorganic piezoelectrics. This can be tuned for future MOFs by 1) choosing polar MOFs with a spontaneous polarization. Some examples of polar MOFs include Zn-isonicotinate (Zn-IN) MOFs and Zn/Cd/Co-Pyridylacrylate MOFs (Zn/Cd/Co-PAA) and 2) MOFs with metal nodes which can show anomalous Born effective charges (Z^*) similar to best-performing inorganics $BaTiO_3$.

Even though e values for current ZIFs are low, the highest magnitude of piezoelectric constant d is seen for CdIF-1 with Cd metal node and methyl (CH_3) imidazolate as a linker with a theoretical value of $38 - 46$ pC/N. This value is comparable to the most common organic piezoelectric PVDF and the main contributing factor for this high d value is the low shear modulus (high flexibility) of the framework. The estimated figure of merit (FOM) of CdIF-1 calculated using an experimentally measured dielectric constant value of ZIF-8 (2.33) and d values obtained in this work is ~ $620/\varepsilon_0$ to $900/\varepsilon_0$ (pC/N)^2. This is quite high compared to FOM_{ij} of PZT (410 pC/N, ε=1800) and PVDF (30 pC/N, ε=10)[75] $93/\varepsilon_0$ and $90/\varepsilon_0$ (pC/N)^2 respectively. Hence, when tunable parameters like structural building units are optimized to obtain high flexibility, high Born effective charges and favorable

non-centrosymmetric symmetry, MOFs should be exceptional candidates to be used as piezoelectric energy harvesters.

Appendix to chapter 2

2.A.1 Theory

Piezoelectricity is mathematically described in the IEEE standard for piezoelectricity[36] by a set of four constitutive equations that describe the response of a piezoelectric material to a mechanical load (stress/strain) and electric fields. Of relevance in this work are a set of constitutive equations shown in equation 2.5.

$$D_i = e_{ikl}S_{kl} + \varepsilon_{ij}^S E_k$$
$$S_{ij} = s_{ijkl}^E T_{kl} + d_{kij}E_k \qquad\qquad (2.5)$$

where D, S, ε, E, s, T represent electric displacement [C/m^2] strain tensor (dimensionless), dielectric constant [F/m], electric field [V/m], elastic compliance tensor [m^2/N] and stress tensor [N/m^2] respectively. e and d are piezoelectric tensors with units [C/m^2] and [pC/N] respectively. Note that of importance in piezoelectric applications is the value of d which effectively links the applied electrical field to the deformation of the material (strain S), relevant for transducers, or the applied stress (T) to the electric displacement (D) which can be stored as energy in piezoelectric energy harvesting. This relation between electrical and mechanical properties is pictorially shown by Heckmann diagram in Figure 2.A.1 adapted from the book by JF Nye.[76] We will use Voigt notation for the fourth-order elastic (s_{ijkl}^E) and third order piezoelectric tensors (e_{ikl}, d_{kij}) where the indices are given in compressed matrix notation instead of the tensor notation. This means that the indices ij or kl where $i, j, k, l = 1, 2, 3$ are replaced by p or q and pairs of contracted cartesian directions $p, q = 1, 2, 3, 4, 5, 6$ where 11:1; 22:2; 33:3; 23, 32:4; 13, 31:5; 12, 21:6. The piezoelectric constant d_{ip} can be computed from the piezoelectric constant e and the elastic compliance constant s using $d_{ip} = e_{iq}s_{qp}^E$. Computationally, the piezoelectric constant e_{iq} is calculated as the first derivative of the magnitude of the polarization P induced by strain $e_{iq} = \left(\frac{\partial P_i}{\partial \varepsilon_q}\right)_E$.

2.A.2 Geometry Optimization

Experimental structures deposited in CSD database[55] were used as starting geometry for full relaxation of ZIF structures except for ZIF-90 for which the structure was obtained from single crystal XRD measurements of synthesized crystals in the group. We adopted a series of five different functionals (B3LYP-D3, PBE0-D3, M06-D3, M06L-D3 & M062X) and with all functionals geometry optimization, vibrational frequency calculation followed by a piezoelectric calculation was done. Clamped Ion contribution to piezoelectric constant was calculated in a separate calculation. Vibrational frequency calculation was done to ensure the equilibrium structure is at the minima of the potential energy surface.

Note on Methyl ZIFs: ZIF-8 and CdIF-1 belong to $I\bar{4}3m$ space group where the hydrogens of methyl group are disordered due to free rotation of methyl groups.[77] Hence, for modelling purposes, the symmetry was lowered to $I23$ where orientation of methyl group can be present in two orientations as shown in Figure 2.A.2. For each DFT functional, we compared the final energies of the two equilibrium structures, the vibrational frequencies and convergence of the piezoelectric calculations for the structures. Piezoelectric constants
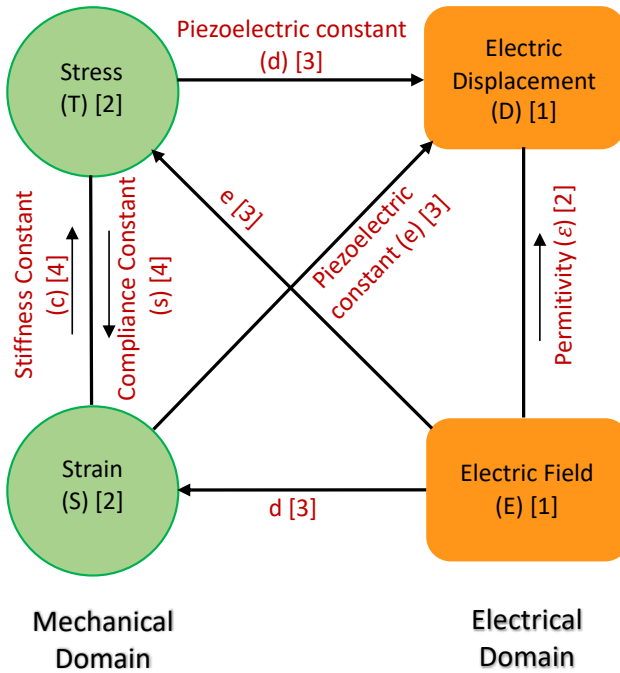
Figure 2.A.1: Part of Heckmann diagram showing the relation between mechanical and electrical properties, various variables, and their symbols. The tensor rank of the properties and variables is shown in square brackets.

of the structure with the lowest energy, absence of negative frequencies and converged piezoelectric calculation was considered for each functional and shown in the next sections of appendix. For ZIF-8, the orientation of methyl groups shown on the left in Figure 2.A.2 was considered final for all DFT functionals except for M062X functional. With M062X functional, the methyl orientation on the right in Figure 2.A.2 had the lowest energy, and the piezoelectric calculation converged well for this structure. In case of CdIF-1, with B3LYP-D3 and PBE0-D3 orientation shown on left in Figure 2.A.2 was used and with M06L-D3 and M06-D3 functionals, structure on the left was considered for comparison of final piezoelectric and mechanical properties. For CdIF-1, the piezoelectric calculations did not converge with M062X DFT functional for both orientations even with stringent convergence criteria. Hence, this result was not considered for comparisons and marked separately in all graphs in the next sections of appendix. Note on ZIF-90: The experimental structure of ZIF-90 published in the CSD database belongs to space group $I\bar{4}3m$ and oxygen, hydrogen of the aldehyde group are disordered due to symmetry.[78] Hence, for modeling, the symmetry was reduced to I23. On geometry optimization of this lower symmetry structure, it converged to a structure similar to the single crystal XRD structure we obtained from synthesis in the group. Hence, the unpublished single crystal XRD structure was used as the starting structure for all further piezoelectric calculations.
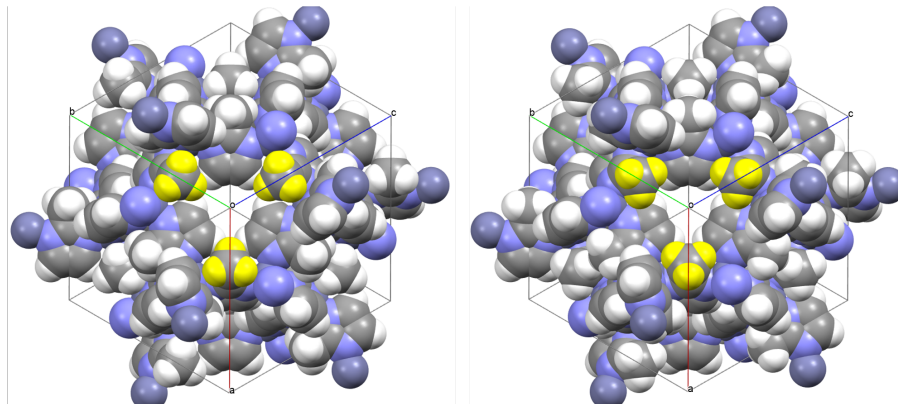
Figure 2.A.2: Two possible orientations of Methyl groups highlighted for the case of ZIF-8.

The simulated parameters of final optimized structures and deviation from experimental parameters for each DFT functional is shown in Table 2.A.1.

Table 2.A.1: Experimental and Optimized lattice parameter along with deviation ($\Delta\%$) for all five different DFT functionals in each ZIF.

DFT Functional	Lattice Parameter	ZIF-8	CdIF-1	ZIF-90	ZIF-Cl	ZIF-65	CdIF-8
Experimental	a (Å)	17.009[79]	18.121[34]	17.060[1]	17.037[80]	17.000[81]	18.077[34]
M06L-D3	a (Å)	16.877	17.953	17.148	17.041	17.152	18.035
	Δ(%)	-0.78	-0.92	0.52	0.03	0.90	-0.23
B3LYP-D3	a (Å)	17.078	18.126	17.261	17.116	17.294	18.127
	Δ(%)	0.40	0.03	1.18	0.46	1.73	0.27
PBE0-D3	a (Å)	17.007	18.037	17.043	17.053	17.212	18.045
	Δ(%)	-0.01	-0.46	-0.10	0.09	1.25	-0.18
M06-D3	a (Å)	16.819	17.870	17.077	16.941	17.184	17.962
	Δ(%)	-1.12	-1.39	0.10	-0.56	1.08	-0.64
M062X	a (Å)	16.927	18.045	17.006	17.182	17.212	18.019
	Δ(%)	-0.48	-0.42	-0.32	0.85	1.25	-0.32

[1] Structure taken from unpublished single crystal XRD data with a spacegroup of I23

2.A.3 Variation of Piezoelectric constant 'e' and its components with DFT functional

Variation of piezoelectric constant 'e' is inconsistent across all types of ZIF, meaning the variation with functional is large for some ZIFs, and it is small for others, as shown in Figure 2.A.3. In e_{14}^0 (clamped ion) calculations, we found that the ratio of standard deviation (SD) to average e_{14}^0 with DFT functionals ranges between $1 - 14\%$ for all ZIFs. This is the same for e_{14}^{int} (internal strain) except for ZIF-90 and CdIF-8 a large deviation of 24% and

27% is observed. Similar variation of piezoelectric constants of about 40% was observed in inorganics based on the choice of LDA or GGA approximation to exchange-correlation energy, even though change in lattice constants is 1-2%.[82] In the case of ZIF8, CdIF-1 and ZIF-65 for all DFT functionals, the sign of e_{14} follows the sign of e_{14}^{int} indicating $e_{14}^{int} > e_{14}^{0}$ i.e., internal strain values are larger than the clamped ion values for these ZIFs. For CdIF-8, we see that for all functionals $e_{14}^{int} < e_{14}^{0}$, thus e_{14} has the same sign as e_{14}^{0}. For ZIF-90 and ZIF-Cl the sign of e_{14} differs based on the choice of functional. In the case of B3LYP and PBE0 for ZIF-Cl $e_{14}^{int} = e_{14}^{0}$, so e_{14} is zero. In Figure 2.A.3, internal strain e_{14}^{int} and e_{14} are marked in the graph for CdIF-1 with M062X functional and for ZIF-65 with M06-D3 functional. These specific piezoelectric calculations did not converge properly even with stringent convergence criteria on energy, hence these results were excluded for conclusions obtained in the main text of the chapter.
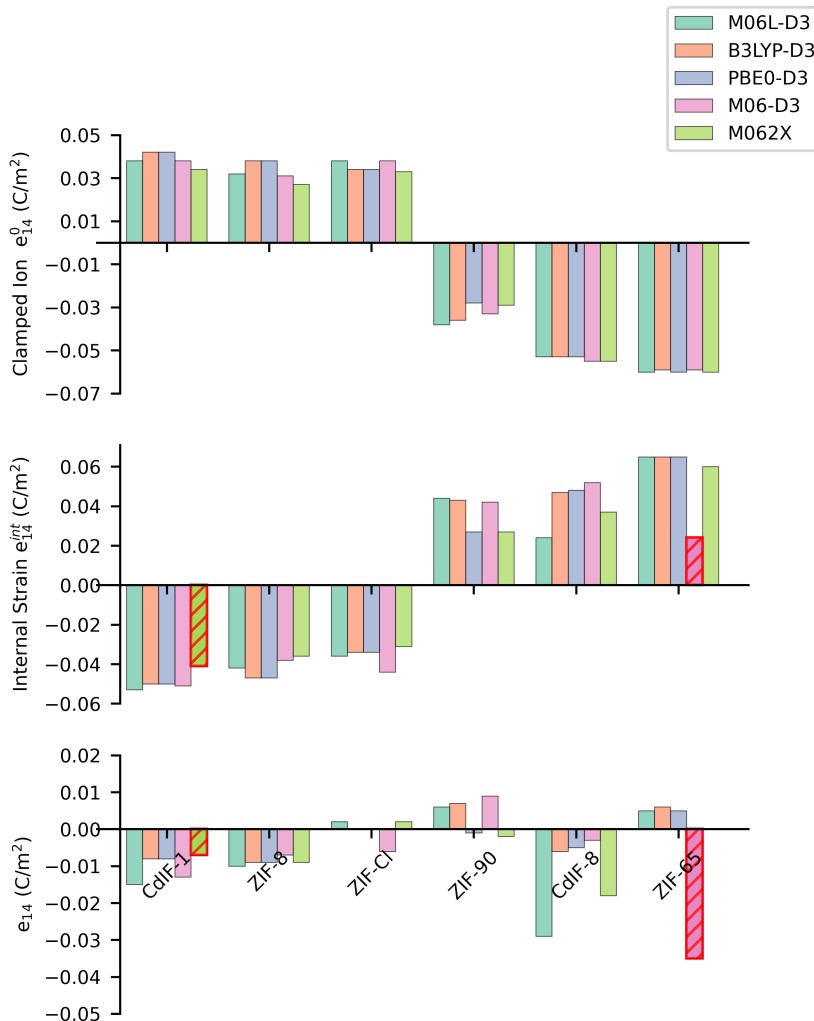
Figure 2.A.3: Clamped ion e_{14}^0, Internal Strain contributions e_{14}^{int} and total piezoelectric constant e_{14} with five different DFT functionals for the considered ZIFs.

2.A.4 Different parts of Internal Strain Contribution e_{14}^{int}

2.A.4.1 Bond lengths

For all ZIFs we see that the highest change in bond length occurs in the Metal-N bonds, ranging from 0.24% for ZIF-65 to 0.06% for ZIF8 (see Table 2.A.2). In methyl ZIFs (ZIF-8 and CdIF-1), the second-largest change in bond length was in the C-N bonds of the imidazolate ring, with the C bonded to the methyl substituent. In the other 4 ZIFs, substituted with -Cl, CHO and -NO$_2$, we find that apart from the Metal–N bonds, the largest changes in bond length occur in a) the carbon–substituent bonds, b) bonds within the substituent itself and c) for ZIF-90 and ZIF-65, the C–N bond within the imidazolate ring with C not bonded to the substituent , and for ZIF-Cl and CdIF-8 the C–N bond with C bonded to the substituent.

Table 2.A.2: Variation due to external shear in bond lengths and bond angles above for all ZIF structures. A cutoff of 0.05% for bond lengths and 1° change for bond angles was chosen and values higher are shown in the table.

MOF	Atoms Involved	Relative Bond length change (%)	Atoms Involved	Bond angle change (°)
ZIF-8	Zn-N	0.06	N-Zn-N	3.12
	C-N (where C is bonded to -CH$_3$ substituent)	0.04	Zn-N-C	0.89
CdIF-1	Cd-N	0.10	N-Cd-N	3.41
	C-N (where C is bonded to -CH$_3$ substituent)	0.03	Cd-N-C	0.80
ZIF-90	Zn-N	0.14	N-Zn-N	3.48
	C-C (where C is bonded to -CHO substituent)	0.10	Zn-N-C	1.44
	C-O (Bond in the -CHO substituent)	0.08		
	C-H (Bond in the -CHO substituent)	0.08		
	C-N (where C is not bonded to -CHO substituent)	0.07		
ZIF-Cl	Zn-N	0.06	N-Zn-N	3.27
	C-N (where C is bonded to -Cl substituent)	0.05	Zn-N-C	0.69
	Cl-C (where C is bonded to -Cl substituent)	0.05		
ZIF-65	Zn-N	0.24	N-Zn-N	2.90
	C-N (where C is bonded to -NO$_2$ substituent)	0.09	Zn-N-C	1.18
	C-N (where C is not bonded to -NO$_2$ substituent)	0.08		
	N-O (Bond in the -NO$_2$ substituent)	0.07		
CdIF-8	Cd-N	0.10	N-Cd-N	3.23
	N-O (Bond in the -NO$_2$ substituent)	0.06	Cd-N-C	1.13
	C-N (where C is bonded to -NO$_2$ substituent)	0.04		

2.A.4.2 Born effective Charges (Z^*)

The labeling of the different atom types in the organic linker can be found in Figure 2.A.4. Born effective charges Z^* of all the atoms in the organic linker C1, C2/C3,N, H and X are shown in Figure 2.A.5. Within the imidazolate ring, the Z^* values vary between ±1 for C1, ±0.6 for C2/C3 and −1.00 to +0.75 for N. This varied distribution of charges in the atoms

of the linkers ranging from +1 to -1 for different types of C and N atoms indicates a covalent nature of bonds between them. Unlike non-substituent linker atoms, the BEC of different elements in the substituent (X) for each ZIF show distinct values, as seen in Figure 2.A.5(e). In ZIF-8 and CdIF-1 i.e. -CH$_3$ ZIFs, all BEC's of C and H are in ±0.15. For ZIF-Cl, all Cl atoms have BECs in +0.25 to −0.4, in ZIF-90, ZIF-65 and CdIF-8 most BEC values of C, H, N, O fall in the range −0.8 to + 1.0. In ZIF-90, the BEC value of C and O of some linkers is higher than other linkers with a value as high as ±1.5. A similar trend is seen in ZIF-65 and CdIF-8 with N and O having higher BEC values of +2.2 and −1.6 respectively.
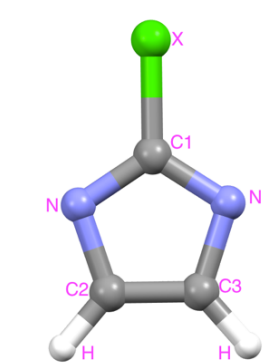
Figure 2.A.4: Atoms in the organic unit labeled according to the asymmetric unit of the ZIF system.
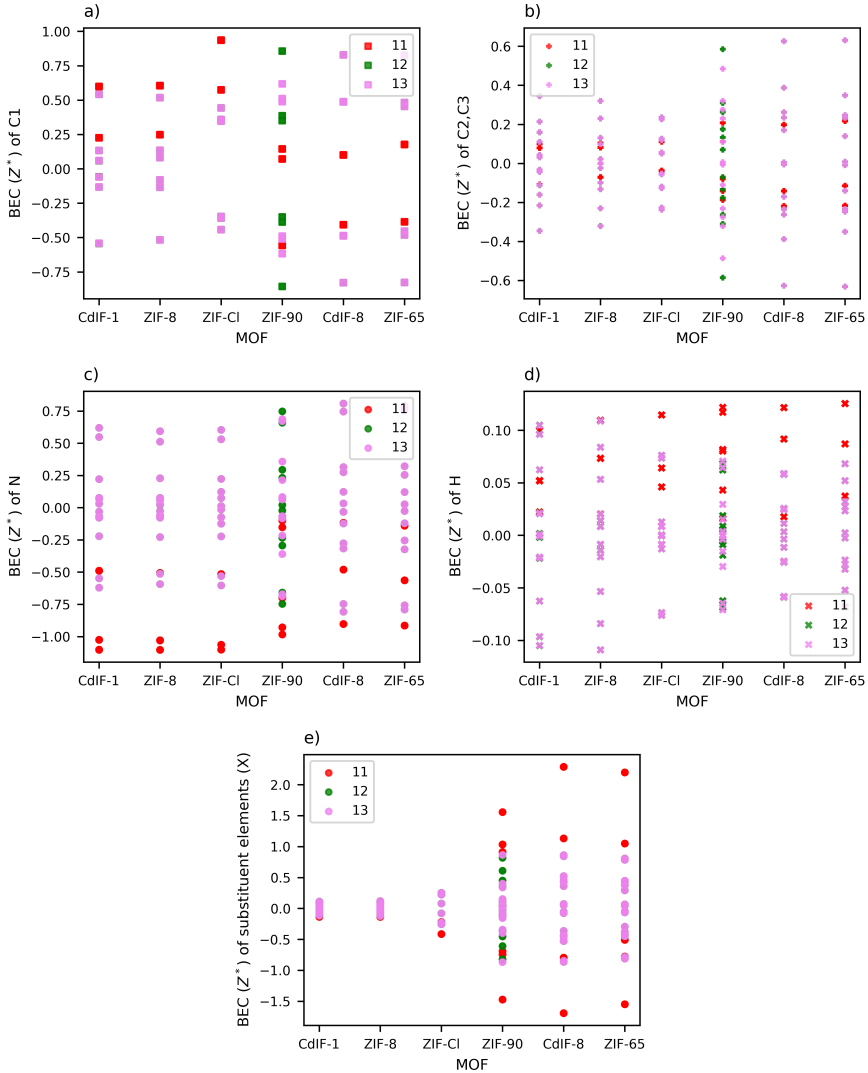
Figure 2.A.5: Born effective charges Z^* in relevant directions (11,12,13) for a) C1 carbon b) C2/C3 carbon c) N atoms d) H atoms e) substituent atoms in X.

2.A.4.3 Combined contribution of Born effective charges and relaxation coefficients 'A'

As e_{14}^{int} is defined by the product of the BEC's and relaxation coefficients, we identified the atoms which have the highest magnitude for this product 'A' = $\left(Z_{s,1j}^{*} * \frac{\partial x_{sj}}{\partial \varepsilon_4} \right)$ to e_{14}^{int} in all ZIFs. For each ZIF, a cutoff value of 5% of $|e_{14}^{int}|$ was chosen to consider the product 'A' = $\left| Z_{s,1j}^{*} * \frac{\partial x_{sj}}{\partial \varepsilon_4} \right|$ for all atoms. All atoms with absolute contributions greater than this value are highlighted in Figure 2.A.6, where green indicates a positive contribution and red indicates a negative contribution to internal strain contribution e_{14}^{int}. In ZIF-Cl (Figure 2.A.6(b)), C1, C2/C3 and H atoms of the imidazolate have product greater than cutoff and metal atoms have low contribution than the cutoff. However, in ZIF-90, ZIF-65 and CdIF-8, (Figure 2.A.6(a, c, d)) metal atoms (Cd or Zn) have both positive and negative product 'A'> cutoff. In the organic part for these 3 ZIFs, C1, some C2/C3 carbons, some N atoms, and atoms in the substituent groups i.e., C, O of -CHO and N, O of -NO$_2$ all of them have higher contributions than the cutoff. For the same cutoff on the product 'A' for all ZIFs, a clear difference in the number of atoms that have 'A' > cutoff is seen in ZIF-90, Nitro ZIFs vs methyl ZIFs and ZIF-Cl.
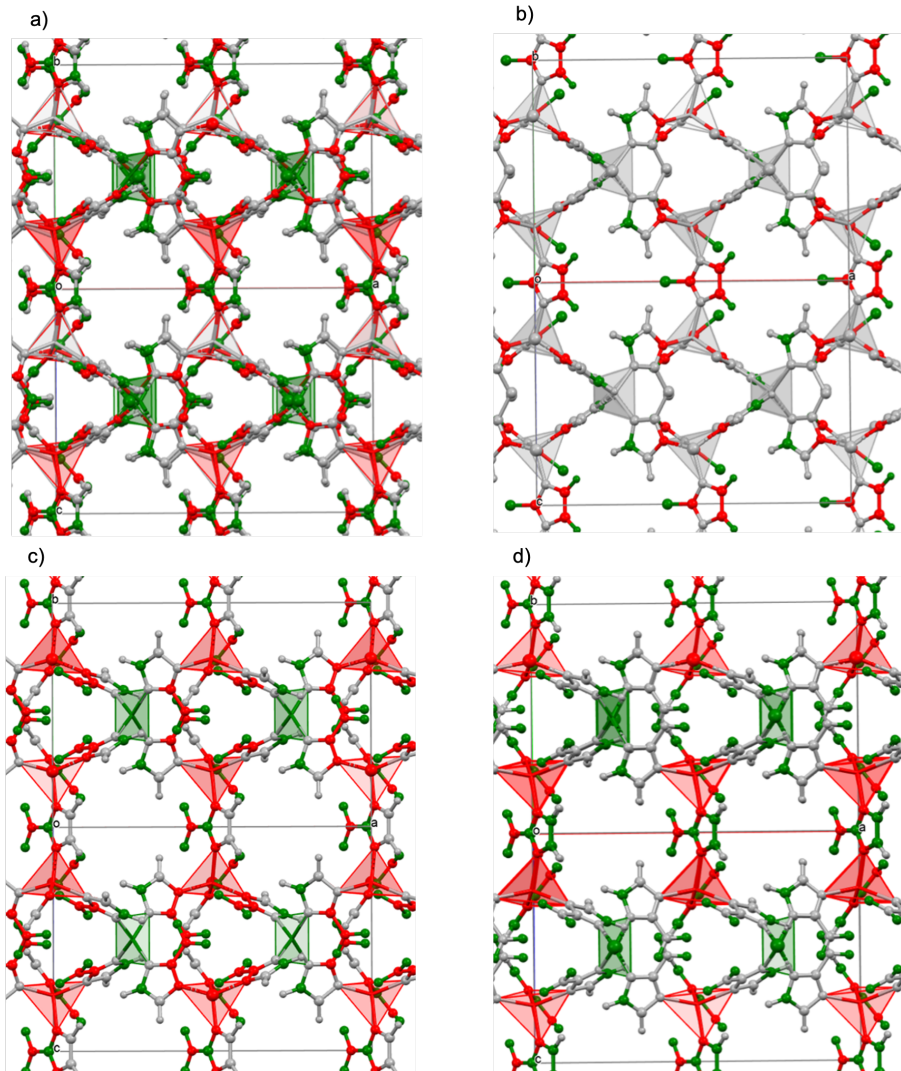
Figure 2.A.6: ZIF structures highlighting the atoms with contribution 'A' = $\left| Z^*_{s,1j} * \dfrac{\partial x_{sj}}{\partial \varepsilon_4} \right|$
greater than 5% of e^{int}_{14} a) ZIF-90 b) ZIF-Cl c) ZIF-65 and d) CdIF-8. The positive contribution of 'A' is indicated with green color and negative contribution in red colour.

2.A.5 Variation of Mechanical Properties and Piezoelectric constant 'd' with DFT functional

In Figures 2.A.7a, 2.A.7b, 2.A.8, 2.A.9 and 2.A.10, c_{44}, s_{44}, bulk properties and d_{14} are marked in the graph for CdIF-1 with M062X functional and for ZIF-65 with M06-D3 functional. These specific piezoelectric calculations did not converge properly even with stringent convergence criteria on energy, hence these results were excluded for conclusions obtained in the main text of the chapter.

2.A.5.1 Shear constant c_{44} and Compliance constant s_{44}

For mechanical properties c_{44} and s_{44}, the ratio of the standard deviation to the average varies from 0.1 – 18% except for CdIF-1 and CdIF-8 a deviation of 30% is observed. Although c_{44} and s_{44} vary with the choice of DFT functionals for each ZIF, variation between different ZIFs is consistent in most cases.
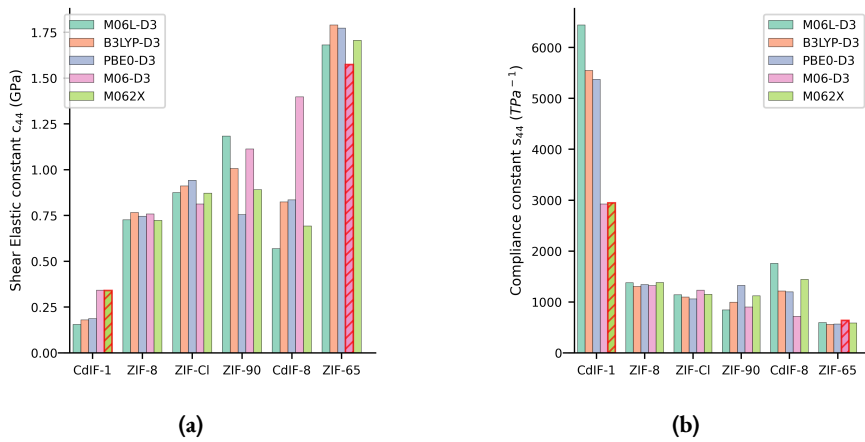
Figure 2.A.7: Bar plots of (a) Shear elastic constant (c_{44}) and (b) Compliance constant (s_{44}) for all ZIFs with five DFT functionals.

2.A.5.2 Bulk properties

From the complete elastic tensor obtained in the calculations, mechanical properties like Young's modulus, Bulk modulus and Poisson ratio are also computed using Voigt-Reuss-Hill(VRH) approximation. Hence, we show in Figure 2.A.8 these properties for all ZIFs calculated with different DFT functionals. Bulk moduli for all ZIFs in this work are less than 13 GPa. They are much smaller than Bulk moduli of inorganic perovskite $BaTiO_3$ (162 GPa), $PbTiO_3$ (144 GPa).[83] Young's moduli of ZIFs are all below 5 GPa which are the same order of magnitude as PVDF (4.18 GPa) and PVDF-TrFE (~1.5 GPa), but lower than piezoelectric ceramics like PZT and $BaTiO_3$.[3]
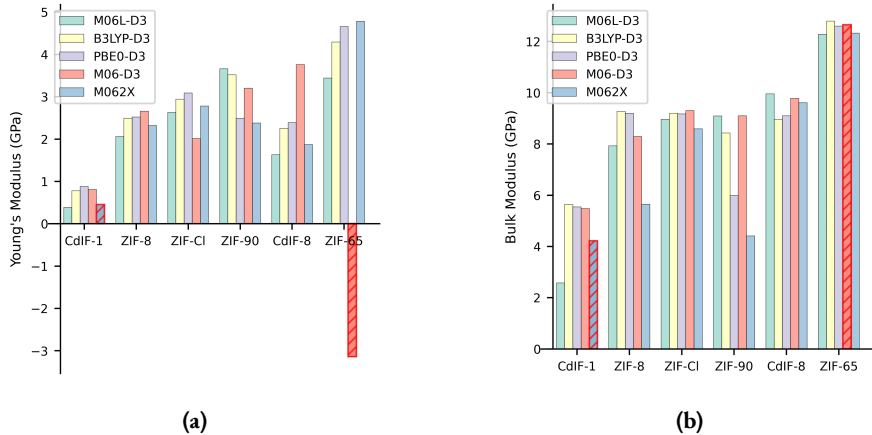
Figure 2.A.8: Bar plots of (a) Young's Modulus and (b) Bulk Modulus for all ZIFs with five DFT functionals.
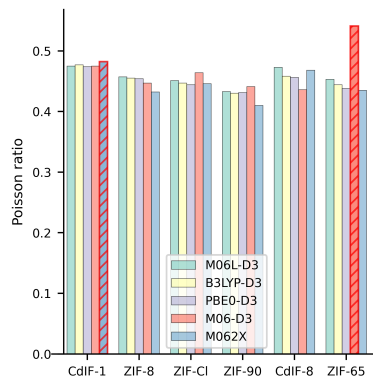

Figure 2.A.9: Poisson's ratio, obtained with five different DFT functionals for all ZIFs.

2.A.5.3 Piezoelectric constant 'd'

As shown in Figure 2.A.10, there is a lot of variation of d_{14} with the choice of DFT functional, due to the variability of both e_{14} (Figure 2.A.3) and s_{44} (Figure 2.A.7b) with choice of functional.
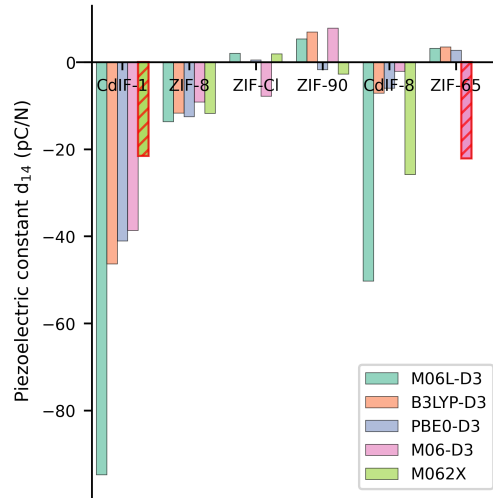

Figure 2.A.10: Piezoelectric constant d_{14} obtained with five different DFT functionals for all ZIFs.

(a)

(b)
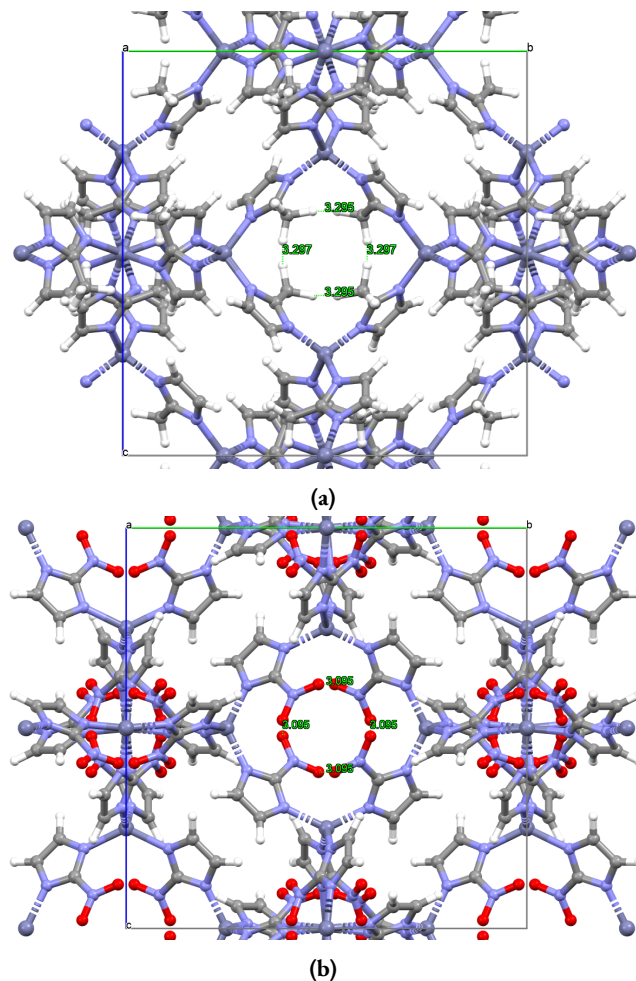
Figure 2.A.11: Structures of a) ZIF-8 and b) ZIF-65 showing the (100) plane with the distance between H–H of -CH$_3$ groups and O–O of -NO$_2$ groups in the pore indicated.

2.A.6 Acoustic Properties of ZIFs

The acoustic velocities are obtained as a part of the calculations, by solving the Christoffel equations based on the elastic constants and densities.

Table 2.A.3: Acoustic properties of all six ZIFs.

Properties	ZIF-8	CdIF-1	ZIF-90	ZIF-Cl	ZIF-65	CdIF-8
Density (kg/m^3)	904	923	984	1057	1109	1131
Minimum velocities (km/s)						
Longitudinal	3.373	2.524	3.151	3.140	3.590	2.957
Transverse (v_1)	0.920	0.442	1.011	0.929	1.102	0.810
Transverse (v_2)	0.920	0.442	1.011	0.929	1.008	0.787
Maximum velocities (km/s)						
Longitudinal	3.427	2.602	3.289	3.198	3.699	2.982
Transverse (v_1)	1.015	0.705	1.298	1.066	1.270	0.854
Transverse (v_2)	1.015	0.629	1.210	1.022	1.270	0.854
Acoustic Impedance (Longitudinal)(MRayl)						
Minimum	3.05	2.33	3.10	3.32	3.98	3.34
Maximum	3.10	2.40	3.24	3.38	4.10	3.37

Bibliography

(1)   R. M. Martin, "Piezoelectricity," *Physical Review B*, 1972, **5**, 1607–1613.

(2)   T. Vijayakanth, D. J. Liptrot, E. Gazit, R. Boomishankar and C. R. Bowen, "Recent Advances in Organic and Organic–Inorganic Hybrid Materials for Piezoelectric Mechanical Energy Harvesting," *Advanced Functional Materials*, 2022, **32**, 2109492.

(3)   M. Habib, I. Lantgios and K. Hornbostel, "A Review of Ceramic, Polymer and Composite Piezoelectric Materials," *Journal of Physics D: Applied Physics*, 2022, **55**, 423002.

(4)   D. M. Shin, S. W. Hong and Y. H. Hwang, "Recent Advances in Organic Piezoelectric Biomaterials for Energy and Biomedical Applications," *Nanomaterials*, 2020, **10**, 123.

(5)   V. T. Rathod, "A Review of Acoustic Impedance Matching Techniques for Piezoelectric Sensors and Transducers," *Sensors*, 2020, **20**, 4051.

(6)   Y.-M. You, W.-Q. Liao, D. Zhao, H.-Y. Ye, Y. Zhang, Q. Zhou, X. Niu, J. Wang, P.-F. Li, D.-W. Fu, Z. Wang, S. Gao, K. Yang, J.-M. Liu, J. Li, Y. Yan and R.-G. Xiong, "An Organic-Inorganic Perovskite Ferroelectric with Large Piezoelectric Response," *Science*, 2017, **357**, 306–309.

(7)   W.-Q. Liao, D. Zhao, Y.-Y. Tang, Y. Zhang, P.-F. Li, P.-P. Shi, X.-G. Chen, Y.-M. You and R.-G. Xiong, "A Molecular Perovskite Solid Solution with Piezoelectricity Stronger than Lead Zirconate Titanate," *Science*, 2019, **363**, 1206–1210.

(8)   C. Shi, J.-J. Ma, J.-Y. Jiang, M.-M. Hua, Q. Xu, H. Yu, Y. Zhang and H.-Y. Ye, "Large Piezoelectric Response in Hybrid Rare-Earth Double Perovskite Relaxor Ferroelectrics," *Journal of the American Chemical Society*, 2020, **142**, 9634–9641.

(9)   P. K. Panda, "Review: Environmental Friendly Lead-Free Piezoelectric Materials," *Journal of Materials Science*, 2009, **44**, 5049–5062.

(10) Y. Zhang, H. Kim, Q. Wang, W. Jo, A. I. Kingon, S.-H. Kim and C. K. Jeong, "Progress in Lead-Free Piezoelectric Nanofiller Materials and Related Composite Nanogenerator Devices," *Nanoscale Advances*, 2020, **2**, 3131–3149.

(11) H. Wang, H. Liu, Z. Zhang, Z. Liu, Z. Lv, T. Li, W. Ju, H. Li, X. Cai and H. Han, "Large Piezoelectric Response in a Family of Metal-Free Perovskite Ferroelectric Compounds from First-Principles Calculations," *npj Computational Materials*, 2019, **5**, 1–9.

(12) Y. V. Kaneti, J. Tang, R. R. Salunkhe, X. Jiang, A. Yu, K. C.-W. Wu and Y. Yamauchi, "Nanoarchitectured Design of Porous Materials and Nanocomposites from Metal-Organic Frameworks," *Advanced Materials*, 2017, **29**, 1604898.

(13) A. Kirchon, L. Feng, H. F. Drake, E. A. Joseph and H. C. Zhou, "From Fundamentals to Applications: A Toolbox for Robust and Multifunctional MOF Materials," *Chemical Society Reviews*, 2018, **47**, 8611–8638.

(14) L. R. Mingabudinova, V. V. Vinogradov, V. A. Milichko, E. Hey-Hawkins and A. V. Vinogradov, "Metal–Organic Frameworks as Competitive Materials for Non-Linear Optics," *Chemical Society Reviews*, 2016, **45**, 5408–5431.

(15) C. Wang, T. Zhang and W. Lin, "Rational Synthesis of Noncentrosymmetric Metal–Organic Frameworks for Second-Order Nonlinear Optics," *Chemical Reviews*, 2012, **112**, 1084–1104.

(16) X. Jiang, L. Zhang, S. Liu, Y. Zhang, Z. He, W. Li, F. Zhang, Y. Shi, W. Lü, Y. Li, Q. Wen, J. Li, J. Feng, S. Ruan, Y.-J. Zeng, X. Zhu, Y. Lu and H. Zhang, "Ultrathin Metal–Organic Framework: An Emerging Broadband Nonlinear Optical Material for Ultrafast Photonics," *Advanced Optical Materials*, 2018, **6**, 1800561.

(17) D.-W. Fu, W. Zhang and R.-G. Xiong, "The First Metal–Organic Framework (MOF) of Imazethapyr and Its SHG, Piezoelectric and Ferroelectric Properties," *Dalton Transactions*, 2008, 3946.

(18) P. Yang, X. He, M.-X. Li, Q. Ye, J.-Z. Ge, Z.-X. Wang, S.-R. Zhu, M. Shao and H.-L. Cai, "The First Homochiral Coordination Polymer with Temperature-Independent Piezoelectric and Dielectric Properties," *Journal of Materials Chemistry*, 2012, **22**, 2398.

(19) Y. Sun, J. Gao, Y. Cheng, Y.-W. Zhang and K. Zeng, "Design of the Hybrid Metal–Organic Frameworks as Potential Supramolecular Piezo-/Ferroelectrics," *The Journal of Physical Chemistry C*, 2019, **123**, 3122–3129.

(20) F. Xue, J. Cao, X. Li, J. Feng, M. Tao and B. Xue, "Continuous-Flow Synthesis of MIL-53(Cr) with a Polar Linker: Probing the Nanoscale Piezoelectric Effect," *Journal of Materials Chemistry C*, 2021, **9**, 7568–7574.

(21) Y. Sun, Z. Hu, D. Zhao and K. Zeng, "Probing Nanoscale Functionalities of Metal-Organic Framework Nanocrystals," *Nanoscale*, 2017, **9**, 12163–12169.

(22) T. Jungk, Á. Hoffmann and E. Soergel, "Challenges for the Determination of Piezoelectric Constants with Piezoresponse Force Microscopy," *Applied Physics Letters*, 2007, **91**, 253511.

(23) D. Seol, B. Kim and Y. Kim, "Non-Piezoelectric Effects in Piezoresponse Force Microscopy," *Current Applied Physics*, 2017, **17**, 661–674.

(24) E. Soergel, "Piezoresponse Force Microscopy (PFM)," *Journal of Physics D: Applied Physics*, 2011, **44**, 464003.

(25) Z.-G. Li, K. Li, L.-Y. Dong, T.-M. Guo, M. Azeem, W. Li and X.-H. Bu, "Acoustic Properties of Metal-Organic Frameworks," *Research*, 2021, **2021**, 1–11.

(26) Y. Zhang, M. Xie, J. Roscow, Y. Bao, K. Zhou, D. Zhang and C. R. Bowen, "Enhanced Pyroelectric and Piezoelectric Properties of PZT with Aligned Porosity for Energy Harvesting Applications," *Journal of Materials Chemistry A*, 2017, **5**, 6569–6580.

(27) S. Eslava, L. Zhang, S. Esconjauregui, J. Yang, K. Vanstreels, M. R. Baklanov and E. Saiz, "Metal-Organic Framework ZIF-8 Films As Low-κ Dielectrics in Microelectronics," *Chemistry of Materials*, 2013, **25**, 27–33.

(28) S. Mendiratta, C. H. Lee, M. Usman and K. L. Lu, "Metal-Organic Frameworks for Electronics: Emerging Second Order Nonlinear Optical and Dielectric Materials," *Science and Technology of Advanced Materials*, 2015, **16**, 054204.

(29) S. Mendiratta, M. Usman and K.-L. Lu, "Expanding the Dimensions of Metal–Organic Framework Research towards Dielectrics," *Coordination Chemistry Reviews*, 2018, **360**, 77–91.

(30) M. R. Ryder, L. Donà, J. G. Vitillo and B. Civalleri, "Understanding and Controlling the Dielectric Response of Metal–Organic Frameworks," *ChemPlusChem*, 2018, **83**, 308–316.

(31) Y. C. Kao, S. Mendiratta, M. Usman, Y. S. Wen, C. M. Wang, L. Zhao, M. K. Wu and K. L. Lu, "Exceptional Low Dielectric Behavior of Chemically Robust, Guest-Free Co- and Mn-Based Coordination Polymers," *ChemElectroChem*, 2019, **6**, 623–626.

(32) D.-L. Zhang, Q.-K. Feng, S.-L. Zhong, D.-F. Liu, Y. Zhao and Z.-M. Dang, "Tunable Dielectric Performance of Porphyrin Based Metal−organic Frameworks with Polar Molecule Confinement," *Composites Communications*, 2021, **25**, 100734.

(33) K. S. Park, Z. Ni, A. P. Côté, J. Y. Choi, R. Huang, F. J. Uribe-Romo, H. K. Chae, M. O'Keeffe and O. M. Yaghi, "Exceptional Chemical and Thermal Stability of Zeolitic Imidazolate Frameworks," *Proceedings of the National Academy of Sciences*, 2006, **103**, 10186–10191.

(34)   Y.-Q. Tian, S.-Y. Yao, D. Gu, K.-H. Cui, D.-W. Guo, G. Zhang, Z.-X. Chen and D.-Y. Zhao, "Cadmium Imidazolate Frameworks with Polymorphism, High Thermal Stability, and a Large Surface Area," *Chemistry - A European Journal*, 2010, **16**, 1137–1141.

(35)   M. R. Ryder, Z. Zeng, K. Titov, Y. Sun, E. M. Mahdi, I. Flyagina, T. D. Bennett, B. Civalleri, C. S. Kelley, M. D. Frogley, G. Cinque and J. C. Tan, "Dielectric Properties of Zeolitic Imidazolate Frameworks in the Broad-Band Infrared Regime," *Journal of Physical Chemistry Letters*, 2018, **9**, 2678–2684.

(36)   "IEEE Standard on Piezoelectricity," *ANSI/IEEE Std 176-1987*, 1988, 0_1–.

(37)   A. Dal Corso, M. Posternak, R. Resta and A. Baldereschi, "Ab Initio Study of Piezoelectricity and Spontaneous Polarization in ZnO," *Physical Review B*, 1994, **50**, 10715–10721.

(38)   F. Bernardini, V. Fiorentini and D. Vanderbilt, "Polarization-Based Calculation of the Dielectric Tensor of Polar Crystals," *Physical Review Letters*, 1997.

(39)   G. Sághi-Szabó, R. E. Cohen and H. Krakauer, "First-Principles Study of Piezoelectricity in PbTiO3," *Physical Review Letters*, 1998, **80**, 4321–4324.

(40)   M. Catti, Y. Noel and R. Dovesi, "Full Piezoelectric Tensors of Wurtzite and Zinc Blende ZnO and ZnS by First-Principles Calculations," *Journal of Physics and Chemistry of Solids*, 2003, **64**, 2183–2190.

(41)   P. Ghosez, J. Michenaud and X. Gonze, "Dynamical Atomic Charges: The Case of ABO3 Compounds," *Physical Review B - Condensed Matter and Materials Physics*, 1998, **58**, 6224–6240.

(42)   R. Dovesi, A. Erba, R. Orlando, C. M. Zicovich-Wilson, B. Civalleri, L. Maschio, M. Rérat, S. Casassa, J. Baima, S. Salustro and B. Kirtman, "Quantum-mechanical Condensed Matter Simulations with CRYSTAL," *WIREs Computational Molecular Science*, 2018, **8**, e1360.

(43)   M. M. Francl, W. J. Pietro, W. J. Hehre, J. S. Binkley, M. S. Gordon, D. J. DeFrees and J. A. Pople, "Self-Consistent Molecular Orbital Methods. XXIII. A Polarization-Type Basis Set for Second-Row Elements," *The Journal of Chemical Physics*, 1982, **77**, 3654–3665.

(44)   R. Krishnan, J. S. Binkley, R. Seeger and J. A. Pople, "Self-Consistent Molecular Orbital Methods. XX. A Basis Set for Correlated Wave Functions," *The Journal of Chemical Physics*, 1980, **72**, 650–654.

(45)   A. D. McLean and G. S. Chandler, "Contracted Gaussian Basis Sets for Molecular Calculations. I. Second Row Atoms, Z=11-18," *The Journal of Chemical Physics*, 1980, **72**, 5639–5648.

(46)   J. Heyd, J. E. Peralta, G. E. Scuseria and R. L. Martin, "Energy Band Gaps and Lattice Parameters Evaluated with the Heyd-Scuseria-Ernzerhof Screened Hybrid Functional," *Journal of Chemical Physics*, 2005, **123**, 174101.

(47)   B. P. Pritchard, D. Altarawy, B. Didier, T. D. Gibson and T. L. Windus, "New Basis Set Exchange: An Open, Up-to-Date Resource for the Molecular Sciences Community," *Journal of Chemical Information and Modeling*, 2019, **59**, 4814–4820.

(48)   S. Grimme, J. Antony, S. Ehrlich and H. Krieg, "A Consistent and Accurate Ab Initio Parametrization of Density Functional Dispersion Correction (DFT-D) for the 94 Elements H-Pu," *The Journal of Chemical Physics*, 2010, **132**, 154104.

(49)   J. Laun, D. Vilela Oliveira and T. Bredow, "Consistent Gaussian Basis Sets of Double- and Triple-Zeta Valence with Polarization Quality of the Fifth Period for Solid-State Calculations," *Journal of Computational Chemistry*, 2018, **39**, 1285–1290.

(50) M. F. Peintinger, D. V. Oliveira and T. Bredow, "Consistent Gaussian Basis Sets of Triple-Zeta Valence with Polarization Quality for Solid-State Calculations," *Journal of Computational Chemistry*, 2013, **34**, 451–459.

(51) K. Raghavachari, "Perspective on "Density Functional Thermochemistry. III. The Role of Exact Exchange"," *Theoretical Chemistry Accounts: Theory, Computation, and Modeling (Theoretica Chimica Acta)*, 2000, **103**, 361–363.

(52) C. Adamo and V. Barone, "Toward Reliable Density Functional Methods without Adjustable Parameters: The PBE0 Model," *J. Chem. Phys*, 1999, **110**, 6158.

(53) Y. Zhao and D. G. Truhlar, "A New Local Density Functional for Main-Group Thermochemistry, Transition Metal Bonding, Thermochemical Kinetics, and Noncovalent Interactions," *J. Chem. Phys*, 2006, **125**, 194101.

(54) Y. Zhao and D. G. Truhlar, "The M06 Suite of Density Functionals for Main Group Thermochemistry, Thermochemical Kinetics, Noncovalent Interactions, Excited States, and Transition Elements: Two New Functionals and Systematic Testing of Four M06-class Functionals and 12 Other Function," *Theoretical Chemistry Accounts*, 2008, **120**, 215–241.

(55) C. R. Groom, I. J. Bruno, M. P. Lightfoot and S. C. Ward, "The Cambridge Structural Database," *Acta Crystallographica Section B Structural Science, Crystal Engineering and Materials*, 2016, **72**, 171–179.

(56) R. D. King-Smith and D. Vanderbilt, "Theory of Polarization of Crystalline Solids," *Physical Review B*, 1993, **47**, 1651–1654.

(57) R. Resta, "Macroscopic Polarization in Crystalline Dielectrics: The Geometric Phase Approach," *Reviews of Modern Physics*, 1994, **66**, 899–915.

(58) D. Vanderbilt, "Berry-Phase Theory of Proper Piezoelectric Response," *Journal of Physics and Chemistry of Solids*, 2000, **61**, 147–151.

(59) S. Dall'Olio, R. Dovesi and R. Resta, "Spontaneous Polarization as a Berry Phase of the Hartree-Fock Wave Function: The Case of KNbO3," *Physical Review B*, 1997, **56**, 10105–10114.

(60) Y. Noel, C. M. Zicovich-Wilson, B. Civalleri, Ph. D'Arco and R. Dovesi, "Polarization Properties of ZnO and BeO: An Ab Initio Study through the Berry Phase and Wannier Functions Approaches," *Physical Review B*, 2001, **65**, 014111.

(61) A. Erba, D. Caglioti, C. M. Zicovich-Wilson and R. Dovesi, "Nuclear-Relaxed Elastic and Piezoelectric Constants of Materials: Computational Aspects of Two Quantum-Mechanical Approaches," *Journal of Computational Chemistry*, 2017, **38**, 257–264.

(62) Y. Noel, M. Llunell, R. Orlando, P. D'Arco and R. Dovesi, "Performance of Various Hamiltonians in the Study of the Piezoelectric Properties of Crystalline Compounds: The Case of BeO and ZnO," *Physical Review B*, 2002, **66**, 214107.

(63) J.-C. Tan, B. Civalleri, C.-C. Lin, L. Valenzano, R. Galvelis, P.-F. Chen, T. D. Bennett, C. Mellot-Draznieks, C. M. Zicovich-Wilson and A. K. Cheetham, "Exceptionally Low Shear Modulus in a Prototypical Imidazole-Based Metal-Organic Framework," *Physical Review Letters*, 2012, **108**, 095502.

(64) C. Hansch, A. Leo and R. W. Taft, "A Survey of Hammett Substituent Constants and Resonance and Field Parameters," *Chemical Reviews*, 1991, **91**, 165–195.

(65) N. Novendra, J. M. Marrett, A. D. Katsenis, H. M. Titi, M. Arhangelskis, T. F. Č. I. Ić and A. Navrotsky, "Linker Substituents Control the Thermodynamic Stability in Metal–Organic Frameworks," *Journal of the American Chemical Society*, 2020, **142**, 21720–21729.

(66)   M. Charton, "Electrical Effects of Ortho Substituents in Imidazoles and Benzimidazoles," *The Journal of Organic Chemistry*, 1965, **30**, 3346–3350.

(67)   C. Bustos, L. Alvarez-Thon, E. Molins, I. Moreno-Villoslada, G. Vallejos-Contreras, C. S. anchez, X. Zarate, D. Mac-Leod Carey and E. Schott, "Tuning the Molecular/Electronic Structure of New Substituted Pyrazoles: Synthesis, Biological Trials, Theoretical Approaches and Hammett Correlations," *Journal of Molecular Structure*, 2018, **1171**, 349–361.

(68)   D. Berlincourt, H. Jaffe and L. R. Shiozawa, "Electroelastic Properties of the Sulfides, Selenides, and Tellurides of Zinc and Cadmium," *Physical Review*, 1963, **129**, 1009–1017.

(69)   I. Kobiakov, "Elastic, Piezoelectric and Dielectric Properties of ZnO and CdS Single Crystals in a Wide Range of Temperatures," *Solid State Communications*, 1980, **35**, 305–310.

(70)   B. Zheng, Y. Zhu, F. Fu, L. L. Wang, J. Wang and H. Du, "Theoretical Prediction of the Mechanical Properties of Zeolitic Imidazolate Frameworks (ZIFs)," *RSC Advances*, 2017, **7**, 41499–41503.

(71)   S. S. Batsanov, "Van Der Waals Radii of Elements," *Inorganic Materials*, 2001, **37**, 871–885.

(72)   K. Omote, H. Ohigashi and K. Koga, "Temperature Dependence of Elastic, Dielectric, and Piezoelectric Properties of "single Crystalline" Films of Vinylidene Fluoride Trifluoroethylene Copolymer," *Journal of Applied Physics*, 1997, **81**, 2760–2769.

(73)   N. J. Ramer and K. A. Stiso, "Structure and Born Effective Charge Determination for Planar-Zigzag β-Poly(Vinylidene Fluoride) Using Density-Functional Theory," *Polymer*, 2005, **46**, 10431–10436.

(74)   H.-S. Wu, B. T. Murti, J. Singh, P.-K. Yang and M.-L. Tsai, "Prospects of Metal-Free Perovskites for Piezoelectric Applications," *Advanced Science*, 2022, **9**, 2104703.

(75)   H. Schlaberg and J. Duffy, "Piezoelectric Polymer Composite Arrays for Ultrasonic Medical Imaging Applications," *Sensors and Actuators A: Physical*, 1994, **44**, 111–117.

(76)   J. F. Nye, *Physical Properties of Crystals: Their Representation by Tensors and Matrices*, Oxford university press, New York, 1985.

(77)   Q. Li, A. J. Zaczek, T. M. Korter, J. A. Zeitler and M. T. Ruggiero, "Methyl-Rotation Dynamics in Metal-Organic Frameworks Probed with Terahertz Spectroscopy," *Chemical Communications*, 2018, **54**, 5776–5779.

(78)   W. Morris, C. J. Doonan, H. Furukawa, R. Banerjee and O. M. Yaghi, "Crystals as Molecules: Postsynthesis Covalent Functionalization of Zeolitic Imidazolate Frameworks," *Journal of the American Chemical Society*, 2008, **130**, 12626–12627.

(79)   W. Morris, C. J. Stevens, R. E. Taylor, C. Dybowski, O. M. Yaghi and M. A. Garcia-Garibay, "NMR and X-ray Study Revealing the Rigidity of Zeolitic Imidazolate Frameworks," *Journal of Physical Chemistry C*, 2012, **116**, 13307–13312.

(80)   G. Chaplais, G. Fraux, J. L. Paillaud, C. Marichal, H. Nouali, A. H. Fuchs, F. X. Coudert and J. Patarin, "Impacts of the Imidazolate Linker Substitution (CH3, Cl, or Br) on the Structural and Adsorptive Properties of ZIF-8," *Journal of Physical Chemistry C*, 2018, **122**, 26945–26955.

(81)   S. Diring, D. O. Wang, C. Kim, M. Kondo, Y. Chen, S. Kitagawa, K.-I. Kamei and S. Furukawa, "Localized Cell Stimulation by Nitric Oxide Using a Photoactive Porous Coordination Polymer Platform," *Nature Communications*, 2013, **4**, 2684.

(82)   M. de Jong, W. Chen, H. Geerlings, M. Asta and K. A. Persson, "A Database to Enable Discovery and Design of Piezoelectric Materials," *Scientific Data*, 2015, **2**, 150053.

(83)   S. Piskunov, E. Heifets, R. Eglitis and G. Borstel, "Bulk Properties and Electronic Structure of SrTiO3, BaTiO3, PbTiO3 Perovskites: An Ab Initio HF/DFT Study," *Computational Materials Science*, 2004, **29**, 165–178.

Chapter 3

Computational Screening of Piezoelectric Properties in Metal–Organic Frameworks

Piezoelectric energy harvesting is a process in which energy in the form of kinetic movements can be harvested and converted into useful electrical energy using piezoelectric materials. Metal–organic frameworks (MOFs) can have a huge potential for piezoelectric energy harvesting owing to their high flexibility, structural tunability, and very low dielectric constants due to their high porosities. The piezoelectric constant d, relevant for energy harvesting, is dependent on piezoelectric constant e and the flexibility or mechanical properties of the structure. The mechanical properties of MOFs have been studied widely in previous works in the literature, whereas the piezoelectric constant e was never explored for MOFs and hence their values are difficult to predict. Here in this chapter, we generate a database of piezoelectric properties, specifically e for around ~ 1608 previously synthesized non-centrosymmetric MOF structures. The calculations were performed using the density functional perturbation theory (DFPT) method. The highest value of e obtained in this work is around ~1.55 C/m^2, which is larger than the piezoelectric constant e of flexible organic piezoelectric polymer polyvinylidene fluoride and its copolymer. In recent years, hybrid materials like metal-free perovskites of type $MDABCO-NH_4-X_3$ (MDABCO is N-methyl-N'-diazabicyclo[2,2,2] octonium) have exhibited a high piezoelectric response (d) that is comparable to d of conventional inorganic ceramics. When comparing the piezoelectric response e of these metal-free perovskites to the results in this study, the highest e value in this work is larger than that of metal-free perovskites (with e values up to 0.35 C/m^2). We further analyzed and identified the structural factors that influence the piezoelectric constant values for MOFs with $e > 1.0$ C/m^2. Based on that, a series of guidelines for the design of MOF structures that can lead to a high piezoelectric constant e are presented.

3.1 Introduction

A major application of piezoelectric materials that has been of wide interest to researchers in recent years, is piezoelectric energy harvesting. It is a process in which wasted energy in the environment in the form of kinetic movements and vibrations can be harvested and converted to useful electrical energy.[1–3] Existing piezoelectrics that have been explored for energy harvesting applications include conventional materials like inorganic ceramics, organic polymers, and composites of organic-inorganic materials. Specific properties of these piezoelectric materials have already been discussed in chapter 1. Hybrid inorganic-organic and metal-free perovskites emerged as potential candidates for piezoelectric energy harvesting owing to their easy processing methods and high piezoelectric response that is on par with that of conventional inorganic ceramics.[4–6] Both hybrid and metal-free perovskites offer great chemical diversity and structural tuneability because of their hybrid nature and organic components respectively. Metal–organic frameworks (MOFs) are porous hybrid crystalline materials consisting of inorganic nodes connected to organic ligands via coordination bonds. They are soft materials and have remarkable mechanical flexibility. Hence, for a polar MOF the application of a small strain could lead to a large change in polarization i.e., a large electromechanical response. Additionally due to their permanent porosity, a very low dielectric constant can be achieved. MOFs owing to their hybrid nature, flexible frameworks, and low dielectric constants show great potential as piezoelectric materials.

In chapter 2, we explored in detail the structure-property relationships of piezoelectric constants e and d for a specific family of MOFs, i.e., Zeolitic Imidazolate Frameworks (ZIFs). The metal node M (Zn or Cd) and the substituent on the imidazolate linker in the ZIFs structure was varied and piezoelectric constants were computed for a set of six ZIFs. The computed piezoelectric constants d of ZIFs, especially for CdIF-1 (Cd metal node and $-CH_3$ substituent) and the estimated figure of merit (FOM) of CdIF-1 show their potential to obtain high piezoelectric efficiencies. Specifically in CdIF-1, high flexibility (high elastic compliance s) of the framework is the key factor for obtaining a high piezoelectric constant d that is comparable to d of widely known organic piezoelectric PVDF. Apart from flexibility, another factor that can influence d is the piezoelectric constant e because of the relation between them: $d_{ip} = e_{iq}s_{qp}$ where s is the elastic compliance constant related to the mechanical properties of the material. In the case of ZIFs in chapter 2, the e values for all the ZIFs were low (<0.01 C/m^2). Hence, if the structural building units of MOFs can be tuned in a way to obtain high e and high mechanical flexibility, very high d values can be achieved.

Mechanical properties of MOFs have been reported in the literature previously and the intrinsic relationship between the structural changes like linker effects, interpenetration, and mechanical properties have also been discussed.[7–9] The complete elastic compliance tensor s relevant for piezoelectric constant d has not been reported for all MOFs, but the Young's and Shear moduli of MOFs are reported in the literature. Low values for these moduli when compared to high-performing inorganic piezoelectrics indicate the high flexibility of MOFs; making them favorable for applications in flexible devices. The piezoelectric constant e, another factor relevant for piezoelectric constant d has hardly been researched for MOFs.

In this chapter, we focus on computing the piezoelectric constant e for a large dataset of experimentally synthesized and computationally-ready MOF structures. Similar high-throughput calculations of piezoelectric constant e and mechanical properties were done

previously for inorganic crystalline materials [10, 11] and the computational results were made publicly accessible. Such databases can enable the accelerated discovery of new materials with novel mechanical and piezoelectric properties. The goal of this chapter is to compute the piezoelectric constants e, and further analyze to identify the trends and factors that can influence the e values for these structures. The influence of the point group of the structure and Born effective charges of the inorganic cation in the secondary building units (SBU) of the MOFs on the piezoelectric tensor of the MOF is presented. The piezoelectric constant values for MOFs in this work are compared with the values of some inorganic and organic piezoelectrics. In the end, for the top MOF candidates with e_{iq} values higher than $1.0\,\text{C/m}^2$ we discuss the structural features that are responsible for such high e_{iq} values. Based on that, we provide a series of guidelines for the design of MOF structures that can contribute to a high piezoelectric constant e.

3.2 Theory

Piezoelectricity is mathematically described in the IEEE standard for piezoelectricity, by a set of four constitutive equations that describe the response of a piezoelectric material to stress/strain and electric fields.[12] The relevant set of constitutive equations for this chapter is shown in Equations 3.1.

$$D_i = e_{ikl}S_{kl} + \varepsilon_{ij}^S E_k$$
$$S_{ij} = s_{ijkl}^E T_{kl} + d_{kij}E_k \tag{3.1}$$

where $D, S, \varepsilon, E, s, T$ represent electric displacement [C/m^2], strain tensor (dimensionless), dielectric constant [F/m], electric field [V/m], elastic compliance tensor [m^2/N] and stress tensor [N/m^2], respectively. e and d are third rank piezoelectric tensors with units [C/m^2] and [pC/N] respectively and $i, j, k, l = 1, 2, 3$. In this work, we compute the piezoelectric tensor, e_{ikl} which relates the polarization generated in the material to application of a strain or a deformation to the material. We will use Voigt notation for the piezoelectric tensor e_{iq}, the elastic compliance tensor s_{pq} and the piezoelectric tensor d_{iq} where the indices are given in compressed matrix notation instead of tensor notation. This means indices kl are replaced with p or q which refer to pairs of contracted cartesian directions $p, q = 1, 2, 3, 4, 5, 6$ refers to $kl = 11, 22, 33, 23$ and $32, 31$ and $13, 12$ and 21 respectively.

Computationally, e_{iq} is calculated as the first derivative of the magnitude of polarization P_i induced by strain at constant electric field E $e_{iq} = \left(\frac{\partial P_i}{\partial S_q}\right)_E$. To understand the microscopic origin of piezoelectricity in a material, the piezoelectric tensor e_{iq} can be further separated into two parts: the clamped-ion (e_{iq}^0) and the internal strain (e_{iq}^{int}) contributions.[13, 14]

For a general case, the piezoelectric constant e_{iq} is shown in equation 3.2.[15]

$$e_{iq} = \frac{\partial P_i}{\partial S_q}$$

$$e_{iq} = \left(\frac{\partial P_i}{\partial S_q}\right)_x + \sum_s \sum_p \left(\frac{\partial P_i}{\partial x_{sp}}\right)_{S_q=0} \left(\frac{\partial x_{sp}}{\partial S_q}\right)_{S_q=0} \quad (3.2)$$

$$e_{iq} = e_{iq}^0 + e_{iq}^{\text{int}}$$

The clamped ion contribution (e_{iq}^0) is the change in polarization P_i due to the reorganization of electron density with external strain S_q, while the fractional coordinates x are kept constant in the strained unit cell. The internal strain contribution (e_{iq}^{int}) provides the change in polarization P_i where the atoms are allowed to relax in the strained unit cell in response to the strain S_q. e_{iq}^{int} is related to Born effective charges (BEC, $Z_{s,ip}^*$) as shown in equation 3.3.[15] The BEC is a dynamical charge introduced by Max Born and Maria Göppert Mayer and it is a second rank tensor. It refers to a change in polarization induced by an atomic displacement under the condition of zero macroscopic electric fields.[16] Thus, the internal strain contribution is obtained by summing the product of BECs, a second-order tensor ($Z_{s,ip}^*$), and the respective relaxation coefficient ($\frac{\partial x_{sp}}{\partial S_q}$) over the total number of atoms s and direction of atoms displacement p.

$$e_{iq}^{\text{int}} = \frac{ea}{V} \sum_s \sum_p Z_{ip}^* \frac{\partial x_{sp}}{\partial S_q} \quad (3.3)$$

The general form of piezoelectric tensor e_{iq} is $\begin{bmatrix} e_{11} & e_{12} & e_{13} & e_{14} & e_{15} & e_{16} \\ e_{21} & e_{22} & e_{23} & e_{24} & e_{25} & e_{26} \\ e_{31} & e_{32} & e_{33} & e_{34} & e_{35} & e_{36} \end{bmatrix}$ and born effective charge for an atom Z_{ij}^* is $\begin{bmatrix} Z_{11}^* & Z_{12}^* & Z_{13}^* \\ Z_{21}^* & Z_{22}^* & Z_{23}^* \\ Z_{31}^* & Z_{32}^* & Z_{33}^* \end{bmatrix}$.

3.3 Methods

3.3.1 Database Selection

We start from the QMOF database (v13), a computational-ready database consisting of 20425 MOF structures.[17] Various criteria as listed below were considered for the candidates selection in this work:

1. Only experimentally deposited structures from the Cambridge Structural Database (CSD)[18] are considered.

2. For a material to be piezoelectric, it must be non-centrosymmetric. Hence, non-centrosymmetric structures, either polar or non-polar were chosen.

3. MOFs with metals like Ag, Au, and most of the Lanthanide metals are excluded. MOFs with exotic metals Ag and Au were excluded because of the low stability of MOFs with Ag and Au. Among the lanthanides, MOFs with only La, Ce, and Yb are included in the database.

4. Originally in the QMOF database, all the experimental structures from CSD database were reduced to "1" point group (no symmetry), and the optimization was performed. However, in this work, since the piezoelectric tensor is dependent on the point group of the structure, the structures were re-optimized while considering the symmetry. These are referred to here as symmetrized QMOF structures.

   MOFs which have the same space group in both the original CSD and symmetrized QMOF structures were chosen. This is to ensure that the space group of symmetrized QMOF structures after making them computational ready is the same as that of the CSD experimental structure.

5. Lastly, the number of atoms per primitive cell in the MOF structure is limited to <= 150 atoms.
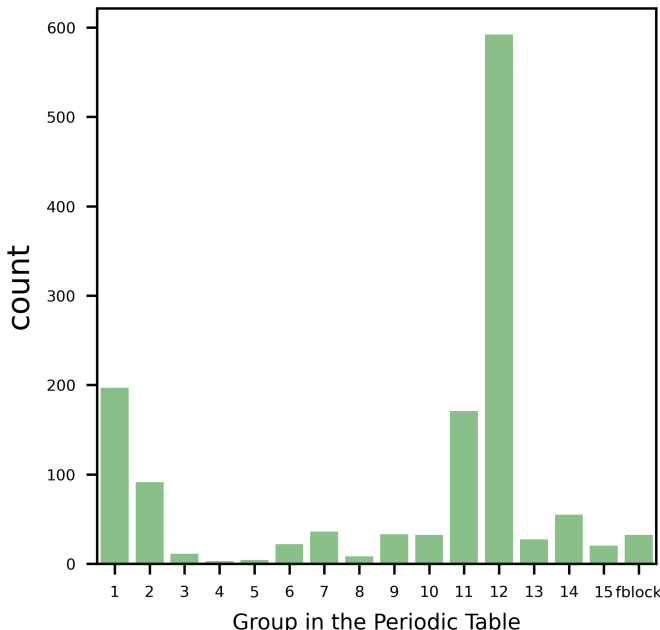
Figure 3.1: Distribution of inorganic cations in the SBU for the selected MOFs based on the group they belong to in the periodic table.

Considering all the above criteria, around 1608 MOF structures are obtained as starting candidates for the piezoelectric calculations. Among these, 442 MOFs belong to non-polar point groups and 1166 MOFs belong to polar point groups. Figure 3.1 shows a distribution of the inorganic cation in the SBU of the selected MOF candidates for the high throughput calculations based on the group in the periodic table they belong to. The database is dominated by MOFs with metal ions from Group 12 (i.e., Zn, Cd) followed by Group 1 (i.e., Li, Na, K) and Group 11(i.e., Cu).

3.3.2 Computational Settings

Piezoelectric DFT calculations were carried out in two steps. As mentioned earlier in section 3.3.1, originally in the QMOF database all structures were reduced to "1" point group (no symmetry). However, in this work, since the piezoelectric tensor is dependent on the point group of the structure the symmetry of the structure should be considered. In the first step, we re-optimize the structures from the QMOF database while considering the symmetry of the unit cell and referred to as symmetrized QMOF structures. In the second step, the piezoelectric constant of the symmetrized QMOF structures is calculated using the Density Functional Perturbation theory (DFPT)[19–21]. DFPT allows computing useful physical properties like elastic and piezoelectric constants, Born effective charges, etc. as a second-order linear response to different perturbations like atomic displacements, electric fields, etc.

All the plane-wave periodic DFT calculations in this work were done using Vienna Ab Initio Simulation Package (VASP v5.4.4).[22, 23] We used Perdew, Becke, and Ernzerhof (PBE) GGA exchange-correlation functional[24] for all the calculations. Grimme's D3 dispersion corrections and Becke-Johnson damping[25, 26] was included for van der Waals dispersion corrections. VASP-recommended projector augmented wave (PAW) pseudopotentials were considered for all elements. (Except for Yb, Yb_3 pseudopotential was used rather than Yb_2 since Yb(III) is more common).[23, 27] For the plane wave cutoff energy and the number of k-points, we performed a convergence study of the piezoelectric tensor with these parameters for two MOFs and this is included in the appendix in section 3.A.1. Based on the convergence study, we use 520 eV as plane wave energy cutoff and a k-point density of ~ 1000 per number of atoms for all calculations in this work.

3.4 Results and Discussion

Piezoelectric calculations were done for around 1608 MOF structures that were obtained after applying various selection criteria mentioned in section 3.3.1. After evaluating the convergence of the calculations based on the consistency checks mentioned in section 3.A.2, we have final piezoelectric results for around 1263 MOFs which is 79% of the number of starting structures. From the calculations, information on the clamped ion (e_{iq}^0), internal strain (e_{iq}^{int}), total piezoelectric tensor (e_{iq}) of the MOF and the Born effective charges (BEC, Z^*) of all the atoms in the structure is obtained. With the available structural information from the QMOF database and the results obtained from the piezoelectric calculations, we present an overall analysis of the database to understand how each factor affects the piezoelectric tensor e.

Note here, that the piezoelectric tensor e_{iq} is a third rank tensor with 18 terms. So, for comparison between different MOF structures, we adopt a simplified value for e_{iq} that has been used previously in high-throughput calculations for inorganic piezoelectrics.[10] The simplified value is the norm value of the final piezoelectric tensor and is denoted as $\left\| e_{iq} \right\|_{max}$. This value corresponds to the maximum attainable absolute value for the longitudinal piezoelectric response in a specific crystallographic direction that is measured among all other directions.

82

3.4.1 Effect of non-polar and polar symmetry on the piezoelectric norm $\left\|e_{iq}\right\|_{max}$

Figure 3.2 shows the spread of piezoelectric constant $\left\|e_{iq}\right\|_{max}$ values for polar and non-polar MOFs. The $\left\|e_{iq}\right\|_{max}$ values for MOFs in this dataset range between 0.004 C/m^2 and 1.55 C/m^2. For non-polar point group MOFs, the distribution's mean value is 0.1 C/m^2 and for polar point groups it is 0.2 C/m^2 i.e., relatively similar. However, very high $\left\|e_{iq}\right\|_{max}$ values greater than ~0.5 C/m^2 are observed mostly for polar point group structures and only for one structure with a non-polar point group. The polar point groups for which $\left\|e_{iq}\right\|_{max}$ is greater than 0.5 C/m^2 is found are 1, 2, m, mm2 and 4. The magnitude of DFT calculated $\left\|e_{iq}\right\|_{max}$ values for inorganic piezoelectrics, range at least up to 20 C/m^2. This is almost an order of magnitude higher than the maximum value obtained for MOFs in this work, which is ~1.6 C/m^2. For inorganics, $\left\|e_{iq}\right\|_{max}$ values between 2.5 to 20 C/m^2 are obtained in structures with point groups 1, 2, 3, 3m, 6mm, mm2, 4, and 4mm; all of them being polar point groups.[10] Hence, a high value for piezoelectric constant e is more likely in structures having a spontaneous polarization.
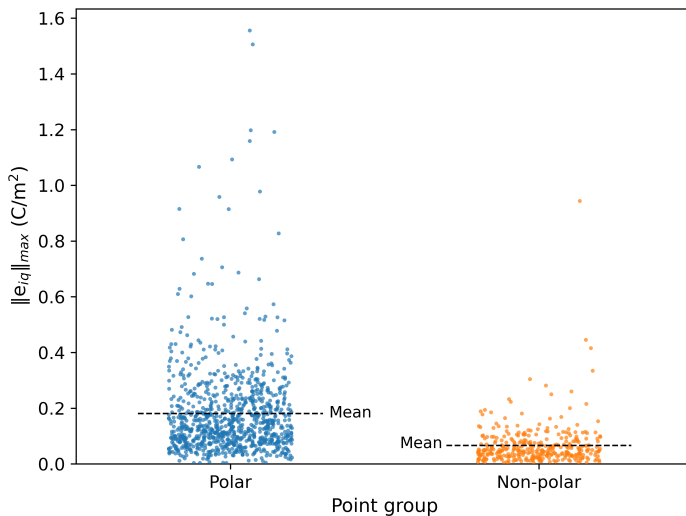
Figure 3.2: Categorical plot showing the distribution of $\left\|e_{iq}\right\|_{max}$ values for Polar and Non-Polar MOFs.

3.4.2 Born effective charge (BEC, Z^*) of inorganic cations in MOFs

In high-performing inorganic piezoelectrics of ABO$_3$ type, it is the anomalously high BEC's of the metal atoms that is responsible for the high piezoelectric constants e. For example, in BaTiO$_3$, SrTiO$_3$, and PbTiO$_3$, Ti with a nominal charge of +4, has a BEC of +6.7 to +7.6 and the e value for BaTiO$_3$, PbTiO$_3$ and SrTiO$_3$ is 6.7, 3.23 and 9.3 C/m^2.[13, 16,

28] Hence, we look at trends and the magnitude of the BEC of the inorganic cations for the MOFs in this work. The Born effective charge (BEC) tensor is a second rank tensor with nine terms in the tensor. The highest change in the BEC when the position of atoms is changed is expected to occur in most cases in 11, 22, and 33 directions. Hence, for the comparison of BEC for inorganic cations in different MOFs the average value of the diagonal elements (Z_{11}^*, Z_{22}^*, Z_{33}^*) of the BEC tensor is used as a representative value for the BEC. Hence, the average values of Z^* in these directions give a good estimate of the total BEC of that atom.
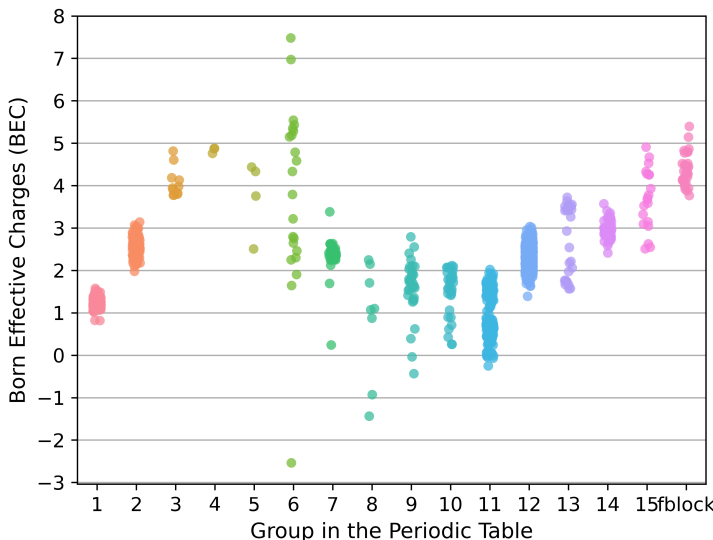
Figure 3.3: Distribution of BEC values of inorganic cations in MOFs belonging to different groups of the periodic table.

The BEC of the inorganic cations of the MOFs versus the group they belong to in the periodic table is shown in Figure 3.3. For Group 1 (alkali metals) which usually have a single oxidation state (OS) of +1, the BEC values are in the range of ~ OS to OS +0.8, and for Group 2 (alkaline earth metals) with an OS of +2, the BEC values are in the range of ~ OS to OS+1. For Groups 3 (Sc family), and 4 (Ti family), which also have a single OS of +3 and +4 respectively, the BEC values are higher and in the range of OS+1 to OS+2. However, the number of MOFs with metal nodes from Groups 3 and 4 is very limited in the database. Other groups in the transition metals (Groups 5 to 12) have multiple oxidation states, hence we also see multiple values with a wide range for BEC. Group 13 (Al to Tl) generally exhibits oxidation states of +1 or +3; BEC values for this group are in the same range of +1.5 to +3.8. Then Group 14 (Ge to Pb) can have an oxidation state of +2 or +4; while their BEC is within the same range of values. Group 15 (Sb, Bi) and f block elements (La, Ce, Yb) have BEC between +2.5 to +5 and +4 to +5.5 respectively. Overall, BEC values of +4 and higher are seen for inorganic cations in MOFs belonging to Groups 3, 4, 5, 6, 15, and f-block

elements.
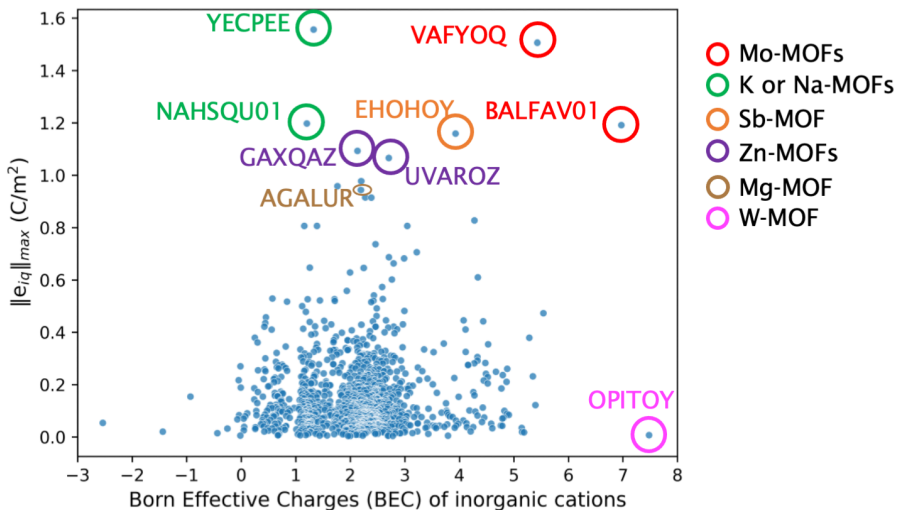
Figure 3.4: BEC values of inorganic cations in MOFs versus the piezoelectric norm $\|e_{iq}\|_{max}$ of the MOF. The CSD refcode for the MOFs with high $\|e_{iq}\|_{max}$ values are also indicated in the figure.

Figure 3.4 shows the relationship between the BEC of the inorganic cation versus the norm piezoelectric constant ($\|e_{iq}\|_{max}$) value of the corresponding MOF. MOFs with a high norm piezoelectric constant are also indicated in the Figure 3.4 whose structures will be discussed in detail in sections 3.4.4. For the majority of the MOFs, BEC ranges between +1 and +3 whereas for inorganics this is higher and is in the range of 2.5 to 5.0.[29] A few inorganic cations in MOFs also have high BEC values of around +7 to +7.5, close to the BEC value of +6.7 for Ti in $BaTiO_3$. This is observed for MOFs with Mo and W elements of Group 6 in the SBUs also indicated in Figure 3.4. MOFs with Mo show a high BEC value for the inorganic cation and also a high e value for the MOFs. MOF with W also show a high BEC value for the inorganic cation, however, in contrast to the Mo-MOFs the e for this W-MOF is low. This could be due to the influence of other structural aspects of the MOF i.e., point group of the structure, coordination environment around the inorganic cation and the organic ligands in the MOF. Highlighted Mo-MOFs belong to a polar point group whereas the W-MOF belongs to non-polar point group. Detailed structure of Mo-MOFs with high BEC, high $\|e_{iq}\|_{max}$ and W-MOF with high BEC but low $\|e_{iq}\|_{max}$ is discussed in section 3.4.4.2 and 3.A.4 respectively. As is clear from Figure 3.4, in MOFs there is no clear correlation between the BEC (Z^*) of the inorganic cation and $\|e_{iq}\|_{max}$ value. High $\|e_{iq}\|_{max}$ values of 1.5 and 1.2 C/m^2 are observed for both low values of Z^* (around +1.3) and high Z^* values (around +7.0). Hence, obtaining a high $\|e_{iq}\|_{max}$ value in MOFs is not simply dependent on the Z^* of the inorganic cations.

Inorganic ceramics with superior piezoelectric properties like PZT, $BaTiO_3$ and $SrTiO_3$

have e_{iq} values of $11.9\,\mathrm{C/m^2}$, $6.7\,\mathrm{C/m^2}$ and $9.3\,\mathrm{C/m^2}$ respectively and organic polymers like PVDF, P(VDF-TrFE) have magnitude for e_{iq} as $0.27\,\mathrm{C/m^2}$ and $0.18\,\mathrm{C/m^2}$. [28, 30–32] Metal-free organic piezoelectric of type $MDABCO - NH_4 - X_3$ (MDABCO is N-methyl-N'-diazabicyclo[2,2,2] octonium) has e_{iq} values in the range of $0.1\,\mathrm{C/m^2}$ to $0.3\,\mathrm{C/m^2}$.[5] The piezoelectric constant values for MOFs in this work range from $0.004\,\mathrm{C/m^2}$ to $1.55\,\mathrm{C/m^2}$. Compared to organic polymers and metal-free perovskites, MOFs have higher e values, whereas MOFs present low values of piezoelectric constant e compared to traditional inorganic ceramics.

3.4.3 Clamped-ion ($\left\|e_{iq}^{0}\right\|_{max}$) and internal strain ($\left\|e_{iq}^{int}\right\|_{max}$) contributions to piezoelectric norm $\left\|e_{iq}\right\|_{max}$

As mentioned in section 3.2, the piezoelectric tensor e_{iq} can be divided into clamped-ion (e_{iq}^{0}) and internal strain (e_{iq}^{int}) contributions, where the BEC and relative change in positions of atoms due to the strain are included in the internal strain contributions. To understand the relative contributions of clamped-ion and internal strain terms to the piezoelectric tensor e, we compare the norm values of the clamped-ion ($\left\|e_{iq}^{0}\right\|_{max}$) and internal strain ($\left\|e_{iq}^{int}\right\|_{max}$) tensors with the norm values of the piezoelectric tensor $\left\|e_{iq}\right\|_{max}$ in Figures 3.5a and 3.5b. For this, we compare the norm values of the clamped-ion ($\left\|e_{iq}^{0}\right\|_{max}$) and internal strain ($\left\|e_{iq}^{int}\right\|_{max}$) tensors with the norm values of the piezoelectric tensor $\left\|e_{iq}\right\|_{max}$. The total piezoelectric constant values for MOFs in this work range between 0.004 to $1.55\,\mathrm{C/m^2}$ while clamped-ion values vary between 2×10^{-5} to $0.724\,\mathrm{C/m^2}$ and internal strain contribution values are in the range of 0.001 to $1.771\,\mathrm{C/m^2}$.
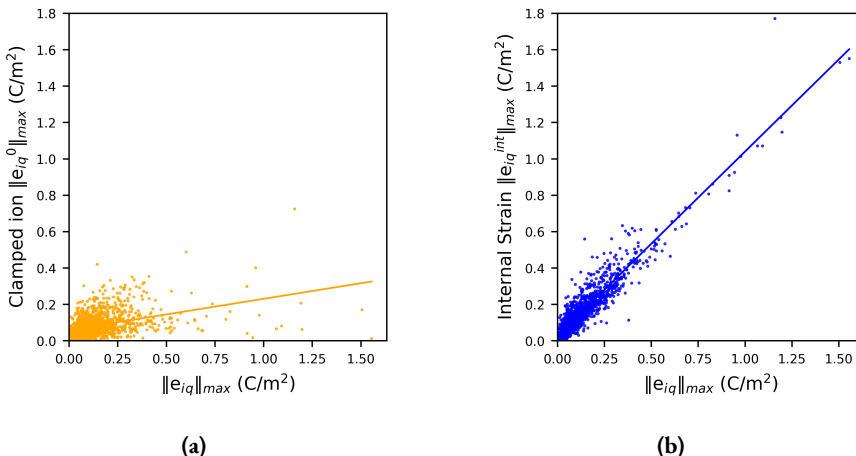
Figure 3.5: Correlation between a) clamped ion $\left\|e_{iq}^{0}\right\|_{max}$ b) internal strain $\left\|e_{iq}^{int}\right\|_{max}$ and total piezoelectric norm $\left\|e_{iq}\right\|_{max}$ values.

A linear fit between clamped ion, internal strain and total piezoelectric norm is also

included in Figure 3.5. Stronger linear correlation is observed between the internal strain norm values and total piezoelectric norm values (Figure 3.5b) compared to between the clamped ion and total piezoelectric norm values (Figure 3.5a). Statistically, the Pearson correlation coefficient is used to show the strength of linear correlation between two data sets. The value of the Pearson correlation coefficient for internal strain and total piezoelectric constant is 0.9 whereas for clamped-ion and total piezoelectric constant is 0.4. Thus, the internal strain contribution $\left\|e_{iq}^{int}\right\|_{max}$ is a dominant factor for obtaining a higher e value in MOFs. The internal strain contribution is due to the combined effect of the BEC of all atoms and the relative changes in positions of atoms due to lattice strain applied. Hence, to understand these contributions structurally, we focus in detail on the MOFs with a high piezoelectric e norm ($\left\|e_{iq}\right\|_{max}$) and elaborate on the structural factors that could lead to a higher $\left\|e_{iq}\right\|_{max}$ value in these MOFs in the next section.

3.4.4 MOFs with high piezoelectric value $\left\|e_{iq}\right\|_{max}$
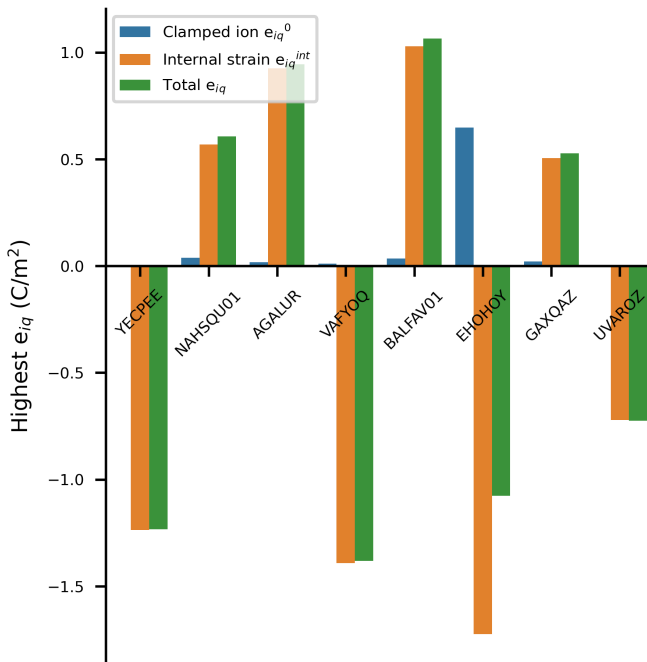
Figure 3.6: Bar plot of highest e_{iq} and the respective clamped ion and internal strain contributions in the same iq direction for the eight MOFs with the highest piezoelectric norm value $\left\|e_{iq}\right\|_{max}$.

Among the MOFs for which the piezoelectric tensor was successfully calculated and finalized after various consistency checks, we consider the top candidates with a $\left\|e_{iq}\right\|_{max}$ value

of $\geq\sim 1.0\,C/m^2$ for elaborate structural analysis. There are eight MOFs which have a $\|e_{iq}\|_{max} \geq 1.0\,C/m^2$, among which all of them belong to polar point groups except for one MOF which is non-polar. Figure 3.6 shows a plot of the highest total e_{iq} value, clamped ion e_{iq}^0 and internal strain e_{iq}^{int} values for these eight MOFs along with their reference code used in the CSD database. Note here, for the bar plot in Figure 3.6, we show the highest e_{iq} value of the tensor (not the norm values i.e., $\|e_{iq}\|_{max}$) and clamped ion and internal strain value in the same iq direction, this is to compare the magnitude of clamped-ion and internal strain piezoelectric coefficient in the same direction. The full piezoelectric tensor e_{iq} and the BEC of inorganic cations in these eight MOFs with high $\|e_{iq}\|_{max}$ values is included in the Appendix 3.A.3.

As seen in the bar plot (Figure 3.6), the clamped ion contribution e_{iq}^0 is quite low compared to the total e_{iq} value for each MOF, except for EHOHOY whose e_{iq}^0 is significant. Clearly, for all eight MOFs, the internal strain value e_{iq}^{int} is dominant and gives rise to a high e_{iq} value. For inorganic piezoelectrics, the magnitude of BEC values and eventually their piezoelectric constants e is affected by the anisotropy of the coordination environment around the metal atoms.[16] Hence, for the eight MOFs with a high piezoelectric constant, the BEC (Z^*) of the inorganic cations and a detailed discussion of the coordination environment is presented.

3.4.4.1 YECPEE, NAHSQU01, and AGALUR
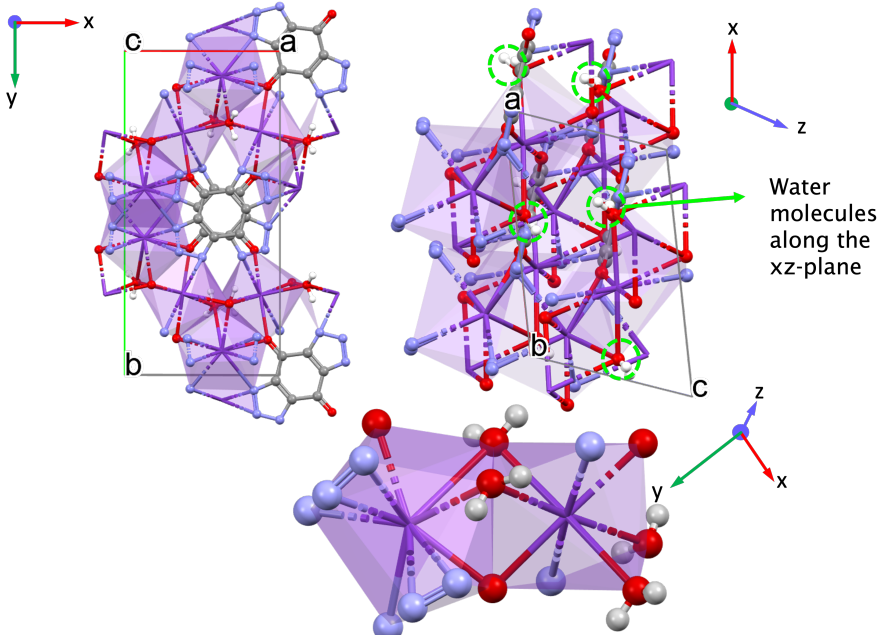
Figure 3.7: Structure of YECPEE shown along the xy, xz planes, and the coordination environment around the inorganic cation K for YECPEE. Purple: Potassium (K), gray: Carbon (C), red: Oxygen (O), white: Hydrogen (H), blue: Nitrogen (N).

YECPEE and NAHSQU01 belong to the polar monoclinic point group 'm' where all the non-zero values of piezoelectric tensor e_{iq} involve the x and/or z-directions because the structure is centrosymmetric in the y-direction due to the mirror plane in the xz plane. These MOFs have K^+ and Na^+ as inorganic cations respectively, which belong to group 1 of the periodic table, however, the connecting linkers in these MOFs are different from each other. YECPEE ($K_2 - btbq \cdot 2\,H_2O$) has bistriazole-p-benzoquinone (btbq), a centrosymmetric linker [33] whereas in NAHSQU01 ($NaHC_4O_4 \cdot H_2O$) hydrogensquarate is the linker which is polar [34]. Both these MOFs have water molecules coordinated to the inorganic cations as shown in Figures 3.7 and 3.8. The total piezoelectric norm values $\|e_{iq}\|_{max}$ for YECPEE and NAHSQU01 are $1.556\,C/m^2$ and $1.198\,C/m^2$. Even though the BEC (Z^*) of the inorganic cations are low (K:+1.36, Na:+1.20), we obtain high e values for these MOFs. For YECPEE, the highest value in the piezoelectric tensor is $e_{31} = -1.233\,C/m^2$ (the full piezoelectric tensor is shown in appendix in section 3.A.3.1)i.e., the largest polarization is observed along the z-direction when a strain is applied along the x-direction. Similarly, for NAHSQU01, $e_{33} = 0.565\,C/m^2$ and $e_{35} = 0.607\,C/m^2$ are very close in magnitude and are the highest values in the tensor (the full piezoelectric tensor is shown in appendix in section 3.A.3.2)) i.e., the largest polarization is observed along the z-direction when a uniaxial strain is applied along the same z-direction or a shear along the xz plane.
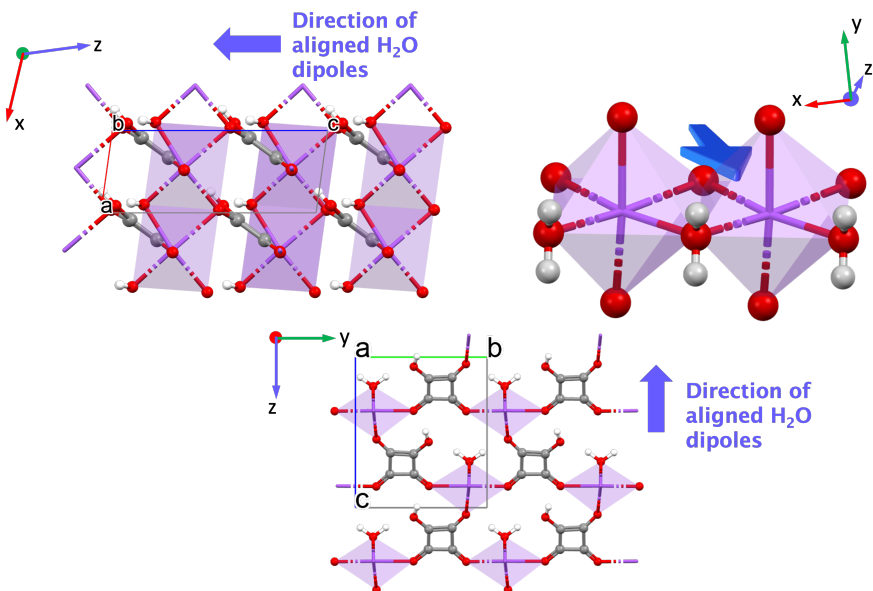
Figure 3.8: Structure of NAHSQU01 shown along the xz, yz planes, and the coordination environment around the inorganic cation Na for NAHSQU01. Purple: Sodium (Na), gray: Carbon (C), red: Oxygen (O), white: Hydrogen (H), blue: Nitrogen (N).

As highlighted in Figure 3.7, for YECPEE, the water molecules are arranged such that their dipole moments do not cancel out along the x and z-direction while a mirror plane along the xz plane cancels out the dipole moments along the y-direction, hence the highest e

value along e_{31}. For NAHSQU01 (Figure 3.8), high e values of e_{33} and e_{35} are not only due to the water dipoles aligned along the z-direction but also from the dipole moment of the organic ligand that is from the partly aligned hydroxy group of the organic ligand along the z-direction (i.e. 3 direction). In MOFs YECPEE and NAHSQU01, the water molecules coordinated to the inorganic cations are aligned along a specific direction in the unit cell. This direction corresponds with the direction along which the highest e values are observed. Hence, we deduce that the aligned water molecules contribute the most for a high e value in these MOFs rather than the BEC of the inorganic cations.
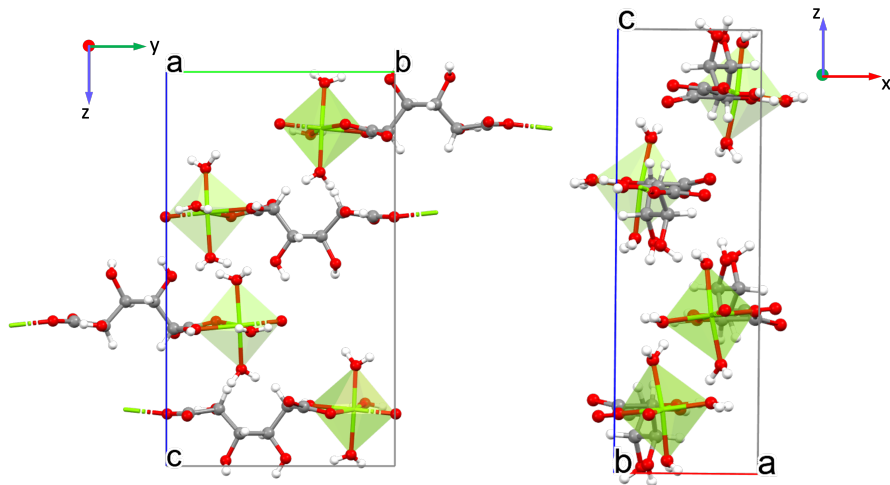
Figure 3.9: Figure showing AGALUR structure in the yz and xz planes. Green: Magnesium (Mg), gray: Carbon (C), red: Oxygen (O), white: Hydrogen (H).

AGALUR is a metal–organic coordination polymer of magnesium saccharate ($Mg(H_2O)_3(sacch)$, Figure 3.9), belonging to non-polar orthorhombic point group '222' where all the non-zero values of e_{iq} involve all three crystal directions (x, y, z-directions). The saccharate linker has a dipole moment. Mg^{2+} has a distorted octahedral environment formed by three water molecules, two carboxylate oxygen atoms from the saccharate anions, and one hydroxyl group.[35] Piezoelectric norm value $\|e_{iq}\|_{max}$ of 0.944 C/m^2 was calculated for AGALUR (the full piezoelectric tensor is shown in appendix in section 3.A.3.3) and the BEC of Mg^{2+} cations in this MOF is around +2.19. Mg^{2+} saccharate coordination chains are arranged along the y-direction (direction 2) of the unit cell, with hydrogen bonding between the chains. The chains are helically arranged. The non-centrosymmetry of the structure is in fact chiral. The highest e value is for e_{25} =0.944 C/m^2 i.e., the largest polarization is obtained along the y-direction when a shear is applied along the xz-plane. The BEC of Mg cations is not high, hence they do not contribute to a large extent for a high e value. We attribute the large contribution to e value rather to the water molecules bonded to the Mg^{2+} cations and the polar -OH groups on the organic chain, akin to YECPEE and NAHSQU01.

3.4.4.2 VAFYOQ and BALFAV01
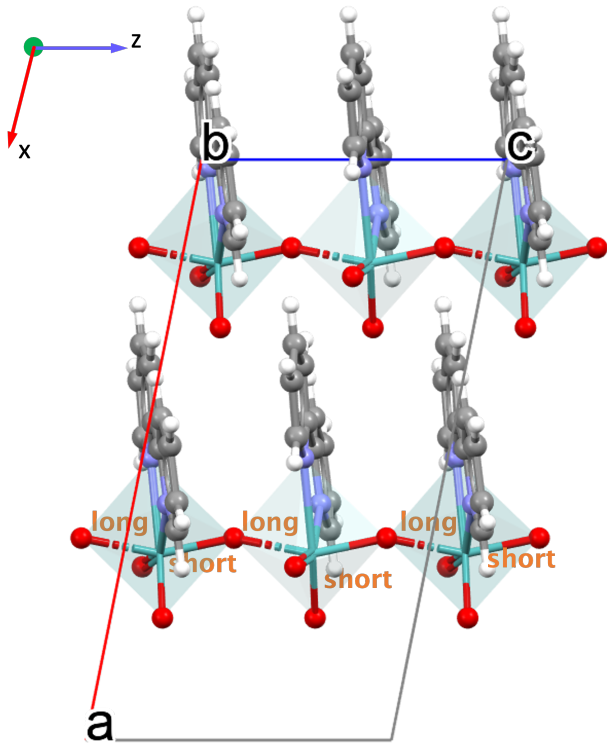
Figure 3.10: Structures of VAFYOQ showing the xz plane and different O1-Mo-O2 short-long-short-long... pattern in the bond lengths along the z-direction. teal: Molybdenum (Mo), gray: Carbon (C), red: Oxygen (O), white: Hydrogen (H), blue: Nitrogen (N).

VAFYOQ and BALFAV01 are Mo MOFs belonging to the monoclinic point groups 'm' and '2', where all the non-zero values of piezoelectric tensor e_{iq} involve the x and/or z-directions and y-direction respectively. They have organic linkers 2,2′-bipyridine and 4,4′-bipyridine respectively. VAFYOQ ($MoO_3(2,2′$-bipy), Figure 3.10) consists of one-dimensional chains of MoO_4N_2 distorted octahedra where each Mo is coordinated by two bridging oxo groups shared between the octahedra, two terminal oxo groups and the two pyridyl nitrogen from the polar 2,2′-bipyridine ligand. The piezoelectric norm $\|e_{iq}\|_{max}$ value for this MOF is 1.506 C/m^2 and the average BEC (Z^*) of Mo cation in VAFYOQ is +5.43 close to the +6 oxidation state. This Z^* value for Mo could contribute to the high e value. Other high e MOF structures have similar magnitudes for the diagonal values of Z^* i.e., Z_{11}^*, Z_{22}^*, and Z_{33}^* and closer to the average value of BEC Z^* values. In contrast to this, VAFYOQ has a high value for $Z_{33}^* = +8.7$ than $Z_{11}^* = +3.8$ and $Z_{22}^* = +3.7$. Additionally, Mo site exhibits two short-two intermediate-two long bond lengths around the coordinating site. Importantly, along the z-direction (direction 3) Mo-bridging oxo group

distances are unsymmetrical (i.e., O1-Mo-O2) giving rise to an alternate short-long-short-long-... Mo-O infinite chain with lengths O1-Mo: 1.822Å and Mo-O2: 2.031Å [36]. Thus along the z-direction (direction 3) anisotropic coordination environment around Mo is observed (see Figure 3.10). While the dipole moments of the organic ligand are aligned closely to the x-direction, the highest e value in the piezoelectric tensor is nonetheless e_{33} = −1.382 C/m^2 (the full piezoelectric tensor is shown in appendix in section 3.A.3.4). The largest polarization is observed along the z-direction upon uniaxial strain along the chains within the 2-D MoO$_3$ network along the z-direction. The very high value of Z^*_{33} in the z-direction will also contribute to obtaining a high e_{33} along the z-direction.
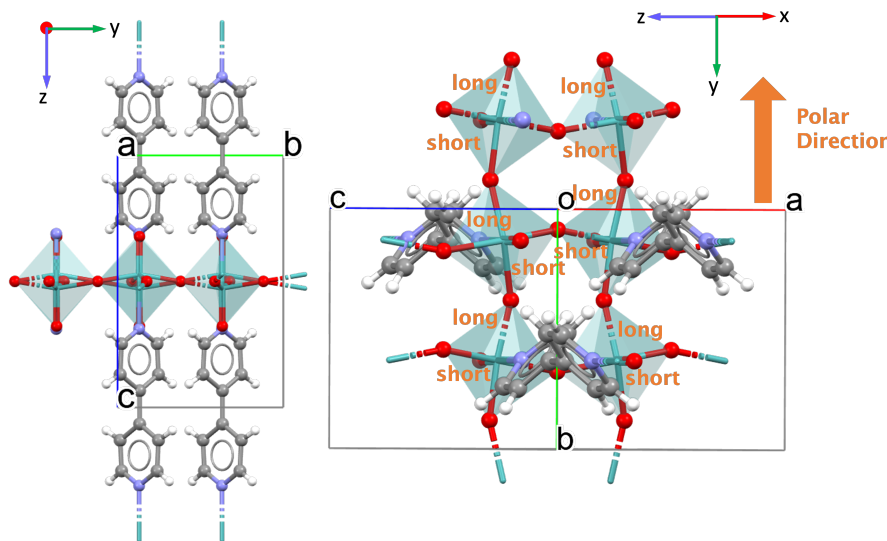
Figure 3.11: Structures of BALFAV01 (showing the yz plane) and different O1-Mo-O2 long-short-long-short-.... pattern in the bond lengths along the y-direction. teal: Molybdenum (Mo), gray: Carbon (C), red: Oxygen (O), white: Hydrogen (H), blue: Nitrogen (N).

For BALFAV01 (MoO$_3$)$_2$(4,4′-bipy), Figure 3.11), the Mo inorganic cations also have a distorted octahedral geometry; coordinated by one terminal oxo-oxygen, four bridging oxygen atoms shared between the octahedra and one nitrogen atom from a centrosymmetric 4,4′-bipyridine linker. N and terminal oxo-oxygen group are 180° apart along the z-direction; the other four atoms are oxygens along the x and y-direction and shared between two Mo atoms. The piezoelectric norm $\left\| e_{iq} \right\|_{max}$ value for this MOF is 1.191 C/m^2 and the average Z^* for Mo is high around +6.97, again close to the oxidation state of +6.0 for Mo. Similar to VAFYOQ, among the diagonal values of Z^*; the highest value is for Z^*_{11} = +9.96. The values of Z^*_{22}, Z^*_{33} are +6.16 and +4.79 respectively. For the experimentally synthesized structure of this MOF, along the y-direction (direction 2), the O1-Mo-O2 bonds slightly differ in the bond lengths (O1-Mo: 1.918Å, Mo-O2: 1.926Å) forming long-short-long-short-....bonds. The difference in bond lengths is more pronounced in the computationally optimized structure and the pattern of long-short-long-short-.... bonds are retained.[37] The highest

e value is e_{22} =1.065 C/m^2 (the full piezoelectric tensor is shown in appendix in section 3.A.3.5) i.e., largest polarization is observed along the polar y-direction, thus along the long-short-long-short..... bond patterns of BALFAV01 when a uniaxial strain is applied along the same y-direction. Even though the Z^* is largest along the x-direction (Z^*_{11}), since the x-direction is not the polar direction contribution of Z^*_{11} to the piezoelectric response is limited.

In both VAFYOQ and BALFAV01, the highest e values are seen along the direction of long-short-long-short.... bonds of O1-Mo-O2. This pattern of long-short-long-short... bond lengths, which is seen in both Mo MOFs, is also seen in piezoelectric BaTiO$_3$. In the tetrahedral structure of BaTiO$_3$, along the z-direction the O1-Ti-O2 bond lengths are unsymmetrical, creating an anisotropic coordination environment around Ti along Ti-O chains.[16] Additionally, high-born effective charges for Ti (+6.7) are also shown to enhance the piezoelectric constant of BaTiO$_3$. In these MOFs, Mo^{6+} cations have Z^* of +5.43 and +6.7. Hence, the high BEC of Mo together with the anisotropic coordination environment around the Mo cations due to the long-short-long-short.... bonds pattern cause the high e value. In addition to these MOFs showing high piezoelectric e values, they are potentially ferroelectric exhibiting a spontaneous and reversible polarization on the application of an external electric field. That is, upon application of an external electric field the O1-(short)-Mo-(long)-O2 could be altered to O1-(long)-Mo-(short)-O2 that could result in a change in sign of the polarity of the material, thus behaving as a ferroelectric material.

3.4.4.3 EHOHOY
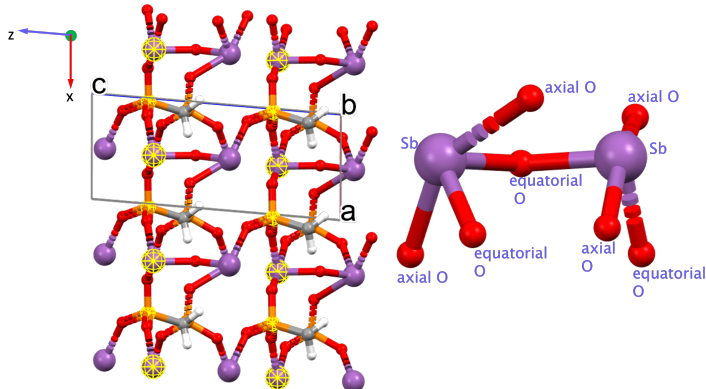
Figure 3.12: Figure showing EHOHOY structure in the xz plane with the chain of Sb, P atoms highlighted in the structure and the trigonal bipyramidal arrangement of SbO$_4$ units. Plum: Antimony (Sb), gray: Carbon (C), red: Oxygen (O), white: Hydrogen (H), orange: Phosphorous (P).

This MOF (Sb$_2$O(O$_3$PCH$_2$PO$_3$)) belonging to point group 'm', where all the non-zero values of e_{iq} involve the x and/or z-directions. Structure of EHOHOY shown in Figure 3.12 consists of Sb^{3+} cation coordinated to methylenediphosphonate (O$_3$PCH$_2$PO$_3$)$^{4-}$ ligand with a dipole moment. The structure exhibits a three-dimensional network comprising

of trigonal bipyramidal SbO_4 units and tetrahedral $[(PO_3(CH_2)]$ units. The SbO_4 units as shown in Figure 3.12 consists of two oxygens in the axial position shared between Sb and P, two other oxygens in the equatorial positions shared between Sb and Sb or Sb and P, and the lone pair of electrons of Sb also in an equatorial position i.e., in the same plane as the plane of equatorial oxygens.[38] The piezoelectric norm $\|e_{iq}\|_{max}$ is 1.159 C/m^2. In this MOF, there are two distinct cations, Sb and P, each with BEC Z^* of +3.93 and +3.60 respectively. $e_{11} = -1.076$ C/m^2 is the highest value in the piezoelectric tensor for EHOHOY indicating the greatest polarization along the x-direction when a strain is also applied along the x-direction (the full piezoelectric tensor is shown in appendix in section 3.A.3.6). The polar bipyramidal SbO_4 units and the polar phosphate units (PO_3^-) are partially aligned along the x-direction. The bonds Sb-O-P-O-Sb-O-P... with varying bond lengths are partly aligned parallel to the x-direction. We attribute the high e value for this MOF, to this alignment of varying bond lengths leading to a net polarization combined with the distinct BECs of both Sb and P.

3.4.4.4 GAXQAZ and UVAROZ

Both these MOFs are Zn-based, crystallizing in the monoclinic 'm' point group, thus all the non-zero values of piezoelectric tensor e_{iq} involve the x and/or z-directions. These are interpenetrated MOFs with 1,4-phenylenediacetate acid (p-pda) and 1,1'-(1,4- butanedidyl)-bis-(imidazole) (biim-4) linkers for GAXQAZ (Zn(p-pda)(biim − 4), shown in Figure 3.13a). The linker in UVAROZ (Zn(pyeb)$_2$) is 4-[2-(4-pyridyl)ethenyl] benzoic acid (pyeb) as shown in Figure 3.13b)[39, 40]. The total piezoelectric norm values for GAXQAZ is 1.092 C/m^2 and for UVAROZ it is 1.066 C/m^2. In both cases, Zn is coordinated with the O and N atoms from the organic linkers creating a polar coordination environment around Zn^{2+}. The BECs of Zn^{2+} in GAXQAZ and UVAROZ are +2.13 and +2.71 respectively, which are not high. GAXQAZ has high e_{ip} values for nearly five indices e_{11} =0.527 C/m^2, e_{31} =−0.518 C/m^2, e_{13} =0.415 C/m^2, e_{15} =0.403 C/m^2 and e_{35} =−0.405 C/m^2 which indicates that the largest polarization is along x and z-directions when a strain is applied along the x, z directions, and the xz-plane (the full piezoelectric tensor is shown in the appendix in section 3.A.3.7). Then for UVAROZ, e_{13} =−0.724 C/m^2 is the e_{ip} with the highest magnitude, which has the largest polarization along the x-direction when a strain is applied along the z-direction (the full piezoelectric tensor is shown in appendix in section 3.A.3.8). Figure 3.13 shows the xz (13) plane of the GAXQAZ and UVAROZ. The biggest contributing factor for high piezoelectric values of MOFs GAXQAZ and UVAROZ is not from the BEC of the inorganic cations. The high e values for these Zn MOFs can be attributed to the polar coordination environment around Zn^{2+} cation and the polar ligands that are aligned in an overall polar manner.

(a)

(b)
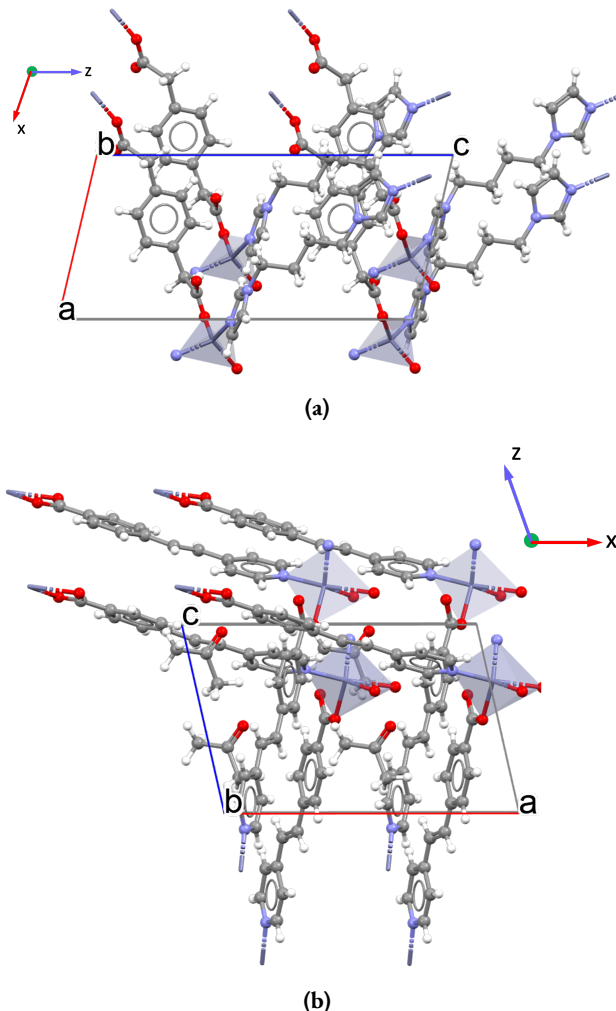
Figure 3.13: Structures of a) GAXQAZ (showing the xz plane) and b) UVAROZ (showing the xz plane). Tetrahedral: Zinc (Zn), gray: Carbon (C), red: Oxygen (O), white: Hydrogen (H), blue: Nitrogen (N).

3.5 Conclusions

In this work, we generated a database of the piezoelectric properties for 1263 previously synthesized MOF structures through high-throughput periodic DFT calculations. The total piezoelectric tensor (e_{iq}) and the two contributions of e_{iq}: clamped-ion (e_{iq}^0) and internal strain tensors (e_{iq}^{int}) along with the born effective charges (BEC) for all the atoms in the structure are obtained from the piezoelectric calculations. Polar MOFs generate more structures with high e values than non-polar MOFs. For the MOFs in this study, the

internal strain contribution is strongly correlated with total piezoelectric coefficient and is the dominant factor for obtaining high e values. BEC values of +4 and higher are seen in inorganic cations belonging to Groups 3, 4, 5, 6, 15 in the periodic table and the included f-block elements. Especially for Mo and W, very high BEC ranging between +7 and +7.5 are observed, which is similar to the high BEC of Ti in ABO_3 inorganic ceramics. Unlike inorganic ceramics, we observed that a high BEC of the inorganic cations isn't necessarily correlated with a high e value in MOFs. The driving factor for obtaining a higher e in MOFs is much more complex and structure dependent, including the combined effect of BEC of all atoms (including inorganic cations of the SBU and atoms in the organic linkers of the MOF) and the relative change in atomic positions.

Hence, for the MOFs that show high piezoelectric constant e values $\geq 1.0 \, C/m^2$, we highlight the key structural factors contributing to their high performance. Based on those observations, we summarize a series of guidelines for MOF structures (not exhaustive) that can lead to a high e value.

1. The structure belongs to a polar point group

2. Mo MOFs in this work (VAFYOQ and BALFAV01) with -O1-Mo-O2-......bonds have a long-short-long-short-....bond length patterns along a specific direction organized in a polar manner. Additionally, Mo cations also have a high born effective charge (BEC) of ~ +6. Hence, having a high born effective charge (BEC) for the inorganic cations together with an anisotropic coordination environment around them due to the long-short-long-short.... pattern of bonds which are organized in a polar manner can lead to high e value.

3. The coexistence of different inorganic cations with varying born effective charges (BEC) within the same structure, linked together by organic atoms. These inorganic-organic chains are further aligned along a specific direction. (like Sb and P in EHO-HOY)

4. The presence of polar molecules such as water, directly bonded to the inorganic cation and aligned along a specific direction (YECPEE, NAHSQU01 and AGALUR).

5. A very polar coordination environment around the inorganic cation together with polar organic ligands aligned in a polar manner (GAXQAZ and UVAROZ). For example, if the inorganic cation is coordinated to two N atoms and two O atoms in a tetrahedral coordination, a polar coordination environment is possible.

Compared to organic polymers and metal-free perovskites, MOFs exhibit ~ one orders of magnitude higher e values, whereas compared to conventional inorganic ceramics, MOFs have ~ one order of magnitude lower piezoelectric constants (e). Nevertheless, MOFs are anticipated to demonstrate higher piezoelectric constants (d) than inorganics owing to their highly flexible frameworks in contrast to the stiffer mechanical properties of conventional inorganic ceramics. The Young's moduli for conventional ceramics (like $PbTiO_3$, $BaTiO_3$, $LiNbO_3$) ranges from 100 GPa to 200 GPa[11] while for MOFs the young's moduli are lower due to their flexible frameworks and values are in between 1 GPa and 20 GPa[41]. The dielectric constants of guest-free MOFs vary between 2.33 and 6.0[42–44] while those of inorganic ceramics like PZT and $BaTiO_3$ are 1300 and 1700 [45, 46]. Hence, due to

their very low dielectric constant and higher flexibility, making them suitable for applications in piezoelectric energy harvesting, MOFs might exhibit higher piezoelectric energy harvesting efficiency than inorganic piezoelectrics. Additionally, the Mo-MOFs in this work (VAFYOQ, BALFAV01) due to their O-Mo-O dipoles may also be ferroelectric showing a spontaneous and reversible polarization upon the application of an electric field. This is especially advantageous for the processability of MOFs into energy harvesting devices.

In summary, this study utilizes high-throughput calculations to investigate the piezoelectric properties of MOFs, facilitating the discovery of novel piezoelectric MOFs. The research has identified eight potentially promising new piezoelectric MOFs, with their structures discussed in detail. By emphasizing the importance of understanding structure-property relationships, this work provides a valuable guide for designing new and previously undiscovered piezoelectric MOFs, accelerating the search for efficient materials for mechanical energy harvesting.

Appendix to chapter 3

3.A.1 Benchmarking of VASP parameters with piezoelectric tensor

Convergence tests were carried out for two MOFs with CCDC codes REDMUL and VES-BEC01. They are Y (Yttrium) and La (Lanthanum) based MOFs respectively. Additionally, the convergence tests were also done for two ZIFs (ZIF-8 and CdIF-1) which were already studied computationally for their piezoelectric properties.

3.A.1.1 Convergence of piezoelectric tensor with ENCUT values

For the convergence tests, in both optimization and piezoelectric calculation steps, we use two ENCUT values of 520 eV and 700 eV while keeping the k-points density to 1000 per number of atoms. We then look at the effect of ENCUT values on the norm of the piezoelectric tensor. For both MOFs, with the change in encut the piezoelectric norm values ($\|e_{iq}\|_{max}$) almost remains the same. Hence, we consider ENCUT=520 eV for all the high-throughput calculations.
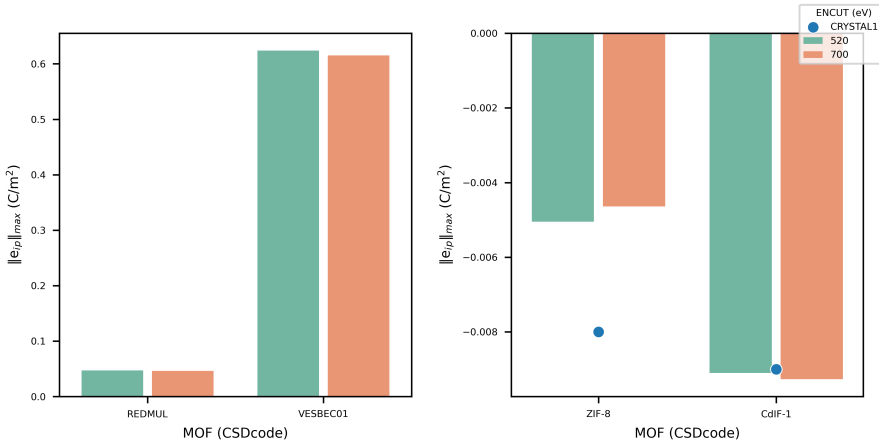
Figure 3.A.1: Piezoelectric constant $\|e_{iq}\|_{max}$ values at two different ENCUT values of 520 eV and 700 eV for MOFs in the QMOF database (left) and for ZIFs (right).

3.A.1.2 Convergence of piezoelectric tensor with k-points values

In this convergence test, the encut value 520 eV is kept constant and we vary the k-points density to 1000 and 2000 per number of atoms. The change in the values of the 'e' norm with the change in k-point density is less than 1.3% percent, hence we use the k-point density of 1000 per number of atoms in the next calculations.

3.A.2 Consistency checks in the DFT calculations

With the finalized ENCUT, k-points values, and other parameters for the calculations, we geometry-optimize the selected MOF structures followed by a DFPT calculation, resulting in
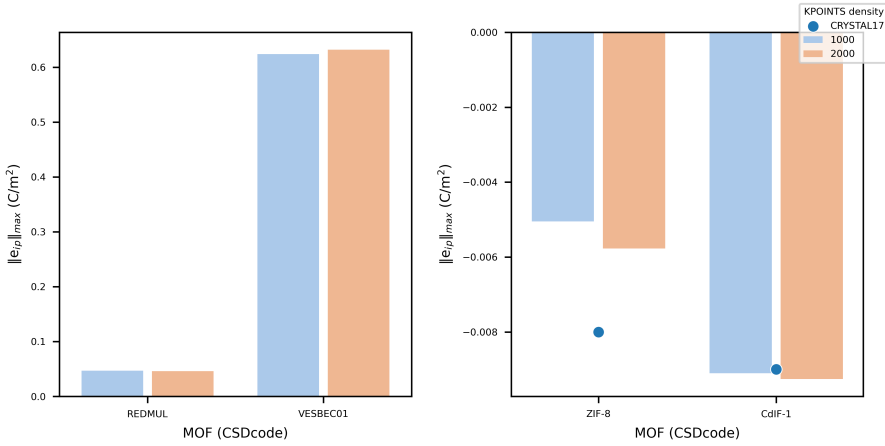
Figure 3.A.2: Piezoelectric constant $\left\|e_{iq}\right\|_{max}$ values at two different KPOINTS of 1000 and 2000 for MOFs in the QMOF database (left) and for ZIFs (right).

the piezoelectric tensor. Several consistency checks at different stages in the calculations are used to detect possible errors, non-converged results, and obtain only reliable piezoelectric tensors. The filters chosen are as follows:

1. Checks on the net magnetic moment:

   a) The final magnetic moment obtained in the calculations (where symmetry is taken into consideration) after geometry optimization should be the same as the net magnetic moment which is deposited in the QMOF database for MOF structures (where symmetry is not considered).

   b) The net magnetic moment at the end of the geometry optimization step and the piezoelectric calculation step should be equal. We expect it to be the same theoretically because the atoms are displaced by a very small strain in the piezo-electric calculations within the harmonic limit, which shouldn't change the net magnetic moment of the entire structure.

2. Checks on the calculated piezoelectric tensor: The following filters are based on symmetry considerations concerning the point group of the structure.

   a) By virtue of symmetry, $\left|e_{iq}\right|$ should be zero for some components in the piezo-electric tensor. This is checked separately in clamped ion and internal strain tensor to be, $\leq 0.1\%$ i.e, $\left|e_{iq}^{0}\right| \leq 0.001 \, C/m^2$ and $\left|e_{iq}^{int}\right| \leq 0.001 \, C/m^2$.

   b) For point group symmetries that have two components e_{ip} and e_{iq} to be equal, these are checked to be within 0.1% in both the clamped ion and internal strain tensors, i.e., $\left|e_{ip}^{0} - e_{iq}^{0}\right| \leq 0.001 \, C/m^2$ and $\left|e_{ip}^{int} - e_{iq}^{int}\right| \leq 0.001 \, C/m^2$.

3.A.3 Piezoelectric tensor e_{iq} and Born effective charges Z^* of the inorganic cations in the top candidate MOFs

3.A.3.1 YECPEE

$$\text{Piezoelectric tensor } e_{iq} = \begin{bmatrix} -0.002 & -0.038 & -0.059 & 0. & -0.062 & 0. \\ 0. & 0. & 0. & 0.169 & 0. & 0.011 \\ -1.234 & 0.594 & -0.124 & 0. & -0.727 & 0. \end{bmatrix}$$

$$\text{Born effective charge (BEC) of K, } Z_K^* = \begin{bmatrix} 1.209 & 0.392 & -0.011 \\ 0.119 & 1.754 & -0.014 \\ 0.006 & -0.031 & 1.119 \end{bmatrix}$$

Norm value of the piezoelectric tensor $\left\| e_{iq} \right\|_{max}$ = 1.556 C/m^2

Average Z_K^* = +1.36

3.A.3.2 NAHSQU01

$$\text{Piezoelectric tensor } e_{iq} = \begin{bmatrix} 0.447 & 0.152 & 0.584 & 0. & 0.426 & 0. \\ 0. & 0. & 0. & 0.095 & 0. & 0.032 \\ 0.195 & 0.103 & 0.565 & 0. & 0.607 & 0. \end{bmatrix}$$

$$\text{Born effective charge (BEC) of Na, } Z_{Na}^* = \begin{bmatrix} 1.045 & 0.044 & 0.079 \\ 0.032 & 1.391 & 0.208 \\ 0.025 & 0.080 & 1.173 \end{bmatrix}$$

Norm value of the piezoelectric tensor $\left\| e_{iq} \right\|_{max}$ = 1.198 C/m^2

Average Z_{Na}^* = +1.20

3.A.3.3 AGALUR

$$\text{Piezoelectric tensor } e_{iq} = \begin{bmatrix} 0. & 0. & 0. & 0.150 & 0. & 0. \\ 0. & 0. & 0. & 0. & 0.944 & 0. \\ 0. & -0.000 & 0. & 0. & 0. & -0.004 \end{bmatrix}$$

$$\text{Born effective charge (BEC) of Mg, } Z_{Mg}^* = \begin{bmatrix} 2.036 & 0.053 & -0.035 \\ -0.121 & 2.497 & -0.021 \\ -0.062 & 0.016 & 2.048 \end{bmatrix}$$

Norm value of the piezoelectric tensor $\left\| e_{iq} \right\|_{max}$ = 0.944 C/m^2

Average Z_{Mg}^* = +2.19

3.A.3.4 VAFYOQ

$$\text{Piezoelectric tensor } e_{iq} = \begin{bmatrix} -0.426 & -0.143 & 0.156 & 0. & 0.019 & 0. \\ 0. & 0. & 0. & -0.034 & 0. & -0.343 \\ 0.371 & 0.295 & -1.382 & 0. & -0.216 & 0. \end{bmatrix}$$

$$\text{Born effective charge (BEC) of Mo, } Z_{Mo}^* = \begin{bmatrix} 3.866 & 0.164 & -0.639 \\ 0.031 & 3.708 & 0.270 \\ -0.423 & -0.782 & 8.715 \end{bmatrix}$$

$$\text{Norm value of the piezoelectric tensor } \left\| e_{iq} \right\|_{max} = 1.506 \, \text{C/m}^2$$

$$\text{Average } Z_{Mo}^* = +5.43$$

3.A.3.5 BALFAV01

$$\text{Piezoelectric tensor } e_{iq} = \begin{bmatrix} 0. & 0. & 0. & -0.379 & 0. & 0.274 \\ -0.497 & 1.065 & -0.160 & 0. & 0.116 & 0. \\ 0. & 0. & 0. & 0.113 & 0.0 & -0.058 \end{bmatrix}$$

$$\text{Born effective charge (BEC) of Mo, } Z_{Mo}^* = \begin{bmatrix} 9.958 & 0.439 & -1.540 \\ 0.084 & 6.157 & 0.488 \\ -1.663 & 0.284 & 4.799 \end{bmatrix}$$

$$\text{Norm value of the piezoelectric tensor } \left\| e_{iq} \right\|_{max} = 1.191 \, \text{C/m}^2$$

$$\text{Average } Z_{Mo}^* = +6.97$$

3.A.3.6 EHOHOY

$$\text{Piezoelectric tensor } e_{iq} = \begin{bmatrix} -1.076 & -0.258 & -0.073 & 0. & -0.227 & 0. \\ 0. & 0. & 0. & 0.294 & 0. & 0.121 \\ -0.173 & 0.225 & 0.316 & 0. & -0.548 & 0. \end{bmatrix}$$

$$\text{Born effective charge (BEC) of Sb, } Z_{Sb}^* = \begin{bmatrix} 4.024 & 0.184 & 0.628 \\ 0.127 & 3.313 & 0.400 \\ 0.533 & 0.443 & 4.448 \end{bmatrix}$$

$$\text{Born effective charge (BEC) of P, } Z_{P}^* = \begin{bmatrix} 3.731 & 0.205 & 0.332 \\ -0.768 & 3.896 & 0.064 \\ -0.102 & -0.902 & 3.188 \end{bmatrix}$$

$$\text{Norm value of the piezoelectric tensor } \left\| e_{iq} \right\|_{max} = 1.159 \, \text{C/m}^2$$

$$\text{Average } Z_{Sb}^* = +3.93$$

$$\text{Average } Z_{P}^* = +3.60$$

3.A.3.7 GAXQAZ

$$\text{Piezoelectric tensor } e_{iq} = \begin{bmatrix} 0.527 & -0.087 & 0.415 & 0. & 0.403 & 0. \\ 0. & 0. & 0. & 0.037 & 0. & 0. \\ -0.518 & 0.0651 & -0.371 & 0. & -0.405 & 0. \end{bmatrix}$$

$$\text{Born effective charge (BEC) of Zn, } Z_{Zn}^* = \begin{bmatrix} 2.242 & 0.065 & 0.153 \\ 0.035 & 1.920 & 0.090 \\ 0.199 & 0.133 & 2.237 \end{bmatrix}$$

$$\text{Norm value of the piezoelectric tensor } \left\| e_{iq} \right\|_{max} = 1.092 \, \text{C/m}^2$$

$$\text{Average } Z_{Zn}^* = +2.13$$

3.A.3.8 UVAROZ

$$\text{Piezoelectric tensor } e_{iq} = \begin{bmatrix} -0.505 & -0.361 & -0.724 & 0. & -0.056 & 0. \\ 0. & 0. & 0. & -0.013 & -0. & 0.041 \\ -0.288 & -0.139 & -0.353 & -0. & 0.017 & -0. \end{bmatrix}$$

$$\text{Born effective charge (BEC) of Zn, } Z_{Zn}^* = \begin{bmatrix} 3.372 & 0.063 & -0.051 \\ -0.028 & 2.011 & -0.002 \\ -0.510 & -0.125 & 2.730 \end{bmatrix}$$

$$\text{Norm value of the piezoelectric tensor } \left\| e_{iq} \right\|_{max} = 1.066 \, \text{C/m}^2$$

$$\text{Average } Z_{Zn}^* = +2.71$$

3.A.4 W-MOF with a low e value

Mo-MOFs described in section 3.4.4.2 have high BEC values for the inorganic cation Mo and high e values. As a counter example, we discuss this W-MOF OPITOY (W_2O_6(trz) (trz=1,2,4-triazole), Figure 3.A.3). This is the only structure in the dataset with a similarly high BEC as Mo-MOFs BALFAV01 and VAFYOQ, yet it's piezoelectric norm $\left\| e_{iq} \right\|_{max}$ is very low around 0.007 C/m^2. This MOF belongs to non-polar, chiral orthorhombic point group '222' where all the non-zero values of e_{iq} involve all three crystal directions (x, y, z-directions). The coordination environment of W^{6+} inorganic cations resembles distored octahedra, in which each W is bonded to four bridging oxygens shared between the octahedra leading to 2-D WO_2 sheets along the x- and y-directions, one terminal oxo-oxygen and one nitrogen atom of the polar 1,2,4-triazole ligand. The terminal oxo-oxygen and N are 170° apart inclined at an angle with respect to the z-direction; the other four O atoms are along the x and y-directions shared between two W atoms.

For the experimentally synthesized structure, along the y-direction the O1-W1-O2-W2-O3 bonds vary in the bond lengths where O1-W1= 1.799 Å, W1-O2= 2.090 Å, O2-W2= 1.692 Å, W2-O3= 1.994 Å forming short1-long1-short2-long2-..... bonds. Along the x-direction, O4-W1-O5 bond lengths O4-W1=2.041 Å and W1-O5=1.828 Å again forming a

long-short-long-short-.... pattern. In this MOF, around each W^{6+} short-long-short-long-... pattern for W-O bond lengths is observed along both the x and y-directions, thus creating an anisotropic coordination environment around each W^{6+} inorganic cation. However, these O-(short)-W-(long)-O dipoles are arranged in an anti-parallel manner. For example along the y-direction, the dipoles of chain 1 indicated in figure 3.A.3 are anti-parallel to that of chain 2 which is also along the y-direction. Similarly along the x-direction, dipoles along O4-W1-O5 is anti-parallel to O4-W2-O5 leading to canceling out of the dipoles. This anti-parallel arrangement is also observed for the N1-W1-O6 and N2-W2-O7 bonds along the z-direction. The Z^* of W is high around +7.48 close to the oxidation state of W of +6, similar to the Z^* of Mo in the above discussed Mo-MOFs. However, in contrast to the high piezoelectric norm values $\|e_{iq}\|_{max}$ of Mo-MOFs, the $\|e_{iq}\|_{max}$ value for OPITOY is very low around 0.007 C/m². Due to the anti-parallel arrangement of the O-(short)-W-(long)-O dipoles in this MOF, the dipoles compensate each other resulting in a low e value for the MOF.
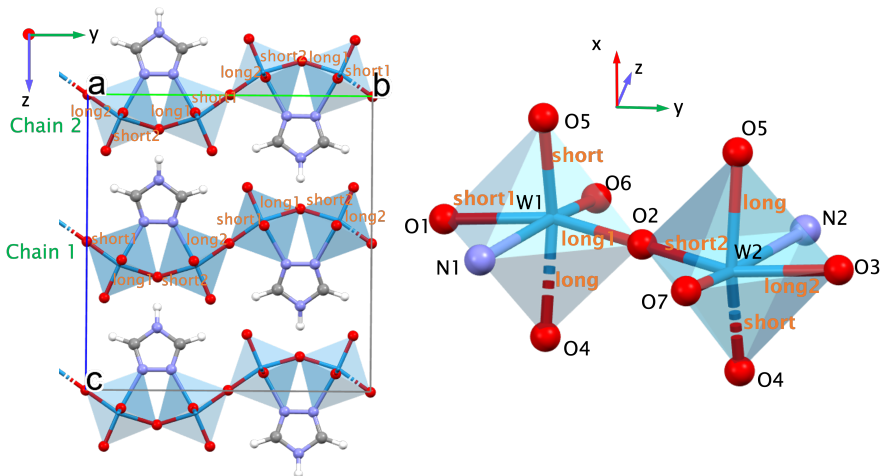
Figure 3.A.3: Structures of OPITOY (showing the yz plane) and the coordination environment of W in OPITOY. sky blue: Tungsten (W), gray: Carbon (C), red: Oxygen (O), white: Hydrogen (H), blue: Nitrogen (N).

$$\text{Piezoelectric tensor } e_{iq} = \begin{bmatrix} -0.002 & 0. & -0.002 & 0. & 0. & 0. \\ 0.002 & 0.004 & 0.003 & -0.002 & 0. & 0. \\ 0.002 & 0.001 & 0. & 0. & 0.001 & 0. \end{bmatrix}$$

$$\text{Born effective charge (BEC) of W, } Z_W^* = \begin{bmatrix} 8.969 & -0.029 & -0.108 \\ -0.396 & 8.786 & -2.306 \\ -0.321 & -0.535 & 4.684 \end{bmatrix}$$

$$\text{Norm value of the piezoelectric tensor } \|e_{iq}\|_{max} = 0.007 \text{ C/m}^2$$

$$\text{Average } Z_W^* = +7.48$$

Bibliography

(1) E. L. Pradeesh, S. Udhayakumar, M. G. Vasundhara and G. K. Kalavathi, "A Review on Piezoelectric Energy Harvesting," *Microsystem Technologies*, 2022, **28**, 1797–1830.

(2) Y. Wu, Y. Ma, H. Zheng and S. Ramakrishna, "Piezoelectric Materials for Flexible and Wearable Electronics: A Review," *Materials & Design*, 2021, **211**, 110164.

(3) N. Sezer and M. Koç, "A Comprehensive Review on the State-of-the-Art of Piezoelectric Energy Harvesting," *Nano Energy*, 2021, **80**, 105567.

(4) Y.-M. You, W.-Q. Liao, D. Zhao, H.-Y. Ye, Y. Zhang, Q. Zhou, X. Niu, J. Wang, P.-F. Li, D.-W. Fu, Z. Wang, S. Gao, K. Yang, J.-M. Liu, J. Li, Y. Yan and R.-G. Xiong, "An Organic-Inorganic Perovskite Ferroelectric with Large Piezoelectric Response," *Science*, 2017, **357**, 306–309.

(5) H. Wang, H. Liu, Z. Zhang, Z. Liu, Z. Lv, T. Li, W. Ju, H. Li, X. Cai and H. Han, "Large Piezoelectric Response in a Family of Metal-Free Perovskite Ferroelectric Compounds from First-Principles Calculations," *npj Computational Materials*, 2019, **5**, 1–9.

(6) H.-P. Lv, W.-Q. Liao, Y.-M. You and R.-G. Xiong, "Inch-Size Molecular Ferroelectric Crystal with a Large Electromechanical Coupling Factor on Par with Barium Titanate," *Journal of the American Chemical Society*, 2022, **144**, 22325–22331.

(7) L. R. Redfern and O. K. Farha, "Mechanical Properties of Metal-Organic Frameworks," *Chemical Science*, 2019, **10**, 10666–10679.

(8) F.-X. Coudert, "Responsive Metal–Organic Frameworks and Framework Materials: Under Pressure, Taking the Heat, in the Spotlight, with Friends," *Chemistry of Materials*, 2015, **27**, 1905–1916.

(9) N. C. Burtch, J. Heinen, T. D. Bennett, D. Dubbeldam and M. D. Allendorf, "Mechanical Properties in Metal-Organic Frameworks: Emerging Opportunities and Challenges for Device Functionality and Technological Applications," *Advanced Materials*, 2018, **30**, 1704124.

(10) M. de Jong, W. Chen, H. Geerlings, M. Asta and K. A. Persson, "A Database to Enable Discovery and Design of Piezoelectric Materials," *Scientific Data*, 2015, **2**, 150053.

(11) M. de Jong, W. Chen, T. Angsten, A. Jain, R. Notestine, A. Gamst, M. Sluiter, C. Krishna Ande, S. van der Zwaag, J. J. Plata, C. Toher, S. Curtarolo, G. Ceder, K. A. Persson and M. Asta, "Charting the Complete Elastic Properties of Inorganic Crystalline Compounds," *Scientific Data*, 2015, **2**, 150009.

(12) "IEEE Standard on Piezoelectricity," *ANSI/IEEE Std 176-1987*, 1988, 0_1–.

(13) G. Sághi-Szabó, R. E. Cohen and H. Krakauer, "First-Principles Study of Piezoelectricity in PbTiO3," *Physical Review Letters*, 1998, **80**, 4321–4324.

(14) A. Dal Corso, M. Posternak, R. Resta and A. Baldereschi, "Ab Initio Study of Piezoelectricity and Spontaneous Polarization in ZnO," *Physical Review B*, 1994, **50**, 10715–10721.

(15) M. Catti, Y. Noel and R. Dovesi, "Full Piezoelectric Tensors of Wurtzite and Zinc Blende ZnO and ZnS by First-Principles Calculations," *Journal of Physics and Chemistry of Solids*, 2003, **64**, 2183–2190.

(16) P. Ghosez, J. Michenaud and X. Gonze, "Dynamical Atomic Charges: The Case of ABO3 Compounds," *Physical Review B - Condensed Matter and Materials Physics*, 1998, **58**, 6224–6240.

(17) A. S. Rosen, S. M. Iyer, D. Ray, Z. Yao, A. Aspuru-Guzik, L. Gagliardi, J. M. Notestein and R. Q. Snurr, "Machine Learning the Quantum-Chemical Properties of Metal–Organic Frameworks for Accelerated Materials Discovery," *Matter*, 2021, **4**, 1578–1597.

(18)   P. Z. Moghadam, A. Li, S. B. Wiggin, A. Tao, A. G. Maloney, P. A. Wood, S. C. Ward and D. Fairen-Jimenez, "Development of a Cambridge Structural Database Subset: A Collection of Metal-Organic Frameworks for Past, Present, and Future," *Chemistry of Materials*, 2017, **29**, 2618–2625.

(19)   S. Baroni, P. Giannozzi and A. Testa, "Green's-Function Approach to Linear Response in Solids," *Physical Review Letters*, 1987, **58**, 1861–1864.

(20)   S. Baroni, S. de Gironcoli, A. Dal Corso and P. Giannozzi, "Phonons and Related Crystal Properties from Density-Functional Perturbation Theory," *Reviews of Modern Physics*, 2001, **73**, 515–562.

(21)   X. Gonze, "Adiabatic Density-Functional Perturbation Theory," *Physical Review A*, 1995, **52**, 1096–1114.

(22)   G. Kresse and J. Furthmüller, "Efficient Iterative Schemes for Ab Initio Total-Energy Calculations Using a Plane-Wave Basis Set," *Physical Review B*, 1996, **54**, 11169–11186.

(23)   G. Kresse and D. Joubert, "From Ultrasoft Pseudopotentials to the Projector Augmented-Wave Method," *Physical Review B*, 1999, **59**, 1758–1775.

(24)   J. P. Perdew, K. Burke and M. Ernzerhof, "Generalized Gradient Approximation Made Simple," *Physical Review Letters*, 1996, **77**, 3865–3868.

(25)   S. Grimme, J. Antony, S. Ehrlich and H. Krieg, "A Consistent and Accurate Ab Initio Parametrization of Density Functional Dispersion Correction (DFT-D) for the 94 Elements H-Pu," *The Journal of Chemical Physics*, 2010, **132**, 154104.

(26)   S. Grimme, S. Ehrlich and L. Goerigk, "Effect of the Damping Function in Dispersion Corrected Density Functional Theory," *Journal of Computational Chemistry*, 2011, **32**, 1456–1465.

(27)   P. E. Blöchl, "Projector Augmented-Wave Method," *Physical Review B*, 1994, **50**, 17953–17979.

(28)   A. Erba, K. E. El-Kelany, M. Ferrero, I. Baraille and M. Rérat, "Piezoelectricity of SrTiO3:An Ab Initio Description," *Physical Review B*, 2013, **88**, 035102.

(29)   K. Choudhary, K. F. Garrity, V. Sharma, A. J. Biacchi, A. R. Hight Walker and F. Tavazza, "High-Throughput Density Functional Perturbation Theory and Machine Learning Predictions of Infrared, Piezoelectric, and Dielectric Responses," *npj Computational Materials*, 2020, **6**, 64.

(30)   Z. Wu and H. Krakauer, "First-Principles Calculations of Piezoelectricity and Polarization Rotation in Pb (Zr 0.5 Ti 0.5) O 3," *Physical Review B*, 2003, **68**, 014112.

(31)   M. Zgonik, P. Bernasconi, M. Duelli, R. Schlesser, P. Günter, M. H. Garrett, D. Rytz, Y. Zhu and X. Wu, "Dielectric, Elastic, Piezoelectric, Electro-Optic, and Elasto-Optic Tensors of BaTiO3 Crystals," *Physical Review B*, 1994, **50**, 5941–5949.

(32)   K. Omote, H. Ohigashi and K. Koga, "Temperature Dependence of Elastic, Dielectric, and Piezoelectric Properties of "single Crystalline" Films of Vinylidene Fluoride Trifluoroethylene Copolymer," *Journal of Applied Physics*, 1997, **81**, 2760–2769.

(33)   H. Bunzen, A. Lamp, M. Grzywa, C. Barkschat and D. Volkmer, "Bistriazole-p-Benzoquinone and Its Alkali Salts: Electrochemical Behaviour in Aqueous Alkaline Solutions," *Dalton Transactions*, 2017, **46**, 12537–12543.

(34)   N. Petrova, B. Shivachev, T. Kolev and R. Petrova, "Sodium Hydrogensquarate Monohydrate," *Acta Crystallographica Section E Structure Reports Online*, 2006, **62**, m1359–m1361.

(35) M. S. Zavakhina, D. G. Samsonenko, D. N. Dybtsev, M. P. Yutkin, A. V. Virovets and V. P. Fedin, "Synthesis and Structure of Chiral Coordination Polymers of CoII, CuII, and MgII Saccharates," *Russian Chemical Bulletin*, 2013, **62**, 716–721.

(36) P. J. Zapf, R. C. Haushalter and J. Zubieta, "Hydrothermal Synthesis and Structural Characterization of a Series of One-Dimensional Organic/Inorganic Hybrid Materials of the [(MoO$_3$)$_n$(2,2'-Bipy)$_m$] Family: [MoO$_3$(2,2'-Bipy)], [Mo$_2$O$_6$(2,2'-Bipy)], and [Mo$_3$O$_9$(2,2'-Bipy)$_2$]," *Chemistry of Materials*, 1997, **9**, 2019–2024.

(37) C.-P. Cui, J.-C. Dai, W.-X. Du, Z.-Y. Fu, S.-M. Hu, L.-M. Wu and X.-T. Wu, "Synthesis, Structure and Fluorescence of a 3-D Polymer {(Mo4O12)(4,4'-Bipy)2}n," *Polyhedron*, 2002, **21**, 175–179.

(38) B. A. Adair, G. Díaz de Delgado, J. Delgado and A. K. Cheetham, "On the Synthesis and Characterization of Open-Framework Antimony(III) Diphosphonates," *Solid State Sciences*, 2000, **2**, 119–126.

(39) Y.-P. Wu, D.-S. Li, J. Zhao, Z.-F. Fang, W.-W. Dong, G.-P. Yang and Y.-Y. Wang, "Isomeric Phenylenediacetates as Modular Tectons for a Series of ZnII/CdII Coordination Polymers Incorporating Flexible Bis(Imidazole) Co-Ligands," *CrystEngComm*, 2012, **14**, 4745.

(40) M. K. Sharma, P. Lama and P. K. Bharadwaj, "Reversible Single-Crystal to Single-Crystal Exchange of Guests in a Seven-Fold Interpenetrated Diamondoid Coordination Polymer," *Crystal Growth & Design*, 2011, **11**, 1411–1416.

(41) J.-C. Tan, Fundamentals of MOF Mechanics & Structure–Mechanical Property Relationships, in *Mechanical Behaviour of Metal – Organic Framework Materials*, ed. J.-C. Tan, The Royal Society of Chemistry, 1st edn., 2023, pp. 1–64.

(42) S. Eslava, L. Zhang, S. Esconjauregui, J. Yang, K. Vanstreels, M. R. Baklanov and E. Saiz, "Metal-Organic Framework ZIF-8 Films As Low-κ Dielectrics in Microelectronics," *Chemistry of Materials*, 2013, **25**, 27–33.

(43) S. Mendiratta, M. Usman, T.-T. Luo, B.-C. Chang, S.-F. Lee, Y.-C. Lin and K.-L. Lu, "Anion-Controlled Dielectric Behavior of Homochiral Tryptophan-Based Metal–Organic Frameworks," *Crystal Growth & Design*, 2014, **14**, 1572–1579.

(44) L.-Z. Chen, J. Zou, Y.-M. Gao, S. Wan and M.-N. Huang, "A 2-D Tetrazole-Based Zn(II) Coordination Polymer: Crystal Structure, Dielectric Constant, and Luminescence," *Journal of Coordination Chemistry*, 2011, **64**, 715–724.

(45) V. T. Rathod, "A Review of Acoustic Impedance Matching Techniques for Piezoelectric Sensors and Transducers," *Sensors*, 2020, **20**, 4051.

(46) H. Schlaberg and J. Duffy, "Piezoelectric Polymer Composite Arrays for Ultrasonic Medical Imaging Applications," *Sensors and Actuators A: Physical*, 1994, **44**, 111–117.

Part II

Rotational Dynamics of linkers in Metal–Organic Frameworks

Chapter 4

Emergence of Coupled Rotor Dynamics in Metal–Organic Frameworks via Tuned Steric Interactions

The organic components in metal–organic frameworks (MOFs) are unique: they are embedded in a crystalline lattice, yet, as they are separated from each other by tunable free space, a large variety of dynamic behavior can emerge. These rotational dynamics of the organic linkers are especially important due to their influence over properties such as gas adsorption and kinetics of guest release. To fully exploit linker rotation, such as in the form of molecular machines, it is necessary to engineer correlated linker dynamics to achieve their cooperative functional motion. Here, we show that for MIL-53, a topology with closely spaced rotors, the phenylene functionalization allows researchers to tune the rotors' steric environment, shifting linker rotation from completely static to rapid motions at frequencies above 100 MHz. For steric interactions that start to inhibit independent rotor motion, we identify for the first time the emergence of coupled rotation modes in linker dynamics. These findings pave the way for function-specific engineering of gear-like cooperative motion in MOFs.

4.1 Introduction

The hybrid nature of metal–organic frameworks (MOFs) goes hand in hand with diverse and often complex behavior. The dynamic traits of these materials are increasingly capturing the curiosity of researchers in the field: MOFs show the potential of displaying intricate dynamics, similar to that observed in other materials built from closely interacting molecules such as crowded movement of proteins in lipid bilayers[1, 2] or concerted molecular motion in liquid crystals.[3] The organic components in MOFs are embedded in a crystalline lattice, yet, in contrast to traditional molecular crystals, they are separated from each other by modifiable free space, providing a handle to tune dynamic behavior in an ordered and stable supramolecular arrangement.[4–7]

A decade ago, Yaghi and Stoddart proposed that "robust dynamics" could be achieved by mechanically interlocking organic components onto the linkers, such that they have the necessary freedom of mobility without compromising the MOF structure.[8] Since then, it has become evident that stable frameworks that display inherent rotational motion are in fact ubiquitous.[9–11] However, not all such frameworks are usable in practice, and the performance of a MOF in specific applications is highly dependent on its dynamic properties, a prime example being adsorption behavior in flexible MOFs.[12–17] Furthermore, MOF-based crystalline molecular machines will require external control of linker motion, making the engineering of correlated dynamics a necessary step to achieve cooperative functional mobility.[5, 6, 18, 19]

Recent achievements in rotor-MOFs include engineering ultrafast rotation by decreasing the rotation energy barrier via molecular design,[20–22] reaching rates as high as those in gas or liquid phases. Additionally, the first example of unidirectional rotation in MOF linkers by the Feringa group [23] represents a crucial step toward attaining nanomotors embedded in a crystalline lattice that can produce useful work.[24] A recent study on rotor-MOFs presented evidence of steric interactions between rotating phenylene units within a single linker.[25] Yet, the understanding, let alone the engineering, of correlated dynamics based on steric interactions between linkers remains extremely limited.

The growing field of rotor-MOFs may benefit from inspiration drawn from the more developed field of crystalline molecular rotors. In many such systems, it has been found that in structures where rotor–rotor distances are small enough, the resulting steric interactions force the rotational dynamics to adopt correlated gear-like mechanisms.[26–29] Here, we present for the first time how correlated motions emerge in linker dynamics as the steric environment of the rotors is gradually modified. We use linker functionalization- in the MIL-53 family of materials to tune both the pore dimensions and the rotor-rotor interactions. The MIL-53 topology proves to be an excellent choice due to its functionalization-dependent pore size configurations, that is, the meta stability of two phases, large pore (lp), and narrow pore (np). Moreover, terephthalate-based organic linkers are very common among MOFs.

4.2 Results and Discussion

To start, we focus on the intramolecular effects of linker functionalization on rotational motion. In terephthalate linkers, the benzene rings can rotate with respect to the carboxyl groups, which are fixed due to their coordination to the metal nodes. As shown in Figure 4.1, the maximum energy corresponds to a conformation where the benzene rings form a

90° angle with both carboxyl groups,[30–32] as the overlap between the p orbitals in the ring and in the carboxyl groups is minimized.
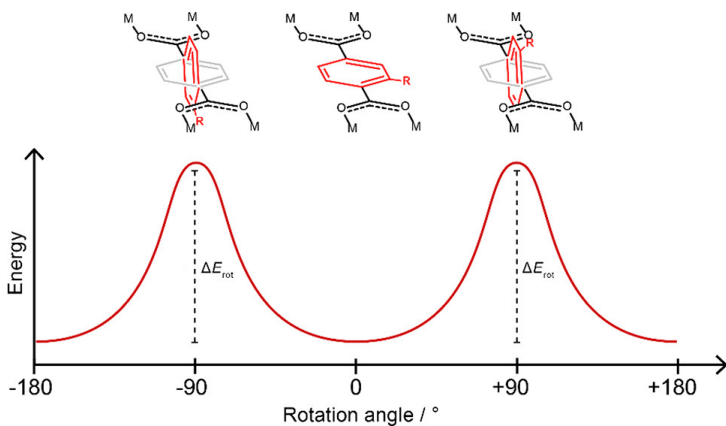

Figure 4.1: Schematic of the Energy Profile of a Terephthalate Rotor Linker

Table 4.1: Calculated Barriers for 180° Rotation on Terephthalic Acid and Its Derivatives. Maximum energy state for each molecule (E_{90}) is obtained from constrained geometry optimizations, setting the dihedral angles between carboxylic groups and ring to 90°. Relative values were obtained with respect to a planar conformation energy; see appendix section 4.B.1 for details.

R	ΔE_{rot}(kJ/mol)
H	47.7
hydroxy	81.8
amino	53.7
methoxy	42.1
cyano	34.5
fluoro	35.9
chloro	25.0
bromo	25.1
nitro	17.1

We modeled with density functional theory (DFT) calculations the intrinsic rotational energy barriers (ΔE_{rot}) of different functionalized terephthalic acids with different functional groups as the relative energy between the transition state and a planar conformer (Table 4.1 and Figure 4.1). With respect to the unsubstituted terephthalic acid, most substituent groups decrease the ΔE_{rot} barrier. In these cases, steric repulsion between the substituent group and the closest carboxyl oxygen likely destabilizes the planar configuration,[28, 33] decreasing the energy difference between the transition state and the ground state. This effect is particularly significant in the nitro-substituted molecule (Figure 4.B.1), where the rotation barrier is the lowest at ΔE_{rot} = 17.1 kJ/mol, that is, less than 7 kT at room temperature.

Only two substituents, the amino and hydroxy groups, cause an increase in ΔE_{rot} with

respect to the unsubstituted molecule. We argue that this is in fact mostly due to stabilization via a hydrogen bond with the adjacent carboxylic acid oxygen (1.93 Å for NH···O and 1.75 Å OH···O, see Figure 4.B.2). Indeed, simply breaking the H-bond by rotating the hydroxy group by 180° results in an energy penalty of 31 kJ/mol. Conversely, the methoxy substituent, which has an electron-donating effect that stabilizes the planar conformation, does not cause a net increase in ΔE_{rot} due to steric effects and lack of H-bond formation.

Experimental work on MIL-53 [34–36] has established that its p-phenylene groups undergo rotation in the form of π-flips, exhibiting similar behavior to several other terephthalate-based MOFs.[32, 37–39] The large-pore (lp) conformation of MIL-53 suggests that the rotating rings should not be subject to significant steric effects. The rotator's closest interactions are between contiguous linkers in the same row (or pore wall): their closest ring-to-ring (−CH···HC−) distance possible is 2.3 Å, which means their van der Waals radii barely overlap. This spacing is limited yet sufficient for unfunctionalized terephthalate rotors to perform full rotations in the form of π-flips, as evidenced experimentally.[35]

This spacing between the linkers in MIL-53 family is still relatively small, in contrast to other MOFs such as IRMOF and UiO-66. This suggests that ring substituents are likely to influence the dynamics of rotors. On the basis of the DFT calculations of the free linkers, we selected two contrasting groups, nitro and amino, to assess the impact of linker functionalization in the complete framework, a "crowded" environment. Moreover, for MIL-53 materials, functionalization has an important impact on the flexible crystalline conformation: guest-free $NO_2 - MIL - 53\,(Al)$ and MIL-53(Al) are usually present in the lp form in a wide temperature range,[40–42] while guest-free $NH_2 - MIL - 53\,(Al)$ remains in the denser narrow-pore (np) form (Figure 4.2).[40, 43, 44] Table 4.2 presents the characteristic distances between rotors in each form of the framework, showing how the difference in pore opening impacts row-to-row distance but not rotor spacing within a row. The row-to-row distance of the np amino-MOF indicates likely inter-row steric effects prohibiting full rotation of rings. For both functionalized frameworks, steric repulsion between neighboring linkers within the same row is expected.

Table 4.2: Unit Cell Geometry Influence on Rotor Spacing

MOF	rotor spacing within row (Å) [2]	pore rhombus angle (deg)	row-to-row distance (Å) [3]
MIL-53(Al) (lp)	6.6	75.0	6.4
$NO_2 - MIL - 53\,(Al)$ (lp)	6.7	79.5	6.8
$NH_2 - MIL - 53\,(Al)$ (np)	6.6	43.8	3.8

[2] Defined as distance between neighboring C–C rotation axes, see the appendix section 4.B.2

[3] For definition, see the appendix section 4.B.2

Each crystallographic unit cell contains four linkers. To explore the energy associated with linker rotation, we forced the rotation steps on one linker starting from the global minimum conformation, followed by partial geometry optimization at each step. The rotational space of a nitroterephthalate linker is defined in Figure 4.3a and b (for aminoterephthalate see Figure 4.B.3. The obtained potential energy curves (or energy profiles as a function of
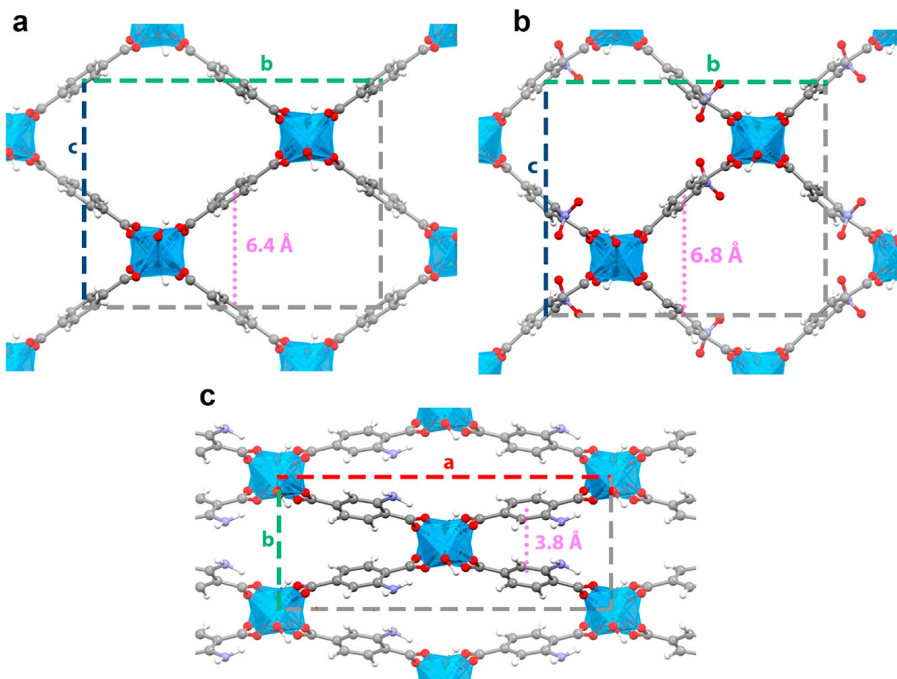
Figure 4.2: Structure of three members of the MIL-53 family viewed along the pore direction. (a) MIL-53(Al) (lp), (b) $NO_2 - MIL - 53$ (Al) (lp), and (c) $NH_2 - MIL - 53$ (Al) (np). This topology is characterized by four distinct rows of linkers per unit cell forming rhombic pores. Closest row distances for each MOF are marked in magenta. For complete unit cell parameters, see Table 4.B.1.

rotation) are shown in Figure 4.3c. The energy profile of $NH_2 - MIL - 53$ shows a very steep increase upon linker rotation, far larger in magnitude than the barrier calculated for the free linker (54 kJ/mol). This is the result of row-to-row steric hindrance in the tightly packed np phase (see Figure 4.B.4, indicating that large amplitude rotations are unlikely to occur in this MOF. For $NO_2 - MIL - 53$ (Al), we find energy minima at ±30° and ±150°, with expected maxima at ±90°, and local maxima at ±0° and ±180° due to steric effects experienced by the linker in the planar conformation (intramolecular, vide supra, and overlap between nitro and a hydrogen atom of the closest adjacent ring). The potential energy maxima of ∼ 40 kJ/mol is in the range of aromatic ring π-flips found in other MOFs,[34, 35, 37, 38, 45] which indicates the feasibility of linker rotation. Nevertheless, these periodic single unit cell calculations force the nitro linkers in a row along [100] to rotate together, as they are periodic images of each other. Such an ordered motion prevents other possible interactions between neighboring linkers in the same row, perhaps most evidently head-to-head interactions between two nitro groups.

To more realistically model these effects in the linker dynamics, 2 × 1 × 1 supercells should be considered. When one linker is rotated in this scenario, the neighbor linker on the same row is not constrained and can move independently. The interaction of a pair
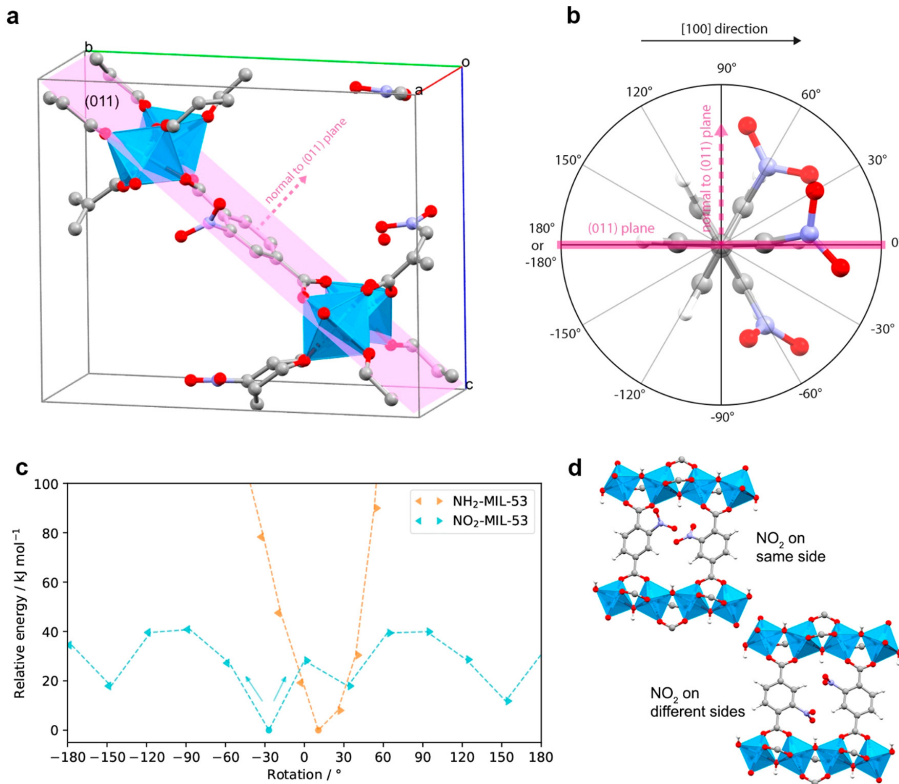
Figure 4.3: Effect of linker rotation on the potential energy as studied by DFT. (a) Unit cell of $NO_2 – MIL – 53\,(Al)$ with central linker in 0° rotation with respect to (011) plane (pink); hydrogens omitted for clarity. (b) Rotation angle is defined as the angle between benzene ring plane and (011) plane, taking 0° as the conformation with the functional group pointing in the positive [100] direction. The sign of the angle is assigned based on the direction normal of the reference plane. (c) Potential energy profiles for the rotation of one linker in a $NH_2 – MIL – 53\,(Al)$ and $NO_2 – MIL – 53\,(Al)$ unit cell. The direction of rotation is indicated by the direction of the marker. (d) Example of an unfavorable head-to-head nitro group encounters in adjacent linkers when they are located on the same side of the ring (top) and on different sides (bottom).

of neighboring linkers in such a supercell will depend on the position of the two nitro groups on their respective benzene rings. Single-crystal XRD analysis shows that there is no preferential configuration set during the formation of the crystal (see Figure 4.B.5). Therefore, a rotating linker's nitro group may encounter its neighbor's nitro group in one of the two configurations shown in Figure 4.3d. Illustrative cases are discussed in the appendix (Figures 4.B.6 and 4.B.7). The configuration where neighbor linkers have nitro groups located on identical carbon positions has the most impactful steric effects between two rotors due to their closer distance. We find that head-to-head NO_2 interactions lead to a steep energy increase, and that the rotational event can only become energetically feasible when

the neighboring linker moves out of the way in a cooperative fashion (Figure 4.B.9). For cases where nitro groups are not on equivalent positions, the extent to which the neighboring linker needs to rotate out of the way to make rotational motion of the linker energetically feasible is significantly lower (Figure 4.B.10). Hence, as no preference with respect to the two situations in Figure 4.3d occurs during synthesis, varying degrees of rotational mobility are expected.

Broadband dielectric spectroscopy (BDS) has proven particularly useful for probing the motion of MOF linkers containing polar functional groups.[46–48] The imaginary part (ε'') of the complex dielectric permittivity ($\varepsilon^* = \varepsilon' - i\varepsilon''$) contains information about the dynamic relaxation processes of dipolar moieties in the dielectric material.[49, 50] The temperature and frequency dependencies of ε'' for MIL–53 (Al), NH_2–MIL–53 (Al), and NO_2–MIL–53 (Al) are presented in Figures 4.4 and 4.B.11. Peaks in ε'' correspond to dielectric losses due to dipolar motion, with the frequency of the maximum of ε'' corresponding to the mean relaxation time of the dipolar motion at that temperature.
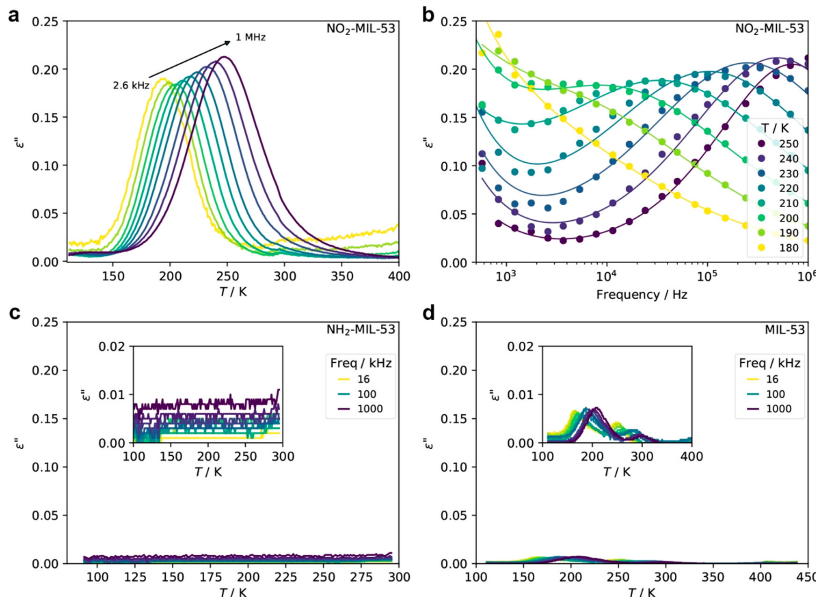
Figure 4.4: Dielectric spectra of the three systems. (a, b) Imaginary part (ε'') of ε^* for NO_2–MIL–53 (Al) with respect to temperature (a) and frequency (b). The latter includes the fitted Cole–Cole model as continuous lines. (c, d) Temperature dependence of ε'' for NH_2–MIL–53 (Al) (c) and MIL–53 (Al) (d).

NO_2–MIL–53 (Al) shows a strong relaxation process with peaks dispersed in terms of both frequency and temperature (Figure 4.4a,b), a feature typical of dipolar linker relaxations in MOFs.[47, 48, 51] In contrast, NH_2–MIL–53 (Al) shows no relaxation process (Figure 4.4c), confirming a strongly hindered environment of the rotors, in correspondence with our DFT results. MIL–53 (Al) (Figure 4.4d) exhibits a very weak dielectric relaxation, even though the mobile p-phenylene units do not have a permanent dipole. This may be due to small deformations of the linkers that lead to spontaneous dipole moments or the presence

of polar impurities.[50] We note here that although some MOFs are known to have large proportions of missing linker defects, MIL – 53 (Al) frameworks are not typically in that category. Thermogravimetric analysis indeed suggests that the linker-to-metal ratio is close to the theoretical value (see appendix sections 4.A.2.1 and 4.A.2.2). As expected, the dispersion frequency of the nitro linker relaxation increases with temperature, more specifically, from 2.6 kHz at 180 K to 1 MHz at 250 K. The frequency dependence of ε^* at different temperatures was fitted using the Cole–Cole equation (Figure 4.4b and Figure 4.B.11). The best fits indicate a gradual increase of the dispersion broadness parameter (α) as temperature is decreased from 0.3 at 250 K to 0.55 at 180 K (Figure 4.B.13). The broadening of the relaxation suggests a larger fraction of interacting dipoles exists when less thermal energy is available. It should be noted, however, that BDS will not detect linkers whose dynamics fall outside the probed frequency range, in particular static linkers, meaning that potential rotation-impeding interactions such as the one illustrated in the DFT curve may not be covered in the dielectric spectra. Fitting the temperature dependence of the mean relaxation times to the Arrhenius equation delivers an activation energy E_a of 32.3 ± 1.3kJ/mol and a pre-exponential factor τ_0 of 3.4×10^{-14} s (Figure 4.B.14). This activation energy is in between the DFT-estimated barriers for a single unit cell of this framework, that is, the smaller barrier at 0° and the larger barrier at ~90°. The obtained τ_0 value, equivalent to 2.9×10^{13} Hz, is larger than the expected attempt frequency based on estimations for p-phenylene rotators (usually on the order of 10^{12} Hz; for an overview of activation energies and pre-exponential factors in MOFs, see ref [9]).[28] This type of result is not uncommon for functionalized p-phenylene rotors,[33, 48, 52] and it may be interpreted as an indication of a small linear dependence of the rotational barrier with temperature (see appendix section 4.B.6 for further discussion).[53] In $NO_2 – MIL – 53$ (Al), this could hint toward the progressive effect that thermal energy has on the rotor's environment due to increased conformational motions and nitro group rotations.[54]

To obtain specific information about the angular and frequency ranges of the nitro-functionalized linker dynamics, we performed variable-temperature solid-state deuterium NMR (^{2}H SSNMR) spectroscopy. Spatial information about the deuteron exchange sites can be extracted from the NMR spectra by using relatively simple geometric models.[55, 56] In addition, this technique is sensitive to all deuterium-labeled rings, and not only to the mobile ones. This enables us to obtain experimental information to complement the BDS data, especially for the nitro-functionalized framework, for which dynamics above 250 K could not be probed due to the high frequency limit. The results for ring-labeled MIL – 53 (Al) – d_4 (Figure 4.B.15) and $NH_2 – MIL – 53$ (Al) – d_3 (Figure 4.B.16) are in line with literature [35, 36, 57] as well as our expectations based on the DFT and BDS analyses. The ^{2}H SSNMR data for MIL – 53 (Al) – d_4 indicate that the phenylene rings undergo an increased rate of 180° reorientations ("π-flips") at increased temperatures in the intermediate motion regime (IMR, 1 kHz < k < 100 MHz, where k is the rate constant for the exchange between deuterium sites). For $NH_2 – MIL – 53$ (Al) – d_3, only static phenylene ring signals are observed in the slow motion limit (SML, k< 1 kHz), evidenced by the Pake doublet (Figure 4.B.16), in agreement with the high rotational barrier that prevents rotational dynamics at these temperatures.

The variable-temperature ^{2}H SSNMR spectra for $NO_2 – MIL – 53$ (Al) – d_3 are remarkably different from the aforementioned situations (Figure 4.5a). At the lowest temperature, the ^{2}H spectrum indicates a stationary phenylene ring in the SML, whereas the spectra

acquired at 409 K and higher indicate dynamics only in the fast motion limit (FML, k > 100 MHz). The spectra in the range of 254 K to 387 K display a superposition of the SML and FML powder patterns, with progressive increase in integrated intensity of the FML pattern with respect to the SML pattern with increasing temperature. No pattern corresponding to the IMR was detected in the entire temperature range, differing from earlier ^{2}H SSNMR studies on MOFs with p-phenylene rotators;[34, 37, 38] this is likely due to diminished intensity of IMR spectra when the rates of motion are on the order of the ^{2}H pattern breadths.[56, 58–60] Furthermore, the fact that contributions from both SML and FML patterns are observed across the entire temperature range indicates the presence of a distribution of correlation times for the dynamics, which further obscures signals arising from IMR motions.[39, 55, 61] Such broad distributions of rotation rates are rarely found in terephthalate MOFs,[9, 33, 35, 37–39] though they are more often observed for p-phenylene moieties in polymeric systems,[62–64] where structural heterogeneity among the rotors is often cited as the cause of a wide variety of rotation barriers, and consequently, rotation rates. This observation is further supported by the BDS results: there is a very broad distribution of detected frequencies for each temperature in the BDS spectra for $NO_2 – MIL – 53$ (Al) (Figure 4.4b). As suggested by the DFT calculations, these broad distributions of rotational rates are a consequence of the varied degree of interlinker steric interactions, which are unique to the nitro-functionalized MOF among the three frameworks.
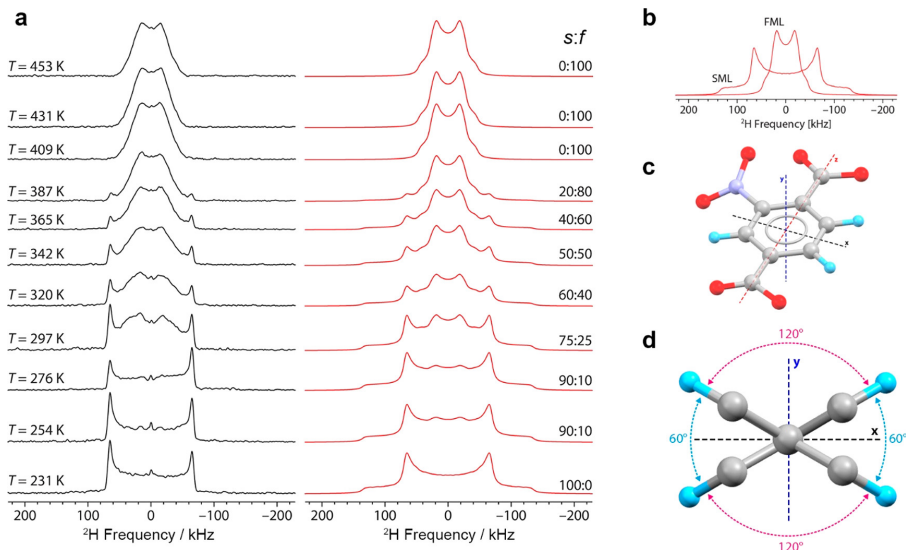
Figure 4.5: Solid-state ^{2}H NMR studies of $NO_2 – MIL – 53$ (Al) – d$_3$. (a) Experimental (black) and simulated (red) variable-temperature ^{2}H SSNMR spectra of $NO_2 – MIL – 53$ (Al) – d$_3$. (b) Spectra are composed of overlapping patterns representing SML (<10^3 Hz) and FML (>10^7-10^8 Hz) motions, with relative integrated intensities indicated to the right of the simulated spectra. (c) Cartesian frame of reference for the rotation model. (d) Representation of ^{2}H exchange sites and angles used in the model; deuterons are shown in light blue.

Although ^{2}H NMR signals corresponding to motions in the IMR are not observed due to their low intensities and broad frequency distributions, it is possible to model motions in the FML and obtain simulations that agree well with experimental data.[65] Single rotational angle models (e.g., 60°, 120°, or 180°) do not adequately fit the line shape (Figure 4.B.17a), suggesting a more complex mechanism. A four-site model based on energy minima separated by two distinct jumps of 60° and 120° (as predicted by DFT calculations, Figure 4.5c,d) was successful. The simulated ^{2}H FML shape was found to be sensitive to small deviations in these angles (Figure 4.B.17b). The complete simulated spectra are shown in Figure 4.5a. For the overlapped spectra at 254-387K, the appropriate ratios of weighted integrated signal intensities for static and mobile components were selected (i.e., s:f, corresponding to the SML and FML patterns, Figure 4.5b) and are included in Figure 4.5a. It should be noted that similar four-site rotations have been observed in p-phenylene rotators within branched linkers that cause intralinker steric interactions.[25, 66]

To summarize the $NO_2 - MIL - 53$ (Al) experimental results, our BDS and ^{2}H SSNMR experiments detect dynamics corresponding to complementary portions of the frequency spectrum. BDS only includes the mobile fraction of linkers up to 1 MHz, which is the mean frequency of motion at ~250 K. ^{2}H SSNMR detects all linkers undergoing slow dynamics below 1 kHz as well as all with fast dynamics above ~ 100 MHz, which go largely unobserved in BDS due to its lower and upper frequency limits. Effectively, the only overlap between the two spectroscopic analyses (i.e., where both methods detect signals) is at 230-250K. At 250 K, the ^{2}H SSNMR model indicates that a large majority of the linkers are static, which means the BDS peak at 1 MHz omits information on a significant population of linkers. For this reason, the estimated activation energy should be taken as valid only for this fraction of rotors. In the high-temperature region of the ^{2}H SSNMR spectra, we observe no signal from the SML, and that all rotational motion likely exists within the FML. Both sets of data provide clear evidence that the rotational motions in $NO_2 - MIL - 53$ (Al) are spread along a very broad frequency range, which is a rare phenomenon that we can attribute to the addition of the bulky nitro substituent.

To understand the observed frequency broadening and the effect of temperature on how neighboring linkers influence rotational motion in $NO_2 - MIL - 53$ (Al), we performed ab initio molecular dynamics (MD) simulations at 300, 450, 700, and 1200 K. To probe the emergence of coupled dynamics, we focused on the situation where $- NO_2$ groups are positioned on equivalent C atoms (NO_2 same side in Figure 4.3d), the situation with highest steric hindrance. The higher temperatures are not directly relevant to the physical situation ($NO_2 - MIL - 53$ (Al) combusts at ~700 K), yet they allow for more rotation events to be observed during shorter simulation times.[67, 68] In periodic MD simulations involving a single unit cell (Figure 4.B.18), clear preferential conformations are observed, consistent with the potential energy minima observed in zero-Kelvin calculations. At lower temperatures (e.g., 300 K), the linkers undergo discrete 60° rotations between 30° and −30°, whose frequency increases with temperature. At higher temperatures, we also see the occurrence of 120° jumps between ±30° and ±150°. Both motions are consistent with the ^{2}H SSNMR data and the DFT predicted energy barriers.

A similar trend in angular mobility ranges is observed for 2 × 1 × 1 supercell simulations. At 300 K, only small angle librations ~20° are observed (Figure 4.B.19). In the mid temperature range (450-700 K), two sets of rotational jumps appear, in addition to librations (Figures 4.B.20 and 4.B.21). At the highest temperature simulated (1200 K), the linkers'

motion becomes so fast and extensive that even rotation beyond 180° occurs (Figure 4.B.22).

Interestingly, barring the 1200 K simulations, the time traces of rotation angles feature repeated occurrences of apparent correlated fluctuations in both librations and jumps of adjacent linker pairs. This is less evident in the 300 K simulations, where rings did not undergo any large-angle jumps. To analyze the relation between this apparent correlated motion and the steric effect of linkers within a row, we compare the distance between nitro groups of each pair of neighboring linkers (defined as the distance between the two nitrogen atoms, see appendix section 4.B.9) with the angle traces at 450 and 700 K. Figure 4.6a shows representative linker dynamics. The rotational angle traces for all linker pairs at 450 and 700 K can be found in Figures 4.B.24 to 4.B.27 It can be observed that the phenylene rings at these temperatures perform mirrored small angle fluctuations (~50°) when the distance between their nitro groups is small (Figure 4.6b). In the portions of the simulations where the nitro distances are large enough as to not cause steric effects, the mirrored correlated motion is not present, and faster, shorter fluctuations are observed.
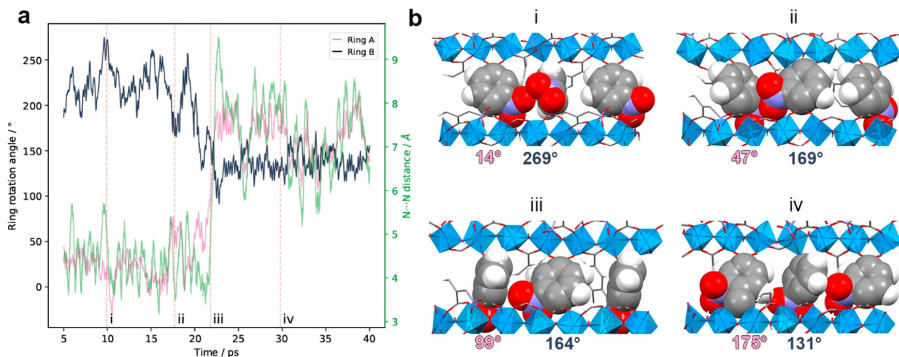
Figure 4.6: Cooperative rotation in $NO_2 – MIL – 53\,(Al)$. (a) Rotation angle traces of two neighboring rings in a $2 \times 1 \times 1$ cell MD simulation at 700 K. Correlated motion is observed, with simultaneous angle changes in opposite directions (i, ii, iii), when nitro groups are in proximity (N···N distance ca. 4 Å). (b) Selected snapshots (i-iv) of linker pair conformation during a coupled rotation. As ring A rotates in the positive direction, ring B reaches the space originally occupied by ring A.

Although large-angle jumps are relatively rare in the supercell simulations, Figures 4.6, 4.B.25, and 4.B.27 show at 700 K examples of correlated large-angle motions that occur when nitro groups are in proximity. A closer analysis of the molecular conformations during a simulation provides a clear example of these coupled dynamics, presented in Figure 4.6. The snapshot sequence presented in Figure 4.6b illustrates how the limited space of the rotors requires cooperative motion to allow the change in angles from i to iv. In this case, ring A could be seen as rotating cooperatively in the positive direction (most noticeable in snapshots ii to iii) allowing ring B to rotate in the negative direction (i-iv), resulting in the pair performing a gear-like rotation. This correlated motion is facilitated by the neighbors' close arrangement, which implies that to achieve certain conformations, cooperative rotation between neighbors is required.

Because of the high computational cost of these calculations, we were not able to reach

long simulation times, which prevented the reliable determination of the free energy profile and further numerical analysis. To overcome these limitations, free energy techniques such as metadynamics simulations or Blue Moon sampling could be adequate options for future work. Nevertheless, the MD simulation data provide qualitative insight into the effect of interlinker interactions. We propose that this type of complex dynamics is in fact what causes $NO_2 - MIL - 53\,(Al)$ to display the intriguing behavior determined by BDS and ^2H SSNMR analysis. The vast array of possible dynamics observed in this MOF, evidenced by the coexistence of both static and rapidly rotating rings at most temperatures, is a result of functionalizing the phenylene rotators with a substituent that (i) drastically decreases the intrinsic rotation barrier and (ii) facilitates intrarow steric interactions. The computational results support the hypothesis that intrarow steric effects lead to coupled motion for fraction of the neighboring linkers, while the static rings are the inevitable result of energetically disfavored non-cooperative rotation.

4.3 Conclusions

To conclude, the MIL-53 topology, where the distance between the rotational axes of phenylene rings along the pore direction is only ~6.6 Å, has proven to be an excellent scaffold in which to tune rotational mobility in different dynamic regimes. By selecting two different ring substituents, nitro and amino, distinct pore geometries, and rotor–rotor interactions were achieved. At the two extremes, there are (i) unfunctionalized phenylene units that can rotate independently, with specific temperature-dependent rates, and (ii) amino-functionalized phenylene units that cannot rotate at all, due to intralinker hydrogen bonding and increased steric hindrance from the narrow-pore configuration. Between these extremes, for nitrophenylene linkers, we observe complex rotational dynamics that evolve with temperature, spanning a broad frequency range. Among these, we identify for the first time the emergence of coupled rotational dynamics between neighboring linkers in MOFs. In fact, such coupled dynamics should be expected in other framework systems, provided that the appropriate degree of rotational mobility and interlinker steric interactions are encountered. This discovery paves the way to engineering gear-like functional motion in MOFs if linker dynamics can also be controlled externally, for example, by electric fields.

Appendix to chapter 4

4.A.1 Computational methods

4.A.1.1 Density functional theory calculations

All density function theory (DFT) calculations were performed using the ab initio CRYS-TAL17[69] code, at the generalized gradient approximation (GGA) level of theory with the PBE exchange–correlation functional[70]. Grimme D3 dispersion corrections were used.[71, 72] Peintinger–Oliveira–Bredow (POB) triple-ζ valence plus polarization basis sets[73] were used for all atoms.

For molecular systems, full geometry optimizations were performed to obtain the global energy minimum E_{min}. The rotary transition state energy (E_{90}) was obtained from constrained geometry optimizations, setting the dihedral angles between carboxylic groups and ring (O-Ccarboxylic-Cring-Cring) to 90°. In the case of non-planar ground state conformations, a forced coplanar carboxyl reference energy (E_{anchor}) was calculated starting from a planar molecule, performed a geometry optimization while applying constraints to the four oxygens to remain coplanar. The reported E_{rot} barriers are relative to E_{min} or E_{anchor} (if applicable).

For periodic MOF systems, experimentally determined unit cell parameters of the guest-free frameworks were used for $NH_2 - MIL - 53\,(Al)$ and $NO_2 - MIL - 53\,(Al)$ (Table 4.B.1).[74] The cell parameters were kept constant in all calculations. Global minimum structures of both MOFs were obtained by geometry optimization of the atomic positions without any symmetry constraints ($P1$ space group). Starting from the minimized structure, one linker in the unit cell was rotated in steps of 15° (for amino) and 30° (for nitro) in either direction (as defined in the main chapter) using the CrystalMaker software. At each step, the rotating ring was fixed within the unit cell by freezing the four off-axis carbons. A geometry optimization was then performed, relaxing all other atomic positions. Each successive rotation step was started from the geometry of the previous step. The relative energy for each step is reported with respect to the global minimum energy.

4.A.1.2 Ab initio molecular dynamics simulations

The dynamics of linkers of $NO_2 - MIL - 53\,(Al)$ was simulated at different temperatures by DFT-based molecular dynamics (MD) using the Quickstep module[75] of the CP2K code package. The geometry- optimized DFT structure with lattice parameters from Ref. [40] was used as starting structure for all MD simulations. Simulations were performed in the (N, V, T) ensemble with fixed size and shape of the unit cell. A timestep of 0.5 fs was used in the MD runs and temperature was controlled by a canonical sampling through velocity rescaling (CSVR) thermostat.[76] MD simulations had an equilibration period of 5 ps and a production period of 35 ps for all temperatures (300 K, 450 K, 700 K and 1200 K). Valence and core electrons were represented by double-ζ polarized basis sets and Goedecker–Teter–Hutter (GTH)[77] pseudopotentials for all atoms (C, H, O, N, Al). The exchange correlation energy was evaluated in Perdew– Burke–Ernzerhof (PBE)[70] approximation and dispersion interactions were treated at DFT-D3[72] level. Plane wave cutoff energy was set to 900 Ry based on the energy convergence to 10^{-4} Ha and relative cutoff energy was set to 60 Ry. Representative structures and input files for calculations are

available online at https://github.com/fxcoudert/citable-data.

4.A.2 Experimental Section

4.A.2.1 MOF synthesis

MIL-53(Al) $AlCl_3$ 6 H_2O (1.97 g, 8.2 mmol) was added to 30 mL demineralized water inside a 45 mL Teflon liner. The solution was homogenized by stirring. Terephthalic acid (1.36 g, 8.2 mmol) was added to the solution, and the mixture was stirred again (terephthalic acid does not completely dissolve in these conditions). The liner was sealed inside a steel autoclave and placed in an oven at 220 °C for 72 h.

To remove unreacted terephthalic acid from the pores, solvent exchange with DMF was performed at 120 °C overnight, followed by exchange with MeOH at 80 °C for five hours. The residual solvent is removed by heating in an oven at 120 °C for three hours. MOF characterization is shown in Figures 4.A.1,4.A.2,4.A.3.

NO2-MIL-53(Al) $Al(NO_3)_3$ 9 H_2O (1.49 g, 3.97 mmol) was dissolved in 50 mL demineralized water inside a 125 mL Teflon liner. 2-Nitroterephthalic acid (0.92 g, 4.36 mmol) was added to the solution. The liner was sealed inside a steel autoclave and placed in an oven at 170 °C for 12 h.

After cooling to room temperature, the white product was collected by filtration and placed in 60 mL MeOH to 80 °C for 20 h. This solvent exchange was performed twice. The product was then dried in an oven at 100 °C for 3 h. MOF characterization is shown in Figures 4.A.1,4.A.2,4.A.3. From the TGA, the linker-to-Al ratio is 0.95, suggesting the material is free from significant missing linker or metal defects.

To obtain large single crystals of $NO_2 - MIL - 53\,(Al)$, a previously published crystal growth modulation method was used.[78] $AlCl_3$ 6 H_2O (966 mg, 4 mmol) and oxalic acid dihydrate (252 mg, 2 mmol) were added to 30 mL demineralized H_2O inside a 45 mL Teflon liner and stirred. 2-Nitroterephthalic acid (845 mg, 4 mmol) was added and the solution was stirred again. The liner was sealed inside a steel autoclave and placed in an oven at temperature for 72 h. After cooling and filtering the product, the crystals were washed with DMF and ethanol several times at room temperature.

$NH_2 - MIL - 53\,(Al)$ $Al(NO_3)_3$ 6 H_2O (2.9 g, 12 mmol) was dissolved in 30 mL demineralized water inside a 45 mL Teflon liner. 2-Aminoterephthalic acid (2.2 g, 12.1 mmol) was added to the solution. The liner was sealed inside a steel autoclave and placed in an oven at 150 °C for 10 h. After cooling, the yellow solids were filtered and washed with DMF (30 mL), and then transferred to the autoclave together with 20 mL DMF, and kept at 130 °C for 16 h. The DMF was subsequently exchanged by methanol at 80 °C for 5 h. After filtration the residual solvent is removed by heating the sample in the vacuum oven at 150 °C overnight. MOF characterization is shown in Figures 4.A.1,4.A.2,4.A.3.

4.A.2.2 Deuterium-labeled MOF synthesis

$MIL - 53\,(Al) - d_4$ $Al(NO_3)_3$ 9 H_2O (0.44 g, 1.17 mmol) was added to 20 mL demineralized water inside a 45 mL Teflon liner. The solution was homogenized by stirring.) Terephthalic acid-d4 (0.349 g, 2.05 mmol, 98%, Eurisotop) was added to the solution, and the
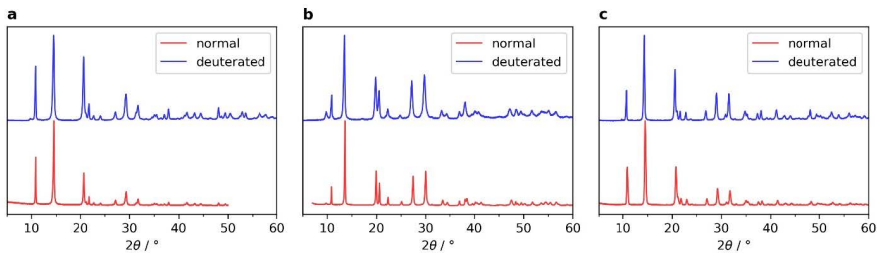
**Figure 4.A.1:** Powder X-ray diffractograms of normal and deuterated MIL – 53 (Al) (a), NO_2 – MIL – 53 (Al) (b), NH_2 – MIL – 53 (Al) (c).
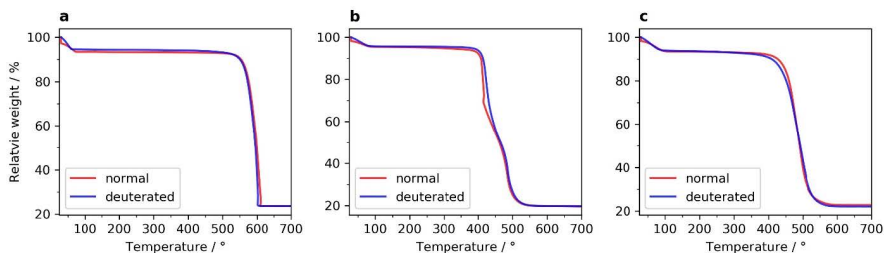
Figure 4.A.2: Thermogravimetric traces of normal and deuterated MIL – 53 (Al) (a), NO_2 – MIL – 53 (Al) (b), NH_2 – MIL – 53 (Al) (c).
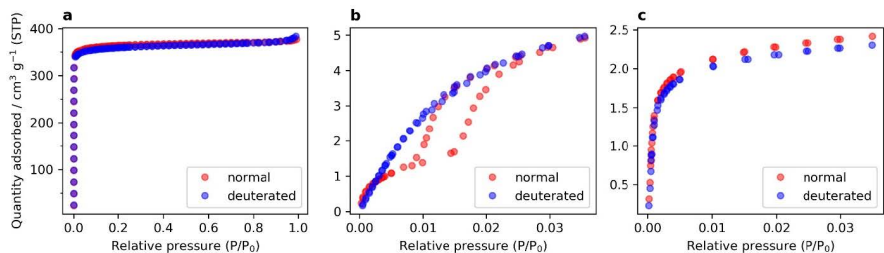
Figure 4.A.3: N2 sorption isotherms of normal and deuterated MIL – 53 (Al); b,c, CO2 sorption isotherms of NO_2 – MIL – 53 (Al) (b) and NH_2 – MIL – 53 (Al) (c).

mixture was stirred again. The liner was sealed inside a steel autoclave and placed in an oven at 220 °C for 72 h.

To remove unreacted terephthalic acid from the pores, we performed solvent exchange with DMF at 120 °C for 16 h, followed by exchange with methanol at 80 °C for 13 hours. The residual solvent is removed by heating in an oven at 120 °C for three hours. The product was finally activated in a vacuum oven at 100 °C for 4 h. Final yield 0.187 g (0.88 mmol, 75%). MOF characterization is shown in Figures 4.A.1,4.A.2,4.A.3.

NO$_2$ – MIL – 53 (Al) – d$_3$ Nitration of dimethyl terephthalate-d$_4$ (1.258 g, 6.35 mmol; ABCR, 95%) in 3.1 mL conc. H$_2$SO$_4$. The mixture was stirred until completely dissolved, cooled to 0 °C in an ice bath, and a mixture of 0.87 mL conc. HNO$_3$ and 0.62 mL conc. H$_2$SO$_4$ was added dropwise while stirring. The reaction was then allowed to reach room temperature gradually. After 2.5 h, the solution was poured into 200 mL ice-water mixture and filtered over a Nylon membrane (0.45 µm). Yield: quantitative.

Dimethyl nitroterephthalate-d$_3$ (1.53 g, 6.3 mmol) was dissolved by stirring in 24 mL methanol. NaOH solution (6.6 mL of 2 mol/dm^3, 528 mg, 13 mmol NaOH) was added, producing an intense yellow color and some precipitation. The mixture was heated to 60 °C for 16 h. An additional 6.6 mL of NaOH 2 mol/dm^3 solution was added to the mixture and the reaction was continued for five more hours. Heating was stopped and the solvent was removed by vacuum evaporation. The solids were dissolved in 3 mL water, neutralized with conc. HCl, and cooled. The precipitated 2-nitroterephthalic acid-d$_3$ was collected by vacuum filtration, washed with ice water, and dried in a vacuum oven at 90 °C for one hour. Yield: 0.933 g (4.36 mmol; overall 69%). The ^{1}H and ^{13}C NMR spectra of 2-nitroterephthalic acid-d$_3$ are shown in Figures 4.A.4 and 4.A.5.

Al(NO$_3$)$_3$ 9 H$_2$O (0.896 g, 2.4 mmol) was dissolved in 30 mL demineralized water inside a 45 mL Teflon liner. 2-Nitroterephthalic acid-d$_3$ (0.91 g, 4.2 mmol) was added to the solution. The liner was sealed inside a steel autoclave and placed in an oven at 170 °C for 12 h. After cooling to room temperature, the white product was collected by filtration and placed in 60 mL MeOH to 80 °C for 20 h. This solvent exchange was performed twice. The product was then dried in an oven at 100 °C for 5 h. Yield: 254 mg (1 mmol; 24%). MOF characterization is shown in Figures 4.A.1,4.A.2,4.A.3. From the TGA, the linker-to-Al ratio is 0.96, suggesting the material is free from significant missing linker or metal defects.
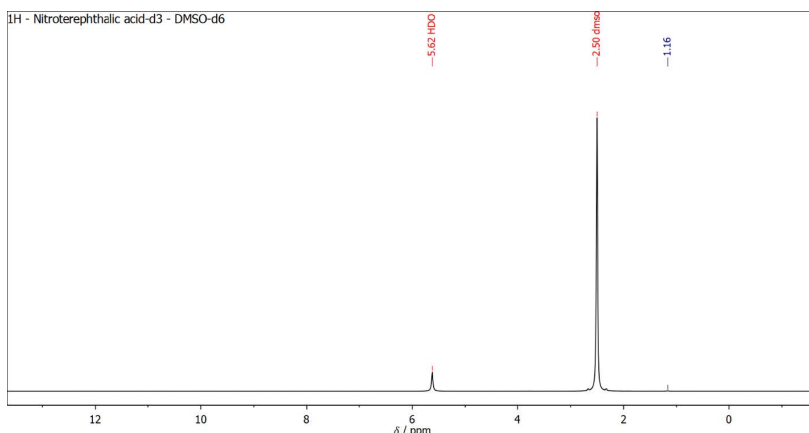
Figure 4.A.4: Proton NMR spectrum of the deuterium-labelled nitroterephthalic acid-d$_3$.

NH$_2$ – MIL – 53 (Al) – d$_3$ 2-aminoterephthalic acid-d$_3$ was prepared by reduction of dimethyl nitroterephthalate-d$_3$ (synthesized as described above). Dimethyl nitroterephthalate-d$_3$ (1.26 g, 5.2 mmol) was dissolved by stirring in 14 mL ethanol at 45 °C, while nitrogen was bubbled through the solution. SnCl$_2$ H$_2$O (4.93 g, 26 mmol) was added, turning the
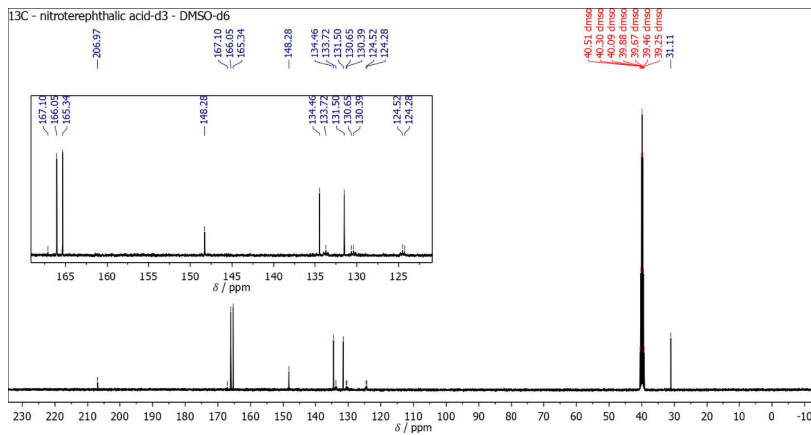
Figure 4.A.5: ^{13}C NMR spectrum of the deuterium-labelled nitroterephthalic acid-d$_3$.

solution to an opaque yellow mixture. The reaction became clear after reaching to reflux temperature, and was left for 16 h under nitrogen flow.

The solution was cooled down and poured into 50 mL ethyl acetate. A 5% NaHCO$_3$ aqueous solution was added dropwise while swirling to neutralize pH, which brought the formation a gel in the aqueous phase. The organic phase was kept. The aqueous phase (gel) was separated and filtered over Celite, washing four times with 20 mL ethyl acetate. The organic fractions were combined, dried over MgSO$_4$, and evaporated. The solids were purified by silica column to remove remaining Sn-based impurities, using ethyl acetate as solvent. Yield: 0.926 g (4.36 mmol; 84%).

Hydrolysis of dimethyl aminoterephthalate-d$_3$. Dimethyl aminoterephthalate-d$_3$ (913 mg, 4.3 mmol) was added to a mixture of 32 mL MeOH and 13 mL H$_2$O. NaOH (1.68 g) was added. The solution was stirred at room temperature for 16 h. The solvent was removed by evaporation, solids were dissolved in minimal water (8.8 mL). Added 2 mol/dm^3 HCl (20 mL, dropwise), until pH starts to decrease. At pH between 4 and 5 a yellow precipitate is formed. Continued adding drops of acid until no more precipitated was formed. The precipitate was recovered by vacuum filtration. The procedure was repeated on the filtrate, washing the solids several times with ice-cold water to remove all salts. The combined solids were dried in a vacuum oven at 100 °C for 5 h. Final yield: 676.2 mg, 3.67 mmol, 85%. The ^{1}H and ^{13}C NMR spectra of 2-aminoterephthalic acid-d$_3$ are shown in Figures 4.A.6 and 4.A.7.

AlCl$_3$ 6 H$_2$O (857 mg, 3.5 mmol) was dissolved in 10 mL deuterium oxide inside a 45 mL Teflon liner. 2-Aminoterephthalic acid-d$_3$ (632 mg, 3.4 mmol) was added to the solution. The liner was sealed inside a steel autoclave and placed in an oven at 150 °C for 10 h. After cooling, the yellow solids were filtered and washed with DMF (30 mL), and then transferred to the autoclave together with 25 mL DMF, and kept at 120 °C for 15 h. The DMF was subsequently exchanged by methanol (20 mL) at 80 °C for 4 h. After filtration the residual solvent is removed by heating the sample in the vacuum oven at 150 °C overnight. MOF characterization is shown in Figures 4.A.1,4.A.2,4.A.3.
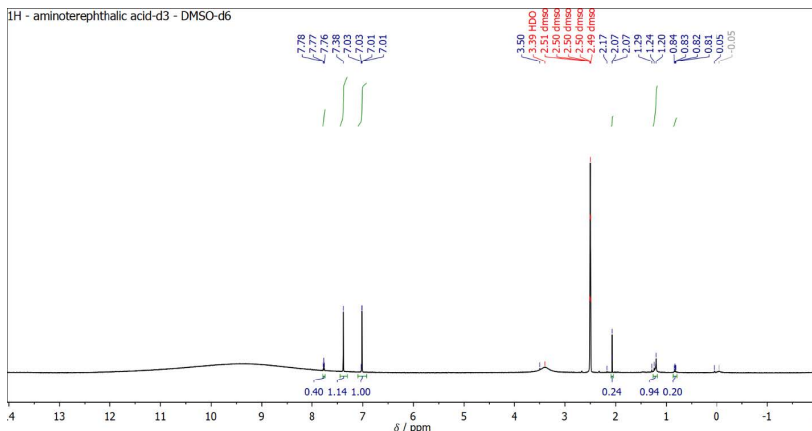
Figure 4.A.6: Proton NMR spectrum of the deuterium-labelled aminoterephthalic acid-d3.
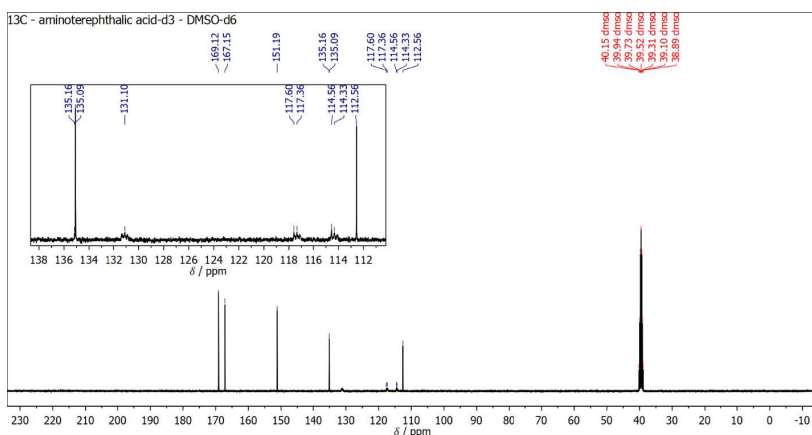
Figure 4.A.7: ^{13}C NMR spectrum of the deuterium-labelled aminoterephthalic acid-d3.

4.A.2.3 Routine characterization

Powder X-ray diffraction was acquired in Bragg–Brentano geometry using a Bruker-AXS D5005 equipped with a Co Kα source operating at 35 kV and 40 mA; a variable divergence slit was used. Thermogravimetric analysis (TGA) was performed using a Mettler Toledo TGA/SDTA 851e under 100 mL min^{-1} air flow, from 30 to 700 °C with a heating rate of 5 °C min^{-1}. Adsorption/desorption isotherms were measured volumetrically in a Tristar II 3020 Micromeritics instrument. N$_2$ sorption was performed at 77 K and CO$_2$ at 273 K. The samples were degassed before measurements under N$_2$ flow at 433 K for 16 h. The pore volume values were obtained from the N$_2$ sorption data at P/P$_0$=0.95. ^{1}H and ^{13}C NMR spectra were acquired in DMSO-d$_6$ using an Agilent 400-MR DD2 equipped with a 5 mm ONE probe.

4.A.2.4 Broadband dielectric spectroscopy

Dielectric measurements of MIL-53(Al), $NH_2 - MIL - 53$ (Al) and $NO_2 - MIL - 53$ (Al) powders were performed using a HP 4284A precision LCR meter in 85 K–425 K temperature and 10^2–10^6 Hz frequency ranges. The powder was pressed (35 kPa) between two round brass electrodes (diameter = 1 cm) in a custom-made cryostat. Temperature was measured using a Keithley 2700 multimeter with a T-type thermocouple. The samples in the measurement cell were kept under constant dry N_2 flow. All heating and cooling cycles were done at 1 K min^{-1}. Low temperatures were achieved using liquid N_2. The dielectric permittivity data were acquired during heating at 1 K min^{-1}, preceded by a full activation cycle (heating to ca. 450 K and cooling down to starting temperature ca. 100 K).

4.A.2.5 Solid-state ^{2}H NMR spectroscopy

Solid-state 2H NMR spectroscopy ^{2}H NMR spectra were acquired using a Bruker Avance III HD console and a 9.4 T Oxford wide-bore magnet at a resonance frequency of $u_0(^2H)$ = 61.422 MHz. A revolution 5 mm double-resonance (HX) ultra-low- temperature (ULT) probe was used for ^{2}H NMR experiments. All data were collected under static conditions (i.e., stationary samples). Spectra were acquired with continuous-wave (CW) ^{1}H decoupling with RF fields ranging between 40 kHz and 50 kHz.

RF pulse powers and the chemical-shift reference frequency were calibrated using neat D_2O (l) with δ_{iso} = $4.8 ppm$. Temperatures of the VT unit and probe were calibrated using the temperature-dependent chemical shift of $Pb(NO_3)_2$.[79, 80] The quadrupolar-echo pulse sequence ($\pi/2 - \tau_1 - \tau_2 - \pi/2 - \tau_2 -$acquire) was used to acquire the full echo, with a $\pi/2$ pulse length = 2.5 μs, echo delays τ_1 = 198.75 μs or 298.75 μs, ringdown delay of τ_2 = 30 μs, and 400 μs or 600 μs.[81] The entire echo is acquired and is processed in MATLAB by multiplication with a Gaussian function for line broadening, then Fourier transformation and magnitude calculation. The quadrupolar parameters of the SML spectra were determined with simulations using SOLA in Topspin 3.6.1. Simulations of the IMR and FML spectra were conducted using EXPRESS.[82] All simulations utilized standard ^{2}H quadrupolar parameters for a C–D bond in an aromatic ring: C_Q= 180 kHz, η_Q= 0.0.

4.A.2.6 Single-crystal X-ray diffraction analysis

Single-crystal XRD experiments on $NO_2 - MIL - 53$ (Al) were performed at the XRD1 beamline of the Elettra Synchrotron facility (CNR Trieste, Basovizza, Italy). Diffraction data were collected using a monochromatic 0.61 Å wavelength at 100 K(NO2-MIL-53), using a cold nitrogen stream produced with an Oxford Cryostream 700 (Oxford Cryosystems Ltd., Oxford, United Kingdom). Diffraction data were processed using the Rigaku CrysAlisPro software version 1.171.38.43 (Rigaku Corporation, Oxford, United Kingdom). Intensities integration was performed using the primitive unit cell, triclinic cell and no Friedel pairs averaging, to make it suitable for a P1 structure modelling. Structure determination was carried out by using the crystallographic software suite Olex2 (Olex2 v1.3 © OlexSys Ltd. 2004 – 2021), where the programs ShelXT and ShelXL were used for structure solution and refinement, respectively.

Table 4.A.1: Crystal data indicators for structure refinement of $NO_2 - MIL - 53$ according to the modeling choices

Identification code	4crystals_box0p75_crystal1
Empirical formula	AlC_8O_5
Formula weight	203.068
Temperature/K	100 K
Crystal system	triclinic
Space group	P1
a/Å	6.6442(5)
b/Å	9.7734(9)
c/Å	10.9201(8)
α/°	116.407(8)
β/°	107.671(6)
γ/°	90.095(7)
Volume/Å^3	597.34(10)
Z	2
ρ_{calc} g/cm^3	1.129
μ/1/mm	0.114
F(000)	202.1
Crystal size/mm^3	0.05 × 0.05 × 0.09
Radiation	synchrotron ($\lambda = 0.6199$)
2Θ range for data collection/°	3.86 to 52.56
Index ranges	$-11 \leq h \leq 11, -15 \leq k \leq 15, -18 \leq l \leq 18$
Reflections collected	14057
Independent reflections	6140 [$R_{int} = 0.0885$, $R_{sigma} = 0.0934$]
Data/restraints/parameters	6140/7/90
Goodness-of-fit on F^2	3.602
Final R indexes [I>=2σ (I)]	$R_1 = 0.3803$, $wR_2 = 0.7216$
Final R indexes [all data]	$R_1 = 0.3972$, $wR_2 = 0.7485$
Largest diff. peak/hole / e 1/Å^3	8.71/-2.94
Flack parameter	0.0(19)

Supplementary data and discussion

4.B.1 DFT structural details

A terephthalate rotor can be divided into three constituent parts: the para-phenylene moiety acts as the rotator, the carboxylic groups act as stators, and the two C–C single bonds function as the axle. In free terephthalate rotors, a 180° rotation (π-flip) can be seen as a transition between two potential energy minima (i.e., two conformers).

Nitroterephthalic acid presents a strong case of non-coplanarity, as can be seen in the optimized structure (Figure 4.B.1, left). Chloro- and bromoterephtalic acids behave similarly (not shown). A partial optimization with carboxyl groups in coplanar conformation better represents the anchoring effect that the MOF lattice imposes on the linker (Figure 4.B.1, right). To allow for an adequate comparison between different functional groups, we use this type of constraint for all molecules that deviate from planarity in full geometry optimizations. In the nitro case, the latter structure has an energy penalty of 10 kJ/mol with respect to the former, mainly attributed to the loss of nitro group π electron delocalization.
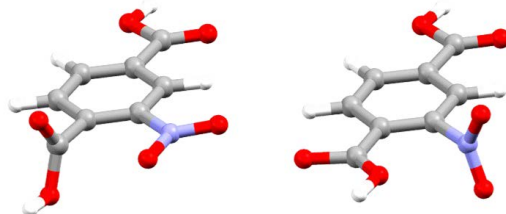
Figure 4.B.1: Nitroterephthalic acid optimized geometries: full optimization (left) and coplanar carboxyl partial optimization (right).

(a)	(b)	(c)
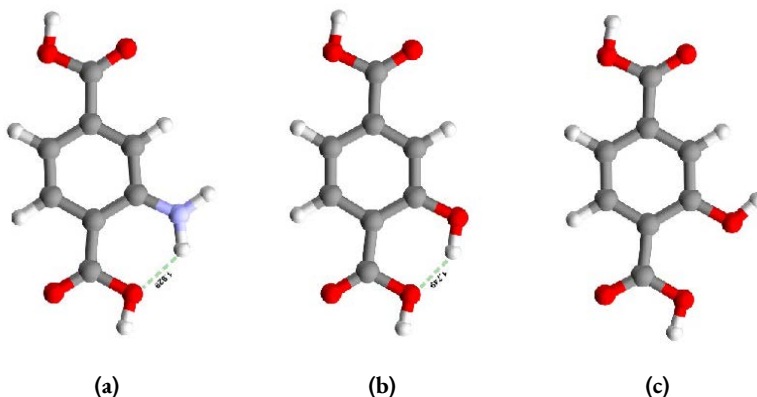
Figure 4.B.2: Geometry-optimized structures of amino- and hydroxyterephthalic acids (a) and b)) showing H-bonding distance. c): Non-H-bonding structure of hydroxyterephthalic acid.

129

4.B.1.1 Free molecule model validation

This simple model estimates a barrier of 48 kJ/mol for the unsubstituted terephthalic acid, which matches the experimentally obtained activation energy of terephthalate linkers in MOF-5 (47.3 ± 8.4 kJ/mol).[38] This result is not surprising as MOF-5 has a characteristic cubic network with ample free volume surrounding each linker, which prevents inter-linker steric hindrance. Similarly, bromine functionalization yields E_{rot} of 25.1 kJ/mol, a reasonable approximation to the experimental value of 30.5 ± 0.4 kJ/mol determined for unhindered IRMOF-2 (bromine-substituted version of MOF-5).[47]

The two functionalizations that increase the barrier with respect to the unfunctionalized linker are amine and hydroxyl (53.7 and 64.2 kJ/mol, respectively). Experimental evidence has shown similar trends, for example in UiO-66, where an activation energy for linker rotation of 30 kJ/mol,[39] increased to 51.9 kJ/mol upon amine functionalization.[48] In addition to both these groups being electron donating which could potentially increase the double bond character of the rotation axis bonds via π electron delocalization their planar conformations also enable hydrogen bond donation to the adjacent carboxylic group oxygen (Figure 4.B.2).

4.B.2 Periodic DFT details

The unit cell parameters of activated frameworks used in DFT calculations are shown in Table 4.B.1. The rotor spacing (i.e., the distance between the rotation axes of two adjacent linkers in a row) in LP frameworks is defined by the cell parameter a. For NP conformation, parameter c defines the spacing. The closest row-to-row distances (presented in Table 4.2 of the main chapter) for the LP frameworks can be defined as half the cell parameter c or half of b for $NH_2 - MIL - 53$.

Table 4.B.1: Experimental unit cell parameters used in periodic DFT calculations.

MOF	a	b	c	α	β	γ
$NO_2 - MIL - 53\,(Al)$ *	6.666	16.254	13.521	90	90	90
$NH_2 - MIL - 53\,(Al)$ †	19.722	7.692	6.578	90	105.1	90

[5] Cell parameters from diffraction collected for this work (vide infra)
[6] Cell parameters reported in [74]

4.B.2.1 $NO_2 - MIL - 53\,(Al)$ PXRD indexing

The PXRD of activated $NO_2 - MIL - 53\,(Al)$ was collected using an Anton–Paar sample cell and heating under N_2 flow. The diffractogram acquired at 220 °C was indexed using DASH.[83] The obtained cell parameters are shown in Table 4.B.1.

4.B.3 Rotation angle definitions

$NO_2 - MIL - 53\,(Al)$. The reported rotation angles correspond to the angle between two planes: the best-fitting plane to the benzene ring and the (011) or (0-11) crystallographic plane. The choice between the two crystallographic planes depends on the row to which the rotating linker belongs to. The (011) or (0-11) planes are absolute reference planes as

they do not change during geometry optimization or MD simulation. For simplicity, we define the full rotation space around the linker's rotation axis in two halves: 0° to 180° and 0° to −180°. The positive part of this space corresponds to the orientations pointing in the direction of the normal of the reference plane (see Fig 4.3a and 4.3b of the main chapter), and the negative portion corresponds to those pointing in the opposite direction of the reference plane normal. 0° is defined based on the [100] direction; i.e., the functional group is pointing approximately in the [100] direction of the unit cell.

$NH_2 - MIL - 53$ (Al). The axis of rotation of linkers in $NH_2 - MIL - 53$ does not correspond to any crystallographic plane. Therefore, we define a reference plane for the rotating linker as the best-fitting plane for its four oxygen atoms in the global minimum structure (see Figure 4.B.3). The rotation angle is the angle between the best-fitting plane of the rotating ring and the reference plane. The sign is defined as positive if the functional group points in the general direction of the normal to the reference plane (dashed arrow in Figure 4.B.3).
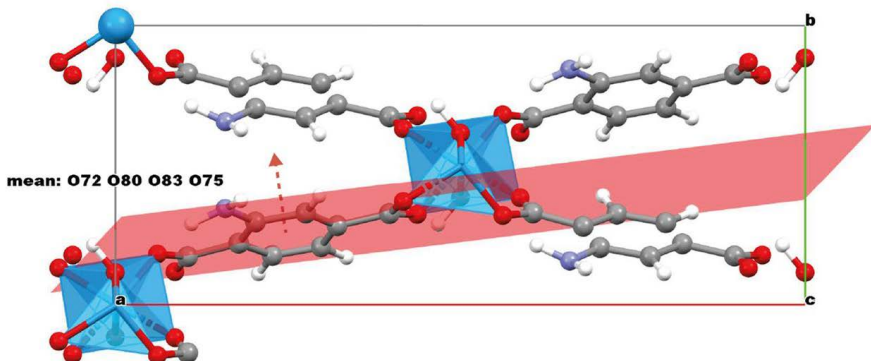
Figure 4.B.3: Reference plane for rotation angle in NH2-MIL-53 DFT calculations. Dashed arrow represents the normal vector of the plane, denoting positive angles.

Due to its NP structure, $NH_2 - MIL - 53$ (Al) suffers from strong steric limitations even at small amplitude rotations. An example is shown in Figure 4.B.4.

4.B.4 Single-crystal XRD analysis of $NO_2 - MIL - 53$ (Al)

To increase the amount of information on the structure disorder in the average structure of $NO_2 - MIL - 53$ (Al), the structure was solved using space group P1. In this way we avoided symmetry averaging of the electron densities belonging to different positions of the nitro groups of the linkers. All atoms except hydrogens and nitro groups of the linkers were modeled and refined isotropically, to make the electron density residues more informative on both substitutional and displacive disorder of the crystal. The difference Fourier map (F_{obs}-F_{calc}) displaying such residues was computed with the software Vesta,[84] using the "Fourier synthesis" tool. The structure factors file compiled by the ShelXL program using the "list 3" command, was loaded in Vesta and the electron residues were plotted using four isovalues: 1.6, 1.2, 0.7, and 0.5. The resulting 3-dimensional map shows that all four sites on the phenylene ring are partially occupied by nitro groups (Figure 4.B.5). This implies that
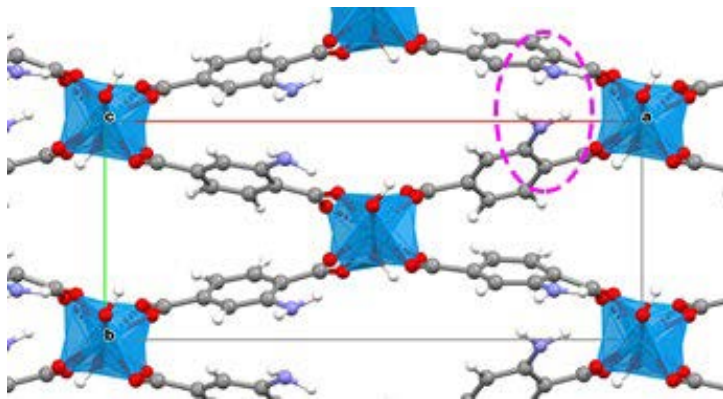
Figure 4.B.4: The linker rotated to ca. $-30°$ in $NH_2 – MIL – 53\,(Al)$ collides with its neighbor in the closest row.

no preferential orientation between adjacent linkers is established during crystal formation. While the occupancies of the four nitro groups' positions appear similar judging from their residues, the refinement of the actual average occupancy factors was not deemed reliable due to the strong static disorder of the linker phenyl ring, which lies rotated at different angles. The resulting average structure features smeared- out densities, whose fitting was not stable and did not produce reliable models for a sensible occupancy determination of the nitro groups.
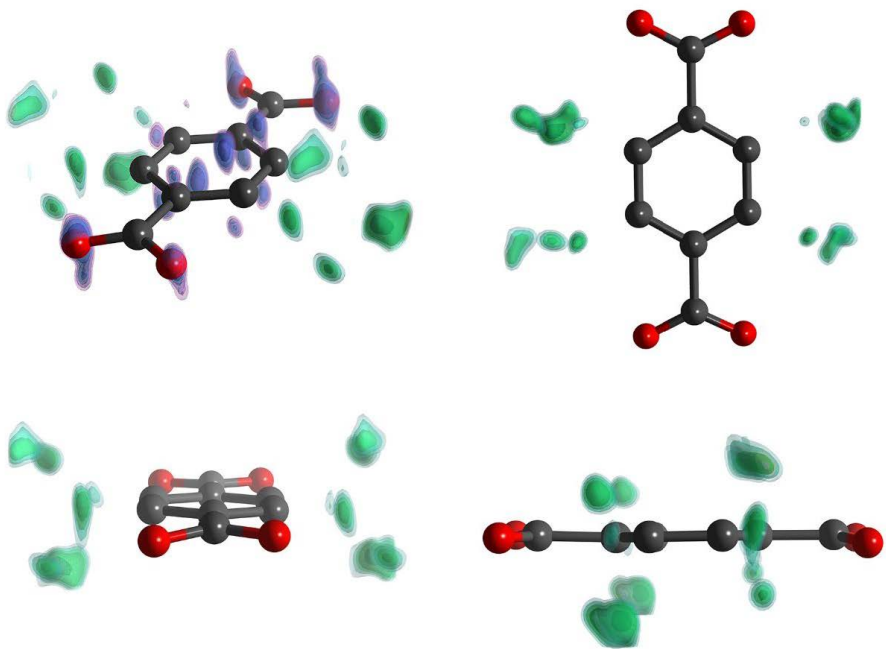
Figure 4.B.5: Difference Fourier map (Fobs-Fcalc) showing the positive electron density residues around each linker in the structure of $NO_2 – MIL – 53$ (Al) refined by single-crystal XRD. The data was obtained from a previous study.[1] Electron density residues attributable to the nitro groups disordered in all four possible positions are displayed in green, while the violet residues signal the presence of disordered pore configurations. For clarity, the violet residual density is omitted from all images except for top-left.

4.B.5 $NO_2 – MIL – 53$ 2x1x1 supercell DFT calculations

4.B.5.1 Alternative nitro group positions

When considering only the pair participating in forced rotation, there are four possible nitro positions for each ring. As concluded from single-crystal XRD analysis, nitro groups do not follow a preferred conformation on the rings. Therefore, the cases shown in Figure 4.B.6 represent likely configurations that pairs of linkers will encounter during full rotation. Case 1 is clearly the most impacted by steric effects between rotors. Additionally, cases 2 and 3 were based on the starting structure of case 1, in which one of the nitro groups in the pair was changed to the adjacent carbon.
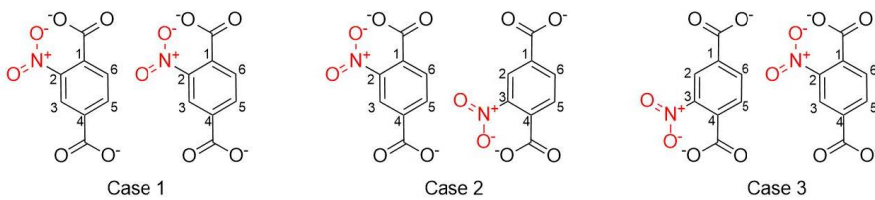
Figure 4.B.6: The three studied cases in 2x1x1 $NO_2 – MIL – 53$ supercell. The rotating ring is on the left for each pair.

The relative energy obtained from DFT calculations for these three cases of double cell simulations are presented in Figure 4.B.7. It is important to note that these results do not necessarily represent global minima for each conformation. Since the rotating linker is manually rotated to each angle starting from a previous structure, the relaxed structures are a result of local optimizations and are history dependent. For example, after global optimization the positive angles above 180° should result in identical structures (and energies) as their corresponding negative angles (e.g., 210° and −150°), which is clearly not the case in our step-by-step approach. Bearing this in mind, we propose that this method is still useful in illustrating the local interactions between neighboring linkers, specifically in how the conformation of the neighbor sterically affects the rotating linker's mobility.

The calculations performed for cases 2 and 3 focus on the portion of the rotational space most relevant to nitro-nitro interactions, skipping small angle rotations that did not cause significant energy increases in case 1. Cases 2 and 3 resulted in significantly lower energies at angles where nitro-nitro interactions in case 1 were highly disfavored (see Figure 4.B.10). Importantly, the unfeasible energy increase observed when rotating below −115° in case 1 was absent in the two alternative cases, for which a maximum of 50-60 kJ/mol was found. When nitro groups are in alternate positions, more space is available for full rotation in either direction. The marked difference between the first case and the latter two suggests that a large variability can be expected from a real population of disordered linkers, ranging from linkers whose neighbors impede rotations (causing slow or no motion) and linkers whose neighbors cooperate (whether by correlated motion or by favorable arrangement) allowing for relatively fast rotation.
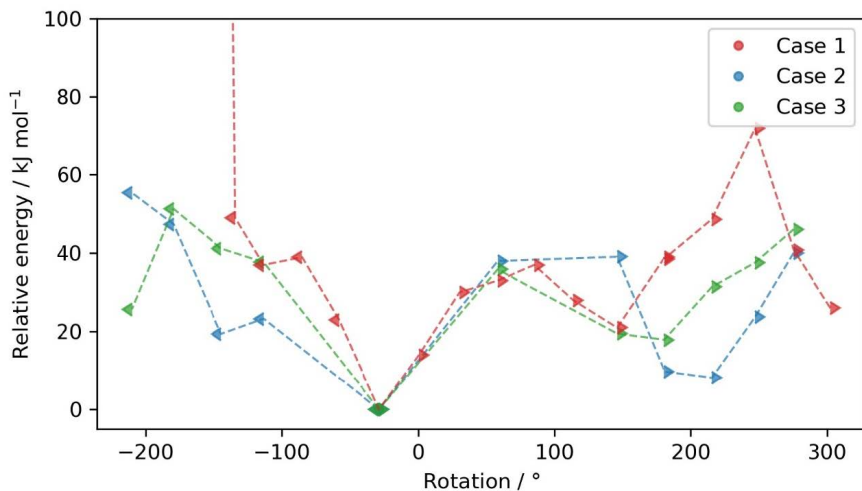
Figure 4.B.7: Potential energy profiles of the three studied cases in 2x1x1 NO_2 – MIL – 53 supercell.

4.B.5.2 DFT structure sequence during neighbor "crash" in case 1

With the rotating linker (left of the cell) at $-91°$, the neighbor is not affected and finds a minimum conformation at ca. $-12°$ (Figure 4.B.8). Upon approaching $-150°$, the nitro group of the rotating linker begins to overlap with the nitro group of the free neighbor. From the progression seen from $-145°$ to $-180°$, it is clear that the combination of direction of approach of rotating linker and starting conformation of the neighbor (right linker) did not allow for the latter ring to reduce this repulsive interaction by rotating away. This is because this free neighbor is being pushed towards the 0° position, and this represents an increase in energy (note the local maximum at 0°) before a more energetically favored conformation can is reached. Instead, at $-180°$ we see the nitro group of the forced rotated ring is bent to an unfeasible configuration, and the neighbor does not cross the 0° barrier. This leads to the steep energy increase below $-145°$ seen in Figure 4.B.7.
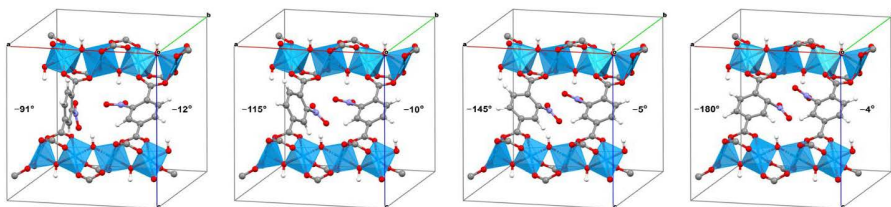
Figure 4.B.8: DFT supercell case 1 converged structure sequence for steps from ca. $-90°$ to $-180°$ (left to right), which resemble a head-to-head crash between the neighboring rings. The rotating linker is on the left side of each cell.

4.B.5.3 DFT structure sequence during neighbor "push" in case 1

Rotation in the opposite direction to reach the same −150° position is different in that the interaction with the free ring resembles a gear; the "push" from the rotating nitro ring causes the free ring to adapt by rotating from its initial −15° conformation to a larger negative value (ca. −56°), as shown in Figure 4.B.9. Once the rotating ring has cleared the shared space between the pair, the neighbor returned to its minimum (−12°). We note that the structure at −115° for this direction of rotation is still a maximum in the potential energy curve, yet feasible in comparison to the previous rotation direction. This result further illustrates the importance of cooperative motion between neighbor linkers.
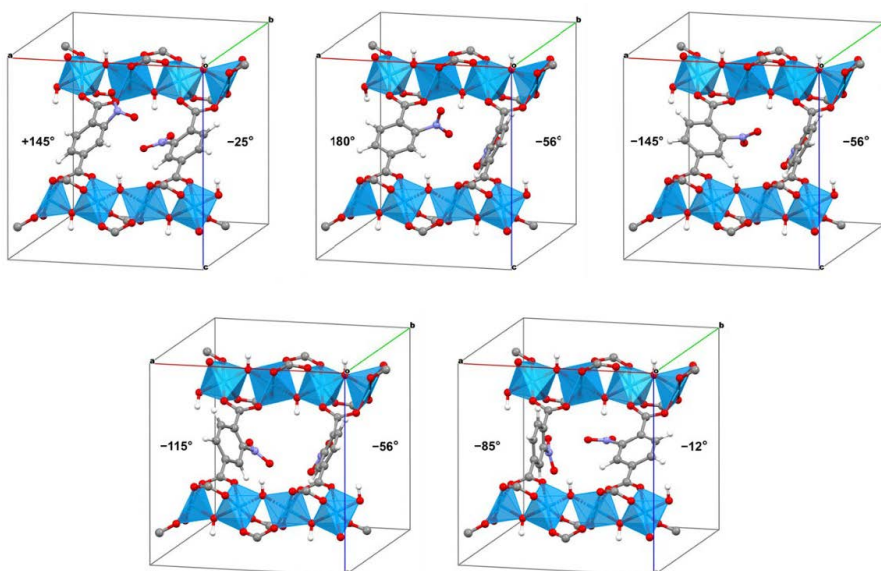
Figure 4.B.9: DFT supercell case 1 converged structure sequence for steps from ca. 145° to −85° (left to right), which resemble a head-to-head push between the neighboring rings. The free neighbor ring cooperates by swinging out of the rotating linker's trajectory. The rotating linker is on the left side of each cell.

4.B.5.4 DFT structures in cases 2 and 3

In the rotation space regions where the neighboring linkers undergo head-to-head interactions, the positioning of nitro groups in cases 2 and 3 clearly allow more space for the functional groups to fit. For the approach from negative direction, shown on the left side in Figure 4.B.10, the pair of nitro groups is accommodated and results in energies around 50 kJ/mol. This is in contrast with the crash that occurred in case 1, where the nitro groups in equal positions are not able to fit. Approaching in the positive direction leads to rotation over a smaller angle needed by the neighbor ring in cases 2 and 3 (−38° and −39°, see appendix Fig. 4.B.10) vs. −56° for case 1, accompanied by significantly lower energies at 180° then for case 1 (Figure 4.B.8).
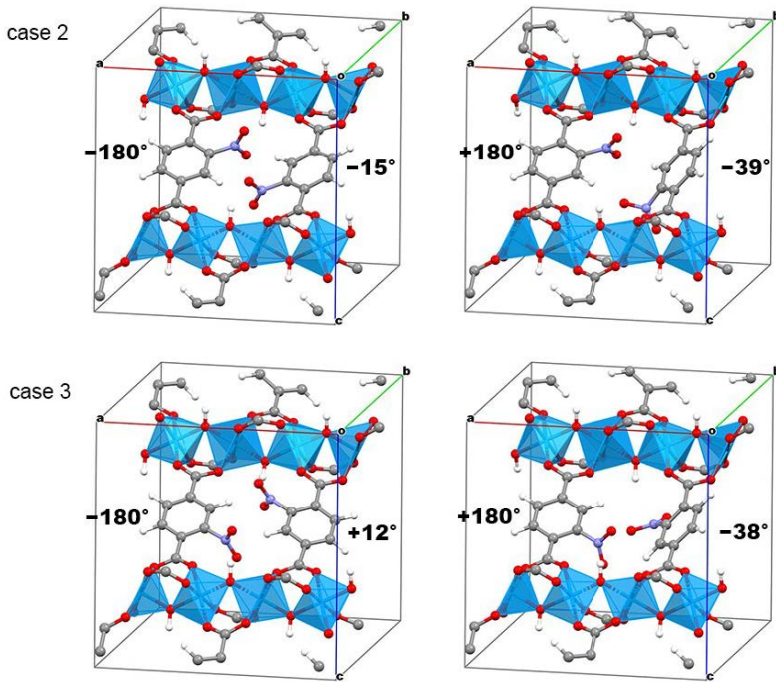
Figure 4.B.10: DFT supercell cases 2 and 3 converged structures at 180° rotation reached in both directions (represented by – or +). The free neighbor ring shows swinging out of the rotating linker's trajectory in the case of positive rotation. The rotating linker is on the left side of each cell.

4.B.6 Supplementary BDS data

We performed BDS measurements on activated powder samples of MIL-53(Al), $NO_2 – MIL – 53\,(Al)$, and $NH_2 – MIL – 53\,(Al)$ under dry N_2 flow.

The Cole–Cole equation (eq. 4.1) was used to fit the $NO_2 – MIL – 53\,(Al)$ dielectric relaxation. Both ε' and ε'' parts of the complex dielectric permittivity ε^* were fitted simultaneously.

$$\varepsilon^* = \varepsilon_\infty + \frac{\Delta\varepsilon}{1 + (i\tau\omega)^{1-\alpha}} \tag{4.1}$$

where ε_∞ is the high frequency limit of the dielectric permittivity, $\delta\varepsilon$ is the relaxation strength, ω denotes the angular frequency, τ is the mean relaxation time, and parameter α describes the width of the relaxation. For $\alpha = 0$, Eq.4.1 reduces to the Debye relaxation of non-interacting electric dipoles in a uniform environment. The obtained α values are presented in Figure 4.B.13. The relaxation strength remained roughly 1.4 in the whole investigated temperature range.

The Arrhenius equation (4.2) was used to fit the determined mean relaxation times τ.

$$\tau = \tau_0 e^{\frac{E_a}{kT}} \tag{4.2}$$

137

(a)   **(b)**
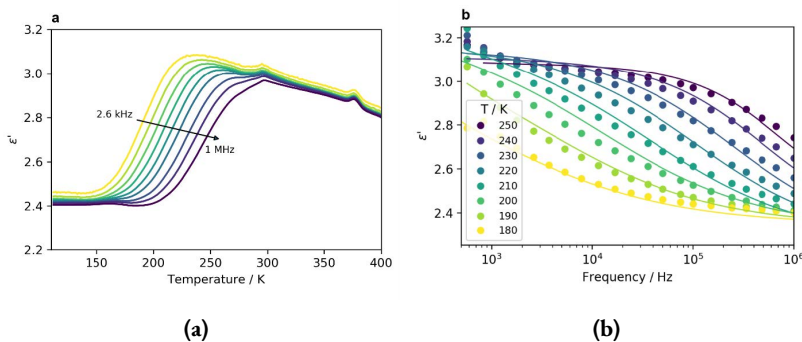
Figure 4.B.11: Real part (ε') of $NO_2 - MIL - 53\,(Al)$ with respect to (a) temperature and (b) frequency. The latter includes the fitted Cole-Cole model equation 4.1 as continuous lines.
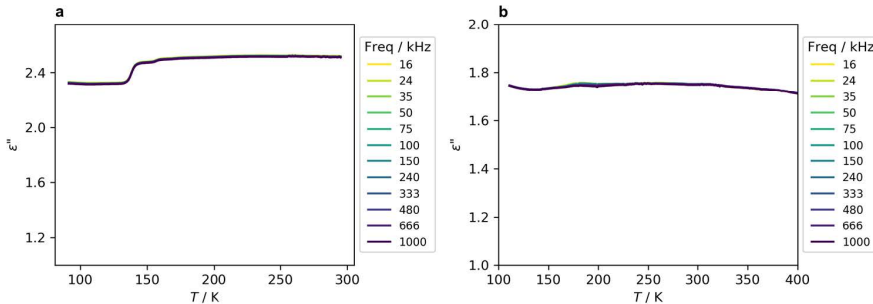
Figure 4.B.12: Temperature domain of ε' for (a) $NH_2 - MIL - 53\,(Al)$ and (b) MIL-53(Al).
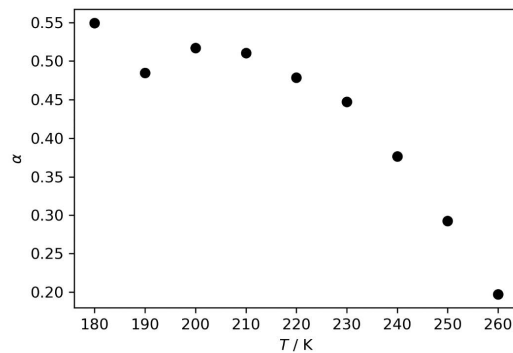
Figure 4.B.13: The α parameters from the Cole-Cole fit for $NO_2 - MIL - 53\,(Al)$ relaxation at different temperatures.

138

where E_a is the activation energy of the process, τ_0 denotes the attempt time, and k is the Boltzmann constant. The best fit and determined values of the fit parameters are shown in Figure 4.B.14.
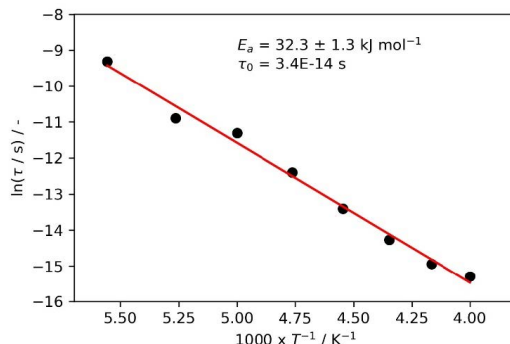
Figure 4.B.14: Fit of the Arrhenius equation (eq.4.2) to the mean relaxation times of $NO_2 - MIL - 53$ (Al) obtained from the Cole-Cole fit. The confidence interval corresponds to the standard deviation of the fit.

The obtained pre-exponential factor is equivalent to 2.9×10^{13} Hz. As explained in the main chapter, a rotator of the dimensions of nitro-p-phenylene is expected to present an attempt or libration frequency in the order of 10^{12} Hz, based on a simple assessment of its rotational inertia.[53] However, it is common to find pre-exponential factors that deviate from the theoretical expectation to higher values, particularly in studies of more complex rotors, such as functionalized p-phenylene rotators.[33, 48, 52, 53]

This deviation to higher attempt frequencies has been interpreted as an indication of a temperature dependence of the rotational energy barrier.[53] The reasoning is that the observable E_a and pre-exponential factor should be taken as effective values, and by fixing the true pre-exponential factor as the expected attempt frequency (estimated at 10^{12} Hz), the true barriers at each temperature can be derived. After applying this analysis to our data, we found the slope of the barrier to be −0.028 kJ K/mol, which is in between of the two slopes reported by Horansky et al. for their molecular crystal rotors.[52, 53] Phenomena that could be accountable of this effective decrease in rotation barrier with temperature are indeed expected in a framework where linkers influence each other during rotational motion, similar to some that have been reported for other complex solid-state rotor systems.[5, 54, 85]

4.B.7 Supplementary solid-state ^{2}H NMR spectroscopy data

Our data for this system (Figure 4.B.15a) mirror those of Kolokolov *et al*.,[35] where the phenylene rings are observed to undergo an increased rate of 180° reorientations (π-flips) at increased temperatures. The modeled rates fitted to an Arrhenius equation yielded an activation energy of 35 kJ/mol (Figure 4.B.15b). It is noted that the fast motion limit (FML, i.e., k >100 MHz) is not reached, even at temperatures as high as *ca*. 453 K.
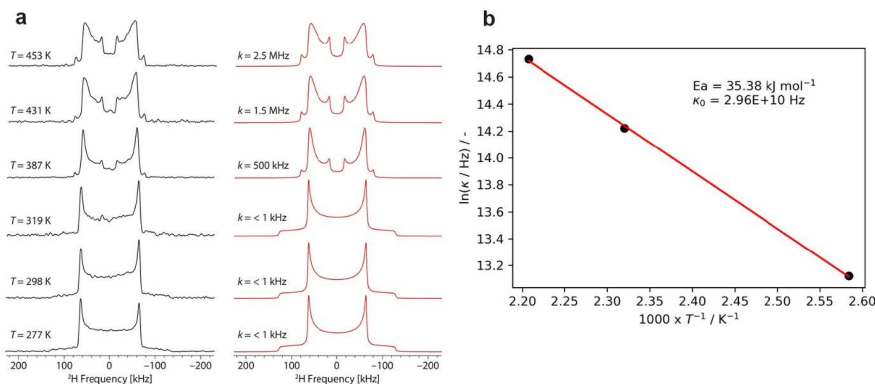
Figure 4.B.15: a, Variable-temperature ^{2}H NMR spectra of MIL – 53 (Al) – d_4 acquired (left column) at 9.4 T and simulated (right column) with the 180°-flip exchange model described in the text, using different exchange rates, k. **b**, Arrhenius fit of the obtained exchange rates.

$ND_2 – MIL – 53 (Al)$ (a deuterated amine version of the MOF) was investigated by Gascon *et al*.,[57] who found that the aromatic rings remain stationary across a temperature range from 298 K to 423 K. Our experiments on ring-labelled $NH_2 – MIL – 53 (Al) – d_3$ (Figure 4.B.16) reveal similar spectra and static behavior of the phenylene rings. This is evidenced by a constant Pake doublet up to 453 Kthat matches a slow motion limit (SML, i.e., <1 kHz) C–^{2}H bond model.
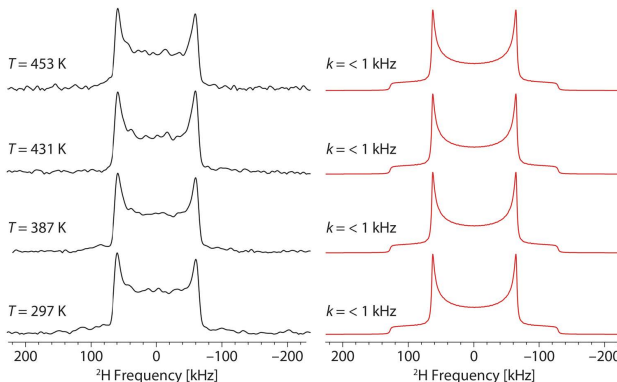
Figure 4.B.16: Variable-temperature ^{2}H NMR spectra of $NH_2 – MIL – 53 (Al) – d_3$ acquired (left column) at 9.4T and simulated (right column) with no exchange/low exchange rates (i.e., slow-motion limit spectra). In each case, exchange rate, k, has an upper limit of 1 kHz.

(a)

(b)
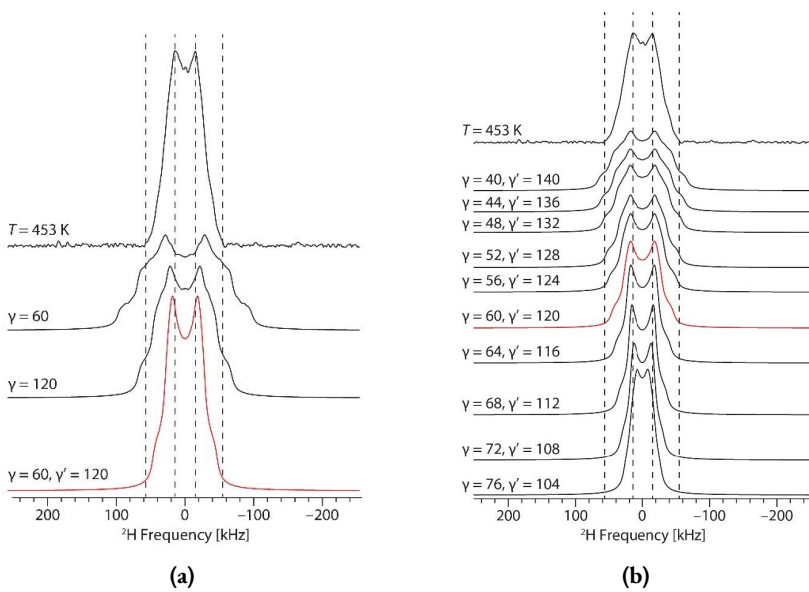
Figure 4.B.17: (a) ^{2}H NMR spectra of $NO_2 - MIL - 53\,(Al) - d_3$ acquired at 453 K(top) and simulated (below) using a two-site exchange model with a single reorientation of the ring described by the angle γ. The red spectrum is simulated with the four-site exchange model described in the main chapter and is used in Figure 4.5 in the main chapter. (b) ^{2}H NMR spectra of $NO_2 - MIL - 53\,(Al) - d_3$ acquired at 453 K (top spectrum) and simulated (below) using a four-site exchange model described in the main chapter. In each case, the two relative orientations of the phenyl ring planes vary according to the angles γ and γ'. The simulated spectrum in red is in best agreement with the experimental spectrum and is used in Figure 4.5 in main chapter.

4.B.8 Ab initio molecular dynamics simulations

Using the MD trajectory structures, rotation angles of all *p*-phenylene rings (Figures 4.B.18, 4.B.19, 4.B.20, 4.B.21, 4.B.22) were obtained using a simple python code described in section 4.B.10 and available online at https://github.com/srinidhimula/supplementary-data.
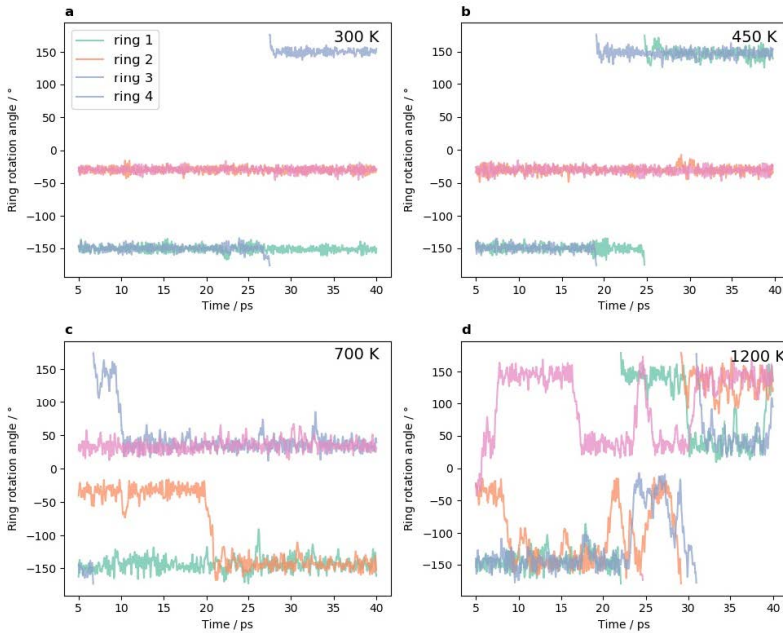
Figure 4.B.18: a-d, Rotation angle traces vs. simulation time for all linkers in a unit cell at different temperatures.
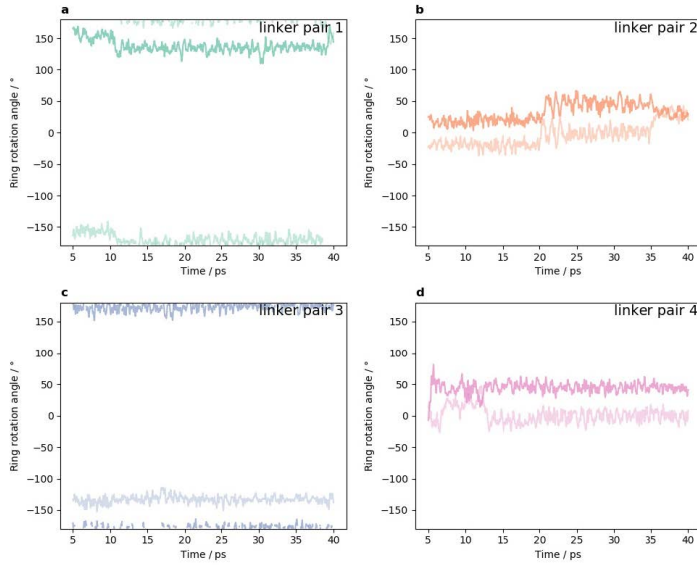
Figure 4.B.19: a-d, Rotation angle traces vs. simulation time for all same-row pairs in a 2x1x1 simulation at 300 K.
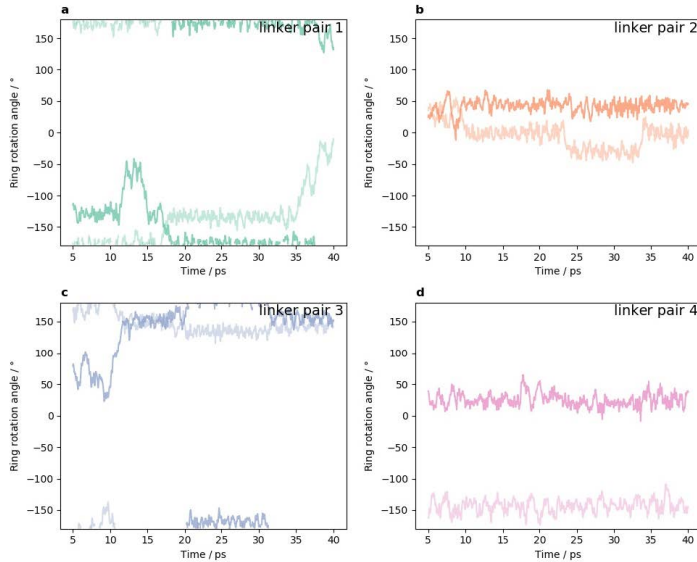
Figure 4.B.20: a-d, Rotation angle traces vs. simulation time for all same-row pairs in a 2x1x1 simulation at 450 K.
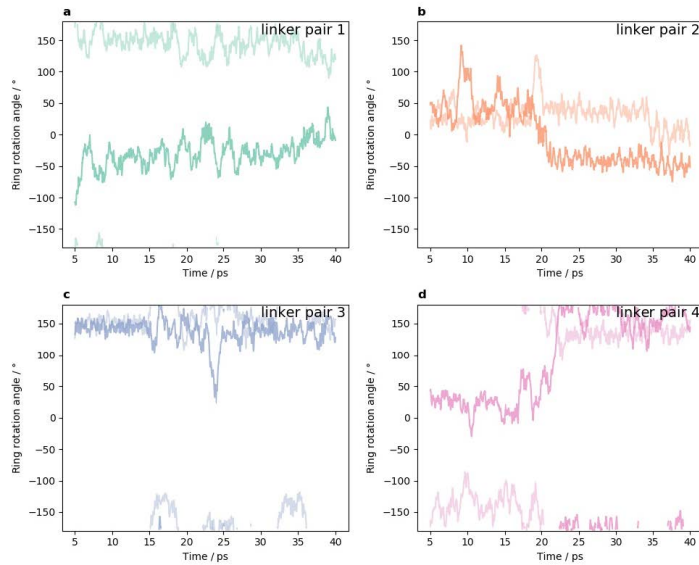
Figure 4.B.21: a-d, Rotation angle traces vs. simulation time for all same-row pairs in a 2x1x1 simulation at 700 K.
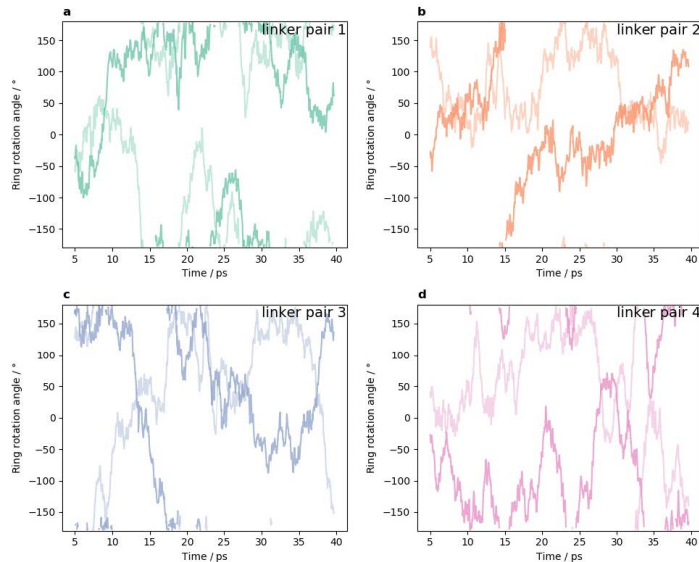
Figure 4.B.22: a-d, Rotation angle traces vs. simulation time for all same-row pairs in a 2x1x1 simulation at 1200 K.

4.B.9 Correlated motion between pairs of linkers

We present the rotation angle traces of all four same row pairs from the 2x1x1 supercell simulations at 450 Kand 700 K along with the corresponding N···N distances between their nitro groups (Figures 4.B.23, 4.B.24, 4.B.25, 4.B.26, 4.B.27). The minimum N···N distance seen in the data is approximately 4 Å, as seen in the distributions at all temperatures (Figure 4.B.23a). Figure 4.B.23b shows that this N···N distance is a reasonable approximation to the closest O···O contact of ca. 3 Å. When N···N distances approach this value, it can be inferred that steric effects between nitro groups start to play a significant role. We highlighted such regions of interest in Figures 4.B.24, 4.B.25, 4.B.26, 4.B.27. In these regions we see that inversely correlated small-angle oscillations occur, such that one trace seems to roughly mirror the other. However, outside these windows, where N···N distance is larger, this correlation is absent, and in fact the frequency of the oscillations is visibly higher (e.g., at 450 K, pair 4 shows correlated fluctuations with lower frequency, while pairs 2 and 3 do not).

Additionally, although rarely observed large-angle jumps occasionally show correlation between same-row pairs when the N···N distance is close to 4 Å. The clearest examples of this are seen at 700 Kfor pair 2 at ca. 20 ps and pair 4 at ca. 22 ps.


(a)   (b)
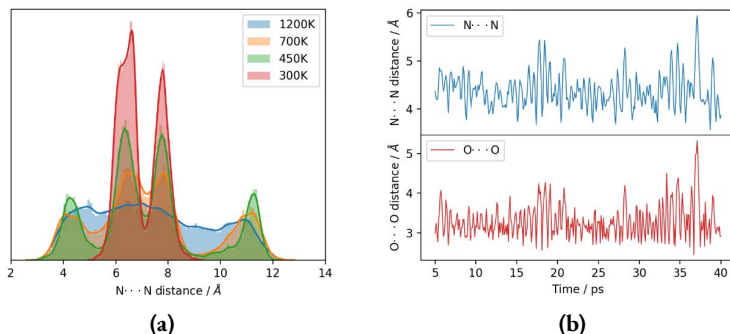
Figure 4.B.23: a, Distribution of N···N distances in 2x1x1 simulations. **b**, Comparison between N···N and shortest O···O distances; N···N represents well enough the steric interactions between nitro groups of neighbor pairs of linkers.
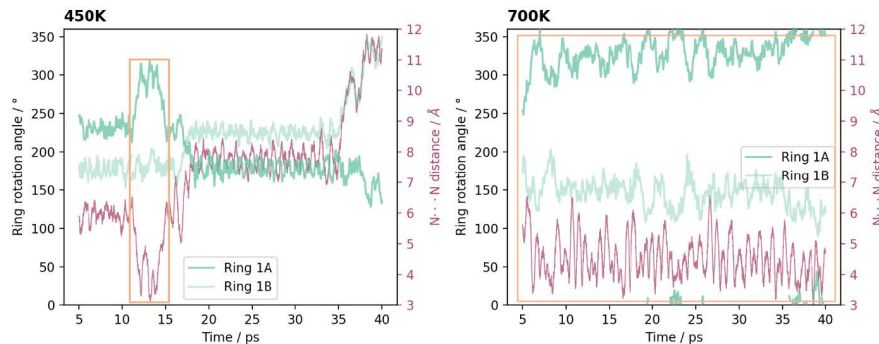
**Figure 4.B.24:** Rotation angle and N···N distance traces for linker pair 1.
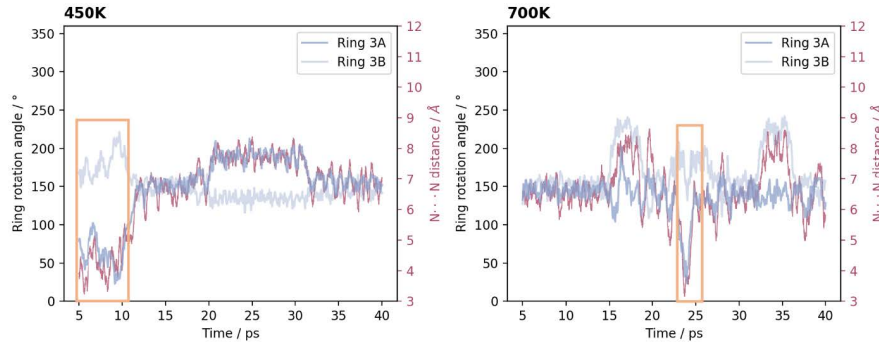
Figure 4.B.26: Rotation angle and N···N distance traces for linker pair 3.
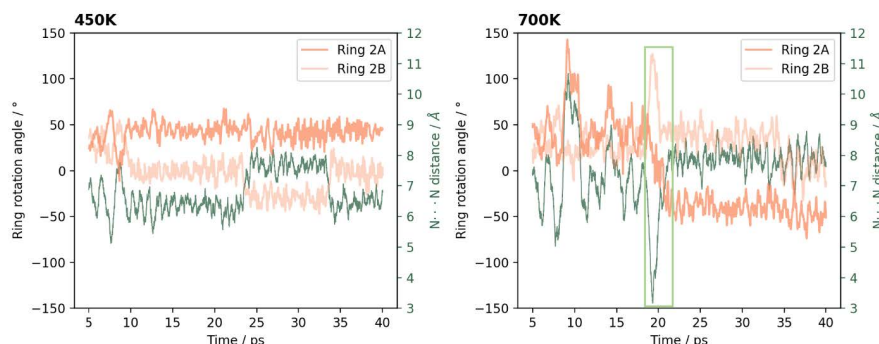

Figure 4.B.25: Rotation angle and N···N distance traces for linker pair 2.
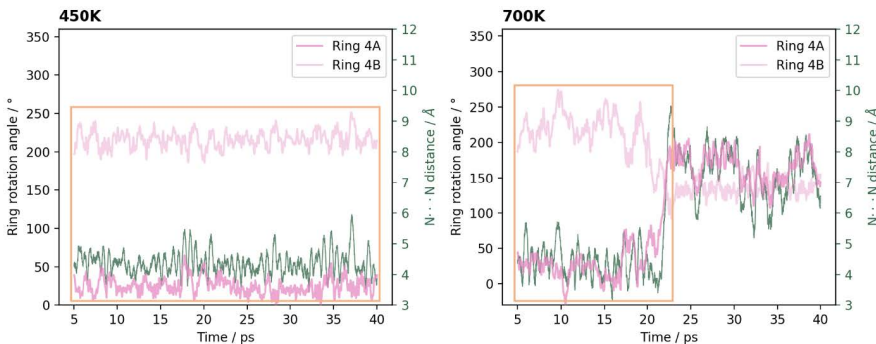
Figure 4.B.27: Rotation angle and N⋯N distance traces for linker pair 4.

4.B.10 Rotation angle pseudocode

A Python code was used to obtain the rotation angles of all benzene rings in the MD simulation structures. This section includes a detailed description of the code's functionality. The code is available online at https://github.com/srinidhimula/supplementary-data.

start= Initial timestep at the start of rotation angle calculation

end= Final timestep at which rotation angle calculation has to be ended

Function load_data_fromxyz:

Takes the path where MD trajectory file is located as input

returns filename and path

Function get_num_steps:

Filename from load_data_fromxyz is given as input

for timesteps in (start, end)

returns timesteps array

Function ring(a)_rotation:

Filename from load_data_fromxyz is given as input

ring_carbon = Contains the 6 carbon labels of that specific benzene ring

ref_plane = Normal vector (**Nref**) of reference crystallographic plane based on which row the rotating linker belongs to.

for timesteps in (start, end):

Read cartesian coordinates of the specified ring labels from the MD trajectory file

Cell parameters are added for specific cases to correct for periodicity.

Call *angle_calculate* function with inputs : cartesian coordinates of 6 carbons, **Nref** and cartesian coordinates of 3 specific carbons (a, b, c)

Last input(a, b, c) is to have consistent ring normal direction and sign for the rotation angle based on notation in Figure 2 of article

returns rotation angle array

Function angle_calculate:

Inputs: ring carbon cartesian coordinates at each time step,

Nref, cartesian coordinates of 3 specific carbons (**a, b, c**)

Normal vector (**N**) of best fitting plane of benzene carbons is calculated from singular value decomposition

Ring plane normal vector direction is made consistent by taking cross product C1=(a × b) a, b inputs depends on the benzene ring.

Direction corrected normal vector **Nfinal**= C1·N Rotation angle= Sign for the angle based on notation in Figure 2 is corrected by sign of ((Nfinal× Nref)· Coord of c)

returns rotation angle

Bibliography

(1) G. Van Meer, D. R. Voelker and G. W. Feigenson, "Membrane Lipids: Where They Are and How They Behave," *Nature Reviews Molecular Cell Biology*, 2008, **9**, 112–124.

(2) A. L. Duncan, T. Reddy, H. Koldsø, J. Hélie, P. W. Fowler, M. Chavent and M. S. P. Sansom, "Protein Crowding and Lipid Complexity Influence the Nanoscale Dynamic Organization of Ion Channels in Cell Membranes," *Scientific Reports*, 2017, **7**, 16647.

(3) H. M. Van Der Kooij, S. A. Semerdzhiev, J. Buijs, D. J. Broer, D. Liu and J. Sprakel, "Morphing of Liquid Crystal Surfaces by Emergent Collectivity," *Nature Communications*, 2019, **10**, 3501.

(4) L. Catalano and P. Naumov, "Exploiting Rotational Motion in Molecular Crystals," *CrystEngComm*, 2018, **20**, 5872–5883.

(5) C. S. Vogelsberg and M. A. Garcia-Garibay, "Crystalline Molecular Machines: Function, Phase Order, Dimensionality, and Composition," *Chem. Soc. Rev.*, 2012, **41**, 1892–1910.

(6) T.-A. V. Khuong, J. E. Nuñez, C. E. Godinez and M. A. Garcia-Garibay, "Crystalline Molecular Machines: A Quest Toward Solid-State Dynamics and Function," *Accounts of Chemical Research*, 2006, **39**, 413–422.

(7) A. Comotti, S. Bracco and P. Sozzani, "Molecular Rotors Built in Porous Materials," *Accounts of Chemical Research*, 2016, **49**, 1701–1710.

(8) H. Deng, M. A. Olson, J. F. Stoddart and O. M. Yaghi, "Robust Dynamics," *Nature Chemistry*, 2010, **2**, 439–443.

(9) A. Gonzalez-Nelson, F.-X. Coudert and M. van der Veen, "Rotational Dynamics of Linkers in Metal–Organic Frameworks," *Nanomaterials*, 2019, **9**, 330.

(10) P. Martinez-Bulit, A. J. Stirk and S. J. Loeb, "Rotors, Motors, and Machines Inside Metal–Organic Frameworks," *Trends in Chemistry*, 2019, **1**, 588–600.

(11) J. Dong, V. Wee, S. B. Peh and D. Zhao, "Molecular-Rotor-Driven Advanced Porous Materials," *Angewandte Chemie International Edition*, 2021, **60**, 16279–16292.

(12) J. A. Gee and D. S. Sholl, "Effect of Framework Flexibility on C8 Aromatic Adsorption at High Loadings in Metal–Organic Frameworks," *The Journal of Physical Chemistry C*, 2016, **120**, 370–376.

(13) J. Park, M. Agrawal, D. F. S. Gallis, J. A. Harvey, J. A. Greathouse and D. S. Sholl, "Impact of Intrinsic Framework Flexibility for Selective Adsorption of Sarin in Non-Aqueous Solvents Using Metal–Organic Frameworks," *Physical Chemistry Chemical Physics*, 2020, **22**, 6441–6448.

(14) M. Agrawal, S. Bhattacharyya, Y. Huang, K. C. Jayachandrababu, C. R. Murdock, J. A. Bentley, A. Rivas-Cardona, M. M. Mertens, K. S. Walton, D. S. Sholl and S. Nair, "Liquid-Phase Multicomponent Adsorption and Separation of Xylene Mixtures by Flexible MIL-53 Adsorbents," *The Journal of Physical Chemistry C*, 2018, **122**, 386–397.

(15) R. J. Verploegh, A. Kulkarni, S. E. Boulfelfel, J. C. Haydak, D. Tang and D. S. Sholl, "Screening Diffusion of Small Molecules in Flexible Zeolitic Imidazolate Frameworks Using a DFT-Parameterized Force Field," *The Journal of Physical Chemistry C*, 2019, **123**, 9153–9167.

(16) M. Witman, S. Ling, S. Jawahery, P. G. Boyd, M. Haranczyk, B. Slater and B. Smit, "The Influence of Intrinsic Framework Flexibility on Adsorption in Nanoporous Materials," *Journal of the American Chemical Society*, 2017, **139**, 5547–5557.

(17)   M. J. Lennox and T. Düren, "Understanding the Kinetic and Thermodynamic Origins of Xylene Separation in UiO-66(Zr) via Molecular Simulation," *The Journal of Physical Chemistry C*, 2016, **120**, 18651–18658.

(18)   J. D. Evans, S. Krause and B. L. Feringa, "Cooperative and Synchronized Rotation in Motorized Porous Frameworks: Impact on Local and Global Transport Properties of Confined Fluids," *Faraday Discussions*, 2021, **225**, 286–300.

(19)   I. Aprahamian, "The Future of Molecular Machines," *ACS Central Science*, 2020, **6**, 347–358.

(20)   C. S. Vogelsberg, F. J. Uribe-Romo, A. S. Lipton, S. Yang, K. N. Hou, S. Brown and M. A. Garcia-Garibay, "Ultrafast Rotation in an Amphidynamic Crystalline Metal Organic Framework," *Proceedings of the National Academy of Sciences of the United States of America*, 2017, **114**, 13613–13618.

(21)   S. Bracco, F. Castiglioni, A. Comotti, S. Galli, M. Negroni, A. Maspero and P. Sozzani, "Ultrafast Molecular Rotors and Their CO2 Tuning in MOFs with Rod-Like Ligands," *Chemistry - A European Journal*, 2017, **23**, 11210–11215.

(22)   J. Perego, S. Bracco, M. Negroni, C. X. Bezuidenhout, G. Prando, P. Carretta, A. Comotti and P. Sozzani, "Fast Motion of Molecular Rotors in Metal–Organic Framework Struts at Very Low Temperatures," *Nature Chemistry*, 2020, **12**, 845–851.

(23)   W. Danowski, T. van Leeuwen, S. Abdolahzadeh, D. Roke, W. R. Browne, S. J. Wezenberg and B. L. Feringa, "Unidirectional Rotary Motion in a Metal–Organic Framework," *Nature Nanotechnology*, 2019, **14**, 488–494.

(24)   G. S. Kottas, L. I. Clarke, D. Horinek and J. Michl, "Artificial Molecular Rotors," *Chemical Reviews*, 2005, **105**, 1281–1376.

(25)   Y. Yan, D. I. Kolokolov, I. Da Silva, A. G. Stepanov, A. J. Blake, A. Dailly, P. Manuel, C. C. Tang, S. Yang and M. Schröder, "Porous Metal–Organic Polyhedral Frameworks with Optimal Molecular Dynamics and Pore Geometry for Methane Storage," *Journal of the American Chemical Society*, 2017, **139**, 13349–13360.

(26)   A. N. Sokolov, D. C. Swenson and L. R. MacGillivray, "Conformational Polymorphism in a Heteromolecular Single Crystal Leads to Concerted Movement Akin to Collective Rack-and-Pinion Gears at the Molecular Level," *Proceedings of the National Academy of Sciences*, 2008, **105**, 1794–1797.

(27)   P. D. Jarowski, K. N. Houk and M. A. Garcia-Garibay, "Importance of Correlated Motions on the Low Barrier Rotational Potentials of Crystalline Molecular Gyroscopes," *Journal of the American Chemical Society*, 2007, **129**, 3110–3117.

(28)   M. E. Howe and M. A. Garcia-Garibay, "The Roles of Intrinsic Barriers and Crystal Fluidity in Determining the Dynamics of Crystalline Molecular Rotors and Molecular Machines," *The Journal of Organic Chemistry*, 2019, **84**, 9835–9849.

(29)   C. Lemouchi, K. Iliopoulos, L. Zorina, S. Simonov, P. Wzietek, T. Cauchy, A. Rodríguez-Fortea, E. Canadell, J. Kaleta, J. Michl, D. Gindre, M. Chrysos and P. Batail, "Crystalline Arrays of Pairs of Molecular Rotors: Correlated Motion, Rotational Barriers, and Space-Inversion Symmetry Breaking Due to Conformational Mutations," *Journal of the American Chemical Society*, 2013, **135**, 9366–9376.

(30)   J. T. Damron, J. Ma, R. Kurz, K. Saalwächter, A. J. Matzger and A. Ramamoorthy, "The Influence of Chemical Modification on Linker Rotational Dynamics in Metal-Organic Frameworks," *Angewandte Chemie International Edition*, 2018, **57**, 8678–8681.

(31)   W. Zhou and T. Yildirim, "Lattice Dynamics of Metal-Organic Frameworks: Neutron Inelastic Scattering and First-Principles Calculations," *Physical Review B*, 2006, **74**, 180301.

(32) M. R. Ryder, B. Van de Voorde, B. Civalleri, T. D. Bennett, S. Mukhopadhyay, G. Cinque, F. Fernandez-Alonso, D. De Vos, S. Rudić and J.-C. Tan, "Detecting Molecular Rotational Dynamics Complementing the Low-Frequency Terahertz Vibrations in a Zirconium-Based Metal-Organic Framework," *Physical Review Letters*, 2017, **118**, 255502.

(33) I. Liepuoniute, C. M. Huynh, S. Perez-Estrada, Y. Wang, S. Khan, K. N. Houk and M. A. Garcia-Garibay, "Enhanced Rotation by Ground State Destabilization in Amphidynamic Crystals of a Dipolar 2,3-Difluorophenylene Rotator as Established by Solid State ^{2}H NMR and Dielectric Spectroscopy," *The Journal of Physical Chemistry C*, 2020, **124**, 15391–15398.

(34) D. I. Kolokolov, H. Jobic, A. G. Stepanov, V. Guillerm, T. Devic, C. Serre and G. Férey, "Dynamics of Benzene Rings in MIL-53(Cr) and MIL-47(V) Frameworks Studied by ^{2}H NMR Spectroscopy," *Angewandte Chemie International Edition*, 2010, **49**, 4791–4794.

(35) D. I. Kolokolov, A. G. Stepanov and H. Jobic, "Guest Controlled Rotational Dynamics of Terephthalate Phenylenes in Metal–Organic Framework MIL-53(Al): Effect of Different Xylene Loadings," *The Journal of Physical Chemistry C*, 2014, **118**, 15978–15984.

(36) A. E. Khudozhitkov, H. Jobic, D. Freude, J. Haase, D. I. Kolokolov and A. G. Stepanov, "Ultraslow Dynamics of a Framework Linker in MIL-53 (Al) as a Sensor for Different Isomers of Xylene," *The Journal of Physical Chemistry C*, 2016, **120**, 21704–21709.

(37) A. E. Khudozhitkov, D. I. Kolokolov, A. G. Stepanov, V. A. Bolotov and D. N. Dybtsev, "Metal-Cation-Independent Dynamics of Phenylene Ring in Microporous MOFs: A ^{2}H Solid-State NMR Study," *The Journal of Physical Chemistry C*, 2015, **119**, 28038–28045.

(38) S. L. Gould, D. Tranchemontagne, O. M. Yaghi and M. A. Garcia-Garibay, "Amphidynamic Character of Crystalline MOF-5: Rotational Dynamics of Terephthalate Phenylenes in a Free-Volume, Sterically Unhindered Environment," *Journal of the American Chemical Society*, 2008, **130**, 3246–3247.

(39) D. I. Kolokolov, A. G. Stepanov, V. Guillerm, C. Serre, B. Frick and H. Jobic, "Probing the Dynamics of the Porous Zr Terephthalate UiO-66 Framework Using ^{2}H NMR and Neutron Scattering," *The Journal of Physical Chemistry C*, 2012, **116**, 12131–12136.

(40) S. Biswas, T. Ahnfeldt and N. Stock, "New Functionalized Flexible Al-MIL-53-X (X = -Cl, -Br, -CH 3 , -NO 2 , -(OH) 2) Solids: Syntheses, Characterization, Sorption, and Breathing Behavior," *Inorganic Chemistry*, 2011, **50**, 9518–9526.

(41) T. Loiseau, C. Serre, C. Huguenard, G. Fink, F. Taulelle, M. Henry, T. Bataille and G. Férey, "A Rationale for the Large Breathing of the Porous Aluminum Terephthalate (MIL-53) Upon Hydration," *Chemistry - A European Journal*, 2004, **10**, 1373–1382.

(42) Y. Liu, J.-H. Her, A. Dailly, A. J. Ramirez-Cuesta, D. A. Neumann and C. M. Brown, "Reversible Structural Transition in MIL-53 with Large Temperature Hysteresis," *Journal of the American Chemical Society*, 2008, **130**, 11813–11818.

(43) A. S. Munn, R. S. Pillai, S. Biswas, N. Stock, G. Maurin and R. I. Walton, "The Flexibility of Modified-Linker MIL-53 Materials," *Dalton Transactions*, 2016, **45**, 4162–4168.

(44) E. Stavitski, E. A. Pidko, S. Couck, T. Remy, E. J. M. Hensen, B. M. Weckhuysen, J. Denayer, J. Gascon and F. Kapteijn, "Complexity behind CO 2 Capture on NH 2 -MIL-53(Al)," *Langmuir*, 2011, **27**, 3970–3976.

(45) N. B. Shustova, T. C. Ong, A. F. Cozzolino, V. K. Michaelis, R. G. Griffin and M. Dincǎ, "Phenyl Ring Dynamics in a Tetraphenylethylene-Bridged Metal-Organic Framework: Implications for the Mechanism of Aggregation-Induced Emission," *Journal of the American Chemical Society*, 2012, **134**, 15061–15070.

(46) S. Balčiūnas, M. Šimėnas, D. Pavlovaitė, M. Kinka, F.-K. Shieh, K. C.-W. Wu, J. Banys and R. Grigalaitis, "Low-Frequency Dipolar Dynamics and Atmospheric Effects in ZIF-90 Metal–Organic Framework," *The Journal of Physical Chemistry C*, 2019, **123**, 631–636.

(47) E. B. Winston, P. J. Lowell, J. Vacek, J. Chocholoušová, J. Michl and J. C. Price, "Dipolar Molecular Rotors in the Metal–Organic Framework Crystal IRMOF-2," *Physical Chemistry Chemical Physics*, 2008, **10**, 5188.

(48) S. Devautour-Vinot, G. Maurin, C. Serre, P. Horcajada, D. Paula Da Cunha, V. Guillerm, E. De Souza Costa, F. Taulelle and C. Martineau, "Structure and Dynamics of the Functionalized MOF Type UiO-66(Zr): NMR and Dielectric Relaxation Spectroscopies Coupled with DFT Calculations," *Chemistry of Materials*, 2012, **24**, 2168–2177.

(49) A. Schönhals and F. Kremer, Theory of Dielectric Relaxation, in *Broadband Dielectric Spectroscopy*, ed. F. Kremer and A. Schönhals, Springer Berlin Heidelberg, Berlin, Heidelberg, 2003, pp. 1–33.

(50) S. Frunza, A. Schönhals, L. Frunza, P. Ganea, H. Kosslick, J. Harloff and A. Schulz, "Molecular Relaxation Processes in a MOF-5 Structure Revealed by Broadband Dielectric Spectroscopy: Signature of Phenylene Ring Fluctuations," *The Journal of Physical Chemistry B*, 2010, **114**, 12840–12846.

(51) A. Knebel, B. Geppert, K. Volgmann, D. I. Kolokolov, A. G. Stepanov, J. Twiefel, P. Heitjans, D. Volkmer and J. Caro, "Defibrillation of Soft Porous Metal-Organic Frameworks with Electric Fields," *Science*, 2017, **358**, 347–351.

(52) R. D. Horansky, L. I. Clarke, J. C. Price, T.-A. V. Khuong, P. D. Jarowski and M. A. Garcia-Garibay, "Dielectric Response of a Dipolar Molecular Rotor Crystal," *Physical Review B*, 2005, **72**, 014302.

(53) R. D. Horansky, L. I. Clarke, E. B. Winston, J. C. Price, S. D. Karlen, P. D. Jarowski, R. Santillan and M. A. Garcia-Garibay, "Dipolar Rotor-Rotor Interactions in a Difluorobenzene Molecular Rotor Crystal," *Physical Review B*, 2006, **74**, 054306.

(54) X. Jiang, Z. J. O'Brien, S. Yang, L. H. Lai, J. Buenaflor, C. Tan, S. Khan, K. N. Houk and M. A. Garcia-Garibay, "Crystal Fluidity Reflected by Fast Rotational Motion at the Core, Branches, and Peripheral Aromatic Groups of a Dendrimeric Molecular Rotor," *Journal of the American Chemical Society*, 2016, **138**, 4650–4656.

(55) M. R. Hansen, R. Graf and H. W. Spiess, "Solid-State NMR in Macromolecular Systems: Insights on How Molecular Entities Move," *Accounts of Chemical Research*, 2013, **46**, 1996–2007.

(56) H. W. Spiess, "Molecular Dynamics of Solid Polymers as Revealed by Deuteron NMR," *Colloid & Polymer Science*, 1983, **261**, 193–209.

(57) P. Serra-Crespo, M. A. van der Veen, E. Gobechiya, K. Houthoofd, Y. Filinchuk, C. E. A. Kirschhock, J. A. Martens, B. F. Sels, D. E. De Vos, F. Kapteijn and J. Gascon, "NH 2 -MIL-53(Al): A High-Contrast Reversible Solid-State Nonlinear Optical Switch," *Journal of the American Chemical Society*, 2012, **134**, 8314–8317.

(58) E. Gedat, A. Schreiber, J. Albrecht, Th. Emmler, I. Shenderovich, G. H. Findenegg, H.-H. Limbach and G. Buntkowsky, "^{2} H-Solid-State NMR Study of Benzene- d_6 Confined in Mesoporous Silica SBA-15," *The Journal of Physical Chemistry B*, 2002, **106**, 1977–1984.

(59) F. H. Larsen, Simulation of Molecular Motion of Quadrupolar Nuclei in Solid-State NMR Spectra, in *Annual Reports on NMR Spectroscopy*, Elsevier, 2010, vol. 71, pp. 103–137.

(60) A. E. Aliev, S. E. Mann, A. S. Rahman, P. F. McMillan, F. Corà, D. Iuga, C. E. Hughes and K. D. M. Harris, "High-Resolution Solid-State ^{2}H NMR Spectroscopy of Polymorphs of Glycine," *The Journal of Physical Chemistry A*, 2011, **115**, 12201–12211.

(61) R. J. Schadt, E. J. Cain and A. D. English, "Simulation of One-Dimensional Deuteron NMR Line Shapes," *The Journal of Physical Chemistry*, 1993, **97**, 8387–8392.

(62) J. Leisen, A. Ohlemacher, C. Boeffel and H. W. Spiess, "Molecular Dynamics in Side-Group Polymers with and without Liquid Crystalline Phases from ^{2}H NMR," *Berichte der Bunsengesellschaft für physikalische Chemie*, 1993, **97**, 1306–1311.

(63) U. Pschorn, H. W. Spiess, B. Hisgen and H. Ringsdorf, "Deuteron NMR Study of Molecular Order and Motion of the Mesogenic Side Groups in Liquid-crystalline Polymers," *Die Makromolekulare Chemie*, 1986, **187**, 2711–2723.

(64) M. Wehrle, G. P. Hellmann and H. W. Spiess, "Phenylene Motion in Polycarbonate and Polycarbonate/Additive Mixtures," *Colloid & Polymer Science*, 1987, **265**, 815–822.

(65) L. A. O'Dell and C. I. Ratcliffe, Quadrupolar NMR to Investigate Dynamics in Solid Materials, in *eMagRes*, ed. R. K. Harris and R. L. Wasylishen, John Wiley & Sons, Ltd, Chichester, UK, 1996, pp. 1–16.

(66) F. Moreau, D. I. Kolokolov, A. G. Stepanov, T. L. Easun, A. Dailly, W. Lewis, A. J. Blake, H. Nowell, M. J. Lennox, E. Besley, S. Yang and M. Schröder, "Tailoring Porosity and Rotational Dynamics in a Series of Octacarboxylate Metal-Organic Frameworks," *Proceedings of the National Academy of Sciences*, 2017, **114**, 3056–3061.

(67) V. Haigis, F.-X. Coudert, R. Vuilleumier, A. Boutin and A. H. Fuchs, "Hydrothermal Breakdown of Flexible Metal–Organic Frameworks: A Study by First-Principles Molecular Dynamics," *The Journal of Physical Chemistry Letters*, 2015, **6**, 4365–4370.

(68) R. Gaillac, P. Pullumbi, K. A. Beyer, K. W. Chapman, D. A. Keen, T. D. Bennett and F.-X. Coudert, "Liquid Metal–Organic Frameworks," *Nature Materials*, 2017, **16**, 1149–1154.

(69) R. Dovesi, A. Erba, R. Orlando, C. M. Zicovich-Wilson, B. Civalleri, L. Maschio, M. Rérat, S. Casassa, J. Baima, S. Salustro and B. Kirtman, "Quantum-mechanical Condensed Matter Simulations with CRYSTAL," *WIREs Computational Molecular Science*, 2018, **8**, e1360.

(70) J. P. Perdew, K. Burke and M. Ernzerhof, "Generalized Gradient Approximation Made Simple," *Physical Review Letters*, 1996, **77**, 3865–3868.

(71) S. Grimme, S. Ehrlich and L. Goerigk, "Effect of the Damping Function in Dispersion Corrected Density Functional Theory," *Journal of Computational Chemistry*, 2011, **32**, 1456–1465.

(72) S. Grimme, J. Antony, S. Ehrlich and H. Krieg, "A Consistent and Accurate Ab Initio Parametrization of Density Functional Dispersion Correction (DFT-D) for the 94 Elements H-Pu," *The Journal of Chemical Physics*, 2010, **132**, 154104.

(73) M. F. Peintinger, D. V. Oliveira and T. Bredow, "Consistent Gaussian Basis Sets of Triple-Zeta Valence with Polarization Quality for Solid-State Calculations," *Journal of Computational Chemistry*, 2013, **34**, 451–459.

(74) T. Ahnfeldt, D. Gunzelmann, T. Loiseau, D. Hirsemann, J. Senker, G. Férey and N. Stock, "Synthesis and Modification of a Functionalized 3D Open-Framework Structure with MIL-53 Topology," *Inorganic Chemistry*, 2009, **48**, 3057–3064.

(75) J. Vandevondele, M. Krack, F. Mohamed, M. Parrinello, T. Chassaing and J. Hutter, "Quickstep: Fast and Accurate Density Functional Calculations Using a Mixed Gaussian and Plane Waves Approach," *Computer Physics Communications*, 2005, **167**, 103–128.

(76) G. Bussi, D. Donadio and M. Parrinello, "Canonical Sampling through Velocity Rescaling," *The Journal of Chemical Physics*, 2007, **126**, 014101.

(77) S. Goedecker, M. Teter and J. Hutter, "Separable Dual-Space Gaussian Pseudopotentials," *Physical Review B*, 1996, **54**, 1703–1710.

(78) S. Canossa, A. Gonzalez-Nelson, L. Shupletsov, M. Del Carmen Martin and M. A. Van Der Veen, "Overcoming Crystallinity Limitations of Aluminium Metal-Organic Frameworks by Oxalic Acid Modulated Synthesis," *Chemistry – A European Journal*, 2020, **26**, 3564–3570.

(79) L. C. M. Van Gorkom, J. M. Hook, M. B. Logan, J. V. Hanna and R. E. Wasylishen, "Solid-state Lead-207 NMR of Lead(II) Nitrate: Localized Heating Effects at High Magic Angle Spinning Speeds," *Magnetic Resonance in Chemistry*, 1995, **33**, 791–795.

(80) A. Bielecki and D. P. Burum, "Temperature Dependence of 207 Pb MAS Spectra of Solid Lead Nitrate. An Accurate, Sensitive Thermometer for Variable-Temperature MAS," *Journal of Magnetic Resonance, Series A*, 1995, **116**, 215–220.

(81) I. Hung and Z. Gan, "On the Practical Aspects of Recording Wideline QCPMG NMR Spectra," *Journal of Magnetic Resonance*, 2010, **204**, 256–265.

(82) R. L. Vold and G. L. Hoatson, "Effects of Jump Dynamics on Solid State Nuclear Magnetic Resonance Line Shapes and Spin Relaxation Times," *Journal of Magnetic Resonance*, 2009, **198**, 57–72.

(83) W. I. F. David, K. Shankland, J. Van De Streek, E. Pidcock, W. D. S. Motherwell and J. C. Cole, "*DASH* : A Program for Crystal Structure Determination from Powder Diffraction Data," *Journal of Applied Crystallography*, 2006, **39**, 910–915.

(84) K. Momma and F. Izumi, "*VESTA 3* for Three-Dimensional Visualization of Crystal, Volumetric and Morphology Data," *Journal of Applied Crystallography*, 2011, **44**, 1272–1276.

(85) X. Jiang, H. B. Duan, S. I. Khan and M. A. Garcia-Garibay, "Diffusion-Controlled Rotation of Triptycene in a Metal-Organic Framework (MOF) Sheds Light on the Viscosity of MOF-confined Solvent," *ACS Central Science*, 2016, **2**, 608–613.

Chapter 5

Exploration of free energy profile and mechanism of long-range rotor dynamics in NO$_2$-MIL-53(Al) using force field molecular dynamics

Abstract

By tuning the rotor's steric environment and free pore space in metal–organic frameworks, a large variety of rotor dynamics can appear. Nitro-functionalized MIL-53 is a terephthalate linker-based MOF that shows coupled rotor dynamics between the neighboring linkers along the pore direction. In this chapter, we use classical molecular dynamics up to 622 supercells to investigate the free energy profiles of neighboring linkers and their dynamics in NO$_2$-MIL-53. Interestingly, we observe an *PNPNPNPN*.... arrangement pattern with fixed conformation *P*=nearly planar and *N*=non-planar, for the linkers in a row along the pore direction in the MOF. We identified correlated linker dynamics emerging among the neighboring linkers along the pore. Due to 180° rotational flips of the planar linkers along the pore 1) a change in the width of librations in their direct neighbors (*PN*) is observed; 2) additionally, their next nearest neighbors which are also planar linkers (*PP*) rotate between 0° and ±180° to attain aligned conformations between them like (0°, 0°) or (±180°, ±180°). The presence of correlated dynamics in these dipolar linkers over long-length scales occurring at nanoseconds timescales is desirable for applications in ferroelectric switching in the presence of an electric field and this work provides insight into the design for such applications.

5.1 Introduction

The flexibility and porosity of metal–organic frameworks (MOFs) offer great potential to demonstrate the dynamic nature of MOFs. They provide a unique platform for embedding molecular rotors into their crystalline lattices. In MOFs, organic linkers connecting the metal nodes often act as rotors and these can be spaced at tunable distances. The linker dynamics of MOFs have a direct impact on properties like gas adsorption and separation.[1–6] These molecular rotors' precise and predictable arrangement while retaining their rotational mobility is crucial for harnessing their collective motion in practical applications.

So far rational design of rotor-MOFs aims for obtaining fast rotation of organic rotors in the frameworks.[7–10]. But we are specifically interested in correlated or collective dynamics between rotors. Recent work by Perego J et al shows the dipolar motion of linkers in Al-FTR-F2 (fluorine functionalized) MOF even at low temperatures of 2 K and this is attributed to the lower energy barriers due to correlated motion involving other neighboring rotors.[11]To fully exploit the potential of molecular rotors, it is necessary to engineer correlated rotor dynamics and achieve cooperative functional motion. Structural factors that can influence the rotor dynamics in MOFs include the size and structural symmetry of the organic linkers, the availability of free pore space in the MOFs, and the chemical nature of the axle and the rotor (axle: the portion of the molecule that carries the rotator and about which the rotator turns).[12]

In chapter 4 of this thesis, by tuning the pore space and linker functionalization in the MIL-53(Al) family with terephthalate linkers, we varied the degree of steric hindrance between the rotors. The two extremes of linker dynamics observed are unhindered rotation of phenylene units in steps of π in unfunctionalized MIL-53 and no rotation of linkers in the amino functionalized phenylene units due to steric hindrance in narrow pore configuration. In between the two extremes we observed coupled linker dynamics between neighboring linkers along the pore direction emerging for nitro-functionalized phenylene linkers. The coupled linker dynamics observed in NO_2-MIL-53 is based on ab initio molecular dynamics (AIMD) simulations of a 211 unit cell. In a 211 unit cell, because of the periodic boundary conditions there are only two rotating linkers per MOF chain along the pore direction. Hence, it was not possible to explore the long-range effects of this coupled linker dynamics or the length up to which these linker interactions can be seen in NO_2-MIL-53. Additionally, due to the high computational cost of the ab initio calculations, long simulation times couldn't be reached which prevented the reliable determination of the free energy profile for this coupled linker dynamics in NO_2-MIL-53. The goal of this chapter is to understand the long-range linker dynamics and free energy profiles of rotational dynamics in NO_2-MIL-53 by developing a force field and use it for the classical molecular dynamics (MD) simulations in this work.

In this chapter, we developed and validated a force field using the AIMD data of 211 unit cell which can predict the rotational linker dynamics for NO_2-MIL-53. Using the developed force field, we performed classical MD simulations for larger supercells of 422 and 622. From the MD data obtained, we discuss the free energy profiles and the long-range effects of rotational angle changes of linkers on their neighboring linkers along the pore direction of the MOF. Additionally, for the linkers along the pore direction, a specific stacking pattern with fixed conformations is observed. The rotational mechanism to maintain this stacking pattern is proposed and discussed in terms of the energetics and time delay between the

linker rotations.

5.2 Force Field (FF) Development

To be able to obtain the free energy profile and numerical analysis of rotational linker dynamics in NO_2-MIL-53(Al), we need to reach longer simulation times and bigger unit cells. Due to the high computational cost of the AIMD calculations, this is not possible with AIMD. Hence, we developed a force field that is generated specifically for predicting the rotational linker dynamics in this MOF. The force field was generated with the QuickFF protocol, a program that can be used for deriving force fields from ab initio inputs.[13, 14] The force field energy consists of three contributions: analytical covalent, electrostatic and van der Waals (vdW) force field terms. The covalent interactions are described in terms of bonds, bends (angles), torsions, out-of-plane distances and cross terms that explicitly couple different internal coordinates in the structure. In the FF generated by QuickFF, the parameters in analytical expressions for these terms are fitted to reproduce the ab initio equilibrium structure and the Hessian matrix. The electrostatic part is based on the atomic charges and here we used Minimal Basis Iterative Stockholder (MBIS) charges.[15] The vdW interactions are modelled by parameters taken from the MM3 model from Allinger et al.[16] In the terephthalate linkers, the benzene rings rotate with respect to the carboxyl groups and this is represented by a change in dihedral angles O_CA C_CA C_PC C_N and O_CA C_CA C_PC C_PH indicated in Figure 5.A.1. In this force field, the torsion for these dihedrals is fitted on the deformation energies for small deviations from the equilibrium as encoded in the Hessian. However, this does not account for full rotations of the linker that are subject of this work.

So, the force field obtained from the QuickFF protocol was then refined (specifically the dihedral angles that vary during rotation of the linkers) by a rigid rotational energy scan of NO_2-MIL-53 in which the dihedral O_CA C_CA C_PC C_N was varied between $-180°$ and $180°$. Note that the force field used in the refinement is the original QuickFF obtained FF while excluding the terms for original O_CA C_CA C_PC C_N dihedrals (as the O_CA C_CA C_PC C_N dihedrals are fitted in this refinement). The energy of these different conformations was calculated with both ab initio (AI) and QuickFF obtained force field and a fourier series functional form was fitted to the difference in the energies between AI and FF. The parameters of the obtained functional form for the dihedrals is added to the final force field which is used in this work to predict the rotational linker dynamics. Detailed steps and the various software used at different steps in the force field generation and fitting procedures can be found in the Appendix (Section 5.A.1).

5.3 Force Field (FF) Validation

We validate the obtained Force field using different methods like comparing the geometry after optimization with FF to that of experimental geometry and the frequencies obtained in DFT with those obtained with FF. Additionally we also validate the linker dynamics for a 211 unit cell with the developed FF via comparison of previously obtained linker dynamics with AIMD for NO_2-MIL-53 in one our previous works.[17]

5.3.1 Geometry Optimization

The obtained FF should accurately predict the geometry of the Nitro functionalized MIL-53 structure. For that, we compare the FF simulated cell parameters with the experimental values of large pore structure of NO_2-MIL-53 (see Table 5.1). The FF simulated structure optimizes to an orthorhombic shape, in agreement with the experimental structure. The deviation between experimental and simulated lattice parameters a, b and c is 0.2%, 6.5% and 3.1% respectively; where deviation on b is the highest among other directions. This is due to the inherent flexibility of the MIL-53 framework in the plane of the wine-rack motif i.e, *bc* plane perpendicular to the inorganic chain. However, the overall predicted structure from the geometry optimization with FF is similar to the experimental structure.

Table 5.1: Comparison of Lattice Parameters of NO_2-MIL-53(Al) structure.

Lattice Parameters	Experimental[18]	FF simulated
a [Å]	13.298	13.331
b [Å]	13.320	14.188
c [Å]	16.382	15.877
[deg]	90	90
[deg]	90	90
[deg]	90	89.98

5.3.2 Comparison of Force Field (FF) frequencies with DFT frequencies

We perform the next validation of the FF by comparing the DFT calculated normal-mode frequencies to that of the FF frequencies as shown in Figure 5.1. They show a very good correlation at all ranges of frequencies. We further compute the Internal energy, the Helmholtz free energy, the entropy and the heat capacity of the NO_2-MIL-53 211 unit cell, as a function of temperature using the computed normal mode frequencies from both DFT and FF. (Figure 5.A.3 in the Appendix) All these thermodynamic properties are reproduced very well with FF frequencies when compared to the DFT computed properties. Validation of the FF with geometry optimization and frequency comparison shows the FF accurately reproduces the experimental geometries, unit cell dimensions and frequencies of normal modes.

5.3.3 Definition of regions indicated in 2D free energy surface plots

Linker dynamics between the neighboring linkers is key in this study, hence we use 2-dimensional free energy surface (FES) plots to describe the phase space for the linker dynamics. The rotational angle data of linkers obtained from molecular dynamics simulations is used to plot the free energy surface (FES) using the ThermoLIB package.[19] The FES estimate was obtained by combining the simulations through the weighted histogram analysis method (WHAM).[20, 21] WHAM is widely used to obtain accurate free energies from biased molecular simulations; in this work we used WHAM for unbiased molecular dynamics simulations.
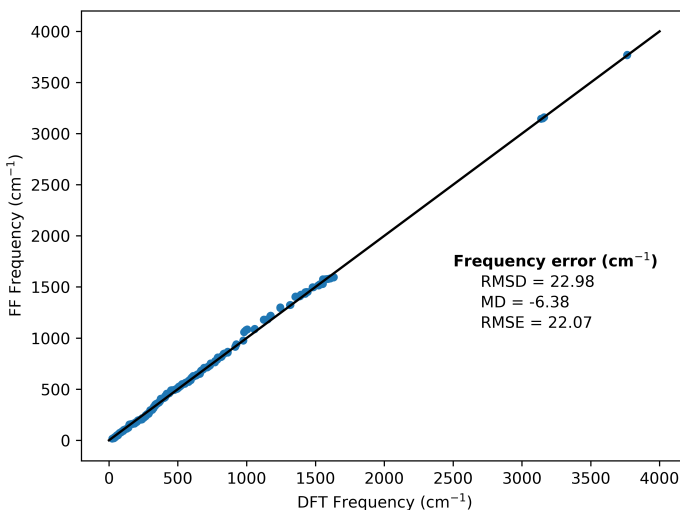
Figure 5.1: Comparison of DFT and FF calculated frequencies. Three measures of error between DFT and force field frequencies are indicated: RMSD the root-mean-square deviation as a measure of total error, MD the mean deviation as a measure of the systematic error, RMSE the root-mean-square error as a measure of the non-systematic error.

The notation of regions used to describe the phase space for all the FES in this work are described below. The X and Y axis in these 2D FES plots indicate the rotational angles of direct neighbors (Angle of Linker a and Linker b) for all the four chains combined. The regions in the FES plots are labeled into three types PN, NN and PP based on the orientation of linkers.

1. **Region PN, "Planar-NonPlanar"** indicates the orientation of linkers at the center of the energy minima where one is almost planar (i.e., rotation angle of linker a= 0°/180°) and the other linker (angle b) is at an acute (angle between 0° and 90° or 0° and −90°) or obtuse angle (angle between 90° and 180° or −90° and −180°). For instance, in Figure 5.4 at 300 K, rotation angle of linker a is close to 0° or ±180° while the angle of linker b is either 50° or 135° and vice versa.

2. **Region NN, "NonPlanar-NonPlanar"** is where both the linkers at the center of energy minima are acute or obtuse angles but neither of the linkers is at a planar orientation (i.e, ≠ 0°/±180°). For example at 300 K in Figure 5.4, (angle of linker a, angle of linker b) are (−25°, 25°). Similar examples are seen in Figure 5.A.4a and 5.A.4b in the appendix, (angle of linker a, angle of linker b) are (−140°, 25°) or (140°, 150°).

3. **Region PP, "Planar-Planar"** where both the linkers at the center of energy minima are at a planar orientation (i.e, 0°/±180°). Examples of this conformation are seen in this work for alternate neighbors in a single chain along the pore direction for a 422 and 622 unit cell which will be discussed later in the text.

5.3.4 Comparison of molecular dynamics based on ab initio and FF calculations

The goal of this work is to use the obtained FF for studying the rotational linker dynamics in NO_2-MIL-53 for bigger supercells. Hence to validate the FF, we did MD simulations with the FF for a 211 supercell and compared these results with AIMD results for the same supercell. These AIMD results were already published in one of the previous works on linker dynamics in NO_2-MIL-53. From the MD simulations with AIMD and FF, the rotational angle of the Nitro terephthalate linkers is obtained using a python code used in the previous work.[17] This rotation angle is defined as the angle between the benzene ring plane and the (011) plane, taking 0° as the conformation with the functional group in the positive [100] direction. The notation for the rotation angles used is shown in Figure 5.2.
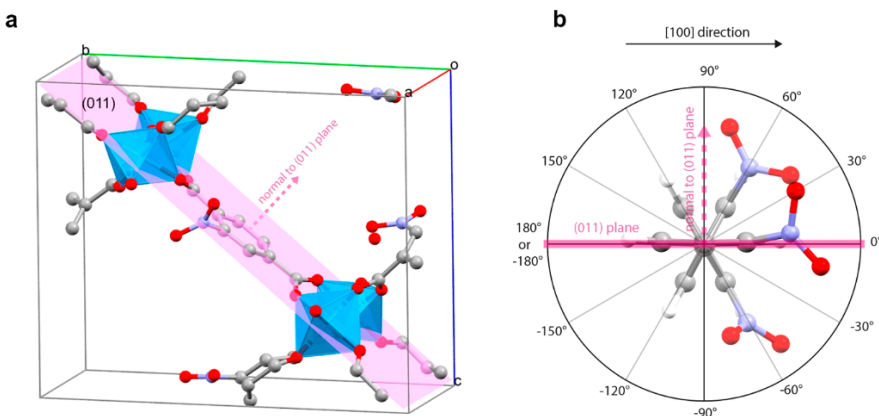
Figure 5.2: a) Unit cell of NO2-MIL-53(Al) with central linker in 0° rotation with respect to (011) plane (pink); hydrogens omitted for clarity. b) Rotation angle is defined as the angle between benzene ring plane and (011) plane, taking 0° as the conformation with the functional group pointing in the positive [100] direction. The sign of the angle is assigned based on the direction normal of the reference plane. Reproduced from ref [17].

Previously with the AIMD simulation for a 211 unit cell, we were able to reach a simulation time of only 40 ps at three temperatures of 300 K, 450 K and 700 K. In this work for comparison with AIMD results, FF MD simulations were done for a simulation time of 1 ns for the same 211 unit cell at 300 K and 450 K. The 211 unit cell has four sets of chains in the unit cell where each chain has two rotating linkers that are direct neighbors along the pore direction.(see Figure 5.3) Hence a total of eight linkers are present in the unit cell. The rotational angle data from AIMD and FF is used to plot the free energy surface (FES) using the ThermoLIB package as mentioned previously.[19]

5.3.4.1 AIMD

In AIMD simulations, at low temperature (300 K, Figure 5.4), the width of the FES minima is around 10°. With an increase in temperature (see the Appendix Figure 5.A.4), the minima
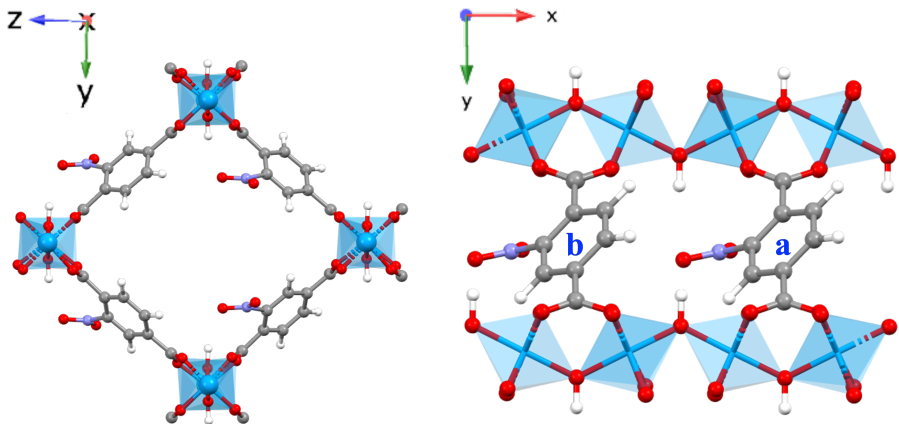
Figure 5.3: Figure showing the pore of the 211 unit cell (left) and (right) two rotating linkers (*a*,*b*) along the pore direction (x) in a single chain in the 211 unit cell.
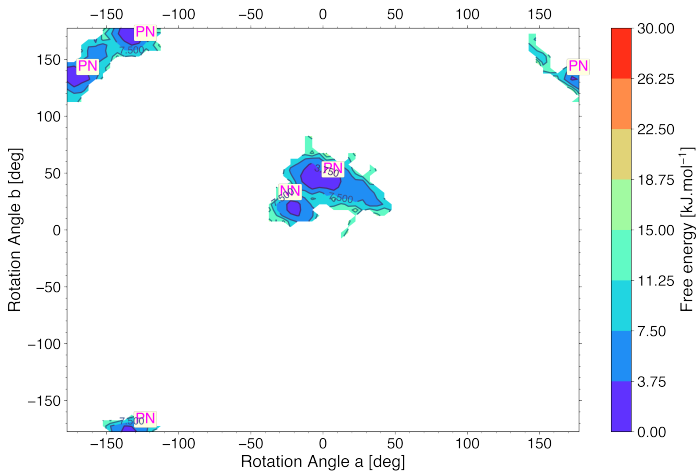

Figure 5.4: Free energy surface (FES) obtained with AIMD from rotational angle data of neighboring linkers in a 211 unit cell at 300 K.

in the FES become wider (20° to 30°), due to the increased librations of the linkers at high temperatures. At 300 K, the lowest energy minima is majorly seen at orientations in *PN* regions where at least one linker is planar, and the other linker is oriented at 50° or ±135°. Region *NN* with acute angles of (−25°, 25°) is also observed in scarce instances at 300 K. With an increase in temperature to 450 K and 700 K region *NN* becomes more prominent, the planar orientation of linkers gradually disappears and we see oblique angles for the linkers i.e., centered around (−140°, 25°) or (140°, 150°).

5.3.4.2 FF

The FES from 1ns FF simulations at two temperatures 300 K and 450 K are shown in Figure 5.5 and 5.A.5 in the appendix. Considering first the FES at 300 K we observe that the minima are wider and mostly seen at orientations in region *PN* where linker *a* is planar (0° or ±180°), and the other linker *b* is oriented between 80° and 130° or ±50° to ±100°. Some sampling of region *NN* is also observed with an acute angle for both linkers *a*, *b* centered around (30°, 30°). With an increase in temperature, region *NN* becomes prominent and centered around (30°, 30°) and (−150°, −150°). Note here, region *NN* may not be a minima, but it is a transition state between the two adjacent *PN* minima regions. This is confirmed later in the longer MD simulations of a 422 unit cell in Figure 5.8.

Overall, looking at the free energy profiles for both AIMD and FF, the linkers have specific preferred orientations. At room temperature of 300 K, we see that the "Planar-NonPlanar" configuration for the sets of neighboring linkers is dominant in both AIMD and FF simulations, showing that they are in agreement. The evolution of free energy profiles with temperature in FF is consistent with that of AIMD. With the increase in temperature/thermal energy, the "Planar-NonPlanar" configuration for the linkers becomes unfavorable and the "NonPlanar-NonPlanar" configuration is increasingly seen. The difference between AIMD and FF FES plots is that, FF underestimates the energy associated with the orientation of a linker at ±90°. So, there is a difference in the location of the *PN* minima region between AIMD and FF simulations, especially the *N* angles. In FF simulations, we see a single broad distribution for *PN* region and *N* angle ranging from ±50° to ±130°, whereas in AIMD two different very narrow distributions which are centered at ±50° and ±135° are observed. It is also important to note here that the simulation time for AIMD was much shorter than the FF molecular dynamics simulations. This would mean that the sampling in AIMD is much less reliable than FF, which could be the reason for the appearance of
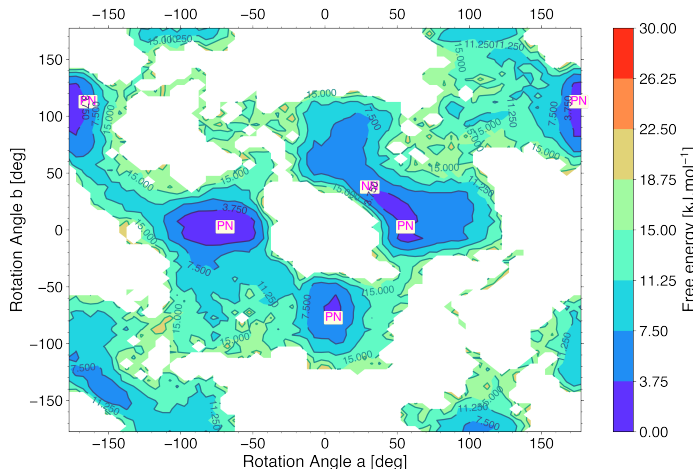

Figure 5.5: Free energy surface (FES) obtained with FF from rotational angle data of neighboring linkers in a 211 unit cell at temperature 300 K.

narrow minima in AIMD FES (Figure 5.4). Moreover, the region that is most energetically unfavorable is the same in AIMD and FF mainly having both linker *a* and *b* at (0°, 0°), (±180°, ±180°), (0°, 0°), (±180°, 0°), (0°, ±180°), (90°, −90°), and (−90°, 90°). With this in consideration, we do not make conclusions based on the magnitude of non-planar angles (N) in *PN*, but only on the type of energy minima regions in the FES plots (i.e., *PN* or *NN*) for the "1, 2" and "1, 3" neighbors. Additionally, how rotation of a specific linker affects the librations and rotational changes in its neighbors is also analyzed.

5.4 Results and Discussion

The AIMD and FF simulations for a 211 unit cell have only two rotating linkers per MOF chain along the pore direction due to the periodic boundary conditions, hence it is not possible to observe long-range linker dynamics along the pore. Using the generated and validated FF, we perform MD simulations for larger simulation times and supercells of 422 and 622 unit cells. In 422 and 622 unit cells there are four and six rotating linkers per MOF chain along the pore direction respectively. With the help of free energy profiles and MD time trajectories for supercells, we observe and analyze the impact of long range linker interactions on their dynamics specifically along the pore direction.

5.4.1 422 unit cell

Note that, we only discuss here in detail neighboring interactions between linkers along the pore direction (along x axis) in a single chain of linkers rather than neighboring interactions between four other neighbors perpendicular to the pore direction (along y and z axis). Based on a qualitative assessment of the time traces of neighboring linkers along y and z axis (i.e., neighbors across the pore direction), we conclude that no correlations persist between the linkers across the pore and in a few cases it is inconclusive. Examples of the perpendicular neighbor time traces are shown and discussed in the Appendix section 5.A.4.1.

The MD simulation for 422 unit cell was done for a simulation time of 70 ns at a temperature of 300 K. There will be a total of 16 chains and four rotating linkers per chain along the pore direction, hence a total of 64 linkers in the 422 unit cell (see Figure 5.A.6). Figure 5.6 shows a schematic of a part of the 422 unit cell i.e., a single pore in the unit cell showing four chains of linkers and Figure 5.7 zooms in on a single chain along the pore direction. Figure 5.7 shows the representation of "1, 2" and "1, 3" type neighbors along the pore direction considered in a 422 unit cell. We show in the results two different kinds of plots from the rotational angle data obtained in the MD simulation. First are the free energy surface (FES) plots with the rotational angle of direct neighbors or "1, 2" type (includes linker pairs *ab*, *bc*, *cd*, *ad*) neighbors along the pore as collective variables and alternate neighbors or "1, 3" type (includes linker pairs ac, bd) neighbors along the pore as collective variables. The second is the time traces of the rotation angle for all four rotating linkers along the pore direction.
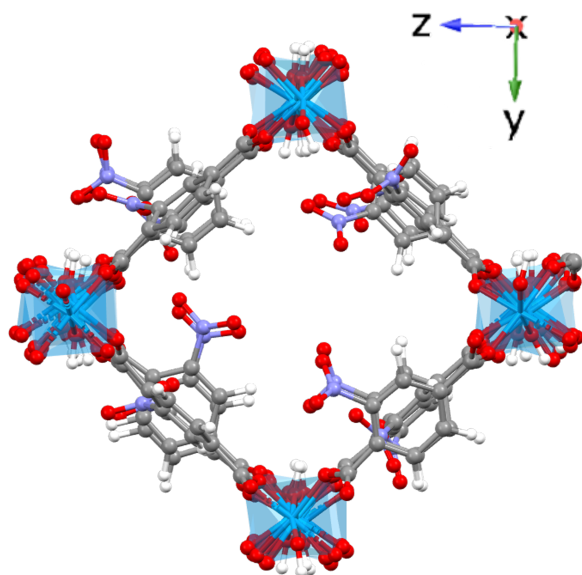
Figure 5.6: Part of the 422 unit cell of NO_2-MIL-53 MOF i.e, single pore of the 422 unit cell consisting of four chains of linkers.
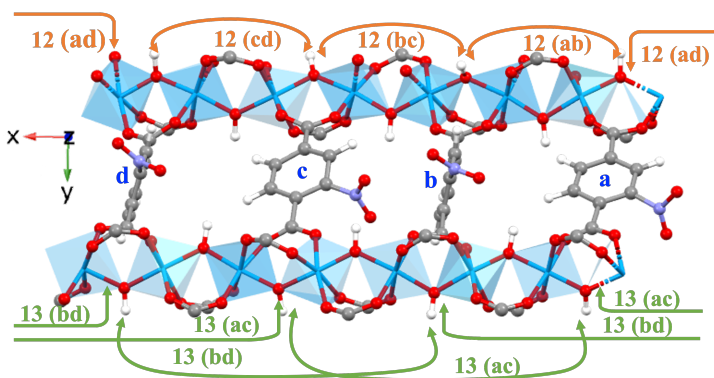

Figure 5.7: Representation of direct neighbors "1, 2" type (orange: includes pairs *ab*, *bc*, *cd*, *ad*) and alternate neighbors "1, 3" type (green: includes pairs *ac*, *bd*) in a single chain along the pore direction (x) for a 422 unit cell.

### 5.4.1.1 Free Energy Surfaces of "1, 2" and "1, 3" type neighbors
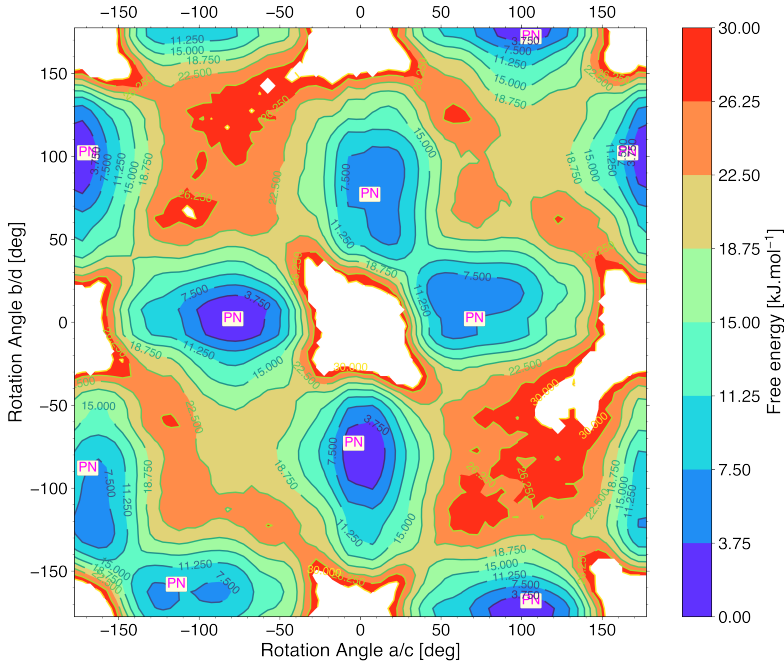
Figure 5.8: Free energy surface (FES) for a 422 unit cell considering rotational angle data of "1, 2" type neighbors as collective variables.

The Free energy surfaces (FES) of the 422 unit cell in Figure 5.8 and 5.9 give an overall picture of the linkers orientation along the complete trajectory of 70 ns and these plots were obtained from the rotational angle data of all the 16 chains of linkers in the 422 unit cell. In the Figure 5.8 with "1, 2" neighbors as collective variables, the minima regions are only of *PN* type where one linker is planar (0°/±180°) and the other linker is non-planar (here ±50° to ±100°/ ±80° to ±120°). In this case, the *PN* minima regions are wider than AIMD *PN* regions for a 211 unit cell and they are elliptical where short width librations are around ±20° and centered on 0°/±180° and long width librations are ~ ±50° centered on ±80° and ±100°. We don't see *NN* regions as minima even for long simulation times of the 422 unit cell at 300 K. Instead, they now occur as transition states between two adjacent *PN* regions (for example, between (0°,80°) and (80°,0°) in Figure 5.8) with a free energy of around 11.25 kJ/mol to 15 kJ/mol. But in the 211 unit cell we observed region *NN* in both AIMD and FF plots. This could be an effect of the smaller unit cell which imposes restrictions with respect to less number of rotating linkers combined with periodic boundary conditions. In the Figure 5.9 with alternate or "1, 3" neighbors as collective variables, the deepest minima are located along the diagonal and corners of the plot at [(−180°, −180°), (0°, 0°), (180°, 180°), (−180°, 180°), (180°, −180°), (−80°, −80°), (100°, 100°)]. This indicates "1, 3" neighbors are librating around the same type of rotational angle all along the trajectory. At the deepest minima, linkers "1, 3" type are parallel aligned
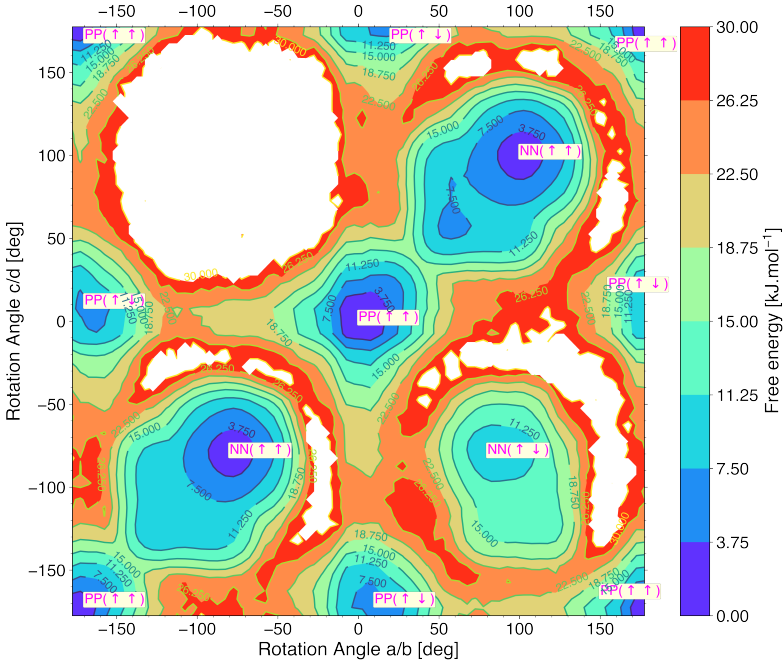
Figure 5.9: Free energy surface (FES) for a 422 unit cell considering rotational angle of "1, 3" type neighbors as collective variables.

(↑↑) and are either both planar PP(↑↑) (both rotational angles centered around 0° or ±180°) or non-planar NN(↑↑) (both rotational angles centered around −80° or 100°). The less deep minima for the planar conformations are located along the edges of the FES at [(0°, ±180°) and (±180°, 0°)]. The planar linkers of "1, 3" type at these minima (PP(↑↓)) are 180° apart in conformation and antiparallel aligned (↑↓) compared to the deepest minima planar conformations (PP(↑↑)) where the linkers have the same conformation. The PP(↑↓) regions have energy between 3.75 kJ/mol and 7.50 kJ/mol. For the non-planar linkers of "1, 3" type with minima centered at (−80°, −80°), (100°, 100°) (NN(↑↑) type); 180° apart or antiparallel (↑↓) conformations would be (−80°, 100°) and (100°, −80°). The energy for these regions indicated as NN(↑↓) in Figure 5.9 is 11.25 kJ/mol. This energy is higher than that of the deepest minima of the planar (PP(↑↑)), the non-planar conformations NN(↑↑) and the less deep minima planar conformations (PP(↑↓)). Note in Figure 5.9, the region where a/b = −150° to 0° and c/d = 30° to 180° is not sampled in the MD simulations of 422 unit cell. However this is equivalent to the sampled region of a/b = 30° to 180° and c/d = −150° to 0° because of the interchangeability of conformation of the linkers. Moreover, there is a region of large free energy barrier between the unsampled minima and the rest of the phase space as also seen from the equivalent conformations.

To summarize, from the FES plots of the linkers along the row i.e., linker a, linker b, linker c, linker d we know direct neighbors or "1, 2" type linkers are in PN configuration where one linker is planar (0° or ±180°) and the other linker is non-planar (here they vary

between ±50° and ±120°). Then for alternate neighbors or "1, 3" type, linkers are librating around the same configuration and parallel or antiparallel aligned meaning both linkers are planar ($PP(\uparrow\uparrow)$), $PP(\uparrow\downarrow)$ or non-planar ($NN(\uparrow\uparrow)$). Figure 5.10 is the time trace of a specific chain among the 16 chains in the 422 unit cell. Among the four linkers in Figure 5.10, for two of them (linkers *b,d*) we see a planar configuration librating around $a = 0°/\pm180°$, and the other two linkers (linkers *a,c*) librate between $b = -50°$ and $-120°$. Combining these results with the FES plots of linkers in Figure 5.8 and 5.9, we see linkers in the 422 unit cell are in an $PNPNPN...$ configuration meaning $abcdabcd... = PNPNPNPN.....$ where P = nearly planar and N = non-planar. Direct neighbors ("1, 2" type linkers) have different configurations P and N while alternate neighbors ("1, 3" type) have the same configuration i.e, P and P or N and N. This is also observed in other chains of linkers in the unit cell.
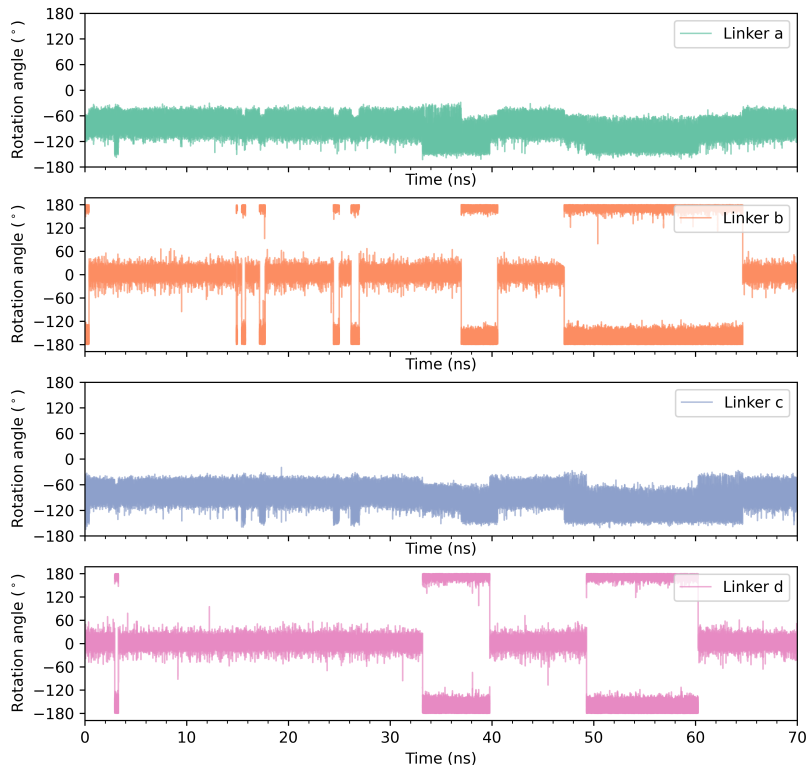

Figure 5.10: MD trajectory of the four linkers along the row for a specific chain in the 422 unit cell.

5.4.1.2 Effect of change in the rotational angle of linkers on its neighbors

FES plots show an overall picture of the conformation of the linkers, whereas the time traces of the rotational angles of the linkers provide insight into the correlated dynamics of the linkers. In Figure 5.10 the time trajectories of the rotational angles of a single row is shown,

we frequently see the rotation of linkers b and d between two planar configurations i.e., 0° and ±180°. This is similar for other rows in the chains of linkers in the 422 unit cell. We analyze the effect of these rotational changes on their neighbors of the same chain along the trajectory. We do this on the two kinds of neighbors i.e the "1, 2" and "1, 3" type.

"1, 2" type interactions   Figure 5.11a shows the time trajectory from 30 ns to 55 ns of the same chain shown in Figure 5.10. The timesteps where linker b and d are in the same conformation (parallel (↑↑) aligned states: (0°, 0°) or (±180°, ±180°)) are highlighted in gray regions and where they are 180° apart (antiparallel (↑↓) aligned states: (0°, ±180°) or (±180°, 0°)) in gold. In general, for parallel (↑↑) aligned states of linkers b and d, the width of the librations for linkers a and c is equal but with a shift in the average rotational angle (in ΔT01, ΔT23). For antiparallel (↑↓) aligned states of linkers b and d, the linkers a and c have either wider or narrower librations (in ΔT12, ΔT34). This relates to both "1, 2" and "1, 3" type interactions and is observed for all chains of linkers in the 422 unit cell (included in data repository). Figure 5.11a shows representative linker dynamics of all linkers in the 422 unit cell. Starting in region ΔT01, linkers b and d are at the same configuration (gray color) between −30° and 30° in a parallel (↑↑) aligned state centered at 0° and linkers a and c are librating between −50° and −110°. A snapshot of the positions of four linkers in region ΔT01 is shown in Figure 5.11b. At t1, linker d flips to a ±180° conformation leading to an antiparallel (↑↓) configuration of linkers b and d. At the same time the width of the librations change in its direct neighbors linkers a and c ("1, 2" type). The width of the librations becomes wider (from (−40° to −110°) to (−40° to −150°)) in linker a and narrower (from (−40° to −110°) to (−60° to −120°)) in linker c is observed. This is related to the direction of nitro group in linker d before and after the 180° flip at t1. In region ΔT01, linker c has only one nitro group pointing towards it (from linker b, (see Figure 5.11b)) whereas in region ΔT12, it has two nitro groups (from linkers b and d) pointing towards it (see Figure 5.11c); hence it is forced to librate narrowly yet more symmetrically around −90° than in region ΔT01. For linker a, in region ΔT01 there is one nitro group pointing towards it (from linker d, (see Figure 5.11b)), while in region ΔT12 there are no nitro groups pointing towards it (see Figure 5.11c), thus it is allowed more freedom resulting in wider librations than in region ΔT01.

At t2, linker b rotates to a ±180° conformation and both linkers b and d are now again in parallel (↑↑) aligned state. In region ΔT23, the width of librations for linkers a and c become equal, as of ΔT01. However in ΔT23, their average rotational angle is shifted compared to average angle in ΔT01. This is due to the position of the nitro groups of the "1, 2" type or direct neighboring linkers; for linkers a and c, in ΔT01 nitro group of direct neighbors points from left (Figure 5.11b), where as in ΔT23 the nitro groups are pointed from right (Figure 5.11d).

"1, 3" type interactions   The FES of "1, 3" type linkers in the Figure 5.9 indicates they are librating around the same rotational angle i.e, both are in planar conformations (PP (↑↑)) centered around 0° or ±180° or both are in non-planar conformations (NN(↑↑)) centered around −80° or 100°. On looking at various time trajectories for all the 16 chains in the 422 unit cell, linkers in planar conformations rotate between the two planar conformations i.e, 0° and ±180°. This is frequently seen, for instance in Figure 5.10 where linkers b and d flip between 0° and ±180°. In Figure 5.11a, following the time trajectory from 30 ns, linker d

(a)
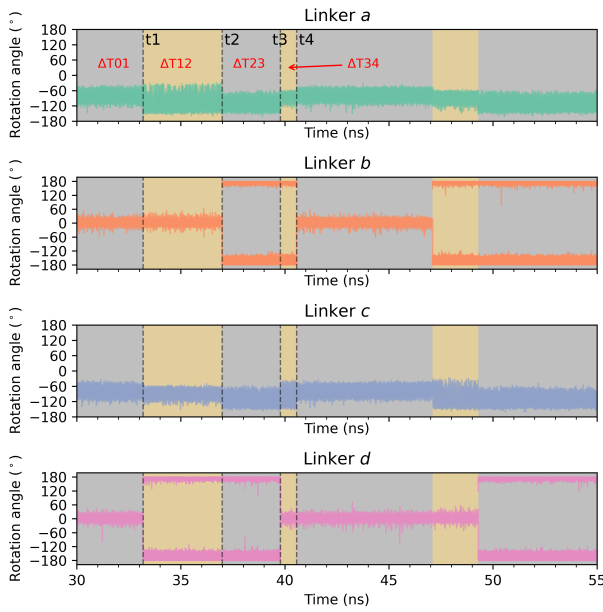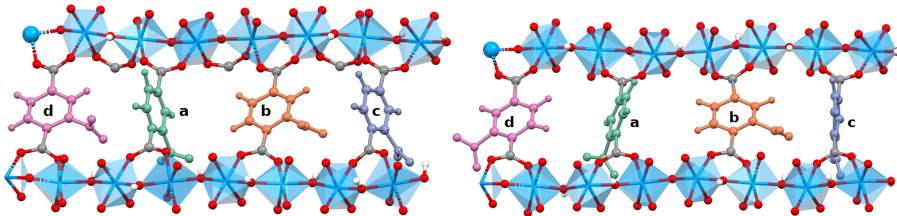
(b) Region ΔT01 at 32 ns
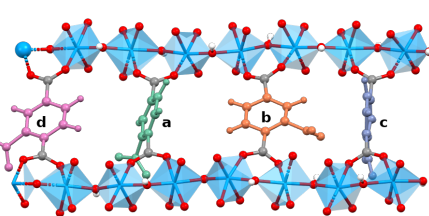
(c) Region ΔT12 at 35 ns
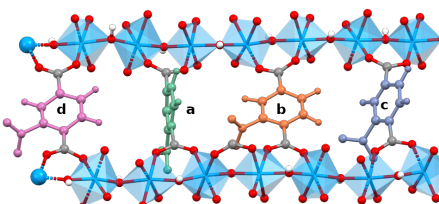
(d) Region ΔT23 at 37.5 ns
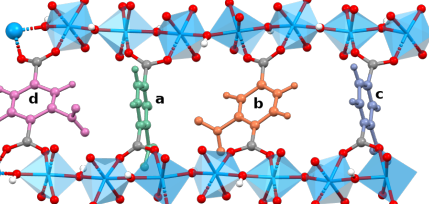
(e) Region ΔT34 at 40 ns

Figure 5.11: a) MD trajectory of linkers highlighting the changes in rotational angle flips of 180° in their neighboring linkers for a specific chain in the 422 unit cell. b-e) Conformations of all the four linkers in the chain in regions ΔT01, ΔT12, ΔT23, and ΔT34 at specific times highlighted in the MD trajectory.

rotates from 0° to ±180° at ~33 ns, which is then followed by rotation of linker *b* at ~37 ns; so a timegap of ~4 ns. Again at ~39.8 ns, linker *d* rotates back to 0° followed by linker *b* rotating back to 0° at ~40.8 ns; a time gap of ~1 ns. Hence, for the "1, 3" type neighbors we not only see frequent flips between the planar conformations but also the linker "3" type follows linker "1" type and the time between the rotation of these alternate neighbor linkers is around 4 ns to 9 ns in majority of chains in the 422 unit cell. The other situation we observed for "1, 3" type linkers is when a linker "1" type rotates from 0° to ±180° or vice versa, then the alternate neighbor linker "3" type doesn't follow unlike the previous case. This is due to the first event of linker "1" type rotation happening for a shorter time, < 1 ns and it flips back to its previous configuration as highlighted in Figure 5.A.12 (linker *b* and *d* in the Appendix). Ofcourse, as these are probablistic events, some exceptions could be seen, where linker "1" type angle changes by 180° (Figure 5.A.13 in appendix, linker *a*, rotation from 0° to −180° at ~35 ns) and continues to be in the same configuration for a longer time (~8 ns), but we don't see a change in the configuration of linker "3" type (Figure 5.A.13 linker *c*, no change in its conformation and continues to librate around 0°). Following a no change in the rotation angle of linker "3" type (here linker *c*), linker "1" type (here linker *a*) rotates back to 0° its original conformation before the change. Then considering "1, 3" type planar linkers together, they rotate between parallel aligned *PP*(↑↑) (in same planar conformations) and antiparallel aligned *PP*(↑↓) (180° apart planar conformations) states. Energetically, this is also observed in FES of "1, 3" neighbors in Figure 5.9, where parallel aligned states (*PP*(↑↑)) are the deepest minima along the diagonal and corners of the FES mentioned in 5.4.1.1 and antiparallel aligned states (*PP*(↑↓)) are less deep minima at the edges of the FES with energy upto 7.50 kJ/mol. Hence, alternate planar neighbors being in a 180° different conformation is possible but less favorable energetically. This is probably due to slightly increased electrostatic repulsion experienced by the linker in between from the two NO_2 groups of the two neighboring planar linkers when these two planar linkers are at different conformations of 0° and ±180°. This is the conformation of linkers *d*, *a* and *b* shown in Figure 5.11e. So, in the antiparallel (*PP*(↑↓)) aligned states for "1, 3" type neighboring linkers there is an instability and they achieve the parallel aligned (*PP*(↑↑)) conformations by either of the two planar linkers ("1" type or "3" type) rotating to match the conformation of the other linker. This delayed but coordinated rotation between "1, 3" type neighbors in NO_2-MIL-53(Al) is a probabilistic mechanism that happens over a time delay of the order of magnitudes of nanoseconds. For the "1, 3" type non-planar linkers centered around (−80°, −80°) or (100°, 100°) rotational flips of 180°, meaning change to (−80°, 100°) or (100°, −80°) is a very rare event observed in the MD trajectories. This can be understood in terms of the higher energy of these regions (*NN*(↑↓)) upto 11.5 kJ/mol when "1, 3" type non-planar linkers are in 180° apart conformations compared to the minima *NN*(↑↑) as already mentioned in Section 5.4.1.1.

To obtain the energy barrier for the 180° flips of a single planar linker, we zoom into one of the rotational flips and show an illustrative path followed on the FES during the flips. Figure 5.12a shows closely the rotational angle change of linker *d* between 33.17 ns and 33.21 ns for the same chain as in Figure 5.11a. The rotational flip occurs between the indicated dotted lines over a time of ~0.004 ns which is 4 ps. The conformational changes occuring during the rotational flip in linker *d* and its direct neighbors linkers *a* and *c* are shown as the rotational path on the FES with direct neighbors as collective variables in Figure 5.12b. Since linker *d* has two direct neighbors *a* and *c*, the transition path considering

(a)

(b)
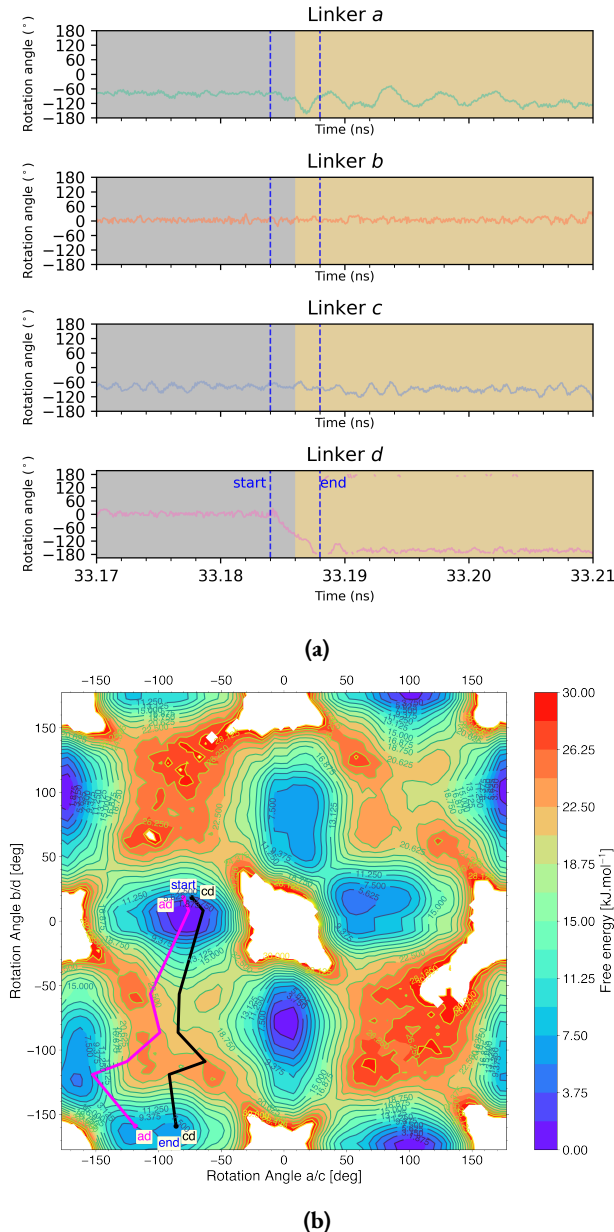
**Figure 5.12:** a) Zoomed in MD trajectory at t1 and between regions ΔT01 and ΔT12 (from Figure 5.11a). Dotted blue lines indicate the start and end of the rotational angle change of the planar linker *d*. b) FES of "1, 2" type neighbors showing an illustrative path of the 180° rotational angle change of planar linker *d* and the "*ad*" and "*cd*" pathway.

both the neighbors is shown during the flip from *start* to *end* for *ad* and *cd*. From the starting conformations in the minima at *start ad* to the final 180° apart conformation for linker *d* at *end ad*, the transition requires for linkers *ad* to overcome a transition state energy of around 24.375 kJ/mol. A similar transition path is also observed for linkers *cd*, with an energy barrier of 24.375 kJ/mol. The energy for these transition states is higher than the rotational energy barrier for a 180° rotation of nitro-substituted terephthalic acid molecule (17.1 kJ/mol) where neighboring interactions are not present but lower than experimentally obtained activation energy values for the NO_2-MIL-53 MOF (32.3 ± 1.3 kJ/mol) presented in chapter 4.

5.4.2 622 unit cell
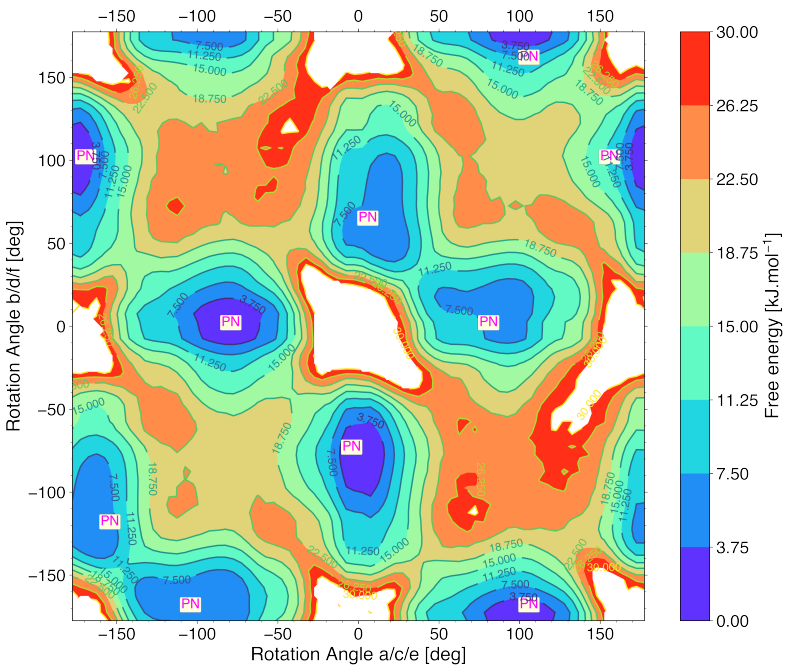
Figure 5.13: Free energy surface (FES) for a 622 unit cell considering rotational angle of "1, 2" type neighbors as collective variables.

To simulate structures closer to the experimental crystal structures, we increase the length of unit cell to 622 with six rotating linkers per MOF chain along the pore direction. The MD simulations in this case were also done for 70 ns at a temperature of 300 K. In a 622 unit cell, there will be a total of 16 chains and in each chain there are six rotating linkers so 96 linkers in the complete unit cell. The schematic of the 622 unit cell showing the six rotating linkers in a single chain along the pore direction is shown in appendix Figure 5.A.14. The rotational angle data obtained from the MD simulations were used to plot the free energy surface plots for "1, 2" type neighbors (includes linker pairs *ab*, *bc*, *cd*, *de*, *ef*, *fa*), "1, 3" type

neighbors (includes linker pairs *ac*, *ae*, *bd*, *bf*) for linkers in the 622 unit cell. Note: For the FES plots of "1, 3" type neighbors, linker pairs *ce* and *df* were not included to maintain the consistency of linkers selection on x axes (i.e., *a, a, b, b*) and y axes (i.e., *c, e, d, f*) of the plot. The FES "1, 3" type neighbors plot remained constant with and without inclusion of *ce* and *df* pairs of linkers.

Figure 5.13 shows the FES of the 622 unit cell ranging from −180° to 180° for the "1, 2" type neighbors as collective variables. In line with the FES of the 422 unit cell for "1, 2" type neighbors (Figure 5.8), we only observe region *PN*, and the locations of minima in the 622 unit cell are at the same rotational angles as for the 422 unit cell. Figure 5.14 shows FES for 622 unit cell with alternate or "1, 3" type neighbors as collective variables. The deepest minima (*PP*(↑↑) and *NN*(↑↑)) in the FES plot of "1, 3" type neighbors for a 622 unit cell are located along the diagonal and corners of the FES plot and the less deep minima (*PP*(↑↓)) are located on the edges of the FES, similar to the 422 unit cell. This implies alternate neighbors or "1, 3" type linkers are librating at the same rotational angles compared to the 422 unit cell. The free energy surface plots of 622 unit cell are qualitatively and quantitatively identical to that of the 422 unit cell.
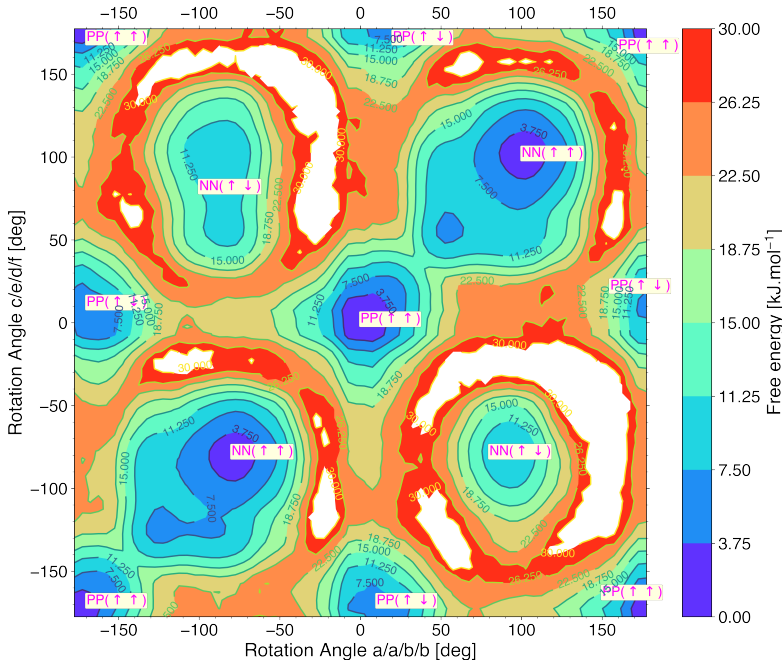
Figure 5.14: Free energy surface (FES) for a 622 unit cell considering rotational angle of "1, 3" type neighbors as collective variables.

Based on the time trajectories of the different chains in the 622 unit cell, we show here representative examples and discuss trends that are generally occuring. For instance, in Figure 5.15 linkers *a, c, e* are librating between *b* = 40° and 120° while linkers *b, d, f* are librating around *a* = 0° or ±180°. Between 10 ns and 14 ns, linkers *b, d, f* are librating

around 0° and are parallel (↑↑↑) aligned with each other. At ~14 ns linker b rotates to ±180°, thus being antiparallel(↓↑↑) aligned with respect to conformations of linkers d, f. As a result, linker c librates over a large angle range ("1, 2" type interaction) as NO_2 groups from both neighboring linkers b,d are pointing away from linker c, while linker a librates over a slightly narrower range due to the NO_2 groups from both neighboring linkers b, d pointing towards it. The rotation of linker b to ±180° at 14 ns is followed by linker d to flip from 0° to ±180°("1, 3" type interaction) around 18 ns and becomes parallel aligned with linker b but antiparallel to linker f (↓↓↑). Due to the rotational change of linker d, wider librations in linker e and narrower librations in linker c are observed ("1, 2" type interaction). This is then followed by linker f to make transition from 0° to ±180° ("1, 3" type interaction) around 24 ns. At this point all three linkers b, d, f are again parallel aligned (↓↓↓).
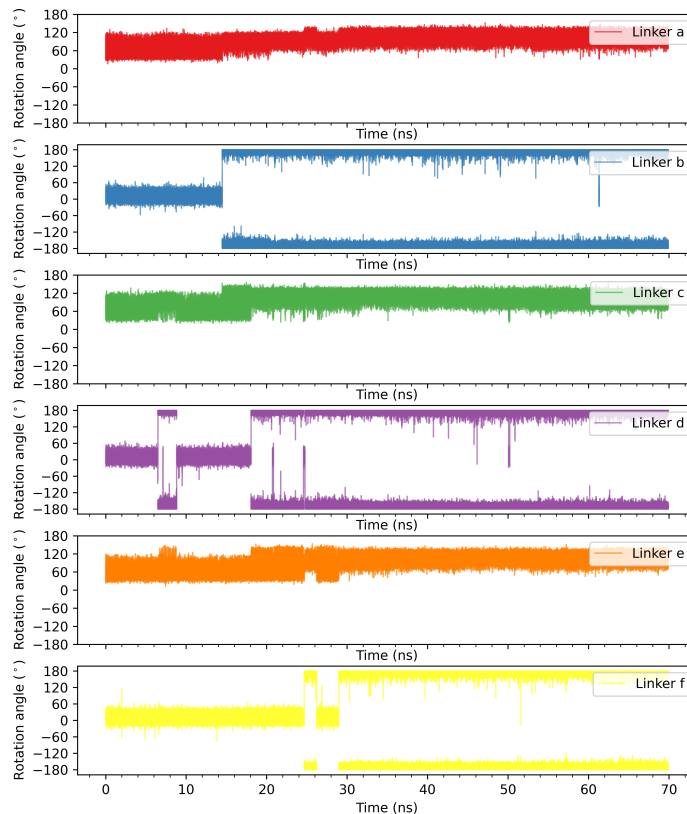
Figure 5.15: MD trajectory of the four linkers along the row for a specific chain in the 622 unit cell.

At ~6 ns, we observe dynamics that are rarely observed compared to the above discussed "1, 3" type interactions. The linker d flips from 0° to ±180° conformation, thus becoming antiparallel (↑↓↑) aligned with linkers b, f. The linkers b, f continue librating at 0° and remain in this conformation, while linker d flips back to its original conformation after a

few nanoseconds at 9.3 ns, restoring the original parallel alignment of the three linkers *b, d, f* (↑↑↑) . A similar situation is observed for linker *f* from 26 ns to 29 ns. At 26 ns, linker *f* flips from ±180° to 0°, thus flips to an antiparallel (↓↓↑) aligned state with linkers *b, d*. At 29 ns, linker *f* rotates back to a parallel alignment with linkers *b, d* (↓↓↓) its "1,3" type neighbors.

The "1, 2" and "1, 3" type interactions in the 622 unit cell are similar to the interactions observed for a 422 unit cell. Additionally, the time between rotational flips of "1, 3" type planar neighbors in the 622 unit cell to restore parallel alignment is also in the order of nanoseconds as in the case of 422 unit cell. For the "1, 3" type non-planar linkers, 180° rotational flips are rare events in the 622 unit cell due to the high energy barrier between the parallel and antiparallel aligned states (red regions and unsampled regions in Figure 5.14), similar to observations in 422 unit cell. From Figures 5.13, 5.14, 5.15 and trajectories of different chains in 622 unit cell we see they are always in *abcdef* = *PNPNPNPNPNPN*... where *P* = nearly planar and *N* = non-planar conformations which is similar to our observations for a 422 unit cell. Thus, the qualitative behavior of linker dynamics in the framework is well described by the 422 unit cell.

5.5 Conclusions

In conclusion, we computationally derived the energetics and correlated linker dynamics in NO_2-MIL-53 using classical molecular dynamics techniques. To achieve this, we first developed and validated a force field that can predict the linker dynamics in this MOF. Using MD simulations for larger supercells and simulation times upto nanoseconds, we observe a distinct *PNPNPNPN*.... arrangement for the linkers along the pore direction where *P* = librations around 0°/±180° [Planar] and *N* = librations between ±50° and ±120° [NonPlanar]. By means of subsequent 180° rotational flips of the planar linkers, this distinct arrangement of linkers is consistently maintained in the MOF structure. The estimated free energy barrier for the 180° flips is around ~24.375 kJ/mol at 300 K. Due to the 180° rotational flips in the planar linkers, we see correlated linker dynamics emerging in the direct neighbors and the next nearest neighbors (alternate neighbors) along the pore direction in the same chain. The direct neighbors are always in "Planar-NonPlanar" conformations whereas the alternate neighbors are either in "Planar-Planar" or "NonPlanar-NonPlanar" conformations. The librations become wider or shift in the average rotational angle in the direct neighbors based on the direction of the nitro group of the rotating planar linker. The alternate neighbors which are planar, are rotating between parallel aligned [(0°, 0°), (±180°, ±180°)] and antiparallel aligned [(0°, ±180°) and vice versa] states. Energetically, the antiparallel aligned states have an free energy upto 7.5 kJ/mol higher than the minima of the parallel aligned states but is still accessible. So, we see coordinated rotations occuring between the alternate neighbors in the same chain which occurs over a timescale of one to ten nanoseconds.

Appendix to chapter 5

5.A.1 Force Field development

QuickFF program is used to derive force fields for metal–organic frameworks from ab initio data of the equilibrium structure as input (http://molmod.github.io/QuickFF/index.html#). The energy expression for the force field including covalent and non-covalent interactions used in QuickFF is:

$$V^{FF} = \underbrace{V_{bond} + V_{bend} + V_{oopd} + V_{torsion} + V_{cross}}_{V_{cov}} + \underbrace{V_{ei} + V_{vdW}}_{V_{noncov}} \tag{5.1}$$

The functional form for each contribution in equation 5.1 is mentioned in previous literature on development of QuickFF program.[14] Specific to this work, the methodology for obtaining the force field is described below. The general steps involved with FF development for predicting the rotational linker dynamics is summarized below.

Step1: Generation of ab initio (AI) data for input to QuickFF program

1. **Covalent interactions**: QuickFF requires ab initio equilibrium geometry and ab initio hessian at equilibrium to estimate the parameters in the covalent contributions of the force field energy expression. We used VASP[22, 23] to obtain the equilibrium structure by geometry optimization followed by performing a frequency calculation to obtain the hessian matrix (analytical second order derivatives of energy with respect to cartesian coordinates) and ab initio forces. With VASP, we worked with a single (111) unit cell, where the cutoff energy of 600 eV, Perdew Becke and Ernzerhof (PBE)[24][GGA exchange-correlation functional and k-points gamma mesh of 6x3x2 was used to obtain the hessian matrix with considerable accuracy. D3 dispersion interactions together with the Becke-Johnson damping scheme (DFT-D3(BJ)) were included.[25, 26] VASP-recommended projector augmented wave (PAW) pseudopotentials were considered for all elements in the MOF.[27] The electronic (ionic) convergence criteria is 10^{-8} (10^{-7}) eV. The output file from frequency calculation "vasprun.xml" contains all the structural information along with the hessian matrix which will be one of the inputs to QuickFF software.

2. The **electrostatic interactions** are modelled by coulomb interactions between Gaussian charge distributions. The atomic charges q_i are obtained from Minimal Basis Iterative Stockholder (MBIS) partitioning scheme.[15]

$$V_{ei} = \frac{1}{2} \sum_{i,j=1, i \neq j} \frac{q_i q_j}{4\pi\epsilon_0 r_{ij}} \mathrm{erf}\left(\frac{r_{ij}}{d_{ij}}\right) \tag{5.2}$$

MBIS scheme is implemented in a package called DensPart[28] that is especially used for periodic structures to get the MBIS charges. DensPart works with GPAW [29–31] output files. We performed a quick single point calculation with GPAW on the equilibrium structure obtained in VASP and "output.gpw" is obtained. This is then used with scripts given in DensPart package to convert GPAW files to DensPart readable "density.npz" file. The output "results.npz" file from DensPart is then used with QuickFF to generate the FF with inclusion of electrostatic interactions.
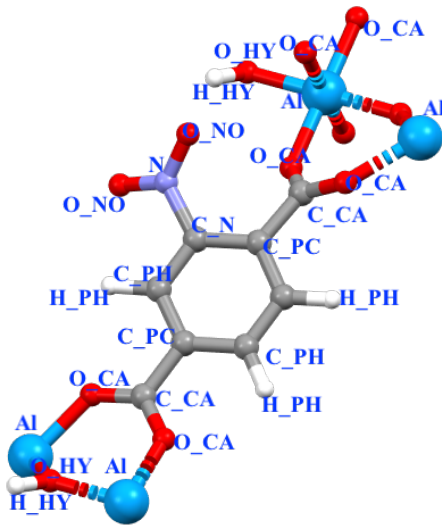
Figure 5.A.1: Figure showing labelled atomtypes in the assymetric unit of NO_2-MIL-53 used for FF generation, FF validation and MD simulations. Elements notation from color are: blue: Aluminium, grey: Carbon, red: Oxygen, white: Hydrogen, lavender: Nitrogen.

3. **Van der waals interactions** are described by MM3 model, parameters are taken from Allinger et al [16] and added manually into the Force field file later.

$$V_{vdw} = \epsilon_{ij} \left[1.84.10^5 \exp\left(-12\frac{r}{\sigma_{ij}}\right) - 2.25 \left(\frac{\sigma_{ij}}{r}\right)^6 \right] \tag{5.3}$$

The parameters σ_{ij} and ϵ_{ij} are the equilibrium distance and depth of the potential. These parameters are determined with mixing rules for interaction between atom i and j:

$$\sigma_{ij} = \sigma_i + \sigma_j$$
$$\epsilon_{ij} = \sqrt{\epsilon_i \epsilon_j}$$

Step2: Generation of Force field using QuickFF program Apart from the hessian matrix in "vasprun.xml" file, atomic charges from DensPart "results.npz" file and van der waals parameters, another file with the system information MolMod.chk file is obtained from "vasprun.xml" by providing atom rules in ATSELECT language (`https://molmod.github.io/yaff/ug_atselect.html`). With all the needed files, an initial FF can be generated by following the procedure in QuickFF documentation. Please note, initially the default settings for the QuickFF were used for deriving the force field.

Step3: Rigid rotational scan with Ab Initio (AI) and generated FF In this work, we are specifically interested in rotational freedom of linkers i.e., change in torsional value of specific dihedrals O_CA C_CA C_PC C_N and O_CA C_CA C_PC C_PH that changes

with the rotation of terephthalate linker with respect to plane containing Al-OH linkages or the (011) plane. To be able to simulate the rotational dynamics accurately, torsional terms for these dihedrals in the previously generated FF in Step2 are replaced and new torsional terms are added. The new terms are obtained by performing a rigid rotational energy scan of structures at different configurations ranging from −180° to 180° of OCCC dihedral angle both with AI and FF (containing all except the torsional OCCC term). The difference in the energies (E_{OCCC}) between AI and FF (containing all except the torsional OCCC term) rotational scans is then fitted to a cosine functional form shown in equation 5.5

$$E_{OCCC} = E_{AI} - E_{FF} \tag{5.4}$$

$$E_{OCCC} = \sum_{i=1}^{N_i} \frac{1}{2} A_i (1 - cos(M_i(\phi_i - \phi_{0,i}))) \tag{5.5}$$

Parameters A_i is obtained by fitting the difference in energies between AI and FF rotational
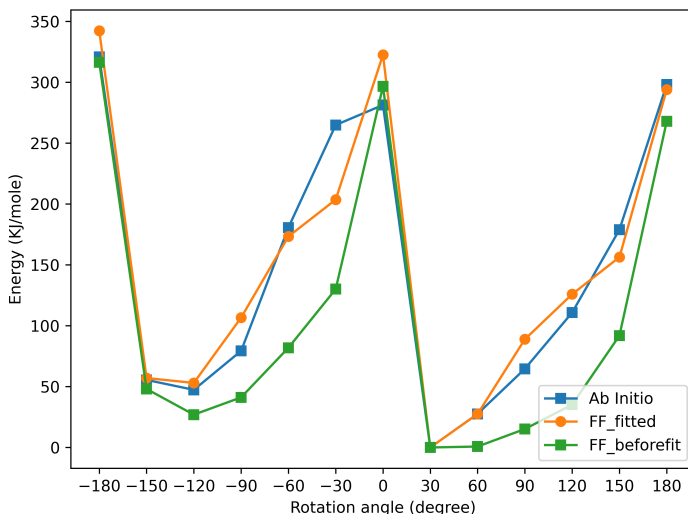
Figure 5.A.2: Figure showing rotational scan energies with Ab Initio, FF before fitting and FF after fitting.

scans into this functional form and $M_i = 2, 4, 6....$ The force constant A_i is estimated by minimizing the cost function method implemented in QuickFF called "boxqp" function (`http://molmod.github.io/QuickFF/_modules/quickff/tools.html#boxqp`). Figure 5.A.2 shows the energies of rotational scan with Ab Initio, Force field before fitting for the OCCC dihedral term and final FF energies after fitting for the OCCC dihedral term.

Note: All the python scripts and input/output files for each step in the FF development are made publicly available on the data repository.

5.A.2 Computational methods

Geometry Optimization and Frequency calculations   One of the force field validation methods was to compare the geometry optimized structure with developed FF to the experimental structure, The geometry optimization for this was done with YAFF[32] (`https://github.com/molmod/molmod`; `https://molmod.github.io/yaff/index.html`) for 211 unit cell. The electrostatic interactions were calculated using an Ewald summation with a real-space cutoff of 15 Å, a splitting parameter α of 0.213/Å, and a reciprocal space cutoff of 0.32/Å. Also the van der Waals interactions were calculated with a smooth cutoff of 15 Å. The structure was optimized with convergence criteria set to 10^{-8} a.u. for the RMS on the cartesian gradient, 10^{-6} a.u. for the RMS of difference in the cartesian coordinates, 10^{-8} a.u. for the RMS on the gradient on the cell parametres and 10^{-6} a.u. for the RMS of the difference in the cell parameters. After the optimization, normal mode frequencies with FF were computed using TAMkin.[33]

Molecular Dynamics   In this work, we did not perform any AIMD simulations of 211 unit cell mentioned in the main chapter. The data from AIMD simulations which were obtained in the previous chapter 4 was used to obtain the free energy surface (FES) plots and compare with the FF generated FES in Section 5.3.4.

Classical MD simulations for 211, 422 and 622 supercells were all performed with LAMMPS software (`https://www.lammps.org/index.html#gsc.tab=0`).[34–36] Starting from the geometry optimized DFT structure, MD simulations were performed in the (N,V,T) ensemble with fixed size and shape of the unit cell. A timestep of 0.5 fs was used in the MD runs and temperature was controlled by a canonical sampling through Nose-Hoover thermostat. The equilibration period for FF validation calculations with 211 unit cell was 10 ps and a production period of 1 ns for all temperatures (300 K and 450 K). For the 422 and 622 unit cells, the equilibration period is 100 ps and a production period of 70 ns.

5.A.3 Force field (FF) Validation

5.A.3.1 Computed Frequencies with DFT and Force field (FF)

We computed the internal energy, Helmholtz energy, entropy and heat capacity of Nitro functionalized MIL-53 as a function of temperature in the quantum-harmonic approximation using the computed ab initio and force field normal mode frequencies:[14]

$$E(T) = \sum_{i=1}^{N_\omega} \left(\frac{\hbar\omega_i}{2} + \frac{\hbar\omega_i}{e^{\beta\hbar\omega_i} - 1} \right) \tag{5.6}$$

$$F(T) = \sum_{i=1}^{N_\omega} \left(\frac{\hbar\omega_i}{2} + k_B T \ln[1 - e^{-\beta\hbar\omega_i}] \right) \tag{5.7}$$

$$C_v(T) = k_B \sum_{i=1}^{N_\omega} \left(\frac{\hbar\omega_i}{k_B T} \right)^2 \frac{e^{\beta\hbar\omega_i}}{(e^{\beta\hbar\omega_i} - 1)^2} \tag{5.8}$$

$$S(T) = k_B \sum_{i=1}^{N_\omega} \left(\frac{\beta\hbar\omega_i}{e^{\beta\hbar\omega_i} - 1} - ln[1 - e^{-\beta\hbar\omega_i}] \right) \tag{5.9}$$

The computed thermodynamic properties are plotted in Figure 5.A.3 and they are reproduced very well with force field developed when compared to the ab initio computed properties.
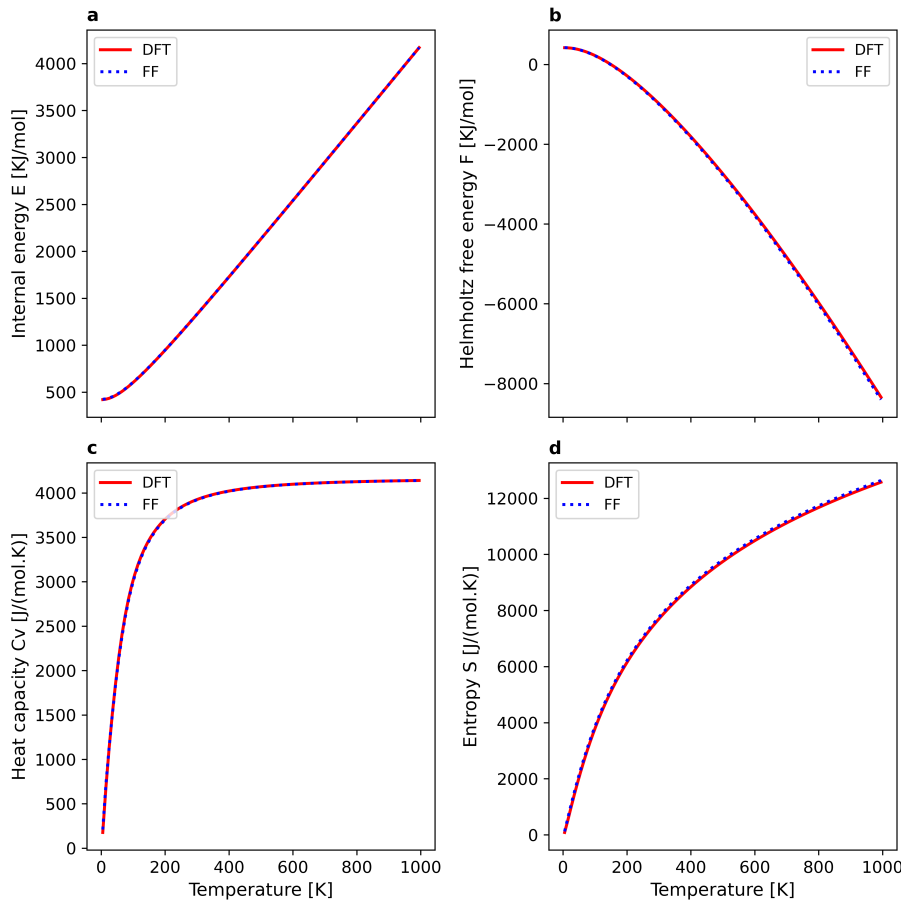
Figure 5.A.3: a) Internal energy E, b) Helmholtz free energy F, c) heat capacity C_v and d) entropy S of nitro functionalized MIL53 as a function of temperature in the harmonic oscillator approximation using the computed DFT (red line) and force field frequencies (blue dotted line).

5.A.3.2 Molecular Dynamics with AIMD and FF

(a)

(b)
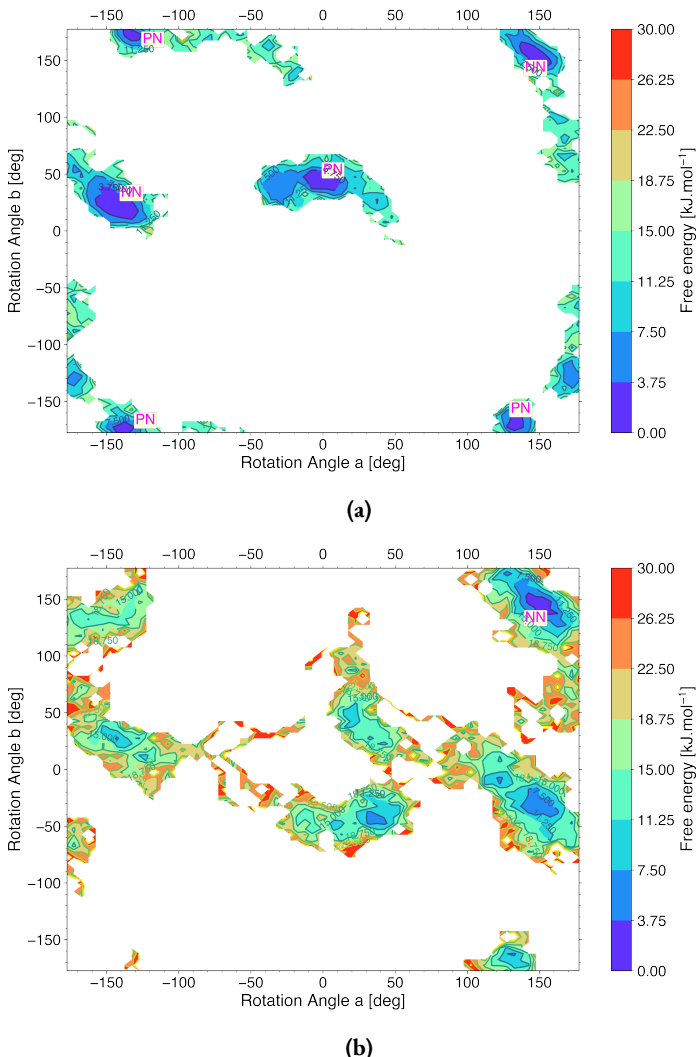
Figure 5.A.4: Free energy surface (FES) plots obtained from rotational angle of neighboring linkers in a 211 unit cell with AIMD at temperatures a) 450 K and b) 700 K.
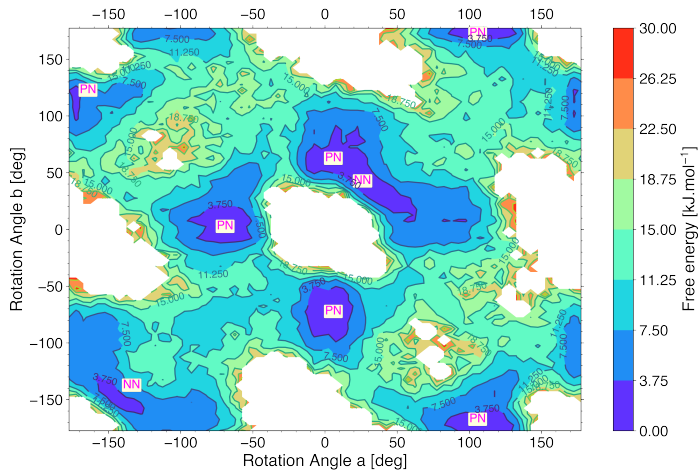
Figure 5.A.5: Free energy surface (FES) plots obtained from rotational angle of neighboring linkers in a 211 unit cell with FF at 450 K.
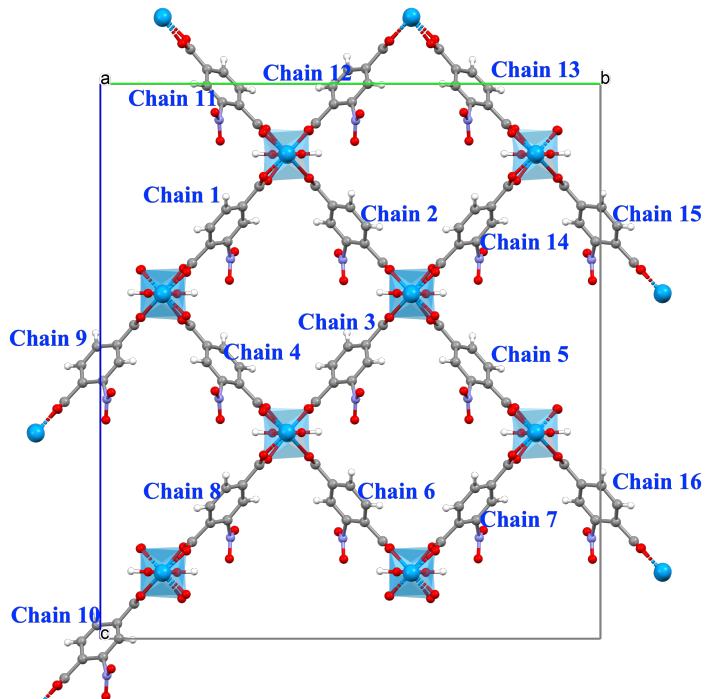
Figure 5.A.6: Figure showing 422 unit cell with all 16 chains in the unit cell.

5.A.4 422 unit cell

5.A.4.1 Interactions with neighboring linkers along perpendicular to pore direction

In the main chapter, we elaborated on neighboring interactions between linkers along the pore direction (x). Here we present and discuss the time trajectories for some of the linkers and its perpendicular neighbors along y or z direction. The notation for the different sets of chains shown in Figure 5.A.6 is followed for the time traces below.

Structurally, linkers from different chains directly stack over each other when there is a hydroxyl group between the chains. For example a hydroxyl group is present between chains (1,4), (2,3), (4,8), (5,7) etc.(shown in Figure 5.A.8a) The other kind of chain pairs are those where the hydroxyl group is not present between them and chains do not directly stack over each other but are alternately stacked. Some examples of these pairs include (3,4), (6,7), (4,9), (2,14) etc.(shown in Figure 5.A.8b) The steric interactions should be higher for the chain pairs with hydroxyl group between them because of the direct stacking along y and z directions. Hence, we look closely into those chain pairs with hydroxyl group between them for linker interactions.
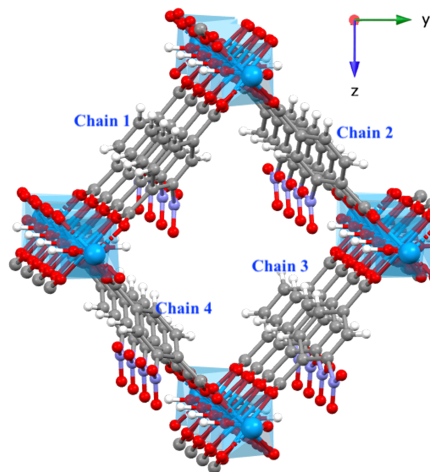
Figure 5.A.7: Figure showing chains 1, 2, 3, and 4 of the 422 unit cell in 5.A.6 along 'x' direction.
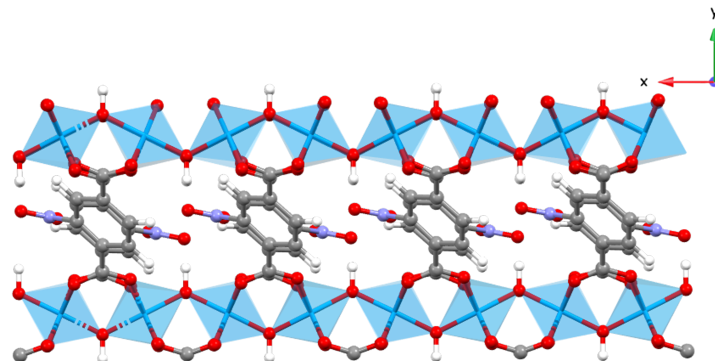
(a) Chains 1 and 4 with hydroxyl group in between showing directly stacked over each other when viewed along 'z' direction.
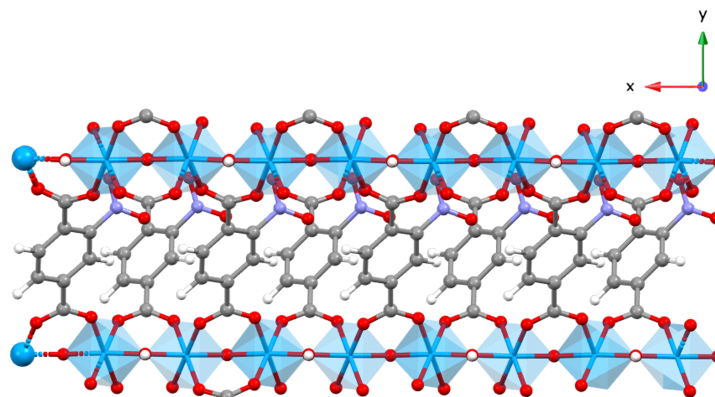
(b) Chains 3 and 4 without hydroxyl group in between showing alternately stacked when viewed along 'z' direction.

Figure 5.A.8: Chains (a) with hydroxyl group in between (b) without hydroxyl group in between.

Qualitatively we look for changes in the perpendicular neighbor linker pairs, when there is a change in conformation from 0° to ±180° or vice versa, or change in width of the librations in either of the linkers. In Figure 5.A.9a and 5.A.9b, linkers librate around (±180°, 0°) and (−90°, 90°) i.e., (*P,P*) and (*N,N*) configurations respectively. In Figure 5.A.10a and 5.A.10b libration of linkers in this case is around (90°, 0°) and (0°, 90°) i.e., (*N, P*) and vice versa. Similarly for linkers in Figure 5.A.11 conformations are (*N, P*) and (*P, P*). So, for all different combinations of linker conformations *P* and *N* where *P* = librations around 0° or ±180° and *N* = librations around ±90° we did not observe a distinct change in the perpendicular linker due to change in the other linker conformation by 180°flips or changed width of librations.

(a)   (b)
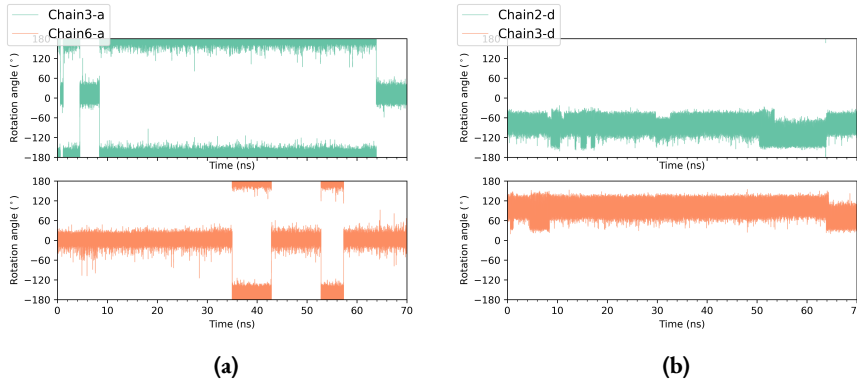
Figure 5.A.9: MD time trajectories of one of the linkers in chains (3,6) and (2,3).

(a)   (b)
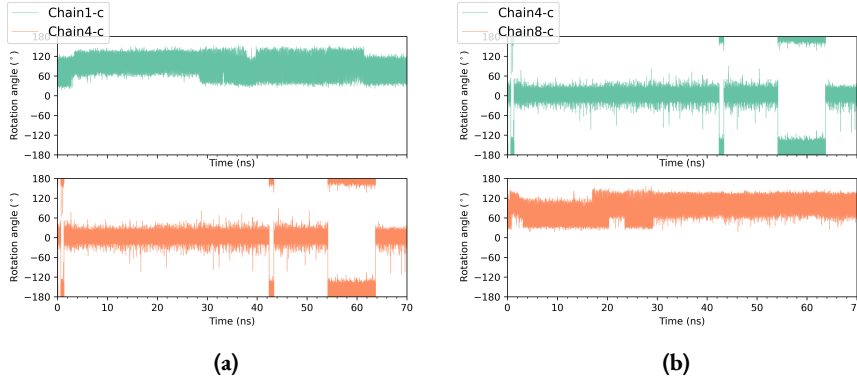
Figure 5.A.10: MD time trajectories of one of the linkers in chains (1,4) and (4,8).

5.A.4.2 "1, 3" type interactions
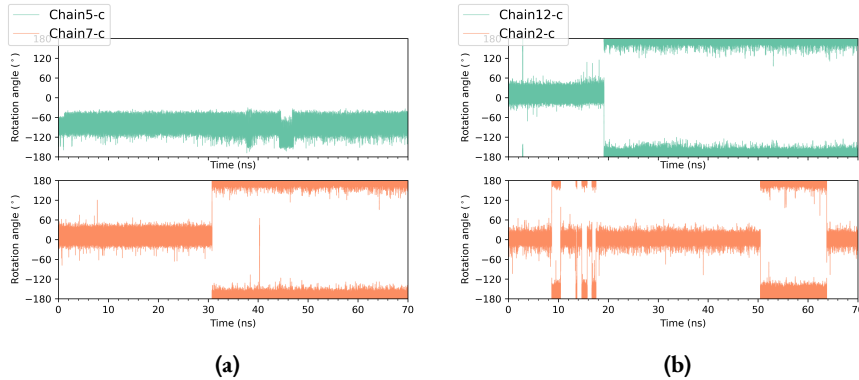
Figure 5.A.11: MD time trajectories of one of the linkers in chains (5,7) and (12,2).
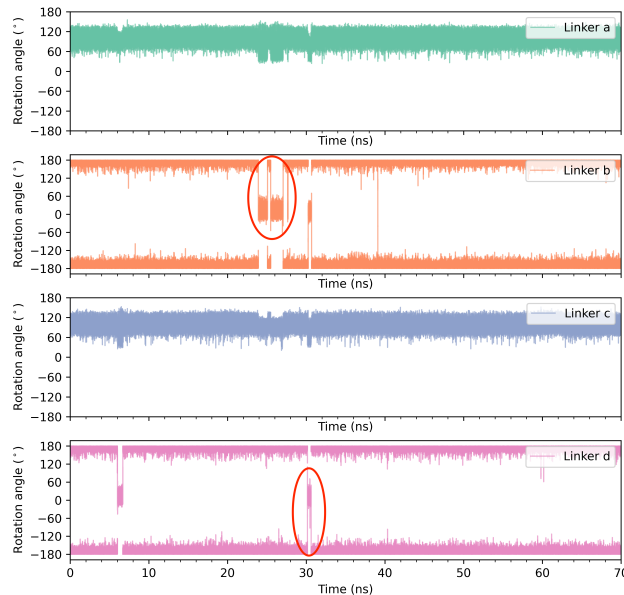
Figure 5.A.12: MD time trajectory of a chain in the 422 unit cell highlighting 180° rotational flips for a short time of ~1.5 ns.
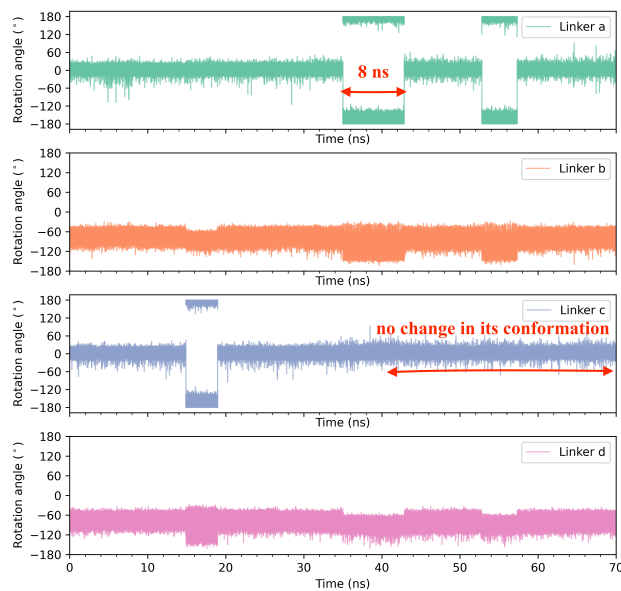
Figure 5.A.13: MD time trajectory of a chain in the 422 unit cell highlighting 180° rotational flips for a time of ~8 ns.

5.A.5 622 unit cell
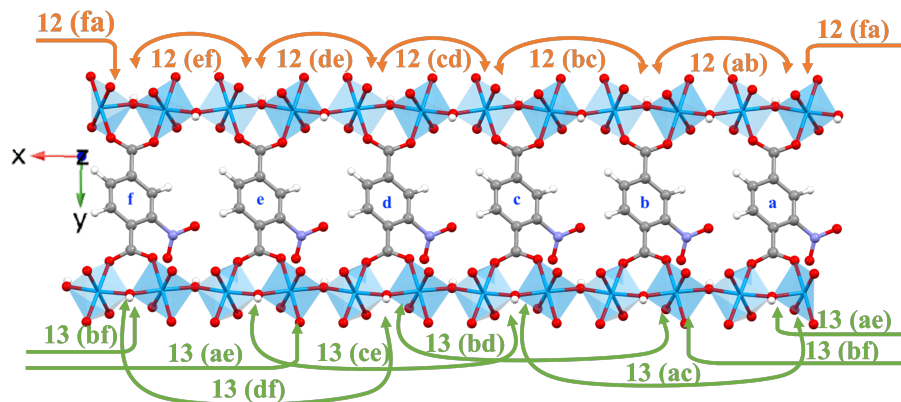
Figure 5.A.14: Figure showing the six rotating linkers (a, b, c, d, e, f) along the pore direction (x) and their 12 (orange: includes pairs ab, bc, cd, de, ef, fa), 13 (green: includes pairs ac, ae, bd, bf, ce, df) type neighbors for a single chain in the 622 unit cell.

5.A.6 Force Field (final) generated after fitting

```
##This FF has OCCCN and OCCCPh parameters added obtained from fitting
    vasp DFT and FF energies in rigid rotational angle  scan
# BONDHARM
#---------
BONDHARM:UNIT  K kjmol/A**2
BONDHARM:UNIT  RO A

BONDHARM:PARS      C_PH      H_PH 3.2546523678e+03  1.0888086683e+00
BONDHARM:PARS      C_PC      C_PH 3.9238891132e+03  1.3968781817e+00
BONDHARM:PARS      C_CA      C_PC 2.6557300720e+03  1.4898994999e+00
BONDHARM:PARS      C_PH      C_PH 4.0181602233e+03  1.3891407878e+00
BONDHARM:PARS      C_N       C_PC 3.7344836810e+03  1.4053377913e+00
BONDHARM:PARS      C_N       C_PH 4.1493987514e+03  1.3865384995e+00
BONDHARM:PARS      C_N       N    2.2601406356e+03  1.4715760385e+00
BONDHARM:PARS      AL        O_CA 9.5394956147e+02  1.9152514663e+00
BONDHARM:PARS      C_CA      O_CA 5.6776918122e+03  1.2744267023e+00
BONDHARM:PARS      AL        O_HY 1.2965069135e+03  1.8552343925e+00
BONDHARM:PARS      H_HY      O_HY 4.6459188246e+03  9.8820112810e-01
BONDHARM:PARS      N         O_NO 5.6516929661e+03  1.2397088277e+00


# BENDAHARM
#----------
BENDAHARM:UNIT  K kjmol/rad**2
BENDAHARM:UNIT  THETA0 deg

BENDAHARM:PARS      O_CA       AL       O_HY 2.2216387265e+02
    9.0448131858e+01
BENDAHARM:PARS      C_PC      C_PH      H_PH 2.9765129191e+02
    1.1979353967e+02
BENDAHARM:PARS      C_PC      C_PH      C_PH 5.5460765707e+02
    1.2053199803e+02
BENDAHARM:PARS      C_PH      C_PH      H_PH 2.9575036714e+02
    1.2094189800e+02
BENDAHARM:PARS      C_N       C_PC      C_PH 4.5945227404e+02
    1.1795833038e+02
BENDAHARM:PARS      C_CA      C_PC      C_N  3.3547275520e+02
    1.2208973111e+02
BENDAHARM:PARS      C_CA      C_PC      C_PH 4.0085803505e+02
    1.1990844269e+02
BENDAHARM:PARS      C_PC      C_CA      O_CA 5.9742043217e+02
    1.1734852682e+02
BENDAHARM:PARS      O_CA      C_CA      O_CA 6.4838336934e+02
    1.2558334895e+02
BENDAHARM:PARS      C_N       C_PH      H_PH 2.6173651803e+02
    1.1868376196e+02
BENDAHARM:PARS      C_N       C_PH      C_PC 4.9306330488e+02
    1.1867575354e+02
BENDAHARM:PARS      C_PC      C_N       C_PH 4.8710456844e+02
    1.2186156006e+02
BENDAHARM:PARS      C_PC      C_N       N    3.9664340756e+02
    1.2073842564e+02
BENDAHARM:PARS      C_PH      C_N       N    5.1425244370e+02
    1.1766387985e+02
```

```
BENDAHARM:PARS         C_PH        C_PC        C_PH  5.1352267332e+02
      1.2036706611e+02
BENDAHARM:PARS          C_N           N        O_NO  6.1749347653e+02
      1.1814184030e+02
BENDAHARM:PARS         O_NO           N        O_NO  9.0812157271e+02
      1.2432745247e+02
BENDAHARM:PARS           AL        O_CA        C_CA  1.4314300222e+02
      1.2850066984e+02
BENDAHARM:PARS           AL        O_HY        H_HY  1.3403302525e+02
      1.1791656706e+02
BENDAHARM:PARS           AL        O_HY          AL  2.6332633313e+02
      1.2398341734e+02


# BENDCOS
#--------
BENDCOS:UNIT  A kjmol
BENDCOS:UNIT  PHI0 deg

BENDCOS:PARS         O_CA          AL        O_CA  4 7.1623123535e+00
      0.0000000000e+00


# TORSION
#--------
TORSION:UNIT  A kjmol
TORSION:UNIT  PHI0 deg

TORSION:PARS          C_N        C_PC        C_PH        C_PH  2 2.8946231245e
      +01  0.0000000000e+00
TORSION:PARS          C_N        C_PC        C_PH        H_PH  2 2.7648146487e
      +01  0.0000000000e+00
TORSION:PARS         C_CA        C_PC        C_PH        C_PH  2 3.5778489858e
      +01  0.0000000000e+00
TORSION:PARS         C_CA        C_PC        C_PH        H_PH  2 2.0702386397e
      +01  0.0000000000e+00
#TORSION:PARS          C_N        C_PC        C_CA        O_CA  2 8.3910148393e
      +00  0.0000000000e+00
#TORSION:PARS         C_PH        C_PC        C_CA        O_CA  2 5.0546566656e
      +00  0.0000000000e+00
TORSION:PARS         C_PC        C_PH        C_PH        H_PH  2 2.8243584139e
      +01  0.0000000000e+00
TORSION:PARS         H_PH        C_PH        C_PH        H_PH  2 1.6523170961e
      +01  0.0000000000e+00
TORSION:PARS         C_PC        C_PH        C_PH        C_PC  2 2.8726383454e
      +01  0.0000000000e+00
TORSION:PARS         C_PH         C_N        C_PC        C_PH  2 3.9309970893e
      +01  0.0000000000e+00
TORSION:PARS         C_CA        C_PC         C_N        C_PH  2 3.1090429835e
      +01  0.0000000000e+00
TORSION:PARS         C_PH        C_PC         C_N           N  2 5.0389876566e
      +01  0.0000000000e+00
TORSION:PARS         C_CA        C_PC         C_N           N  2 2.6591063631e
      +01  0.0000000000e+00
TORSION:PARS         C_PC         C_N        C_PH        H_PH  2 2.1624538465e
      +01  0.0000000000e+00
TORSION:PARS         C_PC         C_N        C_PH        C_PC  2 2.8319537782e
      +01  0.0000000000e+00
```

```
TORSION:PARS        H_PH       C_PH       C_N        N  2 2.2861729507e
    +01   0.0000000000e+00
TORSION:PARS        C_PC       C_PH       C_N        N  2 4.2575495213e
    +01   0.0000000000e+00
TORSION:PARS        C_PH       C_PC       C_PH      H_PH  2 2.6388156565e
    +01   0.0000000000e+00
TORSION:PARS        C_PH       C_PC       C_PH      C_PH  2 3.3695452851e
    +01   0.0000000000e+00
TORSION:PARS        C_N        C_PH       C_PC      C_PH  2 3.1025677143e
    +01   0.0000000000e+00
TORSION:PARS        C_CA       C_PC       C_PH      C_N  2 4.4755984539e
    +01   0.0000000000e+00
TORSION:PARS        C_PC       C_N        N         O_NO  2 8.4255163753e
    +00   0.0000000000e+00
TORSION:PARS        C_PH       C_N        N         O_NO  2 2.4532632371e
    +00   0.0000000000e+00
TORSION:PARS        AL         O_CA       C_CA      C_PC  2 2.2304352161e
    +01   0.0000000000e+00
TORSION:PARS        AL         O_CA       C_CA      O_CA  2 7.1279915245e
    -02   0.0000000000e+00
TORSION:PARS        C_N        C_PC       C_CA      O_CA  2 10.90951871e
    +00    -40.81e+00
TORSION:PARS        C_N        C_PC       C_CA      O_CA  3 1.06607827e+00
        -40.81e+00
TORSION:PARS        C_PH       C_PC       C_CA      O_CA  2 10.90951871e
    +00    142.55e+00
TORSION:PARS        C_PH       C_PC       C_CA      O_CA  3 1.06607827e+00
        142.55e+00


# OOPDIST
#--------
OOPDIST:UNIT  K kjmol/A**2
OOPDIST:UNIT  DO A

OOPDIST:PARS        C_PC       C_PH       H_PH      C_PH 1.5939608446e+02
        0.0000000000e+00
OOPDIST:PARS        C_CA       C_N        C_PH      C_PC 1.1094174618e+02
        0.0000000000e+00
OOPDIST:PARS        C_PC       O_CA       O_CA      C_CA 1.5426217104e+03
        0.0000000000e+00
OOPDIST:PARS        C_N        C_PC       H_PH      C_PH 1.5190020838e+02
        0.0000000000e+00
OOPDIST:PARS        C_CA       C_PH       C_PH      C_PC 1.2053539647e+02
        0.0000000000e+00
OOPDIST:PARS        C_N        O_NO       O_NO      N 1.7131236544e+03
        0.0000000000e+00


# Cross
#------
Cross:UNIT  KSS kjmol/angstrom**2
Cross:UNIT  KBS0 kjmol/(angstrom*rad)
Cross:UNIT  KBS1 kjmol/(angstrom*rad)
Cross:UNIT  R0 angstrom
Cross:UNIT  R1 angstrom
Cross:UNIT  THETA0 deg
```

```
Cross:PARS        O_CA         AL         O_CA     1.0169825140e+02
     0.0000000000e+00   0.0000000000e+00   1.9152514663e+00
     1.9152514663e+00   0.0000000000e+00
Cross:PARS        O_CA         AL         O_HY     8.3897543818e+01
     2.0828578167e+02   1.5337454645e+02   1.9152514663e+00
     1.8552343925e+00   9.0448131858e+01
Cross:PARS        O_HY         AL         O_HY    -2.8040890934e+01
     0.0000000000e+00   0.0000000000e+00   1.8552343925e+00
     1.8552343925e+00   0.0000000000e+00
Cross:PARS        C_PC        C_PH        H_PH     5.3697332717e+01
     1.1195943158e+02   1.1968331600e+02   1.3968781817e+00
     1.0888086683e+00   1.1979353967e+02
Cross:PARS        C_PC        C_PH        H_PH     5.1139558627e+02
     1.1660319383e+02   9.2339246404e+01   1.3968781817e+00
     1.3891407878e+00   1.2053199803e+02
Cross:PARS        C_PH        C_PH        H_PH     5.0146904109e+01
     1.1564608696e+02   1.0771247605e+02   1.3891407878e+00
     1.0888086683e+00   1.2094189800e+02
Cross:PARS         C_N        C_PC        C_PH     5.6923516212e+02
     4.4349696462e+01   7.4483576848e+01   1.4053377913e+00
     1.3968781817e+00   1.1795833038e+02
Cross:PARS        C_CA        C_PC         C_N     2.5685930219e+02
     9.8515488274e+01   9.5606681022e+01   1.4898994999e+00
     1.4053377913e+00   1.2208973111e+02
Cross:PARS        C_CA        C_PC        C_PH     2.8618101799e+02
     1.1661737156e+02   9.8612417759e+01   1.4898994999e+00
     1.3968781817e+00   1.1990844269e+02
Cross:PARS        C_PC        C_CA        O_CA     3.9865348532e+02
     1.8145377360e+02   4.4115353290e+02   1.4898994999e+00
     1.2744267023e+00   1.1734852682e+02
Cross:PARS        O_CA        C_CA        O_CA     7.6198573135e+02
     3.8539662028e+02   3.8539662028e+02   1.2744267023e+00
     1.2744267023e+00   1.2558334895e+02
Cross:PARS         C_N        C_PH        H_PH     4.2650555752e+01
     1.1799860597e+02   1.1945684471e+02   1.3865384995e+00
     1.0888086683e+00   1.1868376196e+02
Cross:PARS         C_N        C_PH        C_PC     5.1836934343e+02
     1.2182486494e+02   1.1220729314e+02   1.3865384995e+00
     1.3968781817e+00   1.1867575354e+02
Cross:PARS        C_PC         C_N        C_PH     5.3331443304e+02
     4.6260833303e+01   4.9860317163e+01   1.4053377913e+00
     1.3865384995e+00   1.2186156006e+02
Cross:PARS        C_PC         C_N           N     3.3759146169e+02
     8.6383953044e+01   2.2193714049e+02   1.4053377913e+00
     1.4715760385e+00   1.2073842564e+02
Cross:PARS        C_PH         C_N           N     4.1410487431e+02
     1.3934644272e+02   2.8716919014e+02   1.3865384995e+00
     1.4715760385e+00   1.1766387985e+02
Cross:PARS        C_PH        C_PC        C_PH     5.4712791599e+02
     5.5992375258e+01   5.5992375258e+01   1.3968781817e+00
     1.3968781817e+00   1.2036706611e+02
Cross:PARS         C_N           N        O_NO     4.3883997072e+02
     1.8275606478e+02   4.1932637207e+02   1.4715760385e+00
     1.2397088277e+00   1.1814184030e+02
Cross:PARS        O_NO           N        O_NO     7.8816689798e+02
     4.6007988234e+02   4.6007988234e+02   1.2397088277e+00
     1.2397088277e+00   1.2432745247e+02
Cross:PARS          AL        O_CA        C_CA     3.1649662163e+02
```

```
      8.1104683405e+01   1.7545535926e+02   1.9152514663e+00
      1.2744267023e+00   1.2850066984e+02
Cross:PARS         AL         O_HY       H_HY    6.0186703987e+00
      6.6729340144e+01   1.1329291821e+02   1.8552343925e+00
      9.8820112810e-01   1.1791656706e+02
Cross:PARS         AL         O_HY         AL    1.7708627349e+02
      7.3276335999e+01   7.3276335999e+01   1.8552343925e+00
      1.8552343925e+00   1.2398341734e+02


# van der Waals
#=============

# The following mathemetical form is supported:
#  - MM3:    EPSILON*(1.84e5*exp(-12*r/SIGMA)-2.25*(SIGMA/r)^6)
#  - LJ:     4.0*EPSILON*((SIGMA/r)^12 - (SIGMA/r)^6)
#
# Remark:
#  In MM3, if ONLYPAULI=1 then only the pauli term will be used.
#  If ONLYPAULI=0, the full MM3 expression is used with 12.

MM3:UNIT SIGMA angstrom
MM3:UNIT EPSILON kcalmol
MM3:SCALE 1 0.0
MM3:SCALE 2 0.0
MM3:SCALE 3 1.0


# ----------------------------------------------
# KEY       ffatype SIGMA EPSILON ONLYPAULI
# ----------------------------------------------

MM3:PARS      AL    2.360   0.116      0
MM3:PARS    O_HY    1.820   0.059      0
MM3:PARS    H_HY    1.600   0.016      0
MM3:PARS    O_CA    1.820   0.059      0
MM3:PARS    C_CA    1.940   0.056      0
MM3:PARS    C_PC    1.940   0.056      0
MM3:PARS    C_PH    1.940   0.056      0
MM3:PARS    H_PH    1.620   0.020      0
MM3:PARS     C_N    1.940   0.056      0
MM3:PARS       N    1.930   0.043      0
MM3:PARS    O_NO    1.820   0.059      0


#Fixed charges
#--------------

FIXQ:UNIT Q0 e
FIXQ:UNIT P e
FIXQ:UNIT R angstrom
FIXQ:SCALE 1 1.0
FIXQ:SCALE 2 1.0
FIXQ:SCALE 3 1.0
FIXQ:DIELECTRIC 1.0

# Atomic parameters
# ----------------------------------------------------
# KEY         label Q_0A               R_A
# ----------------------------------------------------
FIXQ:ATOM          AL 2.0996324793  1.6742000000
```

```
FIXQ:ATOM      H_PH   0.1679264047   0.7308000000
FIXQ:ATOM      H_HY   0.5329694145   0.7308000000
FIXQ:ATOM      C_PH  -0.0982570542   1.1703000000
FIXQ:ATOM      C_PC  -0.1377736303   1.1703000000
FIXQ:ATOM      C_CA   0.8416037982   1.1703000000
FIXQ:ATOM       C_N   0.0432340456   1.1703000000
FIXQ:ATOM         N   0.5760234132   1.1048000000
FIXQ:ATOM      O_CA  -0.7271328887   1.1325000000
FIXQ:ATOM      O_HY  -1.2346200104   1.1325000000
FIXQ:ATOM      O_NO  -0.3628239451   1.1325000000
```

Bibliography

(1)   M. Witman, S. Ling, S. Jawahery, P. G. Boyd, M. Haranczyk, B. Slater and B. Smit, "The Influence of Intrinsic Framework Flexibility on Adsorption in Nanoporous Materials," *Journal of the American Chemical Society*, 2017, **139**, 5547–5557.

(2)   M. J. Lennox and T. Düren, "Understanding the Kinetic and Thermodynamic Origins of Xylene Separation in UiO-66(Zr) via Molecular Simulation," *The Journal of Physical Chemistry C*, 2016, **120**, 18651–18658.

(3)   J. A. Gee and D. S. Sholl, "Effect of Framework Flexibility on C8 Aromatic Adsorption at High Loadings in Metal–Organic Frameworks," *The Journal of Physical Chemistry C*, 2016, **120**, 370–376.

(4)   J. Park, M. Agrawal, D. F. S. Gallis, J. A. Harvey, J. A. Greathouse and D. S. Sholl, "Impact of Intrinsic Framework Flexibility for Selective Adsorption of Sarin in Non-Aqueous Solvents Using Metal–Organic Frameworks," *Physical Chemistry Chemical Physics*, 2020, **22**, 6441–6448.

(5)   M. Agrawal, S. Bhattacharyya, Y. Huang, K. C. Jayachandrababu, C. R. Murdock, J. A. Bentley, A. Rivas-Cardona, M. M. Mertens, K. S. Walton, D. S. Sholl and S. Nair, "Liquid-Phase Multicomponent Adsorption and Separation of Xylene Mixtures by Flexible MIL-53 Adsorbents," *The Journal of Physical Chemistry C*, 2018, **122**, 386–397.

(6)   A. Gonzalez-Nelson, F.-X. Coudert and M. van der Veen, "Rotational Dynamics of Linkers in Metal–Organic Frameworks," *Nanomaterials*, 2019, **9**, 330.

(7)   C. S. Vogelsberg, F. J. Uribe-Romo, A. S. Lipton, S. Yang, K. N. Hou, S. Brown and M. A. Garcia-Garibay, "Ultrafast Rotation in an Amphidynamic Crystalline Metal Organic Framework," *Proceedings of the National Academy of Sciences of the United States of America*, 2017, **114**, 13613–13618.

(8)   S. Bracco, F. Castiglioni, A. Comotti, S. Galli, M. Negroni, A. Maspero and P. Sozzani, "Ultrafast Molecular Rotors and Their CO2 Tuning in MOFs with Rod-Like Ligands," *Chemistry - A European Journal*, 2017, **23**, 11210–11215.

(9)   J. Perego, C. X. Bezuidenhout, S. Bracco, G. Prando, L. Marchiò, M. Negroni, P. Carretta, P. Sozzani and A. Comotti, "Cascade Dynamics of Multiple Molecular Rotors in a MOF: Benchmark Mobility at a Few Kelvins and Dynamics Control by CO $_2$," *Journal of the American Chemical Society*, 2021, **143**, 13082–13090.

(10)   J. Perego, S. Bracco, M. Negroni, C. X. Bezuidenhout, G. Prando, P. Carretta, A. Comotti and P. Sozzani, "Fast Motion of Molecular Rotors in Metal–Organic Framework Struts at Very Low Temperatures," *Nature Chemistry*, 2020, **12**, 845–851.

(11)   J. Perego, C. X. Bezuidenhout, S. Bracco, S. Piva, G. Prando, C. Aloisi, P. Carretta, J. Kaleta, T. P. Le, P. Sozzani, A. Daolio and A. Comotti, "Benchmark Dynamics of Dipolar Molecular Rotors in Fluorinated Metal-Organic Frameworks," *Angewandte Chemie International Edition*, 2023, **135**, e202215893.

(12)   J. Dong, V. Wee and D. Zhao, "Stimuli-Responsive Metal–Organic Frameworks Enabled by Intrinsic Molecular Motion," *Nature Materials*, 2022, **21**, 1334–1340.

(13)   L. Vanduyfhuys, S. Vandenbrande, T. Verstraelen, R. Schmid, M. Waroquier and V. Van Speybroeck, "QuickFF: A Program for a Quick and Easy Derivation of Force Fields for Metal-Organic Frameworks from Ab Initio Input," *Journal of Computational Chemistry*, 2015, **36**, 1015–1027.

(14) L. Vanduyfhuys, S. Vandenbrande, J. Wieme, M. Waroquier, T. Verstraelen and V. Van Speybroeck, "Extension of the QuickFF Force Field Protocol for an Improved Accuracy of Structural, Vibrational, Mechanical and Thermal Properties of Metal-Organic Frameworks," *Journal of Computational Chemistry*, 2018, **39**, 999–1011.

(15) T. Verstraelen, S. Vandenbrande, F. Heidar-Zadeh, L. Vanduyfhuys, V. Van Speybroeck, M. Waroquier and P. W. Ayers, "Minimal Basis Iterative Stockholder: Atoms in Molecules for Force-Field Development," *Journal of Chemical Theory and Computation*, 2016, **12**, 3894–3912.

(16) N. L. Allinger, X. Zhou and J. Bergsma, "Molecular Mechanics Parameters," *Journal of Molecular Structure: THEOCHEM*, 1994, **312**, 69–83.

(17) A. Gonzalez-Nelson, S. Mula, M. Šimėnas, S. Balčiūnas, A. R. Altenhof, C. S. Vojvodin, S. Canossa, J. Banys, R. W. Schurko, F.-X. Coudert and M. A. van der Veen, "Emergence of Coupled Rotor Dynamics in Metal–Organic Frameworks via Tuned Steric Interactions," *Journal of the American Chemical Society*, 2021, **143**, 12053–12062.

(18) S. Biswas, T. Ahnfeldt and N. Stock, "New Functionalized Flexible Al-MIL-53-X (X = -Cl, -Br, -CH 3 , -NO 2 , -(OH) 2) Solids: Syntheses, Characterization, Sorption, and Breathing Behavior," *Inorganic Chemistry*, 2011, **50**, 9518–9526.

(19) *ThermoLIB | Center for Molecular Modeling. https://molmod.ugent.be/software/thermolib*.

(20) F. Zhu and G. Hummer, "Convergence and Error Estimation in Free Energy Calculations Using the Weighted Histogram Analysis Method," *Journal of Computational Chemistry*, 2012, **33**, 453–465.

(21) S. Kumar, J. M. Rosenberg, D. Bouzida, R. H. Swendsen and P. A. Kollman, "THE Weighted Histogram Analysis Method for Free-energy Calculations on Biomolecules. I. The Method," *Journal of Computational Chemistry*, 1992, **13**, 1011–1021.

(22) G. Kresse and J. Furthmüller, "Efficient Iterative Schemes for Ab Initio Total-Energy Calculations Using a Plane-Wave Basis Set," *Physical Review B*, 1996, **54**, 11169–11186.

(23) G. Kresse and D. Joubert, "From Ultrasoft Pseudopotentials to the Projector Augmented-Wave Method," *Physical Review B*, 1999, **59**, 1758–1775.

(24) J. P. Perdew, K. Burke and M. Ernzerhof, "Generalized Gradient Approximation Made Simple," *Physical Review Letters*, 1996, **77**, 3865–3868.

(25) S. Grimme, J. Antony, S. Ehrlich and H. Krieg, "A Consistent and Accurate Ab Initio Parametrization of Density Functional Dispersion Correction (DFT-D) for the 94 Elements H-Pu," *The Journal of Chemical Physics*, 2010, **132**, 154104.

(26) S. Grimme, S. Ehrlich and L. Goerigk, "Effect of the Damping Function in Dispersion Corrected Density Functional Theory," *Journal of Computational Chemistry*, 2011, **32**, 1456–1465.

(27) P. E. Blöchl, "Projector Augmented-Wave Method," *Physical Review B*, 1994, **50**, 17953–17979.

(28) T. Verstraelen, *DensPart (https://github.com/theochem/denspart)*.

(29) J. Enkovaara, C. Rostgaard, J. J. Mortensen, J. Chen, M. Dułak, L. Ferrighi, J. Gavnholt, C. Glinsvad, V. Haikola, H. A. Hansen, H. H. Kristoffersen, M. Kuisma, A. H. Larsen, L. Lehtovaara, M. Ljungberg, O. Lopez-Acevedo, P. G. Moses, J. Ojanen, T. Olsen, V. Petzold, N. A. Romero, J. Stausholm-Møller, M. Strange, G. A. Tritsaris, M. Vanin, M. Walter, B. Hammer, H. Häkkinen, G. K. H. Madsen, R. M. Nieminen, J. K. Nørskov, M. Puska, T. T. Rantala, J. Schiøtz, K. S. Thygesen and K. W. Jacobsen, "Electronic Structure Calculations with GPAW: A Real-Space Implementation of the Projector Augmented-Wave Method," *Journal of Physics: Condensed Matter*, 2010, **22**, 253202.

(30) J. J. Mortensen, L. B. Hansen and K. W. Jacobsen, "Real-Space Grid Implementation of the Projector Augmented Wave Method," *Physical Review B*, 2005, **71**, 035109.

(31) A. H. Larsen, J. J. Mortensen, J. Blomqvist, I. E. Castelli, R. Christensen, M. Dułak, J. Friis, M. N. Groves, B. Hammer, C. Hargus, E. D. Hermes, P. C. Jennings, P. B. Jensen, J. Kermode, J. R. Kitchin, E. L. Kolsbjerg, J. Kubal, K. Kaasbjerg, S. Lysgaard, J. B. Maronsson, T. Maxson, T. Olsen, L. Pastewka, A. Peterson, C. Rostgaard, J. Schiøtz, O. Schütt, M. Strange, K. S. Thygesen, T. Vegge, L. Vilhelmsen, M. Walter, Z. Zeng and K. W. Jacobsen, "The Atomic Simulation Environment—a Python Library for Working with Atoms," *Journal of Physics: Condensed Matter*, 2017, **29**, 273002.

(32) *Yaff, yet Another Force Field; https://github.com/molmod/molmod*, in collab. with T. Verstraelen, L. Vanduyfhuys, S. Vandenbrande and S. Rogge.

(33) A. Ghysels, T. Verstraelen, K. Hemelsoet, M. Waroquier and V. Van Speybroeck, "TAMkin: A Versatile Package for Vibrational Analysis and Chemical Kinetics," *Journal of Chemical Information and Modeling*, 2010, **50**, 1736–1750.

(34) A. P. Thompson, H. M. Aktulga, R. Berger, D. S. Bolintineanu, W. M. Brown, P. S. Crozier, P. J. in 't Veld, A. Kohlmeyer, S. G. Moore, T. D. Nguyen, R. Shan, M. J. Stevens, J. Tranchida, C. Trott and S. J. Plimpton, "LAMMPS - a Flexible Simulation Tool for Particle-Based Materials Modeling at the Atomic, Meso, and Continuum Scales," *Computer Physics Communications*, 2022, **271**, 108171.

(35) T. Shire, K. J. Hanley and K. Stratford, "DEM Simulations of Polydisperse Media: Efficient Contact Detection Applied to Investigate the Quasi-Static Limit," *Computational Particle Mechanics*, 2021, **8**, 653–663.

(36) P. J. in 't Veld, S. J. Plimpton and G. S. Grest, "Accurate and Efficient Methods for Modeling Colloidal Mixtures in an Explicit Solvent Using Molecular Dynamics," *Computer Physics Communications*, 2008, **179**, 320–329.

Outlook

In this thesis, we explored two topics in an emerging field i.e., piezoelectricity of metal-organic frameworks (MOFs) for energy harvesting and rotational dynamics of linkers in metal-organic frameworks (MOFs). While piezoelectricity is a well-established phenomenon that is extensively studied in both inorganic and organic materials, its detailed exploration within MOFs for applications in energy harvesting has not been done so far. Owing to the well-known features of MOFs, they can have huge potential for piezoelectric energy harvesting. On the other hand, the second topic, which concerns the rotational dynamics of linkers in MOFs, represents a specialized area of research. It has the potential for intriguing applications, such as artificial molecular machines, but requires an extensive understanding of rotor dynamics for effective design and engineering.

Piezoelectric energy harvesting is becoming more and more important in our world as environmental concerns and the need for sustainable energy grow. It is an evolving field that has found applications in many diverse emerging fields including transportation, wireless electronics, the Internet of Things, and wearable and implantable biomedical devices.[1] Existing piezoelectric materials include inorganic ceramics, polymers, composites, and hybrid materials like organic-inorganic perovskites. Even though inorganic ceramics have high piezoelectric response, they have stiffer mechanical properties and high dielectric constants making them unfavorable for wearable and flexible device applications. On the other hand organic polymers are naturally flexible and have much lower dielectric constants than ceramics. However, organic polymers have lower piezoelectric response than ceramics. In that aspect, hybrid materials like metal-organic frameworks (MOFs) can show great potential for piezoelectric energy harvesting owing to their remarkable flexibility and low dielectric constants due to the high porosity of MOFs.[2, 3] These characteristics, combined with high piezoelectric constants e and d for MOFs, can lead to a high figure of merit (FOM) for piezoelectric energy harvesting.

Chapter 2 and Chapter 3 of this thesis are among the few studies that examine the structure-property relationships of piezoelectric properties in MOFs computationally. In chapter 2, the figure of merit (FOM) of Zeolitic Imidazolate Frameworks (ZIFs) (estimated from the piezoelectric constant d) is higher than the FOM of inorganic PZT and organic piezoelectric PVDF, demonstrating the future potential of MOFs as energy harvesters. Building on this work, chapter 3 reported the piezoelectric constant e for a dataset of MOFs. MOFs in this work exhibit higher e values compared to organic polymers and metal-free perovskites, but lower values when compared to conventional inorganic ceramics. Nevertheless, MOFs can be expected to show high piezoelectric constants (d) due to their highly flexible frameworks and very low dielectric constants favorable for energy harvesting. Moreover, among the piezoelectric MOFs identified in chapter 3, MOFs comprising of an asymmetric motif A-(short)M-(long)-A due to different bond lengths between A and M (where M is the inorganic cation, and A are the coordinating non-metal atoms) may exhibit ferroelectricity i.e., reversible and spontaneous polarization upon the application

of an external electric field. This is possible when A-M-A motifs which may be dipolar are organized in the MOF structure in a polar manner. It is especially advantageous for the processability of MOFs into energy harvesting devices.

The piezoelectric constant d, relevant for energy harvesting is influenced by both the mechanical properties of material and the piezoelectric constant e. However, due to the significant computational cost associated with calculating the mechanical properties, only the piezoelectric constant e was calculated for the extensive MOF database in chapter 3. Hence, exploring the calculation of d for high e MOF candidates identified in chapter 3 may be beneficial, as this could lead to discovering exceptional piezoelectric MOFs. Furthermore, the structural design guidelines provided in chapter 3 for achieving a high e value may be used as criteria for the search for new piezoelectric MOF candidates.

The rotational motion of organic components is a type of flexibility that is prevalent in MOFs and has a significant impact on their gas adsorption, separation, and diffusion properties. MOFs offer ideal platforms for spatially organizing these molecular rotors in a precise and predictable manner to achieve collectively working artificial molecular machines. External stimuli like light and electric fields may be used to control the rotational motion of organic linkers. As an example, the work by the group of Feringa *et al* demonstrated the light-driven unidirectional motion of molecular rotors in the crystalline state in the MOF framework.[4] This represents a crucial step toward attaining nanomotors embedded in a crystalline lattice that can produce useful work. To achieve cooperative functional motion, the engineering of correlated dynamics is necessary to realize the full potential of MOF-based crystalline molecular machines. A recent study by Evans *et al* also emphasizes the importance of cooperative rotation and specific arrangement of unidirectional rotation for achieving directional transport properties in molecular machine-containing frameworks.[5] Maximizing dynamic effects and obtaining cooperative molecular motion along long-length scales to achieve nano- and macroscopic function requires specific engineered design.[6] In that aspect, chapters 4 and 5 provide valuable insights on correlated linker dynamics emerging in MOFs.

In Chapter 4 we identified for the first time correlated rotor dynamics emerging between neighboring linkers in MOFs by the introduction of simple steric interactions between the linkers. In a 211 unit cell with two rotating organic linkers per MOF chain along the pore, gear-like rotational motion between them was identified, which is facilitated by their close arrangement. This work was extended in chapter 5 by simulating four and six rotating linkers per MOF chain along the pore direction in the unit cell. The presence of correlated rotor dynamics between the neighboring linkers is still observed and extends over long-length scales occurring at nanosecond timescales. However, the type of correlated rotor dynamics varies based on the kind of neighbor pairs (i.e., immediate neighbors or alternate neighbors). Some examples include, an increase or decrease in the width of the linker's librations in the immediate neighbors, whereas among the alternate neighbors coordinated rotations of large angles occur. This indicates the large number of rotational degrees of freedom possible for the organic linkers. Hence to achieve a collective motion of rotors or organic linkers in MOFs it requires a specific rotational degree of freedom for all linkers to be the only possibility. This requires specific design criteria like the rotor spacing, pore space around the rotors, and size of the rotor are some of them.

References

(1) N. Sezer and M. Koç, "A Comprehensive Review on the State-of-the-Art of Piezoelectric Energy Harvesting," *Nano Energy*, 2021, **80**, 105567.

(2) S. Eslava, L. Zhang, S. Esconjauregui, J. Yang, K. Vanstreels, M. R. Baklanov and E. Saiz, "Metal-Organic Framework ZIF-8 Films As Low-κ Dielectrics in Microelectronics," *Chemistry of Materials*, 2013, **25**, 27–33.

(3) S. Mendiratta, M. Usman, T.-T. Luo, B.-C. Chang, S.-F. Lee, Y.-C. Lin and K.-L. Lu, "Anion-Controlled Dielectric Behavior of Homochiral Tryptophan-Based Metal–Organic Frameworks," *Crystal Growth & Design*, 2014, **14**, 1572–1579.

(4) W. Danowski, F. Castiglioni, A. S. Sardjan, S. Krause, L. Pfeifer, D. Roke, A. Comotti, W. R. Browne and B. L. Feringa, "Visible-Light-Driven Rotation of Molecular Motors in a Dual-Function Metal–Organic Framework Enabled by Energy Transfer," *Journal of the American Chemical Society*, 2020, **142**, 9048–9056.

(5) J. D. Evans, S. Krause and B. L. Feringa, "Cooperative and Synchronized Rotation in Motorized Porous Frameworks: Impact on Local and Global Transport Properties of Confined Fluids," *Faraday Discussions*, 2021, **225**, 286–300.

(6) C. Stähler, L. Grunenberg, M. W. Terban, W. R. Browne, D. Doellerer, M. Kathan, M. Etter, B. V. Lotsch, B. L. Feringa and S. Krause, "Light-Driven Molecular Motors Embedded in Covalent Organic Frameworks," *Chemical Science*, 2022, **13**, 8253–8264.

Acknowledgments

As I start writing this on the last day of the year 2023 and reflect on the past few years of my PhD journey, I feel immensely grateful for all the people who have helped me throughout my academic and personal journey.

My Promotors I am deeply thankful to *Monique*, first for offering me the chance to work on this very interesting project on MOFs, despite my limited knowledge of MOFs. Thank you for assisting me at every small step during the initial years of my learning about MOFs. I always enjoyed our biweekly meetings with interesting discussions of my computational results and added knowledge of experimental and crystallography topics. There were many instances where the project execution became very difficult, and Monique was always there to support and guide me through. I am very appreciative of the autonomy in the project, which allowed me to explore and navigate the complexities of my research independently. Apart from the support in the PhD journey, I am extremely grateful for all her help and understanding during my tough personal circumstances, especially in my pregnancy.

Ferdinand, thank you for taking the role of promotor. Your inputs during the go-no-go meetings were very valuable in getting an external point of view on the progress of the project. Fortunately, we also got a chance to collaborate on the high-throughput piezoelectric chapter. Thank you for your practical contributions to this project and your feedback towards the final thesis. Also, thanks for organizing the DFT meetings with other PhDs working on computational projects and providing a platform for sharing our work.

I would sincerely like to thank the committee members *Prof. Freek Kapteijn, Prof. Evgeny Pidko, and Dr. Atul Bansode* for their valuable effort and time in reading, assessing the thesis and participating in the defense ceremony.

Throughout my PhD, I have had the opportunity to collaborate with different research groups for various chapters of my thesis and indeed spend some time in beautiful cities like Paris, Ghent, and Turin. Being part of an experimental group, this computational thesis would not have been possible without our collaborators. *Prof.F.X. Coudert (FX)*, I had a very welcoming research stay in Paris in your group. Thank you for your supervision, valuable time, and discussions on the rotational dynamics using the ab initio molecular dynamics chapter 4. *Dr. Louis Vanduyfhuys (Louis)*, thank you for guiding me through the process of force field development for the rotational dynamics using the classical molecular dynamics chapter 5. I appreciate your valuable time and effort throughout the project, especially in the writing of this chapter. I had a great time with the CMM group during my short visits to Ghent. Thanks to FX and Louis for also being a part of the defense committee and assessing all my chapters of the thesis.

Prof. Bartolomeo Civalleri (Mimmo) and *Lorenzo*, thank you for teaching me how to use CRYSTAL17 software and for your valuable contributions to the ZIFs chapter 2. Thank you, *Dr. Joris Bierkens (Joris)*, for collaborating with us on the statistical analysis of molecular dynamics trajectories of Nitro MIL-53. Even though that work is not a part of this thesis, it is an important addition to the manuscript which will be submitted soon to a journal. Thank you, *Dr. Artur Schweidtmann (Artur)*, for your time and suggestions on the selection of the database for the high throughput chapter 3.

Several attempts conducted by my students have contributed to the results presented in different chapters of this thesis. Ravi and Kevin, it was a pleasure supervising you through your master's and bachelor's theses. Ravi, thank you for your Python scripts for the analysis of the output files, which I could use for my calculations as well. Kevin, it was a difficult project we started on the force fields for MIL-53, especially for a bachelor's thesis. Thank you for your efforts and work which helped me determine the next steps for the chapter 5.

Monique's group The computational projects, both piezoelectricity and rotational dynamics of linkers, involved my experimental counterparts Davide and Adrian. Davide, you had a more challenging goal to achieve than I had. You never gave up; I only saw you trying new experimental methods and synthesizing various MOFs to make it work. I always looked forward to hearing more about your results, discussing them, and exchanging ideas for MOFs that could show high piezoelectric properties. I wish we found the interesting Mo-MOFs earlier in my PhD; that could have been interesting for you as well. Cannot wait to read your thesis and looking forward to your defense. All the best for your future and your fight for climate change. Adrian, during our first interaction via email, thank you for answering all the questions I had about the group and TU Delft before I decided to join the group. That helped me decide to join the group. Thank you for being the senior PhD person of the group (at the time) and sharing your knowledge on the rotational dynamics of linkers. It was great collaborating with you on the computational part of the chapter 4 (also the JACS paper). I am very glad the paper has both the experimental and computational results complementing each other.

Han (alias JCJ Mertens) Something is not working in my Python code, how to optimize for the speed of the calculation, latex formatting, and more... Only one name comes to my mind, of course after Google, Han! You are a lifesaver. Thank you for patiently helping me and giving your very valuable suggestions even in your very busy schedule. Unfortunately, our plan to have a combined defense party won't happen. But I am eagerly waiting for your defense.

Jelco, senior PhD among the new generation PhDs of Monique's group, Thank you for helping me at times with formatting in Latex. I have always enjoyed our interactions in the PhD office. All the best with your research! Chunyu, thanks for your ongoing experimental work on the Mo-MOFs. Very excited to see it happen. All the best for your PhD.

Thanks to all the E2.220 PhD office and Monique's group members; Jelco, Han, Davide, Sven, Begum, Chunyu, Jintao, Hugo, Usman, and Vitalii. I had a great time sharing the PhD office with some of you and sharing our research in group meetings every week. I

always enjoyed our discussions on random topics, sharing the ups and downs of PhD and more. Had a good time during the lunch breaks outside in the sun, and Friday drinks. All the memories in that office will stay with me! All the best to you guys for your PhD and your future. Stefano, thanks for sharing your valuable knowledge of crystallography and MOFs with me. It was very helpful for me to visualize the MOF structures.

Former E2.220 PhD office members Thank you, Anahid, for passing on your former place by the window in the office. Thank you, Eduardo, for all the fun Friday drinks and fun moments in the office.

Els, special thanks to you. Starting from welcoming to the CE group, helping with various paperwork, contract changes and finally printing my thesis, you helped me with all the administrative things at every step. Thanks for making our life easier.

CE group Being part of the CE group, I got a chance to learn about the work of other research members, very different from mine (from Freek's and Atsushi's group) during the CE lunch meetings. Thanks to all the other members of the CE group, Atsushi, and technicians (Willy, Bart, Harrie, and Liliana) for our conversations in the corridor, Christmas dinners, and lunches, and for making me feel comfortable in the group. Finally, thanks to all the people at TU Delft who I might have missed and who were a part of my PhD journey.

I would specifically like to thank *Prof. Richard Hennig* (University of Florida (UF)) for piquing my interest in computational chemistry and giving me the opportunity to work on my first project related to computational chemistry during my Master's. This is one of the reasons why I decided to choose this project for my PhD. Chaitanya, thank you for supervising me in my Master's project and teaching me to use VASP. Biswas ji and other members of the Hennig group, thanks for making my stay memorable at UF.

Family and Friends I cannot look at the last few years in isolation without expressing my immense gratitude to my family and friends who helped me to be where I am today. Mummy (Nagaphani) and Papa (Satyanarayana), thank you for your dedication and the sacrifices you made for our (Me and my sister's) education. My dad's motto in life, keep learning/doing something new every day and their constant moral support is one of the things that pushed me to reach this far. Aaklu (Srikari), my very smart big sister encouraged me to be strong and motivated. Thank you for constantly checking on me despite my frustrations and always encouraging me to not give up. Bavagaru (brother-in-law), thank you for being an inspiration. Suryansh and Sisira, I love you. You bring cheer into my life.

My in-laws (Attayyagaru, mavvayyagaru, and Subha Vadina), thank you for your constant support during this tough PhD journey. Your support especially in the last few months was needed to finish writing my thesis. అమ్మమ్మ, తాతగారు చిన్నప్పటి నుంచి మమ్మల్ని జాగ్రత్తగా చూసుకుని ఏది కాదనకుండా మీరు మాకు ఇచ్చిన తీపి జ్ఞాపకాలకి థాంక్ యు. Miss you very much taatagaaru.

My favorite mavvayyas (uncles), One unique aspect about my uncles, each one of them helped me at different stages of my education. Ravi mamu, thank you for your constant care and supervision (sometimes a bit too much) during my Bachelor's at NITW, and Sheshu

Atta's yummy food on the weekends was a change from the hostel food. While doing my master's in the USA, it was indeed difficult being away from my parents alone in a new country. Thanks to Ramu mamu and Anitha atta, because of whom I was never homesick. Again, I was lucky to get yummy food made by Anitha atta. Nagesh mamu and Vaishali atta, thanks for all the financial help and for making sure I settled in well in the USA. I had a memorable time during Thanksgiving, spending time with you all. My dear cousins Radhir, Rajeev, and Rahav, I enjoyed all the fun in India and hope we continue to have many more.

My friends from NITW, Navya, Sindhu, Nehuu, Ujju, thank you for keeping up with my nerdiness. Harini, Sri Vidhya, and Raja thanks for the fun times in GG342. Mounika, Deeksha, and Geethu, friends from what almost feels like childhood. All these people have been part of my tight friends' circle. Even though we do not spend a lot of time now, just a phone call, and in no time we are back together. I am very grateful for having such special friends in my life.

Friends in Amsterdam: Tulika, Abhishek, Sonia (we miss you), Vipul and Arka, thank you for making the gloomy covid times cheerful and most memorable. Alpi and Priya, I am glad I met you guys and I always enjoyed our girls meets.

Saving the best for the last, my husband and partner in everything PV (Pramod), thank you for your immense patience and support during the highs and lows of this PhD journey. Your advice and encouragement during the tough times are what kept me going. Special mention to our daughter Ishanvi for coming into our life and spreading her smiles and cuteness every day.

List of Publications

Journal articles

S. Mula, L. Donà, B. Civalleri, and M. A. van der Veen, ACS Applied Materials & Interfaces 2022 14 (45), 50803-50814.

A.G. Nelson, **S. Mula**, M. Šimėnas, S. Balčiūnas, A.R. Altenhof, C.S. Vojvodin, S. Canossa, J. Banys, R. W. Schurko, F.X. Coudert, and M.A. van der Veen, Journal of the American Chemical Society 2021 143 (31), 12053-12062.

S. Mula, L. Vanduyfhuys, and M. A. van der Veen, Exploration of free energy profile and mechanism of long-range rotor dynamics in NO_2-MIL-53(Al) using force field molecular dynamics, *Manuscript in preparation*.

Patents

S. Mula, M.A. van der Veen, Piezoelectric Hybrid Organic-Inorganic frameworks, Patent filed on 26 May 2023, N2034922.

Oral Contributions

S. Mula, F.C. Grozema and M.A. van der Veen, "Computational Screening of Piezo-electric Properties in Metal-Organic Frameworks". Seventh International Conference on Multi functional, Hybrid and Nanomaterials, Italy, 2022.

S. Mula, A.G. Nelson, et al. "Emergence of Coupled Rotor Dynamics in Metal–Organic Frameworks via Tuned Steric Interactions". NWO CHAINS, The Netherlands, 2021.

S. Mula and D. Rega, "Structure–Property Relationship of Piezoelectric Properties in Zeolitic Imidazolate Frameworks: A Computational Study". IEEE, 2021 and EMRS, 2021.

Curriculum Vitae

Srinidhi Mula was born on 26th February 1993, in Kazipet (Warangal district, Telangana state), India. Most of her schooling happened in Hyderabad, where she finished her secondary school education in 2008 at The Mother's Integral High School. In August 2010, she enrolled in Metallurgical and Materials Science and Engineering at the National Institute of Technology, Warangal (NITW). Here, with a final year project on "Effect of Heat Treatment on microstructure and corrosion behavior of AZ61 Mg alloy", obtained her Bachelor's in April 2014. From July 2014 to July 2016, she worked as a Manager in the Corrosion and Inspection Department for two years at the largest petrochemical company in India, Reliance Industries Limited, Jamnagar. To pursue her master's, she prepared for the GRE while working at Reliance and applied to various universities in the USA. In September 2016, she joined the Materials Science and Engineering (MSE) course at the University of Florida, Gainesville. For her Master's project, she worked on "Validating an implicit self-consistent electrolyte model in plane-wave density-functional theory" under Prof. Dr. Richard Hennig in his group. This shaped her interest to further work on projects using computational chemistry. After obtaining her master's from the University of Florida in May 2018, she started her PhD at the Delft University of Technology, The Netherlands in July 2018. She worked in the Catalysis Engineering section of the Chemical Engineering Department and was supervised by Dr. ir. Monique van der Veen and Prof. dr. F.C. Grozema. In her Ph.D., she worked on modeling properties in metal-organic frameworks for their potential applications in energy harvesting and ferroelectrics. For her PhD research, she collaborated with professors from universities in France, Italy, and Belgium on various chapters of this thesis.